

## The surface chemistry of CO on iron and other bcc metals

**Citation for published version (APA):**

Scheijen, F. J. E. (2010). *The surface chemistry of CO on iron and other bcc metals*. [Phd Thesis 1 (Research TU/e / Graduation TU/e), Chemical Engineering and Chemistry]. Technische Universiteit Eindhoven.  
<https://doi.org/10.6100/IR657952>

**DOI:**

[10.6100/IR657952](https://doi.org/10.6100/IR657952)

**Document status and date:**

Published: 01/01/2010

**Document Version:**

Publisher's PDF, also known as Version of Record (includes final page, issue and volume numbers)

**Please check the document version of this publication:**

- A submitted manuscript is the version of the article upon submission and before peer-review. There can be important differences between the submitted version and the official published version of record. People interested in the research are advised to contact the author for the final version of the publication, or visit the DOI to the publisher's website.
- The final author version and the galley proof are versions of the publication after peer review.
- The final published version features the final layout of the paper including the volume, issue and page numbers.

[Link to publication](#)

**General rights**

Copyright and moral rights for the publications made accessible in the public portal are retained by the authors and/or other copyright owners and it is a condition of accessing publications that users recognise and abide by the legal requirements associated with these rights.

- Users may download and print one copy of any publication from the public portal for the purpose of private study or research.
- You may not further distribute the material or use it for any profit-making activity or commercial gain
- You may freely distribute the URL identifying the publication in the public portal.

If the publication is distributed under the terms of Article 25fa of the Dutch Copyright Act, indicated by the "Taverne" license above, please follow below link for the End User Agreement:

[www.tue.nl/taverne](http://www.tue.nl/taverne)

**Take down policy**

If you believe that this document breaches copyright please contact us at:

[openaccess@tue.nl](mailto:openaccess@tue.nl)

providing details and we will investigate your claim.

# The Surface Chemistry of CO on Iron and other bcc Metals

PROEFSCHRIFT

ter verkrijging van de graad van doctor aan de  
Technische Universiteit Eindhoven, op gezag van de  
rector magnificus, prof.dr.ir. C.J. van Duijn, voor een  
commissie aangewezen door het College voor  
Promoties in het openbaar te verdedigen  
op woensdag 10 maart 2010 om 16.00 uur

door

Freek Johannes Emiel Scheijen

geboren te Sittard



Dit proefschrift is goedgekeurd door de promotor:

prof.dr. J.W. Niemantsverdriet

Copromotor:

dr. D. Curulla-Ferré

Scheijen, Freek J.E.

*The Surface Chemistry of CO on Iron and other bcc Metals*

Technische Universiteit Eindhoven, 2010

A catalogue record is available from the Eindhoven University of Technology Library

ISBN: 978-90-386-2164-7

Copyright © 2010 by Freek J.E. Scheijen

The research described in this thesis was carried out at the Schuit Institute of Catalysis within the Laboratory of Inorganic Chemistry and Catalysis, Eindhoven University of Technology, The Netherlands.

Cover Design by Freek J.E. Scheijen

Printed at Wöhrmann Print Service, Zutphen

*To Ester and my family*



# Table of Contents

<b>Chapter 1</b>	Introduction	1
<b>Chapter 2</b>	Experimental and Computational Details	19
<b>Chapter 3</b>	Density Functional Theory Calculations	35
	a. Adsorption, Desorption, and Dissociation of CO on Molybdenum(100)	37
	b. Adsorption, Desorption, and Dissociation of CO on Tungsten(100)	57
<b>Chapter 4</b>	Adsorption and Dissociation of CO on Body Centered Cubic Transition Metals and Alloys: Effect of Coverage and Scaling Relations	75
<b>Chapter 5</b>	Polycrystalline Iron: CO Adsorption, Desorption, and Dissociation Kinetics and the Influence of Atomic Carbon and Oxygen	97
<b>Chapter 6</b>	Fe(100): CO Adsorption, Desorption, and Dissociation Kinetics and the Influence of Atomic Carbon and Oxygen	125
<b>Chapter 7</b>	Iron Oxide Nano Particles as Model Catalysts for the Fischer-Tropsch Synthesis: Morphology and Composition Study	152
<b>Chapter 8</b>	Summary and Outlook	173
	<b>Acknowledgements</b>	183
	<b>List of Publications</b>	187
	<b>Curriculum Vitae</b>	189



# 1

## Introduction

### *1.1 Catalysis*

Catalysis is a well-known phenomenon for most people in the world. Nevertheless, to the majority the concept of catalysis is limited to the process taking place under their car to clean the exhaust gases. Little do people know that around 90% of all commercially produced chemical products involve catalysis at some point in the process of their manufacture [1]. Thus, nowadays it is simply impossible for us to imagine a world without catalysis.

The origin of the term ‘catalysis’ dates back to 1835 and was introduced by the Swedish chemist Jöns Jakob Berzelius. In his report published in 1836 [2] he summarized his ideas on catalysis and wrote: *“It is, then, proved that several simple or compound bodies, soluble and insoluble, have the property of exercising on other bodies an action very different from chemical affinity. By means of this action they produce, in these bodies, decompositions of their elements and different recombinations of these same elements to which they remain indifferent”*. Next, Berzelius proposed the existence of a new force, which he called the ‘catalytic force’ and he referred to ‘catalysis’ as the decomposition of bodies by this force. In fact the word ‘catalysis’ is derived from the Greek word ‘katalusis’, which means ‘to dissolve’ or ‘loosen’. Basically, this meaning is one of the most trivial properties a catalyst possesses: the ability to ‘loosen’ or break chemical bonds. Berzelius’ ideas on catalysis can in principle be seen as one of the first descriptions of a catalyst. Nowadays, a more popular description of a catalyst is: a substance that accelerates the rate of a chemical reaction by offering different pathways lower in energy than the respective gas-phase reaction without being consumed itself. Within this respect, reactants first adsorb onto the catalyst, which in its turn can break the bonds of the reactants. Secondly, the catalyst enables the reactants to react on the surface by forming new bonds in the products. Finally, these products desorb from the surface leaving the catalyst unaltered and ready for the next reaction. This is the so-called catalytic cycle, which is depicted in

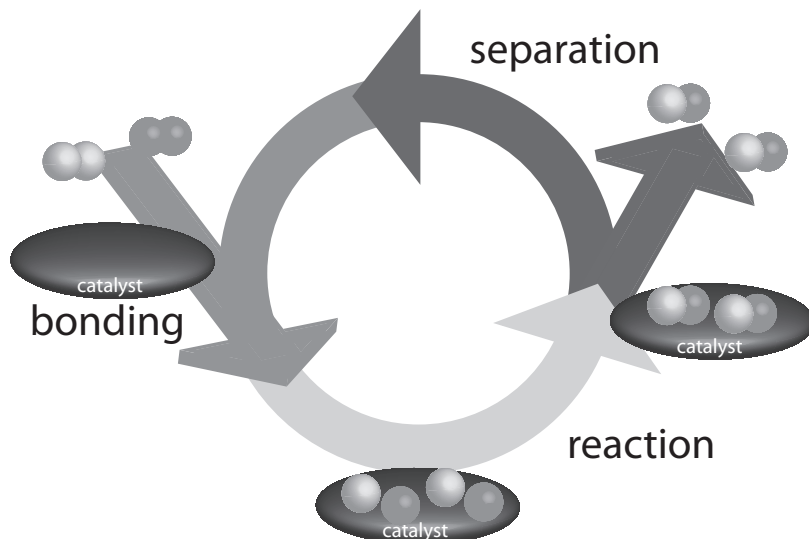


**Figure 1.1** Schematic representation of a catalytic cycle with its sequence of elementary reaction steps: bonding of the molecules to the catalyst surface, reaction of the molecules, and detachment of the products from the catalyst surface, freeing the surface for the next cycle. (Adapted from [3])

Figure 1.1.

To get a better understanding of the catalyst's behavior in terms of accelerating the reaction, a potential energy diagram is presented in Figure 1.2. This figure compares the non-catalytic gas-phase reaction with the catalytic reaction of molecules  $A_2$  and  $B_2$  reacting towards two  $AB$  molecules. As was described before for the catalytic cycle, the first step is the adsorption of the reactants  $A_2$  and  $B_2$ . This is always an exothermic process, leading to a lower energy in the potential energy diagram. Next, the catalyst breaks the  $A-A$  and  $B-B$  bonds of the molecules and when  $A$  and  $B$  atoms are in close proximity of each other due to their respective diffusion on the surface, the catalyst creates a new bond between  $A$  and  $B$  to produce  $AB$ . The activation barrier required for this catalyzed reaction to occur is noticeably lower than the non-catalyzed gas-phase reaction, therefore, leading to a much higher reaction rate at a given temperature and enabling much milder reaction conditions (lower temperatures and pressures). Subsequently,  $AB$  is desorbed from the surface and the reaction starts all over again. Both reaction pathways end at the same energy level, thus, the overall free energy is not changed when the reaction is catalyzed. Hence, a catalyst solely affects the kinetics of the reaction, but not its thermodynamics.

In general, catalysis can be subdivided into three major classes: homogeneous, heterogeneous, and bio catalysis. In homogeneous catalysis the catalyst is usually an organometallic complex that is dissolved in the solvent along with the reactants. Homogeneous catalysts usually have a high activity and selectivity. However,

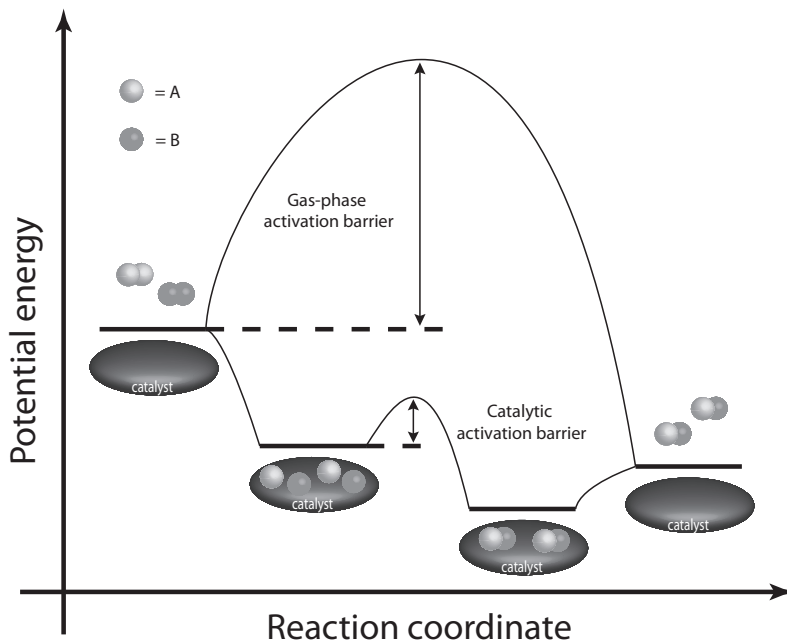


**Figure 1.2** Potential energy diagram of the reaction between two different molecules forming two completely new ones, showing the difference in activation barrier between the gas-phase and catalytic reaction. (Adapted from [3])

separation of the catalyst from the reaction mixture is difficult and because of the high costs of these catalysts they are less employed in industry. Homogeneous reactions are, therefore, mostly applied in the pharmaceutical (and cosmetics) industry where the added value is high, as relatively simple molecules are converted into the much more delicate structures that are used in pharmaceutical (and cosmetic) products.

Bio catalysis is a sort of homogeneous catalysis making use of nature's catalysts, the enzymes. Almost all enzymes can be considered as large proteins with a shape-specific active site. Having these optimal shapes for the reactant molecules (often referred to as substrates) these catalysts are highly specific and extremely active. Their reactivity can be altered by other molecules, in which inhibitors decrease and activators increase the activity. Enzymes are most frequently being used in detergents, the food industry, and for the production of pharmaceuticals.

In heterogeneous catalysis the catalyst is a solid, which catalyzes the reaction of reactants present in either a gas or liquid phase. Because these catalytic reactions occur solely on the surface, the majority of catalysts are nanometer-sized particles, supported on an inert porous material with a high surface area, such as alumina, silica, and carbon. However, unsupported catalysts are also being used (iron catalyst in Fischer-Tropsch synthesis) [4]. Although heterogeneous catalysts are mostly less active than



homogeneous catalysts, separation of the catalyst from the reaction system is relatively easy, thus, the catalyst can be re-used more often, which lowers their costs significantly. Therefore, heterogeneous catalysts are the most applied catalysts in the (petro)chemical industry. In this thesis all work presented is regarded as heterogeneous catalysis.

## ***1.2 Catalysis Research***

### **1.2.1 Ultimate Goal**

The past decades catalysis research has evolved from the description of catalysis to comprehending reaction mechanisms and kinetics at a molecular level and be able to relate it to the exact composition and structure of the catalyst. The evolution of catalysis research will ultimately lead to the prediction of an industrial catalyst that is able to produce the desired products under the ideal reaction conditions (most preferably environmentally friendly).

### **1.2.2 Different Areas of Research**

To be able to predict an industrial catalyst that produces the desired products under ideal reaction conditions sounds a lot easier in theory than it is in reality. A commercial catalyst system does not consist solely of the catalyst itself, but supporting materials and a wide variety of additives (promoters) are being used as well. Due to this addition of support material and extra additives, the commercial catalyst system is not suited for studies at a molecular level for several reasons. First, due to the porous structure of the support material the exposed surface area of the active phase is generally relatively low, thus limiting the use of spectroscopic characterization techniques, which in general require a high surface area. Second, as such, the active phase of the catalyst is also hard to identify, because the porous support blocks most of it. Third, the active phase is only a small part of the complete catalyst system, making it difficult to link macroscopic properties to its microscopic structure.

A system that is suited to study at a molecular level is the so-called flat model catalyst (Figure 1.3). Such a system consists of a flat substrate covered with a thin layer of supporting material on which the active catalyst material is deposited [5]. As a result, the exposed surface area of active material is relatively high, rendering it applicable for spectroscopic techniques. Moreover, additives are left out of the system and the influence of the support can be neglected. This approach has been used in our group extensively to study the thiophene hydrodesulfurization reaction [6-12], the mechanism of the Phillips ethylene polymerization catalyst [13-16], and more recently to obtain a better understanding of iron-based [17,18] and Ziegler-Natta olefin polymerization catalysts [19,20]. However, the catalyst particles on a supported flat

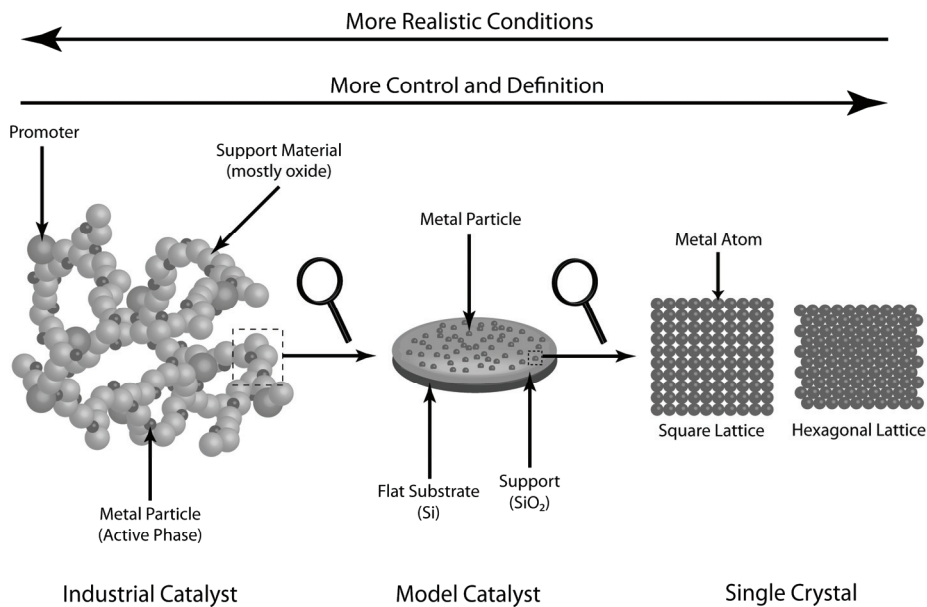


**Figure 1.3** Schematic representation of an industrial catalyst (left), a flat model catalyst (middle), and a single crystal surface (right).

model are mostly undefined in size and shape and exhibit several surface facets. Therefore, the most well-defined way to perform chemistry is still achieved on a single crystal. Such a crystal has a highly clean surface and when cut in a specific direction it only exposes one specific surface orientation.

However, a single crystal may seem as yet one step further away from an industrial catalyst, as is displayed in Figure 1.3. Fortunately this is not completely true. Although in (petro)chemical industry the average catalyst particle size is usually in the micro- to nanometer range, each of these particles often consists out of tiny single crystals. However, some differences exist between the industrial catalyst and single crystal work. First, the single crystals in the commercial catalyst do not display one single surface facet, but expose several surface orientations simultaneously. Second, the single crystals in the industrial catalyst are located on a porous support with additives close by, whereas support and additive interactions with the metal surface are not taken into account on a single crystal. Third, single crystal work is usually performed under ultra-high vacuum (UHV) conditions, whereas industrial catalysts perform under high pressures (the so-called pressure gap between single crystal work and industrial operation). Lastly, there is a ‘reactor environment gap’ between single crystal work and industrial operation, as the geometry of the reactor, mass and heat transfer, etc., are different. In spite of all these differences, single crystal work delivers valuable

information on (intrinsic) reaction kinetics and adsorbate–adsorbate interactions, which would not have been possible with industrial catalysts, and therefore, continues to stay important in unraveling the highly complex catalyst systems.

Since the development of fast computers over the past two decades a new field has emerged that has become important in assisting researchers: molecular modeling with in particular density functional theory (DFT) calculations. Now, the idea that quantum states can be described mathematically dates back to 1926, when Erwin Schrödinger derived his famous Schrödinger equation [21]. However, when a system consists of more than one electron, calculation of the exact wave function in this equation –which is the most complete description that can be given to a physical system– becomes virtually impossible, and approximate methods for the ground-state wave function such as Hartree-Fock [22,23] need to be used. Nonetheless, the wave function depends on many degrees of freedom [24], making it rather time-consuming and costly to calculate. DFT on the hand, which predicts electronic properties of atoms or molecules from the densities of their electron clouds (electron density), requires only three variables (3D space) [25], hence, significantly reducing the calculation time and cost.

Although the foundation of DFT also dates back to the 1920s and is based on the Thomas-Fermi-Dirac model [25], the model was seen as oversimplified and thought to be of no real importance for quantitative predictions of atoms and molecules. The paper by Hohenberg and Kohn [26] in 1964 changed this by providing the fundamental theorems showing that for ground states the Thomas-Fermi-Dirac model could be regarded as an approximation to an exact theory and that all observables of a many electron system are unique functionals of the electron density. Along with the Kohn-Sham equations in 1965 [27], which provided an approximation of these functionals development of DFT really took off.

While most terms in the Kohn-Sham's equation are readily calculated, the one that is not straightforward is the exchange correlation energy. This particular term accounts for the effects of electrons' tendencies to avoid each other. Different ways of dealing with this exchange correlation have been developed into different sets of equations, which are known as functionals. While in theory a perfect exchange correlation functional should exist to accurately describe any system, scientists have no method to systematically search for such a functional.

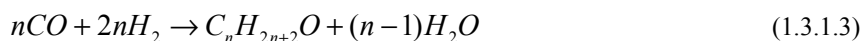
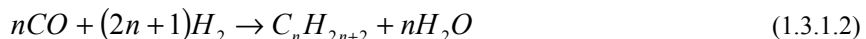
This automatically shows the weakness of DFT: the applied exchange correlation functional cannot be used for any system. DFT's shortcoming has been reported for the so-called overbinding effect of CO [28], but also calculated C-C bond energies for hydrocarbons [29-31], calculated energies for large hydrocarbons isomers [32], and reaction energies for an increasing carbon chain length [33] are quite often inaccurate. Moreover, DFT has difficulty describing systems that involve radical cations, charge transfer, and long-range interactions [34].

Despite all these deficiencies, DFT has proven itself to be very useful in predicting trends in catalytic reactivity [35] and in addition combining this reactivity with raw material costs, selectivity, and catalyst durability to find the best possible catalyst [36,37]. Therefore, DFT (molecular modeling in general) has become a reliable tool that can be integrated as another ‘analytical’ technique in catalysis (and not only catalysis) research.

## 1.3 Fischer-Tropsch Synthesis

### 1.3.1 Fischer-Tropsch Basics

In the Fischer-Tropsch synthesis a mixture of hydrocarbons (olefins, paraffins, and oxygenated products) is produced by reacting the gases hydrogen and carbon monoxide –also referred to as synthesis gas– over mainly either iron- or cobalt-based catalysts. The overall reactions can be presented as follows:



in which, reactions (1.3.1.1), (1.3.1.2), and (1.3.1.3) represent the formation of olefins, paraffins, and oxygenates, respectively. Reaction (1.3.1.4) is the water-gas shift reaction, which mainly occurs on the iron-based catalysts. Moreover, all reactions are highly exothermic and removing heat from the reactor is a major challenge in FTS technology.

The reaction mechanism of the Fischer-Tropsch process has been discussed for over 85 years. During this period three major reaction mechanisms have been proposed:

- (1) the ‘carbide’ mechanism [38,39]
- (2) the ‘enol’ mechanism [40,41]
- (3) the ‘CO insertion’ mechanism [42,43]

In principle, the process is a polymerization reaction with an initiation step to start a chain, propagation steps to grow the chain, and a termination step to stop the growth. The major discrepancy between these models is that the building block of the propagation step is different. The building blocks are  $CH_x$ , H-C-OH, and CO for the carbide, enol, and CO insertion model, respectively. For detailed schematics of the different models the reader is referred to papers by Davis [44] and Dry [45]. Out of these mechanisms the carbide model is the most commonly accepted one. However, since the product distribution is completely different for an iron catalyst (especially more oxygen containing products) than a cobalt-based catalyst, it is likely that the mechanism (or at least the probability of certain reactions) is not the same on both

surfaces.

The chain lengths of hydrocarbons follow a statistical distribution named after Anderson, Schulz, and Flory [46-48] and is given by:

$$w_i = i(1 - \alpha)^2 \alpha^{i-1}, \quad (\text{eq. 1.3.1.1})$$

in which,  $i$  is the number of carbon atoms,  $w_i$  is the weight fraction of chain length  $i$ ,  $\alpha$  is the chain length probability, and  $(1-\alpha)$  is the probability that a certain chain terminates. In Figure 1.4 the product distribution is shown as predicted by equation (1.3.1.1) for different  $\alpha$  values. For a typical iron catalyst the  $\alpha$  is around 0.65-0.70 (which produces predominantly gasoline, C<sub>5</sub>-C<sub>11</sub>), while cobalt catalysts have  $\alpha$  values between 0.75 and 0.90 (generating larger hydrocarbons) [3]. Changing operating conditions also lead to changes in the  $\alpha$  value. Lowering the temperature, reducing the H<sub>2</sub>/CO ratio, and increasing the pressure, all result in a higher  $\alpha$  value (longer chains). In addition, promoters used in the reaction also tend to increase the chain length.

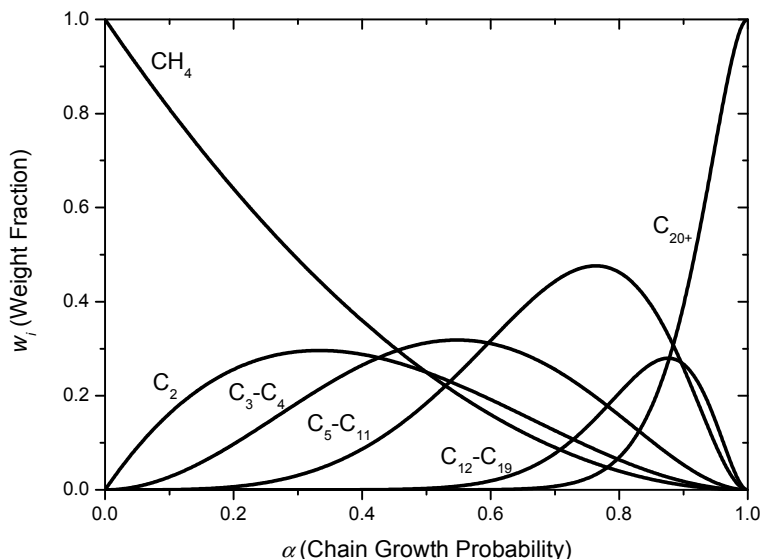


**Figure 1.4** Anderson-Schulz-Flory distribution for different  $\alpha$  values.

### 1.3.2 Historic Development

The catalytic synthesis of hydrocarbons from CO hydrogenation was first discovered in 1902, when Sabatier and Senderens [49,50] reported the reaction of CO and H<sub>2</sub> towards CH<sub>4</sub> over reduced nickel and cobalt catalysts. In 1913, a patent was granted to the Badische Anilin und Soda Fabrik (BASF) [51] for the synthesis of higher hydrocarbons and oxygenated compounds over alkali-activated cobalt and osmium oxides supported

on asbestos. This initial work was not continued at BASF, due to the First World War as well as priorities given to the development of ammonia and methanol synthesis. Instead, Franz Fischer and Hans Tropsch both working at the Kaiser-Wilhelm (currently Max Planck) Institute für Kohlenforschung in Mülheim a/d Ruhr learnt about this patent, which eventually led them to the production of liquid hydrocarbons from synthesis gas over alkalized iron catalysts at 100-150 bar and 400-450 °C in 1923 [52]. They called this mixture 'synthol', which consisted mainly of oxygenates, such as higher alcohols, aldehydes, ketones, and fatty acids. A few years later Fischer and Tropsch succeeded in producing a mixture which contained mainly hydrocarbons and only a little amount of oxygenates by using a cobalt-iron catalyst at reaction conditions of 250-300°C and 1 bar pressure [39,53]. By 1928, the use of an iron-copper catalyst enabled even a milder reaction temperature of 190°C at 1 bar pressure and yielded a mixture that solely consisted of hydrocarbon gases and liquids [54].

Fischer continued his investigations in the 1930s, which resulted in the construction of the first small pilot plant in Mülheim. Two years later the first large scale pilot plant was built by Ruhrchemie AG in Oberhausen-Holten, which operated at 20 bbl/day (1 bbl/day is around 50 tons/yr) using a catalyst with a weight distribution of 100g nickel – 25g manganese oxide – 10g aluminum oxide – 100g kieselguhr [55]. Due to the short life-time of the catalyst, and thus, significant loss of precious metal, Ruhrchemie AG was forced to use the more expensive metal cobalt. This led by the end of 1939 to nine Fischer-Tropsch plants in Germany having a combined production of almost 15 000 barrels of synthetic fuels per day using the 100g Co – 5g ThO<sub>2</sub> – 8g MgO – 200g kieselguhr catalyst developed by Ruhrchemie chemist Otto Roelen in the period of 1933-38 [55].

After the war production of synthetic fuels stopped in Germany, although the interest in Fischer-Tropsch synthesis remained, due to the belief of a limited amount of oil reserves left. The focus, however, changed from cobalt-based towards iron-based catalysts, as a result of some new discoveries made on the iron-based catalysts making them superior from a cost and product selectivity point of view [56]. Renewed interest in cobalt came at 1975 after publication of two papers by Vannice at Exxon [57,58] stating that cobalt and iron were among metals with the highest activity toward CO hydrogenation from the group VIII metals. Nevertheless, it was not until the late 1980s [59-68] that cobalt really returned within the FTS, which could be ascribed for most part to the interest of natural gas to fuel liquids (GTL) [69], mainly driven by stricter rules of the diesel fuel quality and the low prices of natural gas. For more detailed background information about various FT options and improvements in FT reactor technologies over the past 50 years the interested reader is referred to the review of Dry [70].

At present 160 000 bbl/day are produced in plants based on coal to liquids (CTL) technology at Sasol in South Africa and a 20 000 bbl/day plant is commissioned in China. Around 92 000 bbl/day are produced by GTL plants all over the world, from

which the latest large scale plant in Qatar (Oryx-GTL plant) –a joint venture between Sasol and Qatar Petroleum– produces over 34 000 bbl/day. In addition, this year (2010) two other GTL plants commissioned by Shell and NNPC/Chevron will be operational, which have a combined production of 104 000 bbl/day. However, compared to an oil consumption of 86 million barrels per day, synthetic fuels produced by FT technology is still a small percentage as to pumped crude oil.

### 1.3.3 Renewed Interest; Opportunity for Iron-Based Catalysts

Today, 87 years after Fischer and Tropsch made their discovery a renewed interest is shown in their process. The reason for this can be attributed to a couple of factors:

- The price of crude oil. At present (Jan 2010) the oil price is \$80 per barrel. Just a little bit more than a year ago this price spiked at \$140 per barrel. At such high prices the production of synthetic fuels from alternative feedstocks is attractive.
- Fuel quality regulations. Especially within the European Union the quality of diesel fuels needed to improve from a maximum sulfur content of 0.2 weight% in 1994 to 10 ppm in 2009 [71]. Synthetic fuels, produced from natural gas and coal are much cleaner than those obtained from crude oil. For example coal to liquids diesel [72] has a sulfur content of less than 5 ppm, and a cetane number of more than 70.
- Geographic political reasons. A lot of countries are dependent on crude oil from the ‘unstable’ Middle East and may want to reduce this. A good example is the United States, extremely reliant on Middle East oil, on the other hand has the biggest coal reserves in the world, estimated to be around 250 billion recoverable tons [73]. CTL technology may play an important role converting the coal to synthetic fuels in the near future, if a solution is found for the huge amounts of CO<sub>2</sub> produced in the process.
- The rapid economic growth of China and India. Home to more than a third of the world’s population, their energy demand increases more rapidly each day. China having 115 and India 92 billion tons of coal reserves [73], CTL technology can also play a huge part in converting these coal reserves into synthetic fuels. Interesting to mention is that Sasol (largest producer of synthetic fuels through FTS) has announced to build CTL plants in China and India in the near future [74,75].
- Biomass-to-liquids (BTL) or the carbon neutral economy. Biomass is the only ‘renewable’ carbon source that can be used for the production of chemicals and synthetic fuels. By the end of 2020 the European Union wants fuel to contain a minimum content of 8% produced from renewable sources [76]. CHOREN industries is an example of a company that produces a synthetic biodiesel (called SunDiesel) from biomass with the Shell’s Middle Distillate Synthesis [77,78].

All these factors are an opportunity for FTS with iron-based catalysts instead of cobalt-based catalysts for some reasons:

- Iron is almost 200-500 times cheaper than cobalt.
- Iron is the metal of choice when using coal or biomass as a feedstock. Synthesis gas derived from coal and biomass has a low H<sub>2</sub>/CO ratio, with coal typically around 1 [79], which makes cobalt the lesser metal as it needs an H<sub>2</sub>/CO ratio of at least 2. Although an extra water-gas shift reactor before the FTS can increase the H<sub>2</sub>/CO ratio to 2, which makes cobalt applicable as well, this would mean to build and operate one extra reactor. Iron, on the other hand, has water-gas shift activity (reaction 1.3.1.4) by itself, and therefore, can handle H<sub>2</sub>/CO ratios as low as 0.5, without the need of an extra water-gas shift reactor. Cobalt, alternatively, might be used when additional methane is added in the dense phase of the pyrolysis and gasification zone in the cogasification reactor, which leads to H<sub>2</sub>/CO ratios of nearly 2 [79]. Nevertheless, this would require the on-site availability of methane, whereas in the case of iron no such requirement is needed.
- Iron is less susceptible towards impurities in the feed than cobalt.

Because of these advantages, iron-based catalysts look very promising in being the Fischer-Tropsch catalysts of the future regarding coal- and biomass-based FTS. The commercial iron-based FT catalysts consist of precipitated iron with most commonly potassium (impacting both activity and product selectivity) and copper (significantly enhances the time needed for the catalyst to reach maximum activity) as promoters [80]. To reach higher activities and change the selectivity is mostly achieved by varying reaction conditions (such as temperature, pressure, and H<sub>2</sub>/CO ratio) or by adding other promoters, which in principle is altering the chain growth probability  $\alpha$ .

Before FT reaction, the iron-based catalyst consisting of Fe<sub>2</sub>O<sub>3</sub> and Fe<sub>3</sub>O<sub>4</sub> phases is reduced to metallic iron for activation purposes. When syngas is introduced after reduction, the catalyst has an induction period before maximum conversion is reached. Because metallic iron under syngas becomes a mixture of Fe<sub>3</sub>O<sub>4</sub>, iron carbides, and just a little bit of metallic iron [44], the metallic phase does not seem to be the most active one. It appears that either Fe<sub>3</sub>O<sub>4</sub> or iron carbide (or perhaps both) is (are) more active than metallic iron for the FTS. Because of these recent developments, a reaction mechanism has been proposed in our group for FTS on the iron carbide Fe<sub>2</sub>C<sub>5</sub>, instead of metallic iron [81]. Apart from what the most active phase is in the FTS, and which reaction mechanism is the correct one, other aspects of the FTS are still not fully known either and are worth investigating:

- The kinetics of the reaction, in particular the dissociation of carbon monoxide (which is one of the most important steps).
- The influence of other adsorbates such as carbon, oxygen, C<sub>x</sub>H<sub>x</sub>, C<sub>x</sub>H<sub>x+2</sub>, and C<sub>x</sub>H<sub>x+2</sub>O species on the kinetics and possible products of the reaction.
- The influence of other body centered cubic (bcc) transition metals, such as Mo, W, and Cr when alloyed with iron, on the catalyst activity and reaction selectivity.



## **1.4 Reaction Kinetics**

### **1.4.1 Importance of Reaction Kinetics in Catalysis**

Kinetics in catalysis is of great importance to study mechanistic details of a reaction. Traditional kinetic studies are mostly limited to macroscopic kinetics, in which conversion and selectivity are a measure for the catalytic activity and performance, and where process parameters such as concentration, pressure, and temperature are the tools to change the kinetics of the reaction. These kinetic studies are very useful to formulate an empirical kinetic expression that can be used in the design of chemical reactors, the comparison of different brands of catalysts, and studies of deactivation and poisoning of catalysts [82,83]. However, since different reaction mechanisms are able to display a similar macroscopic kinetic behavior, obtaining information of the reaction intermediates is important to determine the true reaction mechanism. Furthermore, it is essential to look at the microscopic level of kinetics. When the reaction mechanism is known, the rate equations of the elementary reactions in the mechanism can be mapped into a kinetic model. This kinetic model, then, can be used to validate or reject a certain reaction mechanism.

The knowledge obtained at the microscopic level can be extrapolated to the macroscopic kinetic behavior. As a result, kinetics provides a bridge between the microscopic world of reacting molecules and the macroscopic world of industrial reaction engineering. Because of this bridge between the microscopic and macroscopic world, understanding the kinetics of a certain reaction on a microscopic level is of utter importance, as understanding the microscopic kinetics of the appropriate mechanism may result in a better overall performance in a chemical plant. However, one should bear in mind that the microscopic kinetics is mostly determined by experiments on well-defined systems or by performing calculations of individual molecules and intermediates, while the reactions in industry are carried out on real catalyst systems under real reaction conditions. Hence, to deduce the macroscopic behavior from microscopic studies several factors are important, because the pressure, temperature, structure, and conversion all may be very different for both cases, which can lead to a different behavior in the reaction kinetics. For more detailed information of these factors as well as other challenges in kinetics studies we refer the interested reader to the review of Stoltze [83].

### **1.4.2 Reaction Kinetics Basics**

To describe the rate of an elementary reaction the transition state theory can be used. This theory was developed by Eyring [84,85], Evans [86], and Polanyi [87] in the mid 1930s and is based on a statistical mechanical approach. The theory states that an elementary reaction proceeds through an ‘activated complex’ called the transition state,

which is located at the top of the energy barrier between the reactants and products, as displayed schematically in Figure 1.5. The reaction event proceeds through one degree of freedom (e.g. vibration in the case of a dissociation reaction) called the reaction coordinate ( $q^{\#}$  in this case) and is only possible in the forward direction. Equilibrium is assumed between reactant and transition state for all other degrees of freedom, in which the corresponding equilibrium constant  $K^{\#}$  can be expressed in terms of partition functions of both the reactant in the ground state,  $q$ , and the excited state,  $q^{\#}$ . Such a partition function is defined as a thermodynamical function of state which, through the sum over all the energy levels contains all properties of the system. The most important contributions within this system can be ascribed to translational, rotational, vibrational, and electronic energies. The reaction coordinate is excluded from the partition state of the transition state  $q^{\#}$ , but is accounted for by the factor  $k_B T/h$  being the effective rate of crossing the energy barrier by the activated complex [3].

This leads to the transition state theory expression for the rate constant  $k_{\text{TST}}$ :

$$k_{\text{TST}} = \frac{k_B T}{h} \cdot \frac{q^{\#}}{q} \cdot e^{-\frac{\Delta E}{k_B T}}, \quad (\text{eq. 1.4.2.1})$$

in which  $k_B$  is the Boltzmann constant,  $T$  the temperature,  $h$  Planck's constant, and  $\Delta E$  the energy difference between the potential energy of  $R$  and  $R^{\#}$  which are both given with respect to the same zero energy level.

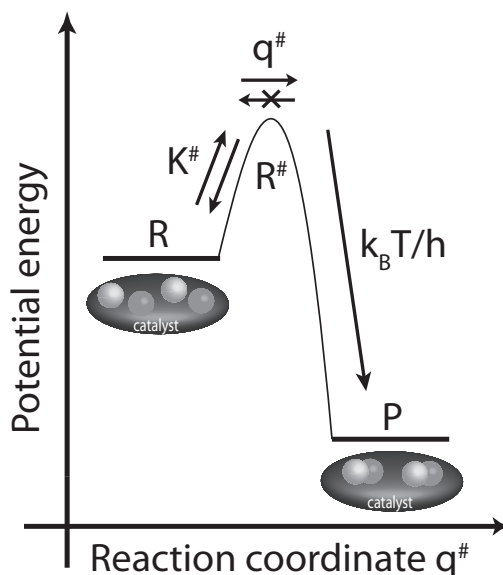


**Figure 1.5** Schematic representation of the transition state theory. The reactant  $R$  is in equilibrium with the activated complex  $R^{\#}$  for all degrees of freedom, except the reaction coordinate  $q^{\#}$ . The effective rate of crossing the energy barrier to produce product  $P$  is equal to  $k_B T/h$ . (Adapted from [3])

The rate constant according to the transition state theory closely resembles the empirical rate constant described by Arrhenius:

$$k_{Arr} = \nu_{Arr} \cdot e^{-\frac{E_{act}}{k_B T}} \quad (\text{eq. 1.4.2.2})$$

However, the pre-exponential factor of the Arrhenius equation is not temperature dependent, thus,  $E_{act}$  and  $\Delta E$  are not identical, although differences are very small [3].

### ***1.5 Interactions of adsorbed Species***

Adsorbed species interact with both the metal substrate as well as with each other. Interaction of adsorbed species with one another is often referred to as a lateral interaction. This lateral interaction consists of several contributions [88], which can be categorized as either direct ('through space') or indirect ('through metal') interactions. Experimentally, it is very difficult to distinguish between the different contributions and most of the times only an overall effect of all these interactions is measurable. This overall interaction effect is either attractive or repulsive, i.e., an adsorbed species is either stabilized or destabilized on the surface, respectively.

Although these interactions are not that important at low adsorbate coverage (adsorbates still have enough space to move around freely) they can become significant at a higher coverage in which they can influence the rate and type of reactions that take place on a catalyst surface and may even open up new reaction pathways that were not available before.

Within our group we performed many studies to understand, quantify, and visualize lateral interactions on rhodium surfaces [89-91]. One of the most straightforward ways to visualize these lateral interactions is by using temperature programmed desorption (TPD). In this technique lateral interactions can lead to new desorption states, induce a broadening of the desorption peak, or shift the temperature of the peak maximum. Another way to display lateral interactions is by utilizing low energy electron diffraction (LEED). When adsorbates have a repulsive interaction they form ordered structures on the surface that can be observed with LEED. When interactions are attractive, the adsorbates tend to form islands on the surface. When the adsorbates adsorb in nearest neighbor sites within the island, the structure is not visible with LEED, due to overlap of the metal atoms' pattern. However, looking at the reaction kinetics of the system the attractive interactions can be detected, since reaction typically occurs at the edge of the island.

## 1.6 Outline of the Thesis

The main inspiration behind the research in this thesis is to elucidate the dissociation reaction of carbon monoxide on body centered cubic (bcc) transition metals –iron in particular– with respect to reaction kinetics and the influence of adsorbate interactions. This was done at different levels of control and definition. At the highest level of control and definition, (100) surfaces of several transition metals were studied by density functional theory (DFT) calculations. At a slightly lower definition and control, a single crystal (most perfect structure available experimentally) of iron with a (100) surface was investigated under ultra-high vacuum (UHV) conditions by applying several surface science techniques such as temperature programmed desorption (TPD), static secondary ion mass spectrometry (SSIMS), and low energy electron diffraction (LEED). One step further to more realistic conditions a poly crystalline iron surface (possessing several surface structures) was explored under UHV environment employing the same experimental methods as the single crystal. The most realistic conditions (closest to a real catalyst) were realized with iron nano particles deposited on a flat surface. However, as the development of well characterized systems needed time, this research could not yet be focused on the dissociation of CO, but on the stability of iron nano particles under hydrogen, carbon monoxide, and a mixture of both (synthesis gas) by using transmission electron microscopy (TEM).

In *Chapter 2* the experimental and theoretical techniques are discussed. An overview is presented of the ultra-high vacuum system, the poly crystalline iron, the iron single crystal, and the cleaning procedure that was used. In addition, spin coating of the iron nano particles on a flat substrate is explained.

The adsorption, desorption, and dissociation of CO on Mo(100) and W(100) has been calculated using DFT in *Chapters 3a and 3b*, respectively. Complete energy schemes are presented of the CO dissociation reaction at 0.25 and 0.5 monolayer (ML) CO coverage. Remarkable results for the CO frequency and the validity of the Brønsted-Evans-Polanyi (BEP) relation are discussed.

A comparison of the adsorption, desorption, and dissociation of CO at 0.25 and 0.5 ML coverages on the (100) surface between the four bcc transition metals Fe, Mo, W, and Cr using DFT calculations is presented in *Chapter 4*. Differences in CO stretching frequency, influence of lateral interactions of adsorbates, as well as the restriction of the BEP relation will be discussed. Moreover, by alloying iron with one of the other bcc metals the energetics of the dissociation reaction pathway can be influenced. It will be shown that scaling relations can also be applied to these bcc metals, as well as certain alloys, simplifying the search for better catalysts.

The adsorption, desorption, and dissociation of carbon monoxide on poly crystalline iron is presented in *Chapter 5* by using a combination of TPD and SIMS. It is shown that using SIMS as a surface sensitive technique to obtain kinetic data of the

dissociation reaction of CO is not straightforward, but can be achieved. In addition, the influence of pre-adsorbed atomic carbon as well as oxygen on the adsorption and desorption of CO is discussed.

Within *Chapter 6* a combination of all three surface science techniques is used for the adsorption, desorption, and dissociation of CO on Fe(100). Kinetic parameters of the dissociation reaction of CO were determined by SIMS measurements, which were fitted by a dissociation model. The influence of pre-adsorbed atomic carbon and oxygen on the adsorption and desorption behavior of CO is shown.

The potency and problems of a flat model approach for the investigation of iron oxide nano particles is shown in *Chapter 7*. The morphology and composition behavior of these nano particles is studied with TEM under different reactive environments of H<sub>2</sub>, CO, and syngas at atmospheric pressure. In addition, the application of XANES and EXAFS on these flat samples will be presented. The intriguing fact that TEM imaging reveals particles to be homogeneous in size and shape, yet the chemical behavior varies from particle to particle is discussed.

Finally, *Chapter 8* summarizes the most important results and conclusions of the thesis and presents an outlook for further work.

## References

- [1] Recognizing the Best in Innovation: Breakthrough Catalyst, R&D Magazine, September 2005, p20.
- [2] J. J. Berzelius, *Anns. Chim. Phys.* **61** (1836) 146.
- [3] I. Chorkendorff, J. W. Niemantsverdriet, Concepts of Modern Catalysis and Kinetics, Wiley-VCH, Weinheim, 2003.
- [4] B. Jager, R. Espinoza, *Catal. Today* **23** (1995) 17.
- [5] P. L. J. Gunter, J. W. Niemantsverdriet, F. H. Ribeiro, G. A. Somorjai, *Catal. Rev. -Sci. Eng.* **39** (1997) 77.
- [6] A. Borgna, E. J. M. Hensen, L. Coulier, M. H. J. M. de Croon, J. C. Schouten, J. A. R. van Veen, J. W. Niemantsverdriet, *Catal. Lett.* **90** (2003) 117.
- [7] A. Borgna, E. J. M. Hensen, J. A. R. van Veen, J. W. Niemantsverdriet, *J. Catal.* **221** (2004) 541.
- [8] L. Coulier, G. Kishan, J. A. R. Van Veen, J. W. Niemantsverdriet, *J. Phys. Chem. B* **106** (2002) 5897.
- [9] L. Coulier, G. Kishan, J. A. R. van Veen, J. W. Niemantsverdriet, *J. Vac. Sci. Technol. A* **19** (2001) 1510.
- [10] L. Coulier, J. A. R. van Veen, J. W. Niemantsverdriet, *Catal. Lett.* **79** (2002) 149.
- [11] G. Kishan, L. Coulier, V. H. J. de Beer, J. A. R. van Veen, J. W. Niemantsverdriet, *J. Catal.* **196** (2000) 180.
- [12] G. Kishan, J. A. R. van Veen, J. W. Niemantsverdriet, *Top. Catal.* **29** (2004) 103.
- [13] E. M. E. van Kimmenade, Ethylene polymerization over flat Phillips model catalysts, PhD Thesis, Eindhoven University of Technology, The Netherlands, 2006.
- [14] P. C. Thüne, A Surface Science Model for the Phillips Ethylene Polymerization Catalyst, PhD Thesis, Eindhoven University of Technology, The Netherlands, 2000.
- [15] P. C. Thüne, J. Loos, X. Chen, E. M. E. Kimmenade, B. Kong, J. W. Niemantsverdriet, *Top. Catal.* **46** (2007) 239.
- [16] E. M. E. van Kimmenade, J. Loos, J. W. Niemantsverdriet, P. C. Thuene, *J. Catal.* **240** (2006) 39.

- [17] W. Han, C. Müller, D. Vogt, H. Niemantsverdriet, P. C. Thüne, *Macromol. Rapid Commun.* **27** (2006) 279.
- [18] W. Han, H. Niemantsverdriet, P. C. Thüne, *Macromol. Symp.* **260** (2007) 147.
- [19] A. Andoni, J. C. Chadwick, S. Milani, H. Niemantsverdriet, P. C. Thüne, *J. Catal.* **247** (2007) 129.
- [20] A. Andoni, A flat model approach to Ziegler-Natta olefin polymerization catalysts, PhD Thesis, Eindhoven University of Technology, The Netherlands, 2009.
- [21] E. Schrödinger, *Phys. Rev.* **28** (1926) 1049.
- [22] V. Z. Fock, *Z. Phys.* **61** (1930) 126.
- [23] D. R. Hartree, *Proc. Camb. Philos. Soc.* **24** (1927) 89.
- [24] A. Szabo, N. S. Ostlund, Modern Quantum Chemistry. Introduction to Advanced Electronic Structure Theory, McGraw-Hill, New York, 1982.
- [25] R. G. Parr, W. Yang, Density-Functional Theory of Atoms and Molecules, Oxford University Press, New York, 1989.
- [26] P. Hohenberg, W. Kohn, *Phys. Rev.* **136** (1964) B864.
- [27] W. Kohn, L. J. Sham, *Phys. Rev.* **140** (1965) A1133.
- [28] G. Kresse, A. Gil, P. Sautet, *Phys. Rev. B* **68** (2003) 073401.
- [29] Y. Feng, L. Liu, J.-T. Wang, H. Huang, Q.-X. Guo, *J. Chem. Inf. Comput. Sci.* **43** (2003) 2005.
- [30] X.-Q. Yao, X.-J. Hou, H. Jiao, H.-W. Xiang, Y.-W. Li, *J. Phys. Chem. A* **107** (2003) 9991.
- [31] L. A. Curtiss, K. Raghavachari, P. C. Redfern, J. A. Pople, *J. Chem. Phys.* **112** (2000) 7374.
- [32] P. R. Schreiner, A. A. Fokin, R. A. Pascal, A. de Meijere, *Org. Lett.* **8** (2006) 3635.
- [33] C. E. Check, T. M. Gilbert, *J. Org. Chem.* **70** (2005) 9828.
- [34] E. K. Wilson, *Chem. Eng. News: Sci. Technol.* **86** (2008) 34.
- [35] J. K. Nørskov, T. Bligaard, A. Logadottir, S. Bahn, L. B. Hansen, M. Bollinger, H. Benggaard, B. Hammer, Z. Sljivancanin, M. Mavrikakis, Y. Xu, S. Dahl, C. J. H. Jacobsen, *J. Catal.* **209** (2002) 275.
- [36] M. P. Andersson, T. Bligaard, A. Kustov, K. E. Larsen, J. Greeley, T. Johannessen, C. H. Christensen, J. K. Nørskov, *J. Catal.* **239** (2006) 501.
- [37] F. Studt, F. Abild-Pedersen, T. Bligaard, R. Z. Sorensen, C. H. Christensen, J. K. Nørskov, *Science (Washington, DC, United States)* **320** (2008) 1320.
- [38] S. R. Craxford, E. K. Rideal, *J. Chem. Soc.* (1939) 1604.
- [39] F. Fischer, *H. Tropisch, Brennstoff-Chem.* **7** (1926) 97.
- [40] R. B. Anderson, Catalysis, in: P. H. Emmett (Eds.), *Kinetics and reaction mechanism of the Fischer-Tropsch synthesis*, Vol. 4, van Nostrand Reinhold, New York, 1956.
- [41] H. H. Storch, N. Golumbic, R. B. Anderson, The Fischer-Tropsch and Related Syntheses, John Wiley & Sons, Inc., New York, 1951.
- [42] H. Pichler, H. Schulz, *Chem.-Ing.-Tech.* **42** (1970) 1162.
- [43] I. Wender, S. Friedman, W. A. Steiner, R. B. Anderson, *Chem. Ind.* (1958) 1694.
- [44] B. H. Davis, *Catal. Today* **141** (2009) 25.
- [45] M. E. Dry, The Fischer-Tropsch synthesis processes, in: G. Ertl, H. Knözinger, F. Schüth, J. Weitkamp (Eds.), *Handbook of Heterogeneous Catalysis*, Wiley-VCH, Weinheim, 2008.
- [46] R. B. Anderson, *J. Catal.* **55** (1978) 114.
- [47] P. J. Flory, *J. Am. Chem. Soc.* **58** (1936) 1877.
- [48] G. V. Schulz, *Z. physik. Chem.* **B32** (1936) 27.
- [49] P. Sabatier, J. B. Senderens, *Compt. Rend. Acad. Sci. (Paris)* **134** (1902) 514.
- [50] P. Sabatier, J. B. Senderens, *J. Soc. Chem. Ind.* **21** (1902) 504.
- [51] A. Mittasch, C. Schneider, German Patent 293 787 (1913); 295 202 (1914); 295 203 (1914), to BASF.
- [52] F. Fischer, *H. Tropisch, Brennstoff-Chem.* **4** (1923) 276.
- [53] F. Fischer, *H. Tropisch*, German Patent 484 337 (1925), to Fischer/Tropsch.
- [54] F. Fischer, *H. Tropisch, Brennstoff-Chem.* **9** (1928) 21.
- [55] A. N. Stranges, Germany's Synthetic Fuel Industry 1927-45, in: AIChE Spring National Meeting, New Orleans, LA, 2003.
- [56] M. E. Dry, Catalysis Science and Technology, J. Anderson, M. Boudard (Eds.), Vol. 1, Springer, Berlin, 1981.
- [57] M. A. Vannice, *J. Catal.* **37** (1975) 462.
- [58] M. A. Vannice, *J. Catal.* **37** (1975) 449.

- [59] K. L. Agee, United States Patent 4 833 170 (1989), to GTG, Inc.
- [60] S. Bessell, United Kingdom Patent 2 225 255 (1990), to Broken Hill Pty. Co. Ltd.
- [61] P. Chaumette, C. Verdon, German Patent 4 219 690 (1992), to Institut Francais du Petrole.
- [62] S. Eri, J. G. Goodwin, Jr., G. Marcelin, T. Riis, United States Patent 4 801 573 (1989), to Den Norske Stats Oljeselskap A/S.
- [63] W. O. Haag, J. C. Kuo, P. B. Weisz, United States Patent 4 906 671 (1990), to Mobil Oil Corp.
- [64] E. Iglesia, S. Soled, R. A. Fiato, United States Patent 4 794 099 (1988), to Exxon.
- [65] C. H. McAteer, European Patent 261 870 (1988), to BP.
- [66] J. G. Miller, J. A. Rabo, United States Patent 4 874 732 (1989), to UOP Inc.
- [67] J. T. Miller, C. A. Radlowski, Canadian Patent 2 018 611 (1990), to Amoco Corp.
- [68] M. F. M. Post, W. A. Van Erp, European Patent 398 420 (1990), to Shell.
- [69] C. H. Bartholomew, Paper for AIChE 2003 Spring National Meeting, New Orleans, LA ([www.fischertropsch.org](http://www.fischertropsch.org)).
- [70] M. E. Dry, *Catal. Today* **71** (2002) 227.
- [71] <http://www.dieselnet.com/standards/eu/fuel.php>, Accessed 2009.
- [72] P. W. Schwaberg, I. S. Myburgh, J. J. Botha, P. N. Roets, L. P. Dancuart, in: Proc. of the 11th World Clean Air Congress, Durban, South Africa, September 1998.
- [73] <http://www.bp.com/CoalReservesTableend2007>, Accessed 2009.
- [74] E. van de Venter, Sasol Coal-to-Liquids Developments, in: Gasification Technologies Council Conference, San Francisco, CA, October 2005.
- [75] J. Sarkar, *Platt's International Coal Report* **840** (2007) 17.
- [76] H. Leibold, A. Hornung, H. Seifert, *Powder Technology* **180** (2008) 265.
- [77] [http://www.choren.com/en/energy\\_for\\_all/sundiesel\\_sup\\_sup\\_facility\\_development/](http://www.choren.com/en/energy_for_all/sundiesel_sup_sup_facility_development/), Accessed 2009.
- [78] B. Hoffmann, *Aufbereitungs Technik* **49** (2008) 6.
- [79] Y. Cao, Z. Gao, J. Jin, H. Zhou, M. Cohron, H. Zhao, H. Liu, W. Pan, *Energy & Fuels* **22** (2008) 1720.
- [80] B. H. Davis, *Catal. Today* **84** (2003) 83.
- [81] J. M. Gracia, F. F. Prinsloo, J. W. Niemantsverdriet, *Catal. Lett.* **133** (2009) 257.
- [82] H. Lynggaard, A. Andreasen, C. Stegelmann, P. Stoltze, *Prog. Surf. Sci.* **77** (2004) 71.
- [83] P. Stoltze, *Prog. Surf. Sci.* **65** (2000) 65.
- [84] H. Eyring, *J. Chem. Phys.* **3** (1935) 107.
- [85] W. F. K. Wynne-Jones, H. Eyring, *J. Chem. Phys.* **3** (1935) 492.
- [86] M. G. Evans, M. Polanyi, *Trans. Faraday Soc.* **31** (1935) 875.
- [87] M. Polanyi, *J. Chem. Soc.* (1937) 629.
- [88] S. J. Lombardo, A. T. Bell, *Surf. Sci. Rep.* **13** (1991) 1.
- [89] M. J. P. Hopstaken, Elementary Reaction Kinetics and Lateral Interactions in the Catalytic Reaction between NO and CO on Rhodium Surfaces, PhD Thesis, Eindhoven University of Technology, The Netherlands, 2000.
- [90] D. L. S. Nieskens, The role of adsorbate interactions in catalysis by metals, PhD Thesis, Eindhoven University of Technology, The Netherlands, 2006.
- [91] A. P. van Bavel, Understanding and Quantifying Interactions between Adsorbates: CO, NO and N- and O-atoms on Rh(100), PhD Thesis, Eindhoven University of Technology, The Netherlands, 2005.

# 2

## Experimental and Computational Details

### **Abstract**

*An overview and physical background of the experimental and computational techniques used to study the adsorption, reaction, interaction, and morphology of species on polycrystalline, single crystals, and model catalysts is provided in this Chapter. The employed experimental techniques are: TPD, SSIMS, LEED, TEM, XANES, and EXAFS. The computational technique used is PW-DFT. In addition to these techniques the UHV system, the cleaning procedure of the polycrystalline iron and Fe(100) single crystal, and spin-coating of the iron nano particles on the flat substrate will be discussed.*



## 2.1 Ultra-High Vacuum (UHV) Set-up

Experiments on the polycrystalline iron foil and Fe(100) single crystal were carried out in a stainless steel ultra-high vacuum (UHV) system with a base pressure of  $5 \cdot 10^{-11}$  mbar. The system consists of one analysis chamber (see Figure 2.1), equipped to perform temperature programmed desorption (TPD), static secondary ion mass spectrometry (SSIMS), and low energy electron diffraction (LEED). A sputter gun (VSW AS10) is used for sample cleaning. The chamber is pumped by a 500 l/s turbomolecular drag pump (Pfeiffer TMH 521) and a water cooled titanium sublimation pump. Gases can be introduced into the chamber by two different leak valves.

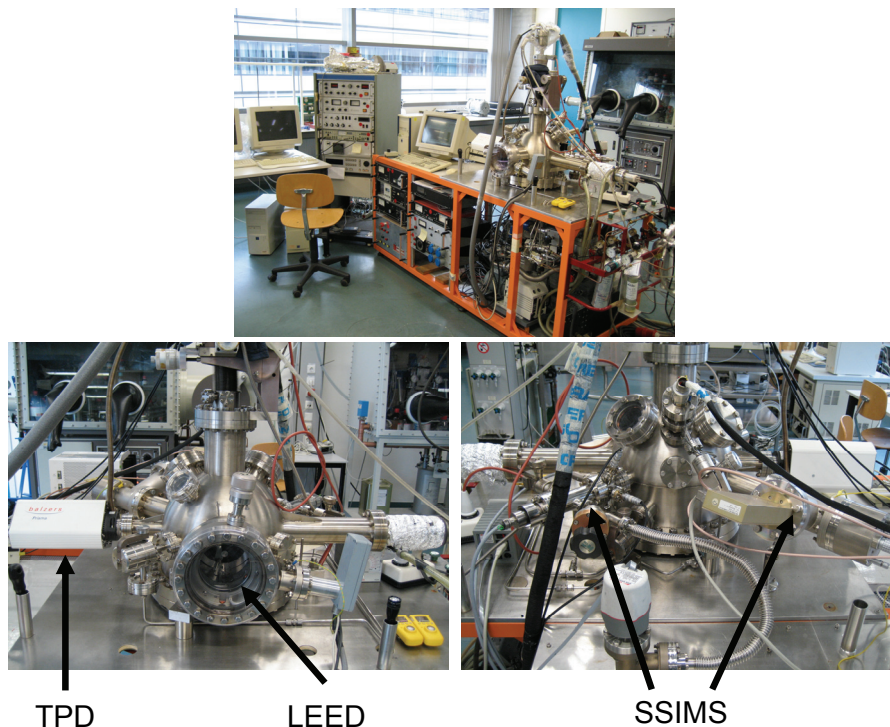


**Figure 2.1** Images of the used ultra-high vacuum equipment. The top picture shows an overview of the whole set-up. The bottom left picture displays the TPD and LEED techniques positioned at the front of the machine, while the bottom right image displays the backside of the set-up with the SIMS ion gun and mass spectrometer.

### 2.1.1 Instrumental Details

TPD experiments and residual gas analysis are performed with a quadrupole mass spectrometer (Balzers, Prisma QMA200) with a mass range  $m/e$  of 0-200 atomic mass

units (amu). SSIMS measurements were carried out employing a differentially pumped ion gun (SPECS PU-IQE 12/38) and a Balzers QMA400 mass spectrometer. The QMA400 module is composed of three units: an ion optics assembly, a quadrupole mass spectrometer (with mass range of 0-512 amu), and ion counting electronics. Attached to the analyzer are an RF generator (Balzers QMH400-5) and an ion counter pre-amplifier (Balzers CP400). Data is transmitted to the control unit (Balzers QMS422) which is subsequently directed to a personal computer (PC) for storage and analysis. LEED experiments have been done with a reverse-view four grid AES/LEED retractable optics (Spectaleed, Omicron Vacuumphysik GmbH). LEED patterns are attained and digitized using a CCD camera (Cohu) connected to a PC for analysis and storage of images.

### **2.1.2 The Polycrystalline Iron Foil and Single Crystal**

The polycrystalline iron foil –99.995% purity– with a diameter of 10 mm and a thickness of 0.27 mm (from Surface Preparation Laboratory, Zaandam) was mounted on a movable sample rod by spot welding two tantalum wires of 0.3 mm in diameter to the back of the iron foil (see Figure 2.2). The iron single crystal –99.98% purity– (from Surface Preparation Laboratory, Zaandam) with a (100) surface orientation within  $0.1^\circ$  (checked by Laue diffraction) and polished by standard procedures having a thickness of 1.2 mm and 10 mm in diameter was mounted on a moveable sample rod by two tantalum wires of 0.3 mm in diameter, pressed into small grooves on the side of the crystal (Figure 2.2). The part of the sample holder surrounding the foil and crystal was coated with gold to prevent adsorption of introduced gas. The temperatures of both samples were measured by a chromel-alumel thermocouple spot welded to the back of the polycrystalline foil and the single crystal. Both constructions enabled resistive heating up to 1500 K. Because iron shifts from the  $\alpha$  to the  $\gamma$  phase at 1183 K, the system was protected in exceeding a temperature of 1100 K. The sample could be cooled to 90 K using flowing liquid nitrogen through the manipulator.

### **2.1.3 Cleaning Procedure**

Prior to mounting the polycrystalline iron foil and iron single crystal in the UHV chamber, the samples were cleaned in an air-tight oven under 1 bar of flowing  $H_2$  at a temperature of 1040 K for a duration of 2 weeks to get rid of impurities such as boron, phosphorus, chlorine, but especially sulfur. Extensive  $Ar^+$  sputtering (0.5 keV,  $5 \mu a/cm^2$ ) at 1000 K was used to get rid of the remaining impurities such as carbon and residual oxygen until the SIMS spectrum revealed a clean surface and LEED pictures showed a clear  $p(1 \times 1)$  pattern. Routine cleaning consisted of 30 minutes of  $Ar^+$  sputtering at a temperature of 1000 K and was done on a daily basis. Since these temperatures are sufficient to anneal the surface, both the foil and single crystal were

kept no longer than 3 minutes at this temperature after  $\text{Ar}^+$  sputtering. This procedure was sufficient to remove the contamination according to SIMS spectra and LEED pictures. Before each experiment, the surface was bombarded at 1000 K with  $\text{Ar}^+$  for another 20 minutes and annealed for an additional 1-3 minutes, to ensure that all remaining carbon and oxygen of the previous measurement is removed.

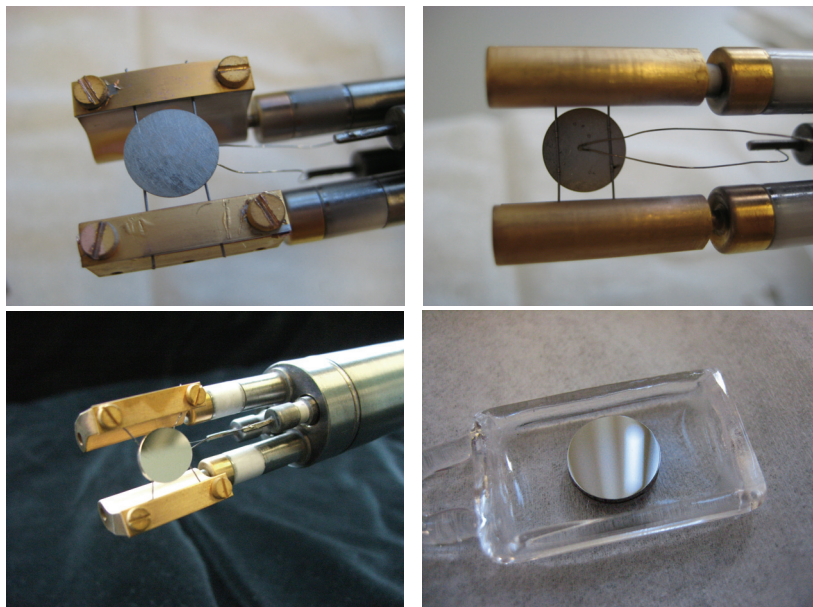


**Figure 2.2** Images of the polycrystalline Fe (top) and the Fe(100) single crystal (bottom).

## 2.2 Temperature Programmed (TP) Techniques

Temperature programmed techniques are used to examine a chemical reaction while linearly increasing the surface temperature [1]. The advantage of these techniques is that they are applicable to all the different areas of catalysis, i.e., single crystals, model catalysts, and industrial catalysts. Moreover, the techniques are inexpensive and experimentally easy to perform. When a reactive gas is passed over the catalyst surface during the linear heating process, such as oxygen or  $\text{H}_2$ , the technique is called temperature programmed oxidation (TPO) or hydrogenation/reduction (TPH/TPR), respectively. When employing a mixture of gases, one usually refers to temperature programmed reaction spectroscopy (TPRS).

Temperature programmed desorption is particularly used in surface science studies to investigate the desorption of gases (dosed at low temperature) from single crystals and polycrystalline foils into the vacuum [2]. The experimental set-up that is

used to perform such TPD experiment is depicted in Figure 2.3. The rate at which adsorbates desorb from the surface is given by the Arrhenius or Polanyi-Wigner equation [3]:

$$r_d = -\frac{d\theta}{dt} = k_{des} \theta^n = v_{des}(\theta) \theta^n \exp\left(-\frac{E_{des}(\theta)}{RT}\right), \quad (\text{eq. 2.2.1})$$

in which

- $r_d$  is the rate of desorption [change in adsorbate coverage per unit time]
- $\theta$  is the coverage in monolayers [number of adsorbates divided by the total number of substrate (metal) surface atoms]
- $t$  is the time [s]
- $k_{des}$  is the reaction rate constant for desorption [ $\text{s}^{-1}$  for first-order desorption]
- $n$  is the order of desorption
- $v_{des}(\theta)$  is the pre-exponential factor of desorption [ $\text{s}^{-1}$ ]
- $E_{des}(\theta)$  is the activation energy of desorption [J/mol]
- $R$  is the gas constant [J/mol/K]
- $T$  is the temperature [K]

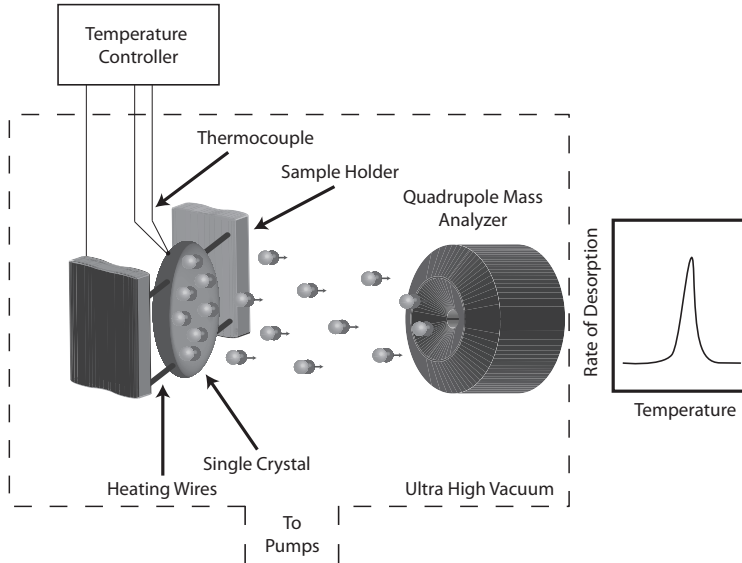


**Figure 2.3** Experimental set-up used to perform a TPD experiment. The single crystal is resistively heated by tantalum heating wires pressed in groves at the side of the crystal. The temperature is measured by a chromel-alumel thermocouple spot-welded to the back of the crystal. Desorption of the gases is analyzed by a quadrupole mass spectrometer. (Adapted from Niemantsverdriet [1])

Since linear heating rates are applied, the temperature can be written as  $T = T_0 + \beta t$  in which  $T_0$  is the initial temperature and  $\beta$  the heating rate. Thus, the desorption rate

can easily be rewritten as a change in adsorbate coverage per unit temperature by  $dT = \beta dt$ .

When the pumping speed is sufficiently high, re-adsorption of gases can be neglected and a linear relation exists between the signal from the mass spectrometer and the rate of desorption. As such, the area underneath the TPD spectrum is proportional to the total amount of desorbed species and, therefore, its initial coverage. Note that this initial coverage is a relative one. Hence, a relation exists between the exposure of an adsorbate, expressed in Langmuir ( $1 \text{ L} = 1.33 \cdot 10^{-6} \text{ mbar s}$ ) and its respective relative coverage.

In order to acquire an absolute coverage in terms of monolayers (ML), i.e., the number of adsorbed species divided by the total number of substrate (metal) surface atoms, a calibration point is needed. A way to achieve this is by using a complementary technique, like low energy electron diffraction, described in section 2.4. When adsorbates form ordered structures on the surface a LEED pattern can be observed. In the case of a bcc(100) metal surface, a  $c(2 \times 2)$  pattern for example corresponds to an absolute coverage of 0.5 ML (see also Figure 2.6 in section 2.4). Knowing the saturation coverage of a certain adsorbate from literature is another good approach to obtain a calibration point. Once a calibration point is available, the areas of the TPD spectra (relative coverage) can be converted into absolute coverages, hence, linking the exposure directly to the absolute coverage.

Apart from determining coverages, TPD can be used to extract kinetic parameters, such as the reaction order, activation energy of desorption, and the pre-exponential factor. Several methods have been developed to determine these parameters, from which the complete analysis proposed by King [3] is the most elaborate and exact. However, because this method is time-consuming, the complete analysis is rarely used in TPD. Simplified methods such as the Redhead [4], Chan, Aris, and Weinberg (CAW) [5], and the leading edge [6] method, therefore, are the most popular ways to obtain kinetic parameters. For more details regarding the different methods, the interested reader is referred to the ‘Spectroscopy in Catalysis’ book by Niemantsverdriet [1].

### **2.3 Secondary Ion Mass Spectrometry (SIMS)**

Secondary ion mass spectrometry is a very sensitive surface technique, able to detect surface species in the parts per million range and even ppb scale for favorable elements [7]. SIMS is most popular in concentration depth-profile and imaging studies of the surface. It can be operated in three different modes: dynamic, static, and imaging. The technique uses a primary ion beam (usually an ionized inert gas) with a typical kinetic energy ranging from 0.5 to 10 keV. Subsequently, the ion beam collides with the surface, transferring its kinetic energy. As a result, the energy is dispersed

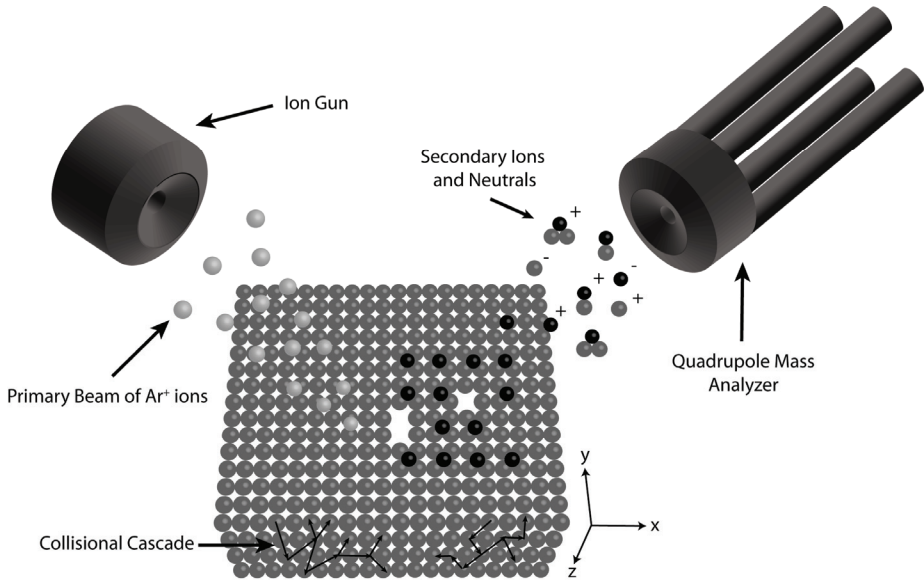


**Figure 2.4** SIMS principle: primary ions cause a collisional cascade in the uppermost surface layers of the sample. Some of these collisions end up at the surface where they stimulate the emission of secondary ion clusters. Consequently, these clusters are detected by a mass spectrometer.

through the upper surface layers, leading to a cascade of collisions. When one of these collisions is directed back toward the outer surface layer, its energy may stimulate the removal of an atom and/or cluster of atoms. These emitted secondary atom or atom clusters can either be neutral or charged. This is displayed schematically in Figure 2.4. In SIMS only charged species (or secondary ions) are detected by either a quadrupole or a time-of-flight mass spectrometer. The signal intensity of such a secondary ion is given by:

$$I_S(X^\pm) = I_p Y_X R^\pm \theta_X T, \quad (\text{eq. 2.3.1})$$

where

$I_S(X^\pm)$  is the intensity of the positively or negatively charged secondary ion  $X$  [ion count per second]

$I_p$  is the flux of primary ions [ion count per second]

$Y_X$  is the sputter yield of element  $X$  [number of atoms ejected per incident ion]

$R^\pm$  is the ionization probability of element  $X$ , i.e., the probability to leave the surface as a positive or negative ion

$\theta_X$  is the fractional concentration of element  $X$  in the surface layer

$T$  is the transmission of the mass spectrometer, which is typically  $10^{-3}$  and  $10^{-1}$  for a quadrupole and time-of-flight instrument, respectively

The signal intensity difference between elements is mainly determined by both



the sputter yield and the ionization probability. The sputter yield is relatively well understood and depends on the properties of the sample (such as mass of the sample atoms, surface roughness, and sample temperature) and the mass, energy, and angle of incidence of the primary ions [1,7]. On the other hand, the ionization probability is not well understood, and although a model has been proposed by Nørskov and Lundqvist [8], it only accounts quantitatively for a number of observations on metals. Because the ionization probability of an atom is also dependent on its surroundings (called the matrix effect), the model can only be used to qualitatively describe the ionization probability, making SIMS an extremely difficult technique for extracting quantitative information. However, dividing the metal–adsorbate intensities by metal ion intensities is a measure for the adsorbate coverage:

$$\theta_X \propto \frac{I_{M_y X^+}}{I_{M_y^+}}, \quad (\text{eq. 2.3.2})$$

in which:

- $\theta_X$  is the surface coverage of species  $X$
- $I_{M_y X^+}$  is the ion intensity of the metal–adsorbate ion  $M_y X^+$
- $I_{M_y^+}$  is the ion intensity of the metal ion

By dividing the intensities, the so-called matrix effect is expected to cancel out (when one assumes that both signals are influenced equally). Thus, using the intensity ratios, quantitative information can still be obtained by SIMS.

Strictly speaking SIMS is a destructive method, especially when used in the dynamic (used for depth-profiling) mode. Hence, probing adsorbates on the iron surface in this thesis is performed with static SIMS. In the static mode a primary ion flux of typically 1-2 nA/cm<sup>2</sup> reaches the surface, which corresponds to 10<sup>10</sup> ions/(cm<sup>2</sup> s). It is believed that each ion on the surface creates collisional effects of 10 nm in diameter, corresponding to an area of roughly speaking 100 nm<sup>2</sup> [9]. For a beam with an ion flux of 1-2 nA/cm<sup>2</sup> it takes ca. 60-30 minutes, respectively, to remove one monolayer of carbon monoxide on an iron surface, when a sputter yield of 4 is taken into account [1,9]. Since an experiment takes roughly 7 minutes at a heating rate of 2 K/s, hence, during which a maximum of 0.25 monolayer of adsorbate is sputtered from the surface, one may still wonder whether or not this is still static. However, static SIMS is always a trade-off between surface damage and signal intensity. As such, the above conditions were chosen as the maximum amount of damage allowed, because a lower ion flux would be insufficient to adequately detect the surface species by the quadrupole analyzer.

## 2.4 Low Energy Electron Diffraction (LEED)

Low energy electron diffraction is used to acquire information of the surface structure

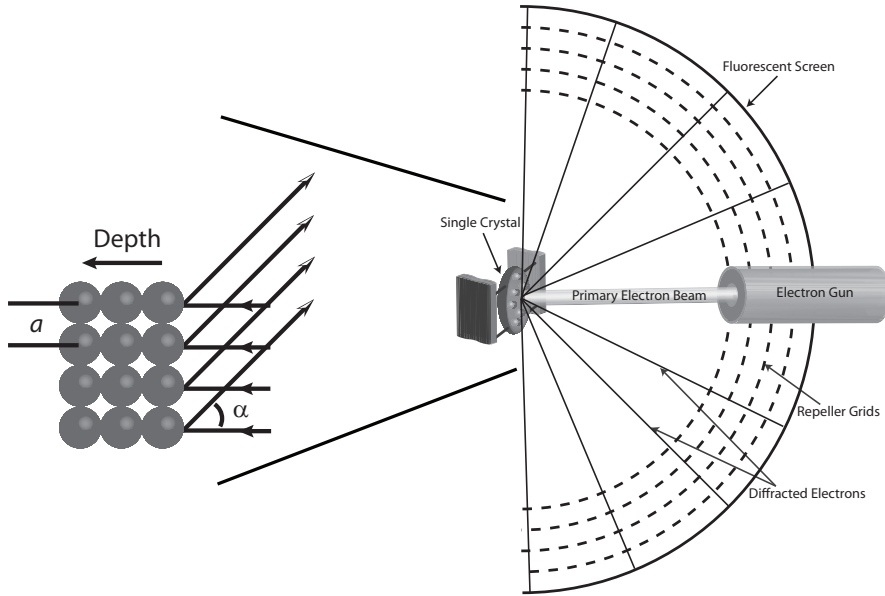


**Figure 2.5** Schematic picture of a low energy electron diffraction set-up. A beam of monochromatic electrons is directed towards the surface. The scattered electrons are detected on a fluorescent screen and form a constructive interference pattern that is related to the surface structure.

of a single crystal and to obtain the structure of ordered adsorbate layers. An electron gun is positioned along the surface normal of the single crystal producing a monochromatic beam of low energy electrons (50-200 eV), which upon hitting the surface scatter back elastically in all directions. The principle is illustrated in Figure 2.5. The electrons can be considered as a wave with a wavelength given by De Broglie relation:

$$\lambda = \frac{h}{\sqrt{2m_e E_{kin}}}, \quad (\text{eq. 2.4.1})$$

in which:

- $\lambda$  is the wavelength of the electrons [m]
- $h$  is Planck's constant [J s] = [kg m<sup>2</sup> s]
- $m_e$  is the mass of an electron [kg]
- $E_{kin}$  is the kinetic energy of an electron [kg m<sup>2</sup> s<sup>-2</sup>]

Since electrons behave like a wave, interference between the backscattered electrons occurs, resulting in a diffraction pattern on the fluorescence screen of the LEED apparatus with constructive interference (Bragg's reflection) in directions with:

$$\sin \alpha = \frac{n\lambda}{a} = \frac{nh}{a\sqrt{2m_e E_{kin}}}, \quad n = 0, 1, 2, \dots, \quad (\text{eq. 2.4.2})$$



where:

- $\alpha$  is the angle between the scattered electrons and the surface normal [ $^\circ$ ]  
 $n$  is the diffraction order  
 $a$  is the distance between scatterers, i.e., the lattice constant of a clean surface [m]

Subsequently, the diffraction pattern on the LEED screen corresponds to a certain surface ordering, shown for example in Figure 2.6 for an empty bcc(100) surface as well as a surface covered with 0.5 ML adsorbates.

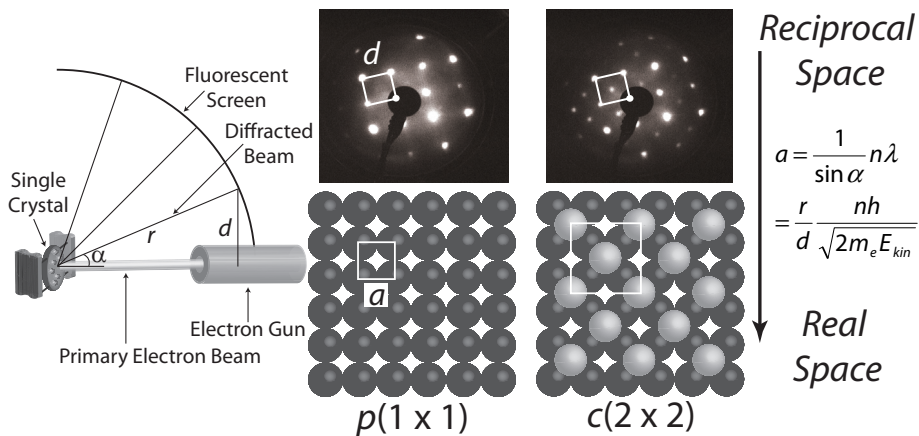


**Figure 2.6** Ordering of adsorbates on a bcc(100) surface. The middle images show the empty surface with a  $p(1 \times 1)$  structure, while the right hand pictures display the surface with 0.5 ML of adsorbed species ordering in a  $c(2 \times 2)$  fashion. The bottom pictures represent the real space, while the top images correspond to the reciprocal space as recorded on the fluorescent screen. The image on the left hand side serves as clarification when converting distance  $d$  in the reciprocal space to lattice constant ( $a$ ) in the real space.

## 2.5 Substrate for Iron Particles and Spin-Coating Technique

The substrates used for the iron nano particles are silica TEM grids that were custom made according to requested specifications. The side view of a typical TEM grid is shown in Figure 2.7. The basic preparation involved the deposition of silicon nitride ( $\text{Si}_3\text{N}_4$ ) both at the back and front of a standard (100) silicon wafer of about 120 mm in diameter. The nitride at the back was patterned to form an appropriate mask which facilitated anisotropic etching of the silicon, until the silicon nitride at the top was left suspended in its framework. The  $\text{Si}_3\text{N}_4$  layer on the top was made as thin as possible ( $\sim 15$  nm) to facilitate efficient TEM analysis. In short this leads to a disk consisting of 9 wafers; each containing 36 grids, all with a square window of  $200 \mu\text{m}$  in diameter serving as TEM imaging area (see Figure 2.7). An amorphous silica surface layer of

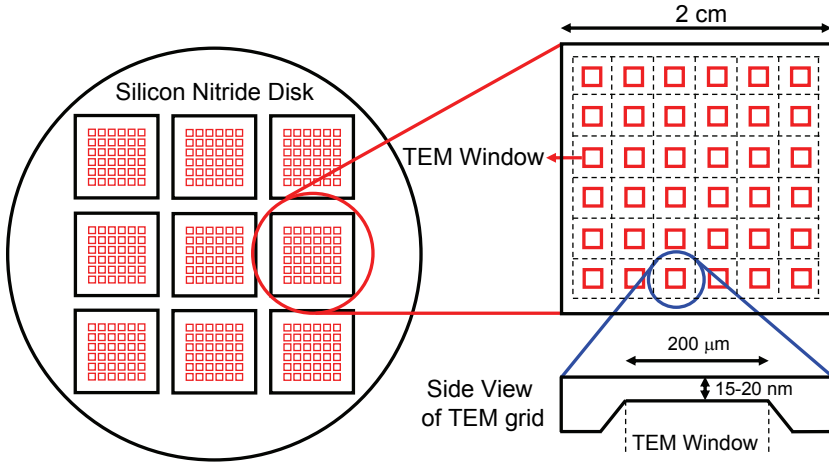


**Figure 2.7** Schematic representation of the silicon nitride disk containing nine wafers; each wafer has 36 grids, which all contain a small square window of  $200\ \mu\text{m}$  in diameter and  $15\text{-}20\ \text{nm}$  thick for TEM measurement.

about 3 nm thickness was formed by calcining the wafer in an oven at  $750\ ^\circ\text{C}$  for 24 hours to make the TEM grids more robust and susceptible for impregnation. The 9 square TEM wafers are then cut from the 120 mm round disk, which subsequently can be used to spin-coat.

Spin-coating is a technique in which an organic, inorganic, or polymeric substance from solution is coated on a substrate surface by high speed spinning. Due to this spinning process the solvent in the solution evaporates, leaving the desired material impregnated on the substrate. A picture and schematic representation of the spin-coat device used is shown in Figure 2.8.

In our case, a calcined silica TEM wafer is placed in the chuck, which is kept in place by small brims. Next, a solution of the desired material is drop casted onto the wafer. After that the chuck is spun at the desired speed of 2800 rpm, which yields a uniform film of solution as centrifugal forces of spinning eject solution from the wafer. At a certain moment this layer becomes so thin that the ejection and evaporation of solvent equally contribute in the thinning process. Henceforth, evaporation is dominant until at a certain time  $t_e$  the solvent is completely evaporated. The amount of deposited material  $M$  is determined by [10-12]:

$$M = 1.35C_0 \sqrt{\frac{\eta}{\rho\omega^2 t_e}}, \quad (\text{eq. 2.5.1})$$

in which:

- $M$  is the deposited amount of material per area [ $\text{kg m}^{-2}$ ]
- $C_0$  is the concentration of material in solution [ $\text{kg m}^{-3}$ ]

- $\eta$  is the viscosity of the solution [ $\text{kg m}^{-1} \text{s}^{-1}$ ]  
 $\rho$  is the density of the solution [ $\text{kg m}^{-3}$ ]  
 $\omega$  is the spinning speed [ $\text{s}^{-1}$ ]  
 $t_e$  is the evaporation time [s]

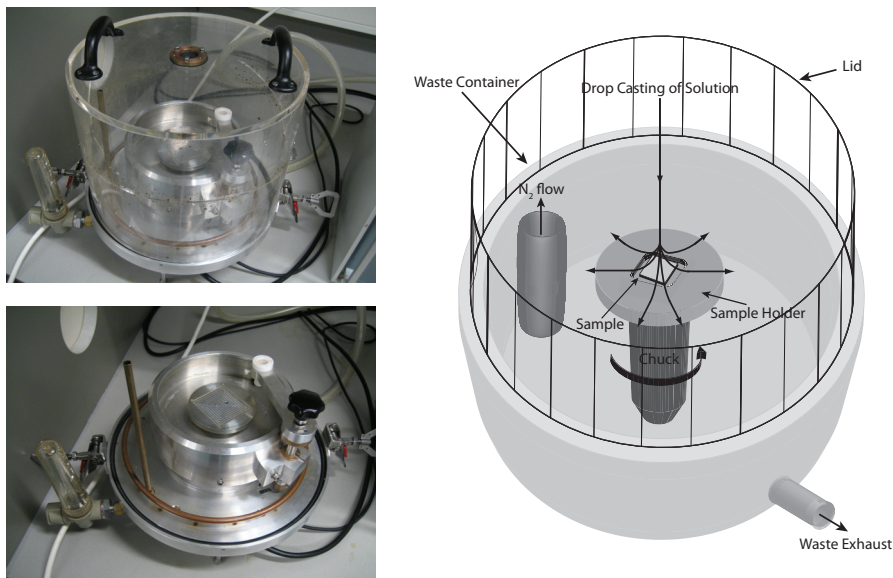


**Figure 2.8** Picture (with and without lid) and schematic representation of the used spin-coat device. The sample is placed in the sample holder and is kept in place by small brims. The sample is spun at 2800 rpm.

## 2.6 Reactor Set-up

Reactions on spin-coated iron oxide nano particles were performed in a standard quartz tube through which the gases Ar, H<sub>2</sub>, CO, and a mixture of H<sub>2</sub> and CO could be flown. The reaction temperature was measured by a thermocouple positioned within the tube. A standard ceramic heating furnace for tubes was used to heat the reactor in which temperatures as high as 800 °C could be reached. Heating is controlled by an Eurotherm controller.

## 2.7 Transmission Electron Microscopy (TEM)

Transmission electron microscopy is used to image a sample within the nm to atomic scale range. The TE microscope and its schematic representation are displayed in Figure 2.9. At the top of the TEM column a high voltage electron emitter generates a beam of

electrons possessing a high energy (100-300 keV) and intensity. This beam passes through a condenser to create parallel rays which impinge on the sample (less than 100 nm in thickness). The electrons then travel through a series of magnifying lenses where they are ultimately focused on the fluorescent screen at the bottom to produce a so-called bright-field image of the sample. Because the attenuation of the beam depends on both the thickness and density of the sample, this image is a two-dimensional representation of the sample mass. The diffracted electron beams, which are slightly off-angle from the transmitted beam, are used to measure a dark-field image.

The complete column is under vacuum ( $10^{-6}$ - $10^{-8}$  mbar) to minimize interactions of the electron beam and the gas molecules. Apertures situated along the column can be used to change the contrast and resolution of the image. Contrast in transmission is not only affected by the attenuation of the electrons by thickness and density variations on the sample, but also by diffraction and interference. For example similar particles can have a different contrast, which may result in a misinterpretation of the TEM image [13]. Hence, care is needed when interpreting TEM images.

A typical sample holder is shown on the bottom-left picture in Figure 2.9.

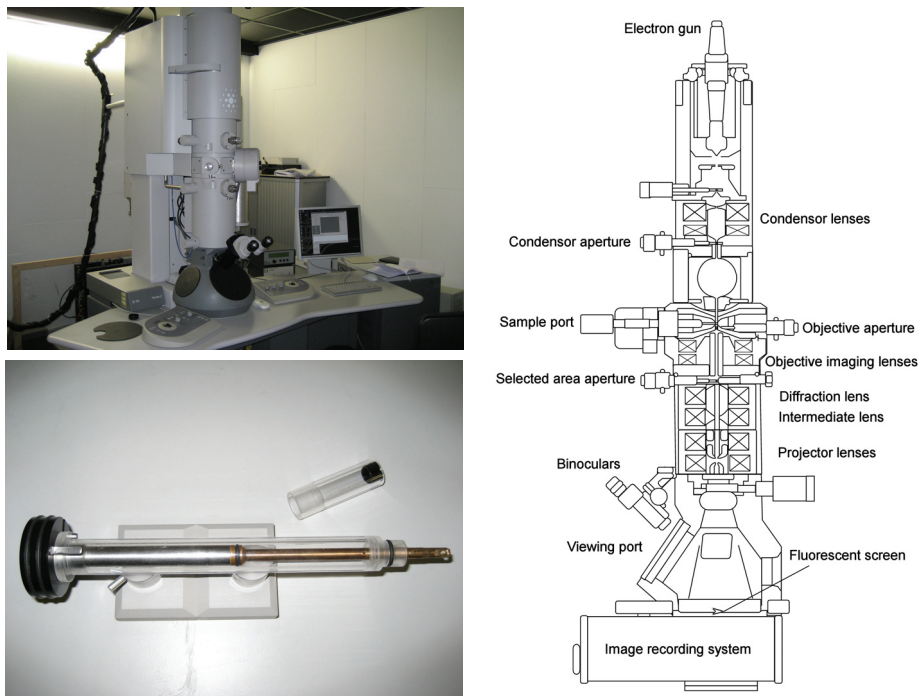


**Figure 2.9:** The top-left picture shows the used TEM set-up and the image on the right side is its schematical representation. The image in the bottom-left is the sample holder.

## 2.8 X-Ray Absorption Near Edge Spectroscopy (XANES) and Extended X-Ray Absorption Fine Structure (EXAFS)

XANES and EXAFS are used to determine the composition of the iron oxide nano particles under in-situ conditions. The techniques are based on the absorption of X-rays and the creation of photoelectrons, which are either excited to holes in the valence levels, or to unbound states and scattered by nearby atoms in a lattice. When a free atom is irradiated with X-rays possessing an energy  $h\nu$ , absorption takes place when the binding energy ( $E_b$ ) of an electron in the atom is lower than the energy of the X-rays. The electron then leaves the atom with a kinetic energy of  $E_k = h\nu - E_b$ . The X-ray absorption spectrum of such as free atom shows edges corresponding to the binding energy of all electron core levels in the atom, but does not contain any further structure. However, when the atom is bound as part of a structure, the absorption is altered due to its local coordination, and a fine structure arises, which contains valuable information.

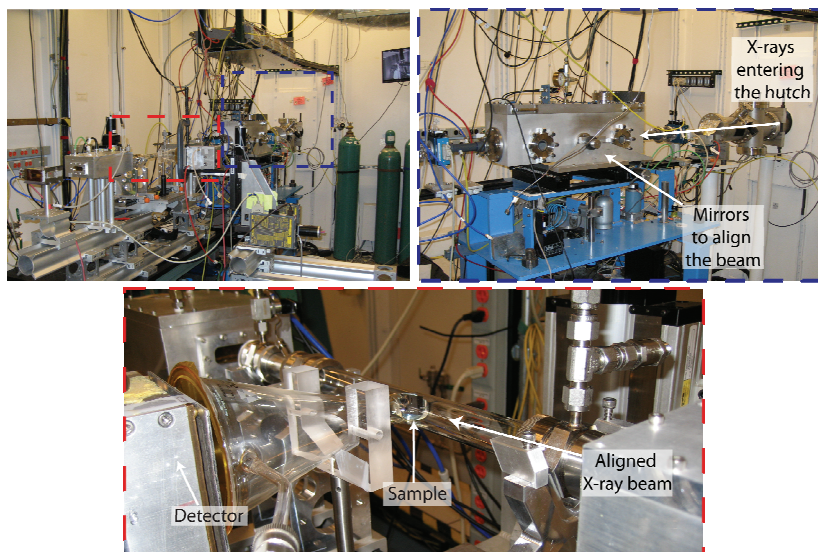


**Figure 2.10:** The top-left picture shows the set-up at the beamline. The top-right image shows the place where the X-ray beam enters the hutch and becomes aligned. The bottom image displays the sample with the detector.

As such, XANES focuses on the shape of the absorption edge, and is highly sensitive for the valence state of the atom and its bonding geometry. EXAFS, on the other hand, looks at the absorption spectrum beyond the edge. In this region interference effects are visible, which provide detailed information on the distance, number, and type of neighbors of the X-ray absorbing atom. For a more detailed background of both

techniques we refer to the ‘Spectroscopy in Catalysis’ book by Niemantsverdriet [1].

The experiments were performed at the Advanced Photon Source (APS) synchrotron at Argonne National Laboratory (ANL) in Chicago, USA. The set-up that was used is shown in Figure 2.10.

## ***2.9 Plane-Wave Density Functional Theory (PW-DFT) Calculations***

Currently, one of the most widely used ab-initio approaches in surface science is density functional theory (DFT). This theory is based on the Thomas-Fermi-Dirac model [14] with the Hohenberg-Kohn approximation [15] as one of the most important theorems, which states that every observable quantity of a system in the ground state is a unique functional of the electron density. However, this functional is unknown in the Hohenberg-Kohn theorem, and thus, the values of the observable quantities can only be approximated. Kohn and Sham [16] were able to express this unknown functional mathematically up to an unknown part that is most commonly known as the exchange-correlation (XC) functional. Although in theory a perfect exchange-correlation functional should exist, in practice the functional is approximated. The first approximation of this XC functional was the local density approximation (LDA). A more sophisticated approximation appeared later, where also a density gradient is included into the functional. This approximation is called the generalized gradient approximation (GGA).

In this thesis, the Vienna ab-initio simulation package (VASP) [14,17-19] is used, which performs an iterative solution of the Kohn-Sham equations in a plane-wave basis set. The many-electron wave function for the system is written as a product of one-electron wave functions. The total energy is split into a kinetic energy term, an electrostatic energy term, and an exchange-correlation term. The exchange-correlation energy has been calculated within the generalized gradient approximation using the revised form of the Perdew, Burke, and Ernzerhof (RPBE) XC functional [20] proposed by Hammer et al. [21]. The electron-ion interactions are described by the projector-augmented wave (PAW) method developed by Blöchl [22]. This is essentially an all-electron frozen core method combining the accuracy of all-electron methods and the computational simplicity of the pseudopotential approach [23]. In the pseudopotential approximation the core electrons are basically removed and described by an effective potential, the pseudopotential. The reciprocal space has been sampled with a  $k$ -points grid generated automatically using the Monkhorst-Pack method [24]. Fractional occupancies were calculated using a first-order Methfessel-Paxton smearing function [25]. Upon convergence, energies were extrapolated to  $T = 0$  K.

Partial geometry optimizations have been performed including relaxation of the two topmost metal layers, using the RMM-DIIS algorithm [26]. In this method, the forces on the atoms and the stress tensor are used to determine the search directions for



finding the equilibrium positions. Geometry optimizations were stopped when all the forces (of the degrees of freedom set in the calculation) were smaller than 0.01 eV/Å. Vibrational frequencies have been calculated within the harmonic approximation. The second-derivative matrix (or Hessian matrix) has been calculated numerically by displacing every atom independently out of its equilibrium position twice ( $\pm 0.02$  Å). The adsorbate–surface coupling has been neglected and only the Hessian matrix of the adsorbate has been calculated [27]. Transition-state structures have been found following a two-step strategy: (1) use of the climbing-image nudged elastic band method (CI-NEB) [28] to find a likely transition-state structure, and (2) refine the structure of the transition-state by performing a geometry optimization calculation (as described above) using as a starting geometry that of the highest energy image out of the CI-NEB calculation. All transition-state structures have been characterized by calculating the vibrational frequencies.

## References

- [1] J. W. Niemantsverdriet, Spectroscopy in Catalysis, 3rd ed., Wiley-VCH, Weinheim, 2007.
- [2] J. L. Falconer, J. A. Schwarz, *Catal. Rev. - Sci. Eng.* **25** (1983) 141.
- [3] D. A. King, *Surf. Sci.* **47** (1975) 384.
- [4] P. A. Redhead, *Vacuum* **12** (1962) 203.
- [5] C. M. Chan, R. Aris, W. H. Weinberg, *Appl. Surf. Sci.* **1** (1978) 360.
- [6] E. Habenschaden, J. Küppers, *Surf. Sci.* **138** (1984) L147.
- [7] R. G. Wilson, F. A. Stevie, C. W. Magee, Secondary Ion Mass Spectrometry: A Practical Handbook for Depth Profiling and Bulk Impurity Analysis, John Wiley & Sons, Inc., New York, 1989.
- [8] J. K. Nørskov, B. I. Lundqvist, *Phys. Rev. B: Condens. Matter* **19** (1979) 5661.
- [9] N. M. Reed, J. C. Vickerman, Practical Surface Analysis Volume 2: Ion and Neutral Spectroscopy, D. Briggs, M. P. Seah (Eds.), 2nd ed., John Wiley & Sons, Chichester, 1992.
- [10] E. W. Kuipers, C. Doornkamp, W. Wieldraaijer, R. E. van den Berg, *Chem. Mater.* **5** (1993) 1367.
- [11] E. W. Kuipers, C. Laszlo, W. Wieldraaijer, *Catal. Lett.* **17** (1993) 71.
- [12] R. M. van Hardeveld, P. L. J. Gunter, L. J. van Ijzendoorn, W. Wieldraaijer, E. W. Kuipers, J. W. Niemantsverdriet, *Appl. Surf. Sci.* **84** (1995) 339.
- [13] M. M. J. Treacy, A. Howie, *J. Catal.* **63** (1980) 265.
- [14] R. G. Parr, W. Yang, Density-Functional Theory of Atoms and Molecules, Oxford University Press, New York, 1989.
- [15] P. Hohenberg, W. Kohn, *Phys. Rev.* **136** (1964) B864.
- [16] W. Kohn, L. J. Sham, *Phys. Rev.* **140** (1965) A1133.
- [17] G. Kresse, J. Furthmüller, *Phys. Rev. B* **54** (1996) 11169.
- [18] G. Kresse, J. Furthmüller, *J. Comput. Mater. Sci.* **6** (1996) 15.
- [19] W. Koch, M. C. Holthausen, A Chemist's Guide to Density Functional Theory, Wiley-VCH, Weinheim, 2000.
- [20] J. P. Perdew, K. Burke, M. Ernzerhof, *Phys. Rev. Lett.* **77** (1996) 3865.
- [21] B. Hammer, L. B. Hansen, J. K. Nørskov, *Phys. Rev. B* **59** (1999) 7413.
- [22] P. E. Blöchl, *Phys. Rev. B* **50** (1994) 17953.
- [23] G. Kresse, D. Joubert, *Phys. Rev. B* **59** (1999) 1758.
- [24] H. J. Monkhorst, J. D. Pack, *Phys. Rev. B* **13** (1976) 5188.
- [25] M. Methfessel, A. T. Paxton, *Phys. Rev. B* **40** (1989) 3616.
- [26] P. Pulay, *Chem. Phys. Lett.* **73** (1980) 393.
- [27] J. D. Head, *Int. J. Quantum Chem.* **65** (1997) 827.
- [28] G. Henkelman, B. P. Uberuaga, H. Jonsson, *J. Chem. Phys.* **113** (2000) 9901.

# 3

## Density Functional Theory Calculations

*This Chapter consists of two parts.*

*In part (A) the adsorption, desorption, and dissociation of CO on molybdenum(100) is investigated with DFT calculations.*

*In part (B) DFT is employed to study the adsorption, desorption, and dissociation of CO on tungsten(100).*





# 3A

## Adsorption, Desorption, and Dissociation of CO on Molybdenum(100)

### Abstract

*The adsorption of CO on Mo(100) has been calculated for several adsorption states at four surface coverages using DFT. Dissociation of CO on Mo(100) has been investigated for two surface coverages: 0.25 and 0.5 ML. A full analysis of the vibrational frequencies of CO was performed, to determine whether structures are stable adsorption states or transition-states. Results show that CO adsorbs molecularly on the Mo(100) surfaces up to coverages of 0.5 ML at fourfold hollow sites with the molecular axis tilted away from the surface normal by 55-57° and dissociates easily with activation energies ranging from 0.45 to 0.56 eV, leading to energy gains of -1.71 eV and -0.59 eV at 0.25 and 0.5 ML, after dissociation, respectively. The adsorption energy of the CO molecule at 0.25 ML is -2.64 eV with a C–O stretching vibration of 1062 cm<sup>-1</sup>. Increasing the CO surface concentration leads to a lower C–O stretching frequency of 958 cm<sup>-1</sup>, which is remarkable, and it is in conflict with the Blyholder model and previous experimental observations for CO on transition-metal surfaces. Furthermore, calculations reveal that reported CO desorption peaks in literature, thought to be due to recombination of carbon and oxygen, are more likely due to molecular desorption of CO at the fourfold hollow position with a tilted geometry. This conclusion is supported by the low recombination energies calculated (one-third of that described in literature).*

### 3A.1 Introduction

As oil becomes scarcer each day, alternative routes for the production of chemicals and fuels are being developed, in which Fischer-Tropsch Synthesis (FTS) is an attractive option using coal, natural gas, and potentially even biomass sources. The process begins with the production of syngas (either by gasification of coal and biomass sources, or reforming of natural gas), which is then reacted over a suitable catalyst to yield a wide range of products varying from methane to waxy paraffins, as well as oxygenates. Several reaction mechanisms have been proposed in literature, although it is generally assumed that not a single reaction pathway exists, but a number of parallel reaction pathways instead [1]. Carbon monoxide (CO) dissociation is regarded as a key step in FTS in some mechanisms, such as the alkyl and the alkenyl mechanisms, though others presume that molecular CO is an active species in the mechanism. Hence, the capacity of the catalyst to dissociate CO is a key issue to understand and elucidate FTS mechanism. Also, the influence of neighboring atoms and molecules on the dissociation of CO is of great importance, as under reaction conditions, a molecule will rarely be isolated on the surface.

Iron and cobalt are among the most extensively used catalysts in FTS. Surface science studies have proven that CO dissociates on iron [2-15], whereas it adsorbs molecularly on cobalt [16-21]. Nickel [22-27] and ruthenium [28-31] have also been studied in relation to FTS; on both metals, CO adsorbs molecularly. On the other hand, studies on chromium [32], tungsten [33,34], and molybdenum [35-38] single crystals have shown that these metals behave similarly to iron and have a large capacity to dissociate CO. Moreover, molybdenum carbides, nitrides, and phosphides have been proven to be active in several processes, including FTS [39-42].

Surface science studies on molybdenum single crystals are, however, scarce compared to other metals of interest in FTS, such as iron. Adsorption of CO on Mo(100) was studied in the 1970s and early 1980s using temperature programmed desorption mass spectroscopy (TPD) in combination with Auger electron spectroscopy (AES) and low energy electron diffraction (LEED). The studies focused on the determination of whether CO adsorbed molecularly or dissociatively [43-45]. TPD experiments showed two distinct sets of desorption features;  $\alpha$  peaks related to molecularly adsorbed CO at  $T < 400$  K and  $\beta$  peaks at 900 ( $\beta_1$ ), 1024 ( $\beta_2$ ), and 1240 ( $\beta_3$ ) K related to dissociated CO. Ko and Madix [44,45] found that CO adsorbed molecularly at 200 K to a saturation value of  $10^{15}$  molecules/cm<sup>2</sup> (which corresponds to 1 monolayer (ML)). Upon heating, half of the CO molecules desorbed below 400 K as CO( $\alpha$ ) states, whereas the other half dissociated into CO( $\beta$ ) states. A  $p(1 \times 1)$  LEED pattern was observed with all three  $\beta$  states present on the surface. Further heating to 1130 K showed a  $c(2 \times 2)$  LEED pattern, after selectively removing the CO( $\beta$ ) states at 900 and 1024 K. These experiments indicated that the total amount of CO( $\beta$ ) on the

Mo(100) surface was about 0.50 ML and that the amount of CO( $\beta_3$ ) was approximately 0.25 ML. On the other hand, Zaera et al. [38] reported similar TPD results (with two  $\alpha$  states at 150 and 290 K and three  $\beta$  states at 840, 940, and 1250 K), but obtained a much larger saturation coverage of approximately 1.7 ML (with 20% error) calculated using the carbon Auger signal. The partial coverages reported for the distinct CO  $\beta$  states were as follows: CO( $\beta_1$ ): 0.22 ML, CO( $\beta_2$ ): 0.32 ML, and CO( $\beta_3$ ): 0.38 ML. However, they also observed a  $c(2 \times 2)$  LEED pattern after heating to 1100 K, when only CO( $\beta_3$ ) was present. This result suggested a CO( $\beta_3$ ) coverage of 0.25 ML in agreement with previous results, but in disagreement with their own results (0.38 ML) from AES. Further, electron energy loss spectroscopy (EELS) experiments showed two distinct losses at 1065 and 1235  $\text{cm}^{-1}$  at low CO coverages. The coupling of EELS and TPD experiments indicated that these two losses were related to the CO( $\beta_3$ ) state. Increasing CO coverage resulted in a fusion between these two EELS losses, being the resulting loss centered at 1085  $\text{cm}^{-1}$ . This seemed to indicate that increasing CO coverage suppressed the adsorption state that yields the loss at 1235  $\text{cm}^{-1}$ . A new loss at 2100  $\text{cm}^{-1}$  was also observed at high CO coverages, indicating the presence of perpendicularly adsorbed CO molecules at on-top sites. EELS-TPD coupling showed that this new loss was related to the presence of CO( $\alpha$ ) molecules. The presence of CO stretching frequencies as low as 1065 or 1235  $\text{cm}^{-1}$  is unusual and has been reported previously only for Fe(100) [10,12] and Cr(110) [32]. The geometry of this low CO stretch adsorption state was resolved using near edge X-ray absorption spectroscopy (NEXAFS) and angle-resolved ultraviolet photoelectron spectroscopy (ARUPS); in such adsorption state, CO is bent over the surface with a tilting angle of 50° with respect to surface normal [36]. Similar tilting angles have been reported for Fe(100) [6,11,13]. As for Fe(100) and Cr(110), this low CO stretch adsorption state was suggested to be the precursor for CO dissociation, which on Mo(100) occurs as low as 230 K [38]. Dissociation of CO at such low temperatures has been reported only for body centered cubic (bcc) metals; 300 K on Mo(110) [35], 170 K and 300 K on Cr(110) [32], and 440 K on Fe(100) [2,4,6-8,10-13,15].

Calculations on Mo surfaces are even scarcer than experiments. Liu and Rodriguez [40] studied the adsorption of CO and S on Mo(100) and MoX (X = C, N and P), and reported that CO adsorbs preferentially at on-top sites, with a tilted configuration and an adsorption energy of -2.3 eV. It is particularly surprising that Liu and Rodriguez reported that CO preferentially adsorbs at on-top sites, since it was postulated experimentally that CO adsorbs tilted at fourfold hollow sites on Mo(100) [36] and also on Fe(100) [6,11,13], for which recent density functional (DFT) calculations confirmed such an adsorption state [3,5,9,14]. Ji and Li [37] recently studied the adsorption and dissociation of CO on Mo(110) using DFT. They reported an adsorption energy of CO of -2.13 eV at 0.25 ML, which is smaller than the adsorption

energy of CO on Mo(100) of -2.64 eV calculated in this Chapter. Ji and Li also reported an activation energy for CO dissociation of 1.71 eV at 0.25 ML; this activation energy is considerably high in order to account for the experimental observation that CO is completely dissociated above 300 K on Mo(110) [35]. In the present Chapter, we report an activation energy as low as 0.45 eV on Mo(100). In addition, Ji and Li reported a calculated lattice constant of 3.89 Å, which corresponds to face centered cubic (fcc) molybdenum [46], while their model corresponds to a bcc Mo(110) surface.

Adsorption of CO on molybdenum surfaces is, thus, an interesting system from both a technological as well as a fundamental point of view, because there are still several open questions regarding the experimentally available data. In this Chapter, the results of our recent study of CO adsorption and dissociation on Mo(100) using density functional theory is presented.

### **3A.2 Computational Details**

We have used the Vienna ab-initio simulation package (VASP) [47,48], which performs an iterative solution of the Kohn-Sham equations in a plane-wave basis set. Plane-waves with a kinetic energy below or equal to 400 eV have been included in the calculation. The exchange-correlation energy has been calculated within the generalized gradient approximation (GGA) using the revised form of the Perdew, Burke, and Ernzerhof (RPBE) exchange-correlation functional [49] proposed by Hammer et al. [50]. The electron-ion interactions for C, O, and Mo are described by the projector-augmented wave (PAW) method developed by Blöchl [51]. This is essentially an all-electron frozen core method combining the accuracy of all-electron methods and the computational simplicity of the pseudopotential approach [52]. Fractional occupancies were calculated using a first-order Methfessel-Paxton smearing function with a width of 0.1 eV [53]. Upon convergence, energies were extrapolated to  $T = 0$  K. Molybdenum exhibits a bcc structure. The relative positions of the metal atoms have been fixed initially as those in the bulk, with an optimized lattice parameter of 3.159 Å (the experimental value is 3.147 Å) [54]. The optimized lattice parameter has been calculated using the smallest unit cell that can be used to model the bulk of molybdenum, and its reciprocal space has been sampled with a  $(15 \times 15 \times 15)$   $k$ -points grid generated automatically using the Monkhorst-Pack method [55].

The CO molecule has been calculated using a  $10 \times 10 \times 10$  Å<sup>3</sup> cubic unit cell, while for atomic carbon and atomic oxygen a  $10 \times 12 \times 14$  Å<sup>3</sup> orthorhombic unit cell has been used. Non-spin-polarized calculations for the CO molecule and spin-polarized calculations for the atoms have been done at the  $\Gamma$  point.

The Mo(100) surface has been modeled within the slab model approximation using a five-metal layer slab model and six vacuum layers ( $> 10$  Å). Different slab models have been used throughout this Chapter: a  $p(3 \times 3)$  unit cell to study surface

coverages as low as 0.11 ML, a  $p(2 \times 2)$  to study surface coverages as low as 0.25 ML, a  $c(2 \times 2)$  to study surface coverages of 0.5 ML, and a  $p(1 \times 1)$  to study surface coverages as large as 1 ML. The reciprocal space of the  $p(3 \times 3)$ ,  $p(2 \times 2)$ ,  $c(2 \times 2)$ , and  $p(1 \times 1)$  unit cells have been sampled with a  $(3 \times 3 \times 1)$ ,  $(5 \times 5 \times 1)$ ,  $(7 \times 7 \times 1)$ , and  $(10 \times 10 \times 1)$   $k$ -points grid, respectively, automatically generated using the Monkhorst-Pack method. Unlike bulk molybdenum, which has no magnetic moment, molybdenum slabs exhibited small magnetic moments;  $0.18 \mu_B/\text{atom}$  for Mo(100)- $c(2 \times 2)$  and  $0.22 \mu_B/\text{atom}$  for Mo(100)- $p(2 \times 2)$ . Tests on the influence of the spin character on the results showed that geometries were unaffected by such small magnetic moments and total energies were slightly more stable. The estimated error that is committed in the calculation of adsorption energies and reaction energies using non-spin-polarized calculations is below 0.05 eV. Consequently, we report here non-spin-polarized results.

Partial geometry optimizations have been performed including relaxation of the two topmost metal layers, using the RMM-DIIS algorithm [56]. In this method, the forces on the atoms and the stress tensor are used to determine the search directions for finding the equilibrium positions. Geometry optimizations were stopped when all the forces (of the degrees of freedom set in the calculation) were smaller than  $0.01 \text{ eV}/\text{\AA}$ . Vibrational frequencies have been calculated within the harmonic approximation. The second-derivative matrix (or Hessian matrix) has been calculated numerically by displacing every atom independently out of its equilibrium position twice ( $\pm 0.02 \text{ \AA}$ ). The adsorbate-surface coupling has been neglected, and only the Hessian matrix of the adsorbate has been calculated [57]. Transition-state (TS) structures have been found following a two-step strategy: (1) use of the climbing-image nudged elastic band method (CI-NEB) [58] to find a likely transition-state structure and (2) refine the structure of the transition-state by performing a geometry optimization calculation (as described above) using as a starting geometry that of the highest energy image out of the CI-NEB calculation. All transition-state structures have been characterized by calculating the vibrational frequencies.

The adsorption of CO was investigated on Mo(100) at four different CO coverages: (1) 0.11 ML using a  $p(3 \times 3)$  unit cell, (2) 0.25 ML using a  $p(2 \times 2)$  unit cell, (3) 0.5 ML using a  $c(2 \times 2)$  unit cell, and (4) 1 ML using a  $p(1 \times 1)$  unit cell. The adsorption energy of CO, and atomic carbon and oxygen, is calculated with respect to its respective gas-phase species. Zero-point-energy (ZPE) corrections were not applied to the energies in the diagrams since ZPE is relevant for X-H bonds, but hardly important for X-Y bonds, such as C-O. Moreover, the energy differences fall within the calculation error (0.05 eV). Dissociation of CO on Mo(100) was investigated at two coverages, at 0.25 and 0.5 ML, using a  $p(2 \times 2)$  model containing one and two CO molecules, respectively.

### 3A.3 Results / Discussion

First, the structure of the (100) surface will be shown. Next, the results of CO adsorption for each surface coverage will be presented, and lastly we discuss dissociation of CO.

#### 3A.3.1 The (100) Surface

The structure of a bcc(100) surface is illustrated in Figure 3A.1, in which all three adsorption sites are displayed. The sequence of metal layers in the  $\langle 001 \rangle$  direction is ABABA, etc. Therefore, every atom of the third layer is positioned above an atom of the first layer.

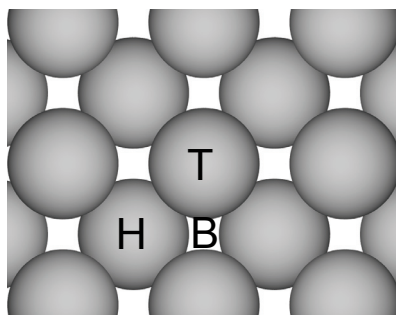


**Figure 3A.1** Top view of the (100) surface of a bcc metal. The sequence of metal layers in the  $\langle 001 \rangle$  direction is ABABA, etc. Thus, every atom of the third layer is positioned above an atom of the first layer. T, B, and H stand for the three adsorption sites; top, bridge, and fourfold hollow, respectively.

#### 3A.3.2 CO Adsorption on Mo(100)

##### 3A.3.2.1 Mo(100)-CO- $p(2 \times 2)$ ( $\theta = 0.25$ ML)

Adsorption of CO on Mo(100) at 0.25 ML was investigated at three adsorption sites: top, bridge, and fourfold hollow sites. The CO molecule adsorbs with the C–O bond perpendicular to the surface at top and bridge sites, whereas two adsorption geometries are observed for CO at fourfold hollow sites: one with the C–O bond perpendicular to the surface and the second with the CO bent over the surface. The CO molecule is the most stable at fourfold hollow sites with the C–O bond axis away from the surface normal by an angle of  $57^\circ$  (see Table 3A.1). According to experimental data obtained using NEXAFS, the tilting angle of CO on Mo(100) should be around the order of  $40 \pm 10^\circ$  [36], with respect to the surface plane, or  $50 \pm 10^\circ$ , with respect to the surface normal, which agrees well with our results. The adsorption energy of CO at the tilted

configuration is -2.64 eV and is considerably larger than at top, bridge, and fourfold hollow sites with the CO perpendicular to the surface, with values of -1.58, -1.48, and -1.76 eV, respectively. The C–O bond is elongated (activation of the CO molecule) for all adsorption geometries. The bond lengths for CO adsorbed vertically to the surface are 1.174, 1.193, and 1.264 Å for top, bridge, and fourfold hollow sites, respectively. However, the most pronounced increase in CO distance is observed for CO in the fourfold hollow tilted adsorption mode (1.354 Å), with an expansion of 0.211 Å with respect to gas-phase CO (1.143 Å). These findings are in line with the belief that the tilted CO molecule is the precursor for dissociation [36,38].

<b>Table 3A.1</b> Adsorption of CO on Mo(100) at $\theta = 0.11, 0.25, 0.5,$ and 1 ML. (results displayed in <i>italics</i> are not true minima in the PES)		$\Delta E_{\text{ads}}^{[a]}$ [eV]	$d_{\text{CO}}^{[b]}$ [Å]	$\Delta d_{\text{CO}}^{[c]}$ [Å]	$z_{\text{CO}}^{[d]}$ [Å]	$\theta^{[e]}$ [°]
$\theta = 0.11$ ML	tilted	-2.93	1.366	0.223	0.786 (1.561)	55.4
$\theta = 0.25$ ML	<i>on-top</i>	<i>-1.58</i>	<i>1.174</i>	<i>0.031</i>	<i>2.034</i>	-
	<i>bridge</i>	<i>-1.48</i>	<i>1.193</i>	<i>0.050</i>	<i>1.682</i>	-
	bridge/tilted <sup>[f]</sup>	-1.59	1.220	0.077	1.502	53.6
	<i>hollow</i>	<i>-1.76</i>	<i>1.264</i>	<i>0.121</i>	<i>0.785</i>	-
	hollow/tilted	-2.64	1.354	0.211	0.716 (1.453)	57.0
$\theta = 0.5$ ML	on-top	-1.50	1.169	0.026	2.047	-
	<i>bridge</i> <sup>[g]</sup>	<i>-1.42</i>	<i>1.192</i>	<i>0.049</i>	<i>1.647</i>	-
	<i>hollow</i>	<i>-1.78</i>	<i>1.263</i>	<i>0.120</i>	<i>0.756</i>	-
	hollow/tilted	-2.63	1.386	0.243	0.613 (1.378)	56.5
Lattice = 3.0824 Å	hollow/tilted	-3.08	1.387	0.244	0.649 (1.462)	55.1
$\theta = 1$ ML	on-top	-1.35	1.161	0.018	2.068	-
	<i>bridge</i>	<i>-1.14</i>	<i>1.175</i>	<i>0.032</i>	<i>1.632</i>	-
	hollow	-1.46	1.235	0.092	0.796	-
	hollow/tilted	-	-	-	-	-

[a]  $\Delta E_{\text{ads}}$  is the adsorption energy. [b]  $d_{\text{CO}}$  is the CO bond length. [c]  $\Delta d_{\text{CO}}$  is the elongation of the CO bond with respect to the gas-phase CO bond length (1.143 Å). [d]  $z_{\text{CO}}$  is the height of the CO molecule with respect to the surface level (the value within the brackets is the height of the oxygen atom and the value without brackets is the height of the carbon atom). [e]  $\theta$  is the angle between the surface normal and the CO molecular axis. [f] the two top layers of molybdenum are not relaxed; only CO is. [g] a  $5 \times 5 \times 1$   $k$ -points grid is used.

Calculations of the vibrational frequencies show that only two out of four adsorption geometries are local minima on the potential energy surface (PES) of Mo(100)–CO– $p(2 \times 2)$  (Table 3A.2). Note however, that two vibrational frequencies of CO at top sites are no more than 22  $\text{cm}^{-1}$ . This value is possibly prone to be of the same



order of the error associated with its calculation, therefore, the adsorption configuration might be disputed as being a stable geometry and might as well be a second-order saddle point (SP) in the PES of Mo(100)–CO– $p(2 \times 2)$ . However, the overall discussion would not change, for the most stable species is clearly CO tilted at fourfold hollow sites. The CO stretching frequencies of CO adsorbed vertically on-top and tilted at fourfold hollow sites are  $1889 \text{ cm}^{-1}$  and  $1062 \text{ cm}^{-1}$ , respectively (Table 3A.2), in good agreement with high resolution electron energy loss spectrometry (HREELS) data reported by Zaera et al., who observed a loss peak for CO adsorbed in a bent configuration at  $1065 \text{ cm}^{-1}$  at similar coverage [38].

<b>Table 3A.2</b> Adsorption of CO on Mo(100) at $\theta = 0.11, 0.25, 0.5,$ and $1 \text{ ML}$ : vibrational frequencies [ $\text{cm}^{-1}$ ] and zero-point-energy corrections to the adsorption energy. (results displayed in <i>italics</i> are not true minima in the PES)									
		v1	v2	v3	v4	v5 <sup>[a]</sup>	v6 <sup>[a]</sup>	ZPE <sup>[b]</sup> [eV]	$\Delta E_{\text{ads}}$ <sup>[c]</sup> [eV]
$\theta = 0.11 \text{ ML}$	tilted	271	274	369	395	433	1043	0.17	-2.89
$\theta = 0.25 \text{ ML}$	<i>on-top</i>	22	22	365	365	359	1889	0.19	-1.52
	<i>bridge</i>	429 <i>i</i>	23	148	277	315	1729	0.15	-1.46
	bridge/tilted <sup>[d]</sup>	43	161	320	331	408	1598	0.18	-1.54
	<i>hollow</i>	245 <i>i</i>	245 <i>i</i>	165	165	277	1378	0.12	-1.77
	hollow/tilted	234	239	291	350	432	1062	0.16	-2.61
$\theta = 0.5 \text{ ML}$	on-top	60	60	376	376	348	1943	0.20	-1.43
	<i>bridge</i> <sup>[e]</sup>	318 <i>i</i>	60	165	283	315	1774	0.16	-1.39
	<i>hollow</i>	228 <i>i</i>	228 <i>i</i>	192	192	307	1386	0.13	-1.78
	hollow/tilted	241	272	316	403	433	958	0.16	-2.60
Lattice = $3.0824 \text{ \AA}$	hollow/tilted	261	291	339	438	456	969	0.17	-3.04
$\theta = 1 \text{ ML}$	on-top	56	56	372	372	342	2032	0.20	-1.28
	<i>bridge</i>	87 <i>i</i>	186 <i>i</i>	162	254	247	1899	0.16	-1.11
	hollow	89	89	191	191	270	1561	0.15	-1.44
	hollow/tilted	-	-	-	-	-	-	-	-

[a]  $\nu_5$  and  $\nu_6$  are the metal–CO stretching and CO stretching frequency, respectively. [b] ZPE is the zero-point-energy. [c]  $\Delta E_{\text{ads}}$  is the adsorption energy including the zero-point-energy of the chemisorbed and gas-phase CO. [d] the two top layers of molybdenum are not relaxed; only CO is. [e] a  $5 \times 5 \times 1$   $k$ -points grid is used.

Analysis of the vibrational frequencies of CO reveals one imaginary frequency at the bridge site and two at the hollow; consequently, the bridge site is a TS structure, whereas the hollow site is a second-order saddle point in the PES of Mo(100)–CO– $p(2 \times 2)$ . Closer inspection of these normal modes shows that the

imaginary vibration of the CO molecule ( $\nu_1$ ) adsorbed at a bridge site corresponds to a rotational movement of the CO molecule, toward a tilted bridge configuration. The small frequency  $\nu_2$  is a movement of the CO molecule to the hollow adsorption site. Because of the same argument as that for the two small vibrational frequencies of CO at the top site, the bridge site might also be a second order saddle point, which makes sense when considering the energies as well. The two imaginary frequencies of carbon monoxide at hollow sites also relate to the rotational behavior of the molecule, moving toward the most stable geometry, the tilted fourfold hollow configuration. Because a rotational movement for CO at the bridge position toward tilted bridge geometry was observed, calculations were performed of CO at this tilted bridge position. However, no optimized geometry could be obtained for the adsorption of CO at the tilted bridge position when relaxing the two top layers of molybdenum. The values displayed in Table 3A.1 are calculated by relaxing only the CO molecule on the surface. The tilting angle thus calculated is  $54^\circ$  and the CO bond length  $1.220 \text{ \AA}$ . The elongation of the bond is not as significant as that for the tilted fourfold hollow geometry, but is somewhat larger than for CO perpendicular at bridge sites and somewhat smaller than for CO at hollow sites. Because the adsorption energy ( $-1.59 \text{ eV}$ ) is around the same magnitude as that for the top adsorption site, and the C–O vibrational frequency of  $1598 \text{ cm}^{-1}$  of CO at the bridge tilted position could not be observed experimentally, the tilted bridge adsorption geometry is not relevant for explaining experiments. Including zero-point-energy corrections gives rise to slightly smaller adsorption energies for all five configurations.

The adsorption energy of CO at fourfold hollow sites with a tilted geometry was found to be  $-2.64 \text{ eV}$ , which corresponds to a temperature of desorption of approximately  $1056 \text{ K}$  [59]. Zaera et al. [38] reported a desorption peak for low CO coverages at higher temperatures, at  $1250 \text{ K}$ , therefore, we calculated the CO adsorption energy for CO adsorbed at fourfold hollow sites at a coverage of  $0.11 \text{ ML}$  using a  $p(3 \times 3)$  slab model to verify whether we could get a larger adsorption energy for tilted CO. The results are displayed in Table 3A.1. The adsorption energy obtained is indeed larger than for CO tilted at  $0.25 \text{ ML}$  and is  $-2.93 \text{ eV}$ , corresponding to a desorption peak at approximately  $1172 \text{ K}$ . This value (using first-order kinetics) correlates nicely to the  $\beta_3$  desorption peak reported by Zaera et al. [38]. The tilting angle is slightly smaller, by  $\sim 2^\circ$ , than that at  $0.25 \text{ ML}$  CO coverage, whereas the C–O elongation is slightly larger ( $0.012 \text{ \AA}$ ). The fourfold hollow tilted adsorption mode is stable in the PES of  $\text{Mo}(100)\text{-CO-}p(3 \times 3)$ , with a CO stretching frequency of  $1043 \text{ cm}^{-1}$ .

#### *3A.3.2.2 Mo(100)-CO-c(2 × 2) ( $\theta = 0.5 \text{ ML}$ )*

The most stable adsorption geometry at  $0.5 \text{ ML}$  CO coverage is again the fourfold hollow site with CO tilted. The angle between the surface normal and the CO molecular

axis is  $57^\circ$ , similar to that for CO at the tilted fourfold hollow configuration at a CO surface coverage of 0.25 ML. The adsorption energy of this tilted CO at fourfold hollow sites is -2.63 eV, while adsorption energies for top, bridge, and fourfold hollow sites with CO vertical to the surface are -1.50, -1.42, and -1.78 eV, respectively. The adsorption energies of CO in both upright and tilted positions at fourfold hollow sites are similar to those calculated for the Mo(100)-CO- $p(2 \times 2)$  system, whereas adsorption energies decrease slightly for top and bridge sites. The CO bond is elongated compared to the gas-phase molecule for all geometries, but significant changes are hardly observed for perpendicular bonded CO at all three adsorption modes compared to the Mo(100)-CO- $p(2 \times 2)$  system, although all bonds are slightly smaller. However, elongation of the CO bond for the bent structure is larger than for the Mo(100)-CO- $p(2 \times 2)$  system, which is a remarkable observation.

Analysis of the vibrational frequencies calculated for Mo(100)-CO- $c(2 \times 2)$  leads to similar results as the Mo(100)-CO- $p(2 \times 2)$  system. The CO at bridge sites is a TS, and at fourfold hollow sites the perpendicular configuration is a second-order saddle point in the PES, while on-top and tilted adsorption geometries are local minima. Calculated CO stretching frequencies for CO positioned at on-top and tilted fourfold hollow configuration are 1943 and 958  $\text{cm}^{-1}$ , respectively. Compared to 0.25 ML of CO coverage, CO stretching frequency has increased by 54  $\text{cm}^{-1}$  for the on-top adsorption mode and decreased by 104  $\text{cm}^{-1}$  for the tilted configuration. The shift in stretching frequency towards a lower frequency (negative shift) for the CO molecule at the tilted position as coverage is increased from 0.25 to 0.50 ML is a striking result. Negative shifts for C-O stretching frequency have only been reported on transition-metals, such as copper, for which the interaction between the CO molecule and the surface metal is weak [60-62]; but never when the interaction is strong, which is the current case on Mo(100). According to the Blyholder model [63], increasing surface coverage results in lower  $\pi$ -back-donation of the metal to the CO molecule (chemical effect), leading to a shorter CO bond; on the other hand, increasing CO surface coverage also leads to a higher dipole-dipole coupling (physical effect), both leading to larger CO stretching frequencies. In addition to  $\pi$ -back-donation and  $\sigma$ -donation, Pauli repulsion also contributes significantly to the C-O stretching frequency; Illas et al. [64,65] and Curulla et al. [66] showed for CO/Pt(111) that  $\sigma$ -donation also lowers the C-O stretching frequency and that the Pauli repulsion shifts the C-O stretching frequency to higher frequencies. From our calculations, one may expect that the Pauli repulsion,  $\sigma$ -donation, and  $\pi$ -back-donation are very similar at 0.25 and 0.50 ML, because the adsorption energy is almost identical for both cases. The lowering of the CO stretching frequency, therefore, is most likely caused by another phenomenon such as a surface reconstruction, which is discussed into more detail in Chapter 4.

Nonetheless, the unusual behavior was checked by investigating two options. First, the results were verified by using a different system; a 2CO- $p(2 \times 2)$  slab was

used (also 0.5 ML CO), with the two CO molecules arranged in a  $c(2 \times 2)$  ordering pattern. The resulting (in-phase) C–O stretching frequency is  $980 \text{ cm}^{-1}$ . Next, we removed one CO molecule from the  $2\text{CO}-p(2 \times 2)$  optimized structure and reoptimized, hence, the  $\text{CO}-p(2 \times 2)$  slab (0.25 ML CO). This calculation leads to the same structure found previously, with same C–O stretching frequency ( $1062 \text{ cm}^{-1}$ ). Second, the lattice parameter may change when adding adsorbates to the surface; so an optimized lattice parameter was calculated for the  $\text{Mo}(100)\text{-CO}-c(2 \times 2)$  system. The optimized lattice parameter was found to be  $3.0824 \text{ \AA}$ , instead of the  $3.159 \text{ \AA}$  used for all calculations. Results, however, show that although the lattice parameter decreased, the CO bond length is not affected (Table 3A.1). Also, the CO stretching frequency reveals no noteworthy change (Table 3A.2). Consequently, we conclude that on  $\text{Mo}(100)$  the CO stretching frequency decreases when increasing CO surface coverage from 0.25 to 0.5 ML.

The imaginary frequency of adsorbed CO molecules at bridge sites is ascribed to rotational movement of CO toward a tilted mode at these bridge sites, whereas the two imaginary frequencies of the CO molecule at fourfold hollow sites can be attributed to rotation of CO into the tilted configuration. Including zero-point-energies does not change the adsorption energies significantly.

### *3A.3.2.3 Mo(100)-CO-p(1 × 1) ( $\theta = 1 \text{ ML}$ )*

Adsorption of CO is slightly more favored at the fourfold hollow sites ( $-1.46 \text{ eV}$ ;  $141 \text{ kJ mol}^{-1}$ ) than on-top ( $-1.35 \text{ eV}$ ;  $130 \text{ kJ mol}^{-1}$ ) and bridge ( $-1.14 \text{ eV}$ ;  $110 \text{ kJ mol}^{-1}$ ) sites at a CO surface coverage of 1 ML (Table 3A.1). Using the Redhead equation and assuming a pre-exponential factor of  $\nu_a = 10^{15}$  Zaera et al. reported adsorption energies for  $\alpha_1$  and  $\alpha_2$  (molecular adsorbed CO) to be  $54 \pm 4$  and  $96 \pm 8 \text{ kJ mol}^{-1}$ , respectively [38,59,67]. These  $\alpha$  peaks are observed after half-saturation (ca. 0.85 ML) of CO on the  $\text{Mo}(100)$  surface at 150 and 290 K for  $\alpha_1$  and  $\alpha_2$ , respectively. Although our calculations predict adsorption energies of  $130 \text{ kJ mol}^{-1}$  (desorption at 540 K) for CO adsorbed at top sites, experiments show that desorption takes place much earlier. A reason for this discrepancy might be that configurations of adsorbed CO are not as simple as our model describes.

Calculated C–O bond distances range from  $1.161 \text{ \AA}$  for CO at top sites to  $1.235 \text{ \AA}$  for CO at fourfold hollow sites. Hence, the CO molecule is activated the most at the hollow position; nevertheless, dissociation is not possible due to lack of space. No stable tilted configuration could be obtained for the  $\text{Mo}(100)\text{-CO}-p(1 \times 1)$  system (such as those found for the lower coverages), which can be correlated to the fact that the tilted configuration is argued to be a precursor species for dissociation. Analysis of the vibrational frequencies show that on-top and fourfold hollow sites are local minima on the PES of  $\text{CO}/\text{Mo}(100)$ , thus, stable adsorption sites (Table 3A.2). The calculated CO

stretching frequency for the top site is  $2032\text{ cm}^{-1}$ , corresponding well with literature ( $2100\text{ cm}^{-1}$ ) [38]. On the other hand, CO adsorbed at a fourfold hollow site has a frequency of  $1561\text{ cm}^{-1}$ , which has not been reported in literature, although calculations predict that fourfold hollow sites should be stable adsorption sites. The fact that no CO stretching frequency of around  $1560\text{ cm}^{-1}$  is found by experiments might be explained by the same argument used to clarify the adsorption energy difference between calculation and experiment: (1) configurations are not as simple as described in the model or (2) the exchange-correlation functional overestimated the adsorption energy of CO. The bridge adsorption mode is a second order saddle-point in the PES of Mo(100)-CO- $p(1 \times 1)$ , in which one imaginary frequency is related to the movement of the CO molecule from the bridge to the fourfold hollow adsorption site, while the other imaginary frequency is ascribed to the movement of CO from the bridge to the top site.

### 3A.3.3 Dissociation of CO on Mo(100) at 0.25 and 0.5 ML

CO dissociation on Mo(100) is reported to happen at temperatures as low as 230 K [38]. Different  $\beta$  peaks, due to the recombination of carbon and oxygen atoms, have been observed between 840 and 1250 K. Apparent activation energies reported for  $\beta_1$ ,  $\beta_2$ , and  $\beta_3$  are 264, 293, and  $389 \pm 8\text{ kJ mol}^{-1}$ , respectively, assuming  $\nu_\beta = 10^{-2}$  [38,59,67]. At low CO coverages the only observed  $\beta$  desorption peak is the  $\beta_3$  at 1250 K. This value corresponds very well with our desorption temperature of fourfold hollow tilted CO at surface coverage of 0.11 ML.

To obtain a complete picture, results calculated for the adsorption of atomic carbon and oxygen on Mo(100) at coverages of 0.25 and 0.5 ML are presented in Table 3A.3. The adsorption energies of carbon at the most stable sites (fourfold hollow) are -8.69 and -8.79 eV at 0.25 and 0.5 ML surface coverage, respectively. The relative adsorption energy of C at on-top and bridge sites with respect to the hollow sites is 3.82 and 2.34 eV at 0.25 ML, respectively; and 4.29 and 2.80 at 0.5 ML. On the other hand, the most stable location of oxygen is at the bridge site, with adsorption energies of -6.65 and -6.45 eV at 0.25 and 0.5 ML coverage. For oxygen, the relative adsorption energy at on-top and fourfold hollow sites with respect to bridge sites is only 0.44 and 0.18 eV at 0.25 ML, respectively; and 0.21 and 0.29 eV at 0.5 ML. Increasing the oxygen coverage, thus, leads to a shift of oxygen being more stable at top than hollow sites, while the bridge site stays the most favorable adsorption geometry even including zero-point-energy corrections (Table 3A.4). Adsorption energies are higher for carbon than for oxygen, hence, carbon is more strongly bound to the Mo(100) surface than oxygen. Carbon becomes slightly more stabilized on the Mo(100) surface for increasing coverage from  $p(2 \times 2)$  to  $c(2 \times 2)$ . Interesting to mention is that according to the vibrational frequencies fourfold hollow sites are the only local minima for carbon, whereas, oxygen is stable at all adsorption modes, at both 0.25 and 0.5 ML

**Table 3A.3** Adsorption of C and O on Mo(100) at  $\theta = 0.25$  and  $\theta = 0.5$  ML. (results displayed in *italics* are not true minima in the PES)

	$\Delta E_{\text{ads}}^{[a]}$ [eV]	$\Delta E_{\text{rel}}^{[b]}$ [eV]	$z_c^{[c]}$ [Å]	$\Delta E_{\text{ads}}^{[a]}$ [eV]	$\Delta E_{\text{rel}}^{[b]}$ [eV]	$z_o^{[c]}$ [Å]
	C at 0.25 ML			O at 0.25 ML		
on-top	<i>-4.87</i>	3.82	<i>1.769</i>	-6.21	0.44	1.740
bridge	<i>-6.35</i>	2.34	<i>0.993</i>	-6.65	0	1.355
hollow	<i>-8.69</i>	0	0.547	-6.47	0.18	0.582
	C at 0.5 ML			O at 0.5 ML		
on-top	<i>-4.50</i>	4.29	<i>1.768</i>	-6.24	0.21	1.728
bridge	<i>-5.99</i>	2.8	<i>0.978</i>	-6.45	0	1.300
hollow	<i>-8.79</i>	0	0.448	-6.16	0.29	0.488

[a]  $\Delta E_{\text{ads}}$  is the adsorption energy. [b]  $\Delta E_{\text{rel}}$  is the relative adsorption energy with respect to the fourfold hollow site and bridge site for carbon and oxygen, respectively. [c]  $z_c$  and  $z_o$  are the height of the carbon and oxygen atom with respect to the surface level.

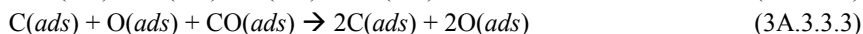
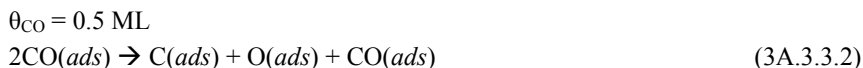
**Table 3A.4** Adsorption of C and O on Mo(100) at  $\theta = 0.25$  and  $\theta = 0.5$  ML: vibrational frequencies [ $\text{cm}^{-1}$ ], zero-point-energy corrections to the adsorption energy and to the relative adsorption energy. (results displayed in *italics* are not true minima in the PES)

	$\nu_1$	$\nu_2$	$\nu_3^{[a]}$	ZPE <sup>[b]</sup> [eV]	$\Delta E_{\text{ads}}^{[c]}$ [eV]	$\Delta E_{\text{rel}}^{[d]}$ [eV]
	C at 0.25 ML					
<i>on-top</i>	<i>89i</i>	<i>89i</i>	<i>850</i>	<i>0.05</i>	<i>-4.82</i>	<i>3.78</i>
<i>bridge</i>	<i>276i</i>	<i>629</i>	<i>462</i>	<i>0.07</i>	<i>-6.28</i>	<i>2.32</i>
hollow	442	442	558	0.09	-8.60	0
	C at 0.5 ML					
<i>on-top</i>	<i>123i</i>	<i>123i</i>	<i>852</i>	<i>0.05</i>	<i>-4.45</i>	<i>4.26</i>
<i>bridge</i>	<i>315i</i>	<i>631</i>	<i>476</i>	<i>0.07</i>	<i>-5.92</i>	<i>2.79</i>
hollow	327	327	558	0.08	-8.71	0
	O at 0.25 ML					
on-top	71	71	830	0.06	-6.15	0.43
bridge	177	336	573	0.07	-6.58	0
hollow	122	122	427	0.04	-6.43	0.15
	O at 0.5 ML					
on-top	92	92	870	0.07	-6.18	0.20
bridge	179	313	552	0.06	-6.38	0
hollow	189	189	403	0.05	-6.11	0.27

[a]  $\nu_3$  is the metal–C / metal–O stretching frequency. [b] ZPE is the zero-point-energy. [c]  $\Delta E_{\text{ads}}$  is the adsorption energy including ZPE. [d]  $\Delta E_{\text{rel}}$  is the relative adsorption energy including ZPE.

(Table 3A.4). In addition, the M–C stretch is  $558\text{ cm}^{-1}$  at both 0.25 and 0.5 ML surface coverage and the M–O stretch is  $573$  and  $552\text{ cm}^{-1}$  at 0.25 and 0.5 ML, respectively. Metal–C stretches found experimentally appear at around  $515\text{ cm}^{-1}$  and M–O stretches at  $590\text{ cm}^{-1}$ .

The activation energy of dissociation of CO on Mo(100) at 0.25 and 0.5 ML CO coverage was calculated according to the following elementary reactions:



The reaction energy of dissociation of CO at 0.25 ML coverage is  $-1.71\text{ eV}$  (3A.3.3.1), including diffusion of oxygen; consequently, dissociation of CO at low CO surface concentrations is an activated process. Increasing the CO surface coverage to 0.5 ML results only in an energy gain of  $-0.59\text{ eV}$  ((3A.3.3.2)+(3A.3.3.3)), nevertheless, a favored process.

Calculations of C and O coadsorption were performed on a Mo(100)- $p(2 \times 2)$  slab model as the dissociated end-state of CO at 0.25 ML. Three configurations were considered; (1) cis, (2) trans, and (3) short-trans (Figure 3A.2). The relative energies for these three situations with respect to carbon monoxide tilted at the fourfold hollow position are  $-0.83$ ,  $-1.71$ , and  $-1.37\text{ eV}$  for cis, trans, and short-trans, respectively. The M–C stretching frequencies are  $536$ ,  $558$ , and  $544\text{ cm}^{-1}$  for cis, trans, and short-trans configuration, respectively, whereas the M–O stretching frequencies are  $410$ ,  $440$ , and  $515\text{ cm}^{-1}$ .

The transition-state structure consists of the carbon atom at a fourfold hollow site and the oxygen atom close to a bridge site (Figure 3A.2) as was also reported for CO on Fe(100) by Bromfield et al. [3]. The activation energy for CO dissociation on Mo(100) at 0.25 ML is  $0.56\text{ eV}$  ( $54\text{ kJ mol}^{-1}$ ), indicating that dissociation takes place at ca.  $224\text{ K}$  [59], which is in good agreement with Zaera et al. who reported a dissociation temperature of CO on Mo(100) of  $230\text{ K}$  [38]. On the other hand, the activation energy of recombination is  $1.39\text{ eV}$  ( $134\text{ kJ mol}^{-1}$ ), thus, much smaller than the apparent activation energy found by Zaera et al. ( $389\text{ kJ mol}^{-1}$ ), hence,  $\beta$  desorption features do not correlate with the activation energy of recombination of atomic carbon and atomic oxygen. This would imply that the desorption peak at  $1250\text{ K}$  is not due to recombination of C and O, but originates from molecular desorption of CO. Including zero-point-energy corrections changes the activation energy of CO dissociation and recombination slightly to  $0.53\text{ eV}$  ( $51\text{ kJ mol}^{-1}$ ) and  $1.38\text{ eV}$  ( $133\text{ kJ mol}^{-1}$ ).

The activation energy for CO dissociation was also calculated on Mo(100) at 0.5 ML coverage. For this purpose, a Mo(100)- $p(2 \times 2)$  slab model was used containing two CO molecules adsorbed in a tilted fourfold hollow geometry, which gives rise to a

CO- $c(2 \times 2)$  overlayer structure (Figure 3A.3). The adsorption energy of the second CO molecule is -2.69 eV, which is slightly higher than the adsorption energy calculated using a Mo(100)- $c(2 \times 2)$  unit cell (-2.63 eV; see Table 3A.1), thus showing a slight stabilization. This behavior is the opposite of that for iron. Dissociating the first half CO molecules yields a surface with C and O coadsorbed in a cis configuration, in which the second half CO molecules is positioned trans with respect to the carbon atom (Figure 3A.3). The activation energy of dissociation of the first half CO molecules is 0.45 eV ( $43 \text{ kJ mol}^{-1}$ ), which is 0.1 eV smaller than CO at 0.25 ML surface coverage and in line with the previous discussion; the longer the C-O bond, the smaller the activation energy of dissociation. Dissociation of CO at 0.25 ML leads to an exothermic reaction yielding 0.83 eV in energy, without diffusion, whereas dissociation of the first CO molecule at 0.5 ML (reaction (3A.3.3.2)) results in an exothermic reaction producing only 0.35 eV energy gain. Moreover, recombination energy is decreased by 0.59 eV to 0.8 eV ( $77 \text{ kJ mol}^{-1}$ ) compared to 0.25 ML, which is again in disagreement with

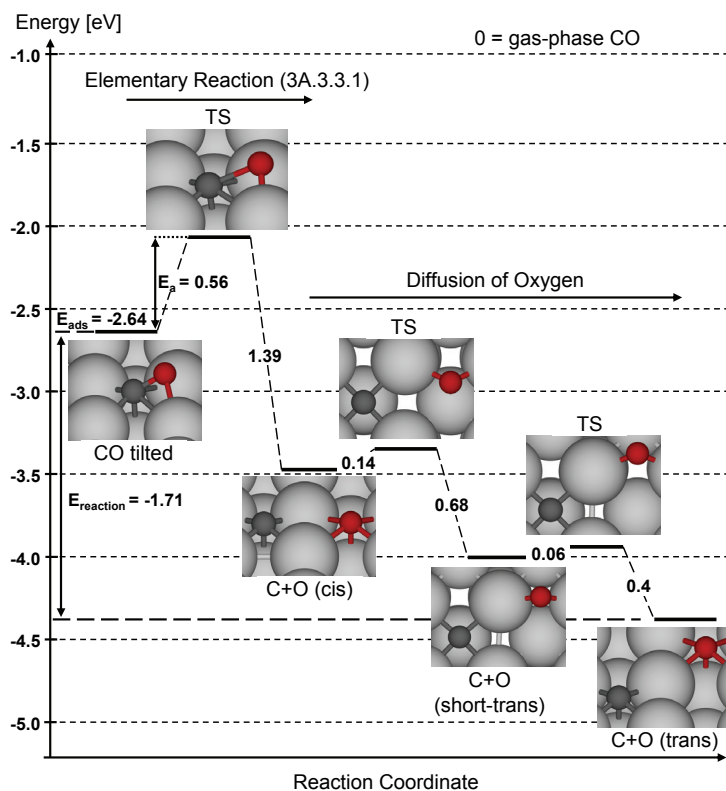


**Figure 3A.2** Energy diagram of dissociation of 0.25 ML CO on Mo(100) using a  $p(2 \times 2)$  unit cell. The numbers inserted represent the activation energies of the elemental steps. Energies are without ZPE correction.



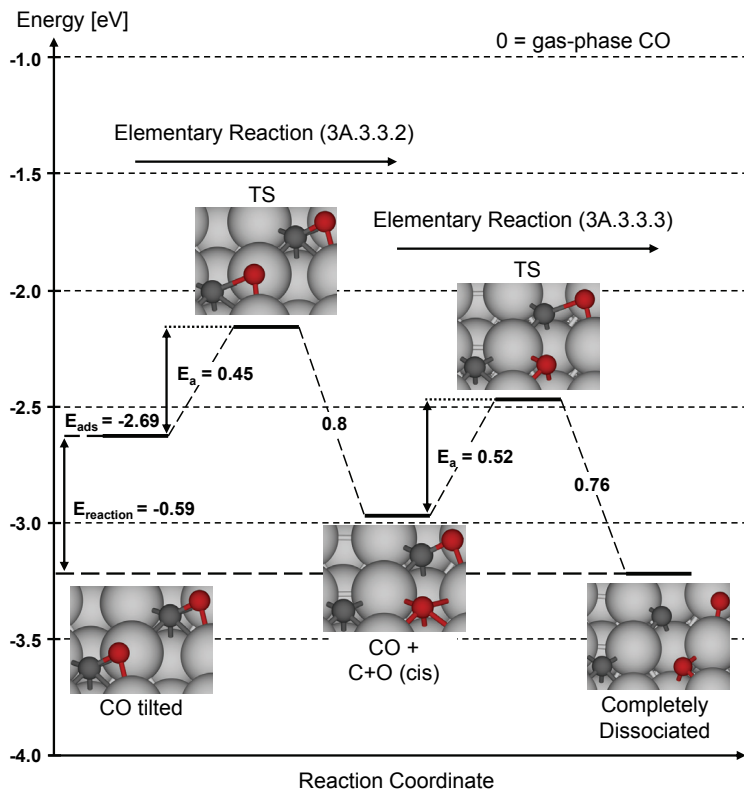


**Figure 3A.3** Energy diagram of dissociation of 0.5 ML CO on Mo(100) using a  $p(2 \times 2)$  unit cell. The numbers inserted represent the activation energies of the elemental steps. Energies are without ZPE correction.

apparent activation energies reported by Zaera et al. (264 and 293  $\text{kJ mol}^{-1}$ ). Zero-point-energy corrections negligibly lower the activation energy of dissociation to 0.44 eV and of recombination to 0.79 eV. Dissociating the second half CO molecules on the surface gives rise to a completely covered surface (1 ML) of coadsorbed C and O atoms, in which one carbon atom is adsorbed at the fourfold hollow position, whereas the other is positioned in a threefold coordinated manner (Figure 3A.3). One of the oxygen atoms is also adsorbed at a threefold hollow site, and the other is located at the bridge site. The activation energy to dissociate the second half CO molecules (reaction (3A.3.3.3)) is slightly higher than the activation energy needed to dissociate the first half (0.52 eV, as compared to 0.45 eV) and the recombination energy is slightly lower (0.76 eV, instead of 0.80 eV). Dissociation of the remaining CO molecules results in an additional gain of 0.24 eV of energy. Thus, the overall CO dissociation reaction energy at 0.5 ML CO coverage is -0.59 eV, which is again an activated process.

We conclude that increasing CO coverage leads to easier CO dissociation on the

molybdenum surface, although the energy gain or exothermicity and hence the driving force for dissociation is much lower. This result is also striking for it seems to go against the Brønsted-Evans-Polanyi relationship that states that the larger the exothermicity, the lower the activation barrier of the reaction, and goes also against the universality principle in heterogeneous catalysis as formulated by Nørskov et al. [68]. Furthermore, it is interesting to note that after the first half CO molecules has dissociated the adsorption energy of the remaining CO molecules is decreased to -2.26 eV; 0.48 eV lower than the adsorption energy of the second half CO molecules at 0.5 ML and 0.38 eV lower than the adsorption of CO at 0.25 ML. After dissociation of the first half CO molecules, the adsorption energy of the second half corresponds to a desorption temperature of 904 K, which is close to the value of the  $\beta_2$  desorption peak (940 K) observed by Zaera et al. [38]. As a result, both the  $\beta_2$  and the  $\beta_3$  peaks found experimentally seem to be more properly labeled as  $\alpha$  (molecular) desorption peaks. In conclusion, our calculations indicate that all five desorption states observed experimentally are molecular desorption states.

### **3A.4 Concluding Remarks**

CO adsorbs molecularly on Mo(100) at fourfold hollow sites with the CO bond axis tilted away from the surface normal by  $57^\circ$  at CO coverage of 0.25 ML. The adsorption energy of the CO molecule is -2.64 eV and the C–O stretching frequency  $1062\text{ cm}^{-1}$ . Decreasing CO coverage to 0.11 ML, results in a significant increase in the adsorption energy to -2.93 eV. The activation energy of dissociation of CO molecules at 0.25 ML is as low as 0.56 eV and the energy gain -0.83 eV, without oxygen diffusion, or -1.71 eV, including oxygen diffusion; thus, dissociation of CO at low coverages is a favorable process that takes place at temperatures as low as 224 K. Furthermore, our calculations show that the energy required for recombination is only 1.39 eV, which is considerably smaller than the apparent activation energy of recombination reported experimentally. At high coverages (0.50 ML), CO still adsorbs tilted at fourfold hollow sites with an adsorption energy very similar to that at 0.25 ML and exhibits a CO stretching frequency of  $958\text{ cm}^{-1}$ , which is surprisingly smaller than that at 0.25 ML. Dissociation of half of the CO molecules leads to a configuration in which the remaining CO molecules have an adsorption energy of -2.26 eV. The activation energy of CO dissociation at 0.50 ML is 0.45 eV, slightly smaller than that at lower coverages, and the activation energy of recombination is 0.80 eV. Moreover, the reaction energy of the dissociation of half of the CO molecules at 0.50 ML is only 0.35 eV. Further dissociation leads to a 1 ML atomic configuration on the surface, with a total reaction energy of 0.59 eV with respect to the initial molecular state. In such 1 ML atomic configuration, some atoms adsorb at fourfold hollow sites, others at threefold-like hollow sites, and others at bridge sites in order to minimize repulsion.

Our calculations demonstrate that the activation energy of recombination is much smaller than the adsorption energy of tilted CO at various coverages, and, therefore, TPD analysis of the high-temperature  $\beta$  desorption peaks observed experimentally does not yield the apparent activation energy of recombination, but the activation energy of desorption. Accordingly, the  $\beta$  desorption peaks reported experimentally should be labeled as  $\alpha$  peaks, for  $\alpha$  stands for molecular desorption features and  $\beta$  for recombination ones.

In addition, our calculations also show that the C–O stretch shifts from 1062  $\text{cm}^{-1}$  to 958  $\text{cm}^{-1}$  when increasing CO surface coverage from 0.25 to 0.50 ML. This result is clearly against the general trend that CO stretching frequency shifts to higher frequency as CO coverage increases, for strongly adsorbed CO. Two factors contribute the most to the shift to higher frequencies: (1) dipole–dipole coupling and (2) chemical effect. Dipole–dipole coupling always shifts the CO stretch to higher frequencies. We can conclude that we observe a negative chemical shift; chemical effect is based on the interpretation of the extended Blyholder model from which we can derive that the chemical shift is a result of a balance between Pauli repulsion, that shift the C–O stretching frequency to higher frequencies, and the  $\pi$ -back-donation and  $\sigma$ -donation that shift the C–O stretching frequency to lower frequencies. In Chapter 4 this phenomenon is investigated into more detail and a possible explanation (surface reconstruction) for the remarkable shift is presented.

Finally, it is also remarkable that both the activation energy and the reaction energy of CO dissociation decrease when CO coverage increases from 0.25 to 0.50 ML. This result is against the Brønsted-Evans-Polanyi (BEP) relationship that states that the larger the exothermicity of the reaction, the lower the activation energy, and it is also an exception to universality principle in heterogeneous catalysis stated by Nørskov and co-workers based on the BEP relationship. However, this principle was formulated for dissociating molecules at a single coverage on a variety of surfaces. In our case, we vary the coverage, and hence the chemical environment of the dissociating molecule, and keep the substrate the same. Further work is needed to investigate the validity of the BEP selection for such situations.

## References

- [1] *Studies in Surface Science and Catalysis*, A. P. Steynberg, M. Dry (Eds.), Vol. 152, Elsevier, Amsterdam, 2004.
- [2] C. E. Bartosch, L. J. Whitman, W. Ho, *J. Chem. Phys.* **85** (1986) 1052.
- [3] T. C. Bromfield, D. Curulla-Ferré, J. W. Niemantsverdriet, *ChemPhysChem* **6** (2005) 254.
- [4] S. D. Cameron, D. J. Dwyer, *Langmuir* **4** (1988) 282.
- [5] D. Curulla-Ferré, A. Govender, T. C. Bromfield, J. W. Niemantsverdriet, *J. Phys. Chem. B* **110** (2006) 13897.

- [6] D. J. Dwyer, B. Rausenberger, J. P. Lu, S. L. Bernasek, D. A. Fischer, S. D. Cameron, D. H. Parker, J. L. Gland, *Surf. Sci.* **224** (1989) 375.
- [7] W. Erley, *J. Vac. Sci. Technol.* **18** (1981) 472.
- [8] L. Gonzalez, R. Miranda, S. Ferrer, *Surf. Sci.* **119** (1982) 61.
- [9] D. E. Jiang, E. A. Carter, *Surf. Sci.* **570** (2004) 167.
- [10] D. W. Moon, S. L. Bernasek, D. J. Dwyer, J. L. Gland, *J. Am. Chem. Soc.* **107** (1985) 4363.
- [11] D. W. Moon, S. Cameron, F. Zaera, W. Eberhardt, R. Carr, S. L. Bernasek, J. L. Gland, D. J. Dwyer, *Surf. Sci. Lett.* **180** (1987) L123.
- [12] D. W. Moon, D. J. Dwyer, S. L. Bernasek, *Surf. Sci.* **163** (1985) 215.
- [13] R. S. Saiki, G. S. Herman, M. Yamada, J. Osterwalder, C. S. Fadley, *Phys. Rev. Lett.* **63** (1989) 283.
- [14] D. C. Sorescu, D. L. Thompson, M. M. Hurley, C. F. Chabalowski, *Phys. Rev. B* **66** (2002) 035416/1.
- [15] L. J. Whitman, L. J. Richter, B. A. Gurney, J. S. Villarrubia, W. Ho, *J. Chem. Phys.* **90** (1989) 2050.
- [16] M. E. Bridge, C. M. Comrie, R. M. Lambert, *Surf. Sci.* **67** (1977) 393.
- [17] Q. Ge, M. Neurock, *J. Phys. Chem. B* **110** (2006) 15368.
- [18] A. A. Gokhale, M. Mavrikakis, *Prepr. Pap. -Am. Chem. Soc., Div. Fuel Chem.* **50** (2005) 149.
- [19] X.-Q. Gong, R. Raval, P. Hu, *Surf. Sci.* **562** (2004) 247.
- [20] J. Lahtinen, J. Vaari, K. Kauraala, *Surf. Sci.* **418** (1998) 502.
- [21] H. Papp, *Surf. Sci.* **129** (1983) 205.
- [22] D. W. Goodman, R. D. Kelley, T. E. Madey, J. M. White, *J. Catal.* **64** (1980) 479.
- [23] T. Li, B. Bhatia, D. S. Sholl, *J. Chem. Phys.* **121** (2004) 10241.
- [24] Y. Morikawa, J. J. Mortensen, B. Hammer, J. K. Nørskov, *Surf. Sci.* **386** (1997) 67.
- [25] V. Shah, T. Li, K. L. Baumert, H. Cheng, D. S. Sholl, *Surf. Sci.* **537** (2003) 217.
- [26] K. Sinniah, J. E. Reutt-Robey, A. R. Brown, D. J. Doren, *J. Chem. Phys.* **101** (1994) 764.
- [27] J. T. Stuckless, N. Al-Sarraf, C. Wartnaby, D. A. King, *J. Chem. Phys.* **99** (1993) 2202.
- [28] I. M. Ciobica, R. A. van Santen, *J. Phys. Chem. B* **107** (2003) 3808.
- [29] H. Pfnür, P. Feulner, D. Menzel, *J. Chem. Phys.* **79** (1983) 4613.
- [30] H. Pfnür, D. Menzel, *J. Chem. Phys.* **79** (1983) 2400.
- [31] H. Pfnür, D. Menzel, F. M. Hoffmann, A. Ortega, A. M. Bradshaw, *Surf. Sci.* **93** (1980) 431.
- [32] N. D. Shinn, T. E. Madey, *J. Chem. Phys.* **83** (1985) 5928.
- [33] J. E. Houston, *Surf. Sci.* **255** (1991) 303.
- [34] G. H. Ryu, S. C. Park, S.-B. Lee, *Surf. Sci.* **427-428** (1999) 419.
- [35] M. L. Colaianni, J. G. Chen, W. H. Weinberg, J. T. Yates, Jr., *J. Am. Chem. Soc.* **114** (1992) 3735.
- [36] J. P. Fulmer, F. Zaera, W. T. Tysoe, *J. Chem. Phys.* **87** (1987) 7265.
- [37] Z. Ji, J.-Q. Li, *J. Phys. Chem. B* **110** (2006) 18363.
- [38] F. Zaera, E. Kollin, J. L. Gland, *Chem. Phys. Lett.* **121** (1985) 464.
- [39] A. Griboval-Constant, J.-M. Giraudon, G. Leclercq, L. Leclercq, *Appl. Catal. A* **260** (2004) 35.
- [40] P. Liu, J. A. Rodriguez, *Catal. Lett.* **91** (2003) 247.
- [41] P. M. Patterson, T. K. Das, B. H. Davis, *Appl. Catal. A* **251** (2003) 449.
- [42] T. Zeng, X.-D. Wen, G.-S. Wu, Y.-W. Li, H. Jiao, *J. Phys. Chem. B* **109** (2005) 2846.
- [43] C. Guillot, R. Riwan, J. Lecante, *Surf. Sci.* **59** (1976) 581.
- [44] E. I. Ko, R. J. Madix, *Surf. Sci.* **100** (1980) L505.
- [45] E. I. Ko, R. J. Madix, *Surf. Sci.* **109** (1981) 221.
- [46] J. C. Boettger, *J. Phys.: Condens. Matter* **11** (1999) 3237.
- [47] G. Kresse, J. Furthmüller, *Phys. Rev. B* **54** (1996) 11169.
- [48] G. Kresse, J. Furthmüller, *J. Comput. Mater. Sci.* **6** (1996) 15.
- [49] J. P. Perdew, K. Burke, M. Ernzerhof, *Phys. Rev. Lett.* **77** (1996) 3865.
- [50] B. Hammer, L. B. Hansen, J. K. Nørskov, *Phys. Rev. B* **59** (1999) 7413.
- [51] P. E. Blöchl, *Phys. Rev. B* **50** (1994) 17953.
- [52] G. Kresse, D. Joubert, *Phys. Rev. B* **59** (1999) 1758.
- [53] M. Methfessel, A. T. Paxton, *Phys. Rev. B* **40** (1989) 3616.
- [54] <http://www.webelements.com>, Accessed 2009.
- [55] H. J. Monkhorst, J. D. Pack, *Phys. Rev. B* **13** (1976) 5188.
- [56] P. Pulay, *Chem. Phys. Lett.* **73** (1980) 393.

- [57] J. D. Head, *Int. J. Quantum Chem.* **65** (1997) 827.
- [58] G. Henkelman, B. P. Uberuaga, H. Jonsson, *J. Chem. Phys.* **113** (2000) 9901.
- [59] Z. Knor, *Surf. Sci.* **154** (1985) L233.
- [60] P. Hollins, J. Pritchard, *Surf. Sci.* **89** (1979) 486.
- [61] R. Ryberg, *Surf. Sci.* **114** (1982) 627.
- [62] H. Ueba, *Surf. Sci.* **188** (1987) 421.
- [63] G. Blyholder, *J. Phys. Chem.* **68** (1964) 2772.
- [64] F. Illas, S. Zurita, A. M. Marquez, J. Rubio, *Surf. Sci.* **376** (1997) 279.
- [65] F. Illas, S. Zurita, J. Rubio, A. M. Marquez, *Phys. Rev. B* **52** (1995) 12372.
- [66] D. Curulla Ferre, A. Clotet, J. M. Ricart, F. Illas, *J. Phys. Chem. B* **103** (1999) 5246.
- [67] P. A. Redhead, *Vacuum* **12** (1962) 203.
- [68] J. K. Nørskov, T. Bligaard, A. Logadottir, S. Bahn, L. B. Hansen, M. Bollinger, H. Bengaard, B. Hammer, Z. Sljivancanin, M. Mavrikakis, Y. Xu, S. Dahl, C. J. H. Jacobsen, *J. Catal.* **209** (2002) 275.

# 3B

## Adsorption, Desorption, and Dissociation of CO on Tungsten(100)

### Abstract

*DFT calculations have been performed to investigate the adsorption of CO on W(100) for several adsorption sites at four different surface coverages. Dissociation of CO on W(100) has been explored for two surface concentrations: 0.25 and 0.5 ML. To establish whether the calculated structures are stable adsorption states or transition-states, a complete analysis of the vibrational frequencies of CO was carried out. For coverages up to 0.5 ML, the CO adsorbs molecularly on the W(100) surface at fourfold hollow sites with the molecular axis tilted away from the surface normal by 58° with an adsorption energy of -3.00 eV. The calculated C–O stretching frequency at 0.25 ML CO coverage is 926 cm<sup>-1</sup>, in good agreement with experiments. Increasing CO coverage to 0.5 ML leads to a lower C–O stretching frequency of 847 cm<sup>-1</sup>, which is extraordinary, since it is not expected from previous experimental observations. CO is able to dissociate very easily with activation energies of only 0.25-0.31 eV, which results in an energy gain of 1.72 and 0.69 eV at 0.25 and 0.5 ML, after dissociation, respectively. In addition, calculations reveal that reported  $\beta$ -CO desorption peaks in literature are due to molecular desorption of tilted CO at the fourfold hollow sites and are not limited by C + O recombination, as was concluded experimentally.*

### 3B.1 Introduction

Adsorption of CO on W(100) was studied in the late 1960s and 1970s using a large variety of surface science techniques, such as temperature programmed desorption (TPD), Auger electron spectroscopy (AES), ultraviolet photoemission spectroscopy (UPS), and electron energy loss spectroscopy (EELS). The studies mainly concentrated on the determination of whether CO adsorbed molecularly or dissociatively [1-6]. TPD experiments showed two distinct sets of desorption features;  $\alpha$  peaks related to molecularly adsorbed CO at 260 ( $\alpha_1$ ) and 360 K ( $\alpha_2$ ), and  $\beta$  peaks at 930 ( $\beta_1$ ), 1070 ( $\beta_2$ ), and 1375 K ( $\beta_3$ ) were assigned to dissociated CO [5]. Adsorption of CO at 80 K leads to simultaneous formation of both molecular and dissociated CO [5,7], which reaches a saturation coverage of  $1.15 \cdot 10^{15}$  molecules  $\text{cm}^{-2}$ , equivalent to 1.15 monolayer (ML). During heating, 0.65 ML of the CO molecules desorbs below 450 K as CO( $\alpha$ ) states, whereas 0.5 ML dissociates into CO( $\beta$ ) states. The full  $\beta$ -layer shows a  $p(1 \times 1)$  LEED pattern, while the CO( $\beta_3$ ) overlayer displays a  $c(2 \times 2)$  LEED pattern [8]. Thus, the full  $\beta$ -layer corresponds to approximately 0.5 ML of CO and the  $\beta_3$  to ca. 0.25 ML. The total amount of CO desorbed from the  $\beta_1$ - and  $\beta_2$ -layer is about 0.125 ML for both layers [5]. Further, at low CO coverages EELS experiments showed two distinct losses at 544 and 624  $\text{cm}^{-1}$ , attributed to the carbon and oxygen atoms, respectively, both adsorbed in a fourfold hollow position. Increasing the CO coverage leads to two additional losses at 360 and 2064  $\text{cm}^{-1}$ , that correspond to M-CO and C-O vibrations of carbon monoxide adsorbed molecularly in upright positions, respectively [4]. Adnot and Carette found an additional peak at 920  $\text{cm}^{-1}$  with a low intensity that disappeared after heating towards 500 K. They assigned this peak to a new  $\alpha$ -state, namely,  $\alpha_3$ , and associated this  $\alpha_3$  to bond to two or more tungsten atoms [1].

Only three theoretical papers could be found for CO adsorption and dissociation on tungsten surfaces. In the early 1970s, Lee and Rabalais [9] calculated the adsorption of CO on W(100) using the extended Hückel molecular orbital (EHMO) theory, whereas two groups studied the adsorption of CO on W(111); Ryu et al. [10] did cluster-model atom superposition and electron delocalization molecular orbital (ASED-MO) calculations, whereas Chen et al. [11] did DFT slab model calculations. According to Lee and Rabalais, the most stable form of CO on W(100) is dissociatively adsorbed CO, with carbon in the fourfold adsorption site and oxygen in either two- or fourfold position. Both Chen et al. and Ryu et al. came to the conclusion that CO on W(111) is adsorbed preferentially in the inclined configuration, with CO adsorbed between two W atoms of the first surface layer. Since cluster models are suitable to study local properties such as adsorption geometries and adsorbate vibrational frequencies, but not to study adsorption energies because these are strongly dependant on the cluster model used and also on the reference electronic state (bond-preparation method by Siegbahn and co-workers) [12], we report only the adsorption energies found by Chen et al. For

the inclined adsorption configuration, they find an adsorption energy of -1.79 eV and a CO stretch of 1318  $\text{cm}^{-1}$ . For the  $\alpha$ -state, the calculated adsorption energy of CO at onefold and threefold shallow sites was -1.37 eV with C–O stretching frequencies of 1920 and 1722  $\text{cm}^{-1}$ , respectively [11]. The activation energy of CO dissociation was calculated for CO in the inclined configuration to be 0.82 eV and the recombination energy of CO 1.44 eV.

In this Chapter, we present the results of our study of CO adsorption and dissociation on W(100) using density functional theory and report an even smaller activation energy of dissociation than Chen et al. on W(111), with barriers as low as 0.31 eV for tilted CO on W(100), which is the smallest activation energy ever reported for CO dissociation.

### **3B.2 Computational Details**

The computational details can be found in Chapter 3A. Specific details concerning the tungsten metal are provided below.

Tungsten exhibits a body centered cubic (bcc) structure. The relative positions of the metal atoms have been fixed initially as those in the bulk, with an optimized lattice parameter of 3.175 Å (the experimental value is 3.165 Å) [13]. Unlike bulk tungsten, which has no magnetic moment, tungsten slabs exhibited small magnetic moments; 0.10  $\mu_{\text{B}}$ /atom for W(100)- $c(2 \times 2)$  and 0.13  $\mu_{\text{B}}$ /atom for W(100)- $p(2 \times 2)$ . Tests on the influence of the spin character on the results showed that geometries were unaffected by such small magnetic moments and total energies were similar or slightly more stable. The estimated error that is committed in the calculation of adsorption energies and reaction energies using non-spin-polarized calculations is below 0.02 eV. Consequently, we report here non-spin-polarized results.

The adsorption of CO was investigated on W(100) at four different coverages: (1) 0.11 ML using a  $p(3 \times 3)$  unit cell, (2) 0.25 ML using a  $p(2 \times 2)$  unit cell, (3) 0.5 ML using a  $c(2 \times 2)$  unit cell, and (4) 1 ML using a  $p(1 \times 1)$  unit cell. The adsorption energy of CO, and atomic carbon and oxygen is calculated with respect to its respective gas-phase species. Zero-point-energy (ZPE) corrections were not applied to the energies in the diagrams since ZPE is relevant for X–H bonds, but hardly important for X–Y bonds, such as C–O. Moreover, the energy differences fall within the calculation error (0.05 eV). Dissociation of CO on W(100) was studied at two coverages, at 0.25 and 0.5 ML, using a  $p(2 \times 2)$  model containing one and two CO molecules, respectively.

### **3B.3 Results and Discussion**

First, the results of CO adsorption will be presented for each coverage. Then a comparison is made between the calculations and experiments and the results for the



dissociation of CO at both 0.25 and 0.5 ML CO coverage will be shown and compared to literature. Lastly, the surface reactivity of the (100) surface will be compared to the (111) surface.

### 3B.3.1 CO Adsorption on W(100)

#### 3B.3.1.1 $W(100)\text{-CO-}p(2 \times 2)$ ( $\theta=0.25$ ML)

The adsorption of CO on W(100) at 0.25 ML was investigated for all three adsorption sites: top, bridge, and fourfold hollow sites, as well as in tilted configuration.

The CO molecule adsorbs with the C–O bond perpendicular to the surface at top and bridge sites, whereas two adsorption geometries are observed for CO at the fourfold hollow site: one with the C–O bond aligned with the surface normal and the other with the CO inclined. The most stable configuration of CO on W(100) is carbon monoxide adsorbed at fourfold hollow sites with the C–O bond axis tilted away from the surface normal by an angle of  $58^\circ$  (see Table 3B.1). The corresponding adsorption energy of CO at this tilted configuration is  $-3.01$  eV and is substantially larger than at top, bridge, and fourfold hollow sites with vertically oriented CO, with adsorption energies of  $-1.78$ ,  $-1.57$ , and  $-1.72$  eV, respectively. The C–O bond is elongated (activation of the CO molecule) for all adsorption geometries, with the largest increase of the C–O bond for CO in the fourfold hollow tilted adsorption mode ( $1.413$  Å), with an expansion of  $0.270$  Å compared to gas-phase carbon monoxide ( $1.143$  Å).

Calculations of the vibrational frequencies reveal that only two out of four adsorption geometries are local minima in the potential energy surface (PES) of  $W(100)\text{-CO-}p(2 \times 2)$  (Table 3B.2). Bear in mind, however, that two vibrational frequencies of CO adsorbed at top sites are only  $11$   $\text{cm}^{-1}$ . This low value might be around the same order of magnitude as the error associated with its calculation; therefore, this adsorption geometry could either be a stable geometry or a second-order saddle point in the PES of  $W(100)\text{-CO-}p(2 \times 2)$ . Nevertheless, since the fourfold hollow tilted configuration is the most stable adsorption geometry, the overall picture will not be affected. The CO stretching frequency of CO in the most stable adsorption configuration is  $926$   $\text{cm}^{-1}$  (Table 3B.2) and for CO adsorbed on-top  $1886$   $\text{cm}^{-1}$ . For CO adsorbed at both bridge and hollow sites, two imaginary frequencies are observed; consequently, both adsorption sites are second-order saddle points in the PES of  $W(100)\text{-CO-}p(2 \times 2)$ . The imaginary vibration  $\nu_1$  of the CO molecule adsorbed at a bridge site corresponds to a rotational movement of the CO molecule, whereas normal mode  $\nu_2$  can be ascribed to the movement of the CO molecule toward the fourfold hollow position. The two imaginary frequencies of CO at fourfold hollow sites ( $\nu_1$  and  $\nu_2$ ) can be attributed to rotation of the carbon monoxide molecule towards the most stable geometry, i.e., the tilted fourfold hollow configuration.

Including zero-point-energy (ZPE) corrections gives rise to slightly smaller adsorption energies for three of the four configurations, while a similar adsorption energy is observed for vertically adsorbed CO at fourfold hollow sites.

**Table 3B.1** Adsorption of CO on W(100) at  $\theta = 0.11, 0.25, 0.5,$  and 1 ML. (results displayed in *italics* are not true minima in the PES)

		$\Delta E_{\text{ads}}^{[\text{a}]}$ [eV]	$d_{\text{CO}}^{[\text{b}]}$ [Å]	$\Delta d_{\text{CO}}^{[\text{c}]}$ [Å]	$z_{\text{CO}}^{[\text{d}]}$ [Å]	$\theta^{[\text{e}]}$ [°]
$\theta = 0.11$ ML	hollow/tilted	-3.57	1.399	0.256	0.767 (1.500)	58.4
$\theta = 0.25$ ML	<i>on-top</i>	<i>-1.78</i>	<i>1.176</i>	<i>0.033</i>	<i>2.028</i>	-
	<i>bridge</i>	<i>-1.57</i>	<i>1.203</i>	<i>0.060</i>	<i>1.589</i>	-
	<i>hollow</i>	<i>-1.72</i>	<i>1.278</i>	<i>0.135</i>	<i>0.932</i>	-
	hollow/tilted	-3.01	1.413	0.270	0.711 (1.453)	58.3
$\theta = 0.5$ ML	<i>on-top</i>	<i>-1.77</i>	<i>1.171</i>	<i>0.028</i>	<i>2.035</i>	-
	<i>bridge</i>	<i>-1.42</i>	<i>1.200</i>	<i>0.057</i>	<i>1.607</i>	-
	<i>hollow</i>	<i>-1.70</i>	<i>1.283</i>	<i>0.140</i>	<i>0.742</i>	-
	hollow/tilted	-3.00	1.439	0.296	0.606 (1.370)	57.9
$\theta = 1$ ML	<i>on-top</i>	<i>-1.63</i>	<i>1.163</i>	<i>0.020</i>	<i>2.056</i>	-
	<i>bridge</i>	<i>-1.31</i>	<i>1.179</i>	<i>0.036</i>	<i>1.628</i>	-
	<i>hollow</i>	<i>-1.27</i>	<i>1.245</i>	<i>0.103</i>	<i>0.815</i>	-
	<i>hollow/tilted</i>	-	-	-	-	-

[a]  $\Delta E_{\text{ads}}$  is the adsorption energy. [b]  $d_{\text{CO}}$  is the CO bond length. [c]  $\Delta d_{\text{CO}}$  is the elongation of the CO bond with respect to the gas-phase CO bond length (1.143 Å). [d]  $z_{\text{CO}}$  is the height of the CO molecule with respect to the surface level (the value within the brackets is the height of the oxygen atom and the value without brackets is the height of the carbon atom). [e]  $\theta$  is the angle between the surface normal and the CO molecular axis.

### 3B.3.1.2 W(100)-CO-c(2 × 2) ( $\theta=0.5$ ML)

Results of 0.5 ML CO on W(100) are similar as for 0.25 ML CO (see Table 3B.1 and 3B.2). Therefore, only the most stable adsorption geometry as well as the most important differences will be addressed.

The most stable adsorption mode at 0.5 ML CO coverage is once more the CO tilted by 58° at fourfold hollow sites with an adsorption energy of -3.00 eV. The biggest difference compared to the lower surface coverage is that the expansion of the CO bond of the tilted structure becomes larger at higher coverages, which is a notable observation. Also the stretching frequencies of CO coordinated at top and tilted fourfold hollow positions changes towards 1935 and 847  $\text{cm}^{-1}$ , respectively. In other words, the CO stretching frequency has increased by 49  $\text{cm}^{-1}$  for on-top adsorption of CO, as expected for perpendicular adsorbed CO, whereas the stretching frequency decreased by 79  $\text{cm}^{-1}$  for the tilted configuration, which is remarkable as it is the opposite behavior to

the general observed trend, yet similar to CO on Mo(100) in Chapter 3A.

**Table 3B.2** Adsorption of CO on W(100) at  $\theta = 0.11$  ML,  $\theta = 0.25$  ML,  $\theta = 0.5$  ML, and  $\theta = 1$  ML: vibrational frequencies [ $\text{cm}^{-1}$ ] and zero-point-energy corrections to the adsorption energy. (results displayed in *italics* are not true minima in the PES)

		$\nu_1$	$\nu_2$	$\nu_3$	$\nu_4$	$\nu_5^{[a]}$	$\nu_6^{[a]}$	ZPE [eV] <sup>[b]</sup>	$\Delta E_{\text{ads}}$ [eV] <sup>[c]</sup>
$\theta = 0.11$ ML	hollow/tilted	298	301	403	448	454	944	0.18	-3.52
$\theta = 0.25$ ML	<i>on-top</i>	<i>11</i>	<i>11</i>	<i>387</i>	<i>387</i>	<i>387</i>	<i>1886</i>	<i>0.19</i>	<i>-1.72</i>
	<i>bridge</i>	<i>55i</i>	<i>453i</i>	<i>181</i>	<i>243</i>	<i>329</i>	<i>1678</i>	<i>0.15</i>	<i>-1.55</i>
	<i>hollow</i>	<i>244i</i>	<i>244i</i>	<i>255</i>	<i>255</i>	<i>232</i>	<i>1293</i>	<i>0.13</i>	<i>-1.73</i>
$\theta = 0.5$ ML	hollow/tilted	273	276	335	388	465	926	0.17	-2.97
	on-top	65	65	402	402	379	1935	0.20	-1.70
	<i>bridge</i>	<i>61i</i>	<i>426i</i>	<i>185</i>	<i>207</i>	<i>322</i>	<i>1713</i>	<i>0.15</i>	<i>-1.40</i>
	<i>hollow</i>	<i>277i</i>	<i>277i</i>	<i>180</i>	<i>180</i>	<i>322</i>	<i>1310</i>	<i>0.12</i>	<i>-1.71</i>
$\theta = 1$ ML	hollow/tilted	260	288	352	440	452	847	0.16	-2.97
	on-top	64	64	395	395	370	2026	0.21	-1.55
	<i>bridge</i>	<i>107i</i>	<i>180i</i>	<i>177</i>	<i>232</i>	<i>272</i>	<i>1868</i>	<i>0.16</i>	<i>-1.29</i>
	<i>hollow</i>	<i>138i</i>	<i>138i</i>	<i>151</i>	<i>151</i>	<i>258</i>	<i>1499</i>	<i>0.13</i>	<i>-1.27</i>
	<i>hollow/tilted</i>	-	-	-	-	-	-	-	-

[a]  $\nu_5$  and  $\nu_6$  are the metal–CO stretching and CO stretching frequency, respectively. [b] ZPE is the zero-point-energy. [c]  $\Delta E_{\text{ads}}$  is the adsorption energy including the zero-point-energy of the chemisorbed and gas-phase CO.

### 3B.3.1.3 W(100)–CO– $p(1 \times 1)$ ( $\theta=1$ ML)

The only stable adsorption configuration at a carbon monoxide surface coverage of 1 ML is the top site with an adsorption energy of -1.63 eV (Table 3B.1). The C–O bond distance for on-top bonded CO is 1.163 Å. No stable tilted configuration could be obtained for the W(100)– $p(1 \times 1)$  system (such as found for the lower CO coverages) due to the high coverage of carbon monoxide. Investigation of the vibrational frequencies shows that the CO stretching frequency of on-top adsorbed CO is 2026  $\text{cm}^{-1}$ .

Including zero-point-energy corrections gives rise to a lower adsorption energy for CO adsorbed on-top of -1.55 eV.

### 3B.3.1.4 Comparison of DFT Calculations with Experiments

To compare the DFT calculations with experiments, only true minima structures are used. At 0.25 ML, the adsorption energy of CO at the tilted configuration on W(100) is

-3.01 eV. On the basis of first-order desorption kinetics and the Redhead equation, one may assume as a rough approximation that  $E/T_m$  is nearly constant. For tungsten this value is  $0.0025 \text{ eV K}^{-1}$ . Thus, the desorption temperature ( $T_m$ ) corresponds to approximately 1200 K. For further details regarding the relation of desorption temperatures to adsorption energies we refer to the article by Knor [14] and references therein. According to Wang and Gomer [5], the only desorption feature present at this surface coverage is the  $\text{CO}(\beta_3)$  desorption peak. They appointed this broad desorption feature to the recombination of atomic carbon and oxygen (0.5 ML) on the surface occurring at temperatures of around 1350 K. This same  $\text{CO}(\beta_3)$  desorption peak has also been reported by several other groups at temperatures ranging 1350-1500K [2,4,15]. Because of the large width of this peak, we also calculated the adsorption energy of inclined CO at fourfold hollow sites at a coverage of 0.11 ML, which resulted in an energy of -3.57 eV (Table 3B.1). This adsorption energy correlates to a desorption temperature on the order of 1400 K. The difference in desorption temperatures at these two coverages, i.e., 0.11 and 0.25 ML, might simply be explained by lateral interactions of the adsorbed species, as was observed with dynamic Monte Carlo (DMC) simulations by Nieskens et al. [16]. In their work, they show that species with repulsive interactions lead to broadening of the TPD peak, which is also seen in the case of the  $\text{CO}(\beta_3)$  desorption peak on W(100) [5].

The CO stretching frequency of tilted CO in the fourfold hollow position was calculated to be  $926 \text{ cm}^{-1}$ , which is in good agreement with high resolution electron energy loss spectrometry (HREELS) data reported by Adnot and Carette [1], who observed a loss peak for CO adsorbed in the  $\alpha_3$ -state of  $920 \text{ cm}^{-1}$ , recorded at a temperature of 350 K at high coverages of CO.

Increasing the surface coverage to 0.5 ML leads to a similar adsorption energy for the tilted CO, but to a lowering of the CO stretching frequency of  $79 \text{ cm}^{-1}$  to  $847 \text{ cm}^{-1}$ . This result for the tilted configuration is against the observed general trend that C–O stretching frequency increases with increasing CO coverage [17-21]. A similar shift to lower frequencies was previously calculated for CO on Mo(100) [22]. Two effects account for a shift to higher frequencies: (1) dipole–dipole coupling and (2) a chemical effect. According to the Blyholder model [23], which establishes that the bond of the CO molecule to a metal surface is the result of electron donation from the CO  $5\sigma$  to surface empty levels and back-donation from the surface to the CO  $2\pi^*$  antibonding orbitals, increasing CO coverage results in a lower back-donation to the CO  $2\pi^*$  orbitals with the consequent shift to higher frequencies. However, several authors [24-27] demonstrated that, in addition to  $\sigma$ -donation and  $\pi$ -back-donation, Pauli repulsion plays a major role in the CO stretching frequency of chemisorbed CO. The balance between Pauli repulsion,  $\sigma$ -donation, and  $\pi$ -back-donation results in a shift to higher frequencies (positive chemical effect) or to lower frequencies (negative chemical effect). Thus, the

shift to lower frequencies calculated for CO on W(100) as well as for Mo(100) [22] could be explained by assuming that, in these two surfaces, increasing the CO coverage results in a negative chemical effect. As mentioned in Chapter 3A, a more elaborate explanation for the shift to lower frequencies is presented in Chapter 4, in which the reconstruction of the surface is discussed as the possible reason for the unusual behavior.

Increasing the CO surface coverage even further to 1 ML leads to adsorption of CO at the top sites with an adsorption energy of -1.63 eV, which corresponds to a desorption temperature of ca. 650 K using the 0.0025 eV K<sup>-1</sup> factor discussed at the beginning of this section [14]. This temperature is significantly higher than that reported by several groups for CO( $\alpha_2$ ), which lies between 360 and 450 K [2,4-6,28,29]. This discrepancy contrasts with the excellent agreement obtained above for CO( $\beta$ ). The origin of this discrepancy might be that the 0.0025 eV K<sup>-1</sup> conversion factor cannot be applied indistinctly to both CO adsorption states. We have performed some simple kinetic simulations using numerical integration of the adsorption–desorption kinetic equations using both a tight and loose transition-state for CO desorption. An activation energy of 1.55 eV, which is the adsorption energy of CO at top sites at 1 ML including ZPE, results in a desorption temperature of 590 K when using a tight transition-state and a temperature ramp of 10 K/s, while it results in a desorption temperature of 490 K using a loose transition-state and the same temperature ramp. Similarly, an activation energy of -2.97 eV, which is the adsorption energy of CO tilted at hollow sites at 0.25 ML including ZPE, results in a desorption temperature of 880 and 1090 K using a loose and tight transition-state, respectively. Therefore, our calculations seem to indicate that, while desorption of CO( $\beta$ ) molecules goes via a tight transition-state, desorption of CO( $\alpha_2$ ) molecules likely goes via a loose transition-state. Moreover, these results also seem to indicate that the 0.0025 eV/K factor reported by Knor [14] works well for desorption via a tight transition-state.

The calculated CO stretching frequency for CO adsorbed on-top is 2026 cm<sup>-1</sup>, which correlates nicely with literature (2048 and 2063 cm<sup>-1</sup>) [1,4].

### 3B.3.2 Dissociation of CO on W(100) at 0.25 and 0.5 ML

Adsorption of atomic carbon and oxygen on W(100) at coverages of 0.25 and 0.5 ML has been calculated (Table 3B.3). The adsorption energy of carbon at the most stable sites (fourfold hollow) is -9.18 and -9.19 eV at 0.25 and 0.5 ML surface coverage, respectively. Conversely, oxygen is most stable at bridge sites with adsorption energies of -7.14 and -7.04 eV at 0.25 and 0.5 ML oxygen coverage, respectively. Adsorption energies are higher for carbon than for oxygen; thus, carbon is more strongly bound to the W(100) surface than oxygen. Analyzing the vibrational frequencies of the calculated structures reveals that fourfold hollow sites are the only stable adsorption locations of

**Table 3B.3** Adsorption of C and O on W(100) at  $\theta = 0.25$  and  $\theta = 0.5$  ML. (results displayed in *italics* are not true minima in the PES)

	$\Delta E_{\text{ads}}^{[\text{a}]}$ [eV]	$\Delta E_{\text{rel}}^{[\text{b}]}$ [eV]	$z_{\text{c}}^{[\text{c}]}$ [Å]	$\Delta E_{\text{ads}}^{[\text{a}]}$ [eV]	$\Delta E_{\text{rel}}^{[\text{b}]}$ [eV]	$z_{\text{o}}^{[\text{c}]}$ [Å]
C at 0.25 ML			O at 0.25 ML			
on-top	-4.87	4.31	1.816	-6.67	0.47	1.746
bridge	-6.55	2.63	0.973	-7.14	0	1.377
hollow	-9.18	0	0.594	-6.31	0.83	0.623
C at 0.5 ML			O at 0.5 ML			
on-top	-4.56	4.63	1.821	-6.87	0.17	1.737
bridge	-6.30	2.89	0.968	-7.04	0	1.321
hollow	-9.19	0	0.488	-5.75	1.29	0.591

[a]  $\Delta E_{\text{ads}}$  is the adsorption energy. [b]  $\Delta E_{\text{rel}}$  is the relative adsorption energy with respect to the fourfold hollow site and bridge site for carbon and oxygen, respectively. [c]  $z_{\text{c}}$  and  $z_{\text{o}}$  are the height of the carbon and oxygen atom with respect to the surface level.

**Table 3B.4** Adsorption of C and O on W(100) at  $\theta = 0.25$  and  $\theta = 0.5$  ML: vibrational frequencies [ $\text{cm}^{-1}$ ], zero-point-energy corrections to the adsorption energy and to the relative adsorption energy. (results displayed in *italics* are not true minima in the PES)

	$\nu_{\text{x}}$	$\nu_{\text{y}}$	$\nu_{\text{z}}^{[\text{a}]}$	ZPE [eV] <sup>[b]</sup>	$\Delta E_{\text{ads}}$ [eV] <sup>[c]</sup>	$\Delta E_{\text{rel}}$ [eV] <sup>[d]</sup>
C at 0.25 ML						
<i>on-top</i>	77i	77i	822	0.05	-4.82	4.26
<i>bridge</i>	699	238i	453	0.07	-6.48	2.60
hollow	492	492	572	0.10	-9.08	0
C at 0.5 ML						
<i>on-top</i>	138i	138i	809	0.05	-4.51	4.60
<i>bridge</i>	704	324i	437	0.07	-6.23	2.88
hollow	331	331	578	0.08	-9.11	0
O at 0.25 ML						
on-top	91	91	865	0.05	-6.62	0.48
bridge	332	210	600	0.04	-7.1	0
<i>hollow</i>	44i	45i	426	0.02	-6.29	0.81
O at 0.5 ML						
on-top	93	93	893	0.07	-6.8	0.17
bridge	338	216	585	0.07	-6.97	0
<i>hollow</i>	12	8	312	0.02	-5.73	1.24

[a]  $\nu_{\text{z}}$  is the metal–C / metal–O stretching frequency. [b] ZPE is the zero-point-energy. [c]  $\Delta E_{\text{ads}}$  is the adsorption energy including ZPE. [d]  $\Delta E_{\text{rel}}$  is the relative adsorption energy including ZPE.

carbon at both coverages, whereas oxygen is stable at both top and bridge sites at 0.25 ML and all adsorption sites at 0.5 ML (Table 3B.4). However, as mentioned before, the low values of  $v_1$  and  $v_2$  of the hollow site at 0.5 ML oxygen coverage are possibly prone to be of the same order of error associated with its calculation; therefore, this adsorption configuration is either a stable geometry or a saddle point in the potential energy surface of  $W(100)\text{-O-}c(2 \times 2)$ . Nevertheless, the overall discussion would not change, because the bridge configuration is the most stable adsorption geometry of adsorbed oxygen.

The metal–carbon (M–C) stretch is  $572$  and  $578\text{ cm}^{-1}$ , while the M–O stretch is  $600$  and  $585\text{ cm}^{-1}$  for  $0.25$  and  $0.5\text{ ML}$  surface coverage, respectively. Experimentally obtained metal–carbon stretches appear around  $552\text{ cm}^{-1}$  and M–O stretches at  $600\text{ cm}^{-1}$  [1,30].

The activation energy of dissociation of CO on  $W(100)$  at  $0.25\text{ ML}$  CO coverage was calculated using the following reaction:



The dissociation of carbon monoxide at  $0.25\text{ ML}$  CO coverage is an exothermic process with a reaction energy of  $-1.72\text{ eV}$  (reaction 3B.3.2.1), which includes diffusion of the oxygen atom; see Figure 3B.1.

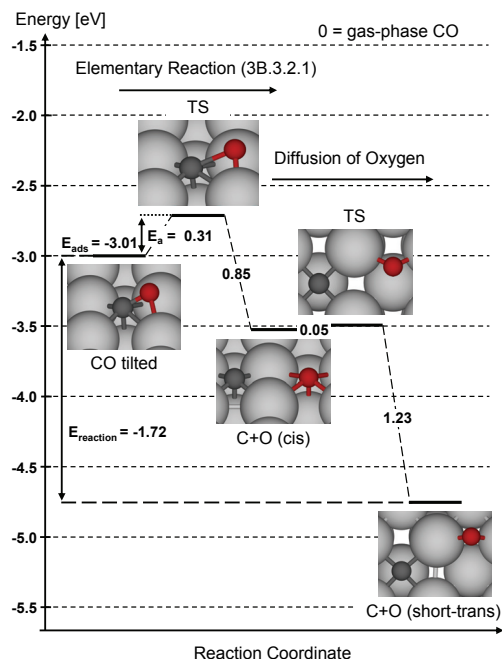


**Figure 3B.1** Energy diagram of dissociation of  $0.25\text{ ML}$  CO on  $W(100)$  using a  $p(2 \times 2)$  unit cell. The numbers inserted represent the activation energies of the elemental steps. Energies are without ZPE correction.

The dissociated end-state of CO at 0.25 ML was calculated using a W(100)- $p(2 \times 2)$  slab model with carbon and oxygen coadsorbed. Three configurations were investigated: (1) cis, (2) short-trans, and (3) trans, in which only the first two are implemented in Figure 3B.1, because the trans configuration is not a local minimum, but a second-order saddle point.

The relative energy of the cis and short-trans configurations with respect to CO tilted at the fourfold hollow site are -0.54 and -1.72 eV, respectively. The corresponding metal-carbon stretching frequencies are 543 and 559  $\text{cm}^{-1}$ , while the M-O stretches are 381 and 540  $\text{cm}^{-1}$  for cis and short-trans positions, respectively.

CO dissociates easily on W(100) at 0.25 ML surface coverage with an activation energy of only 0.31 eV, or a dissociation temperature of approximately 120 K [14]. The activation energy of recombination is 0.85 eV (82  $\text{kJ mol}^{-1}$ ) for the elementary step, whereas the apparent activation energy of recombination is 2.03 eV (196  $\text{kJ mol}^{-1}$ ). Applying ZPE corrections leads to no significant changes in the energy.

Looking closer at the transition-state structure of the CO dissociation reaction reveals that carbon is situated at the fourfold hollow site and the oxygen atom close to a bridge site as was also reported previously [22,31].

We were unable to locate a transition-state for the diffusion of oxygen from the fourfold hollow position toward the bridge site. Nevertheless, we have estimated an upper limit of 0.05 eV for this activation energy (Figure 3B.2). Figure 3B.2 is a representation of the potential energy surface along the direction connecting the O at fourfold hollow sites in the cis configuration and the O at the bridge sites in the

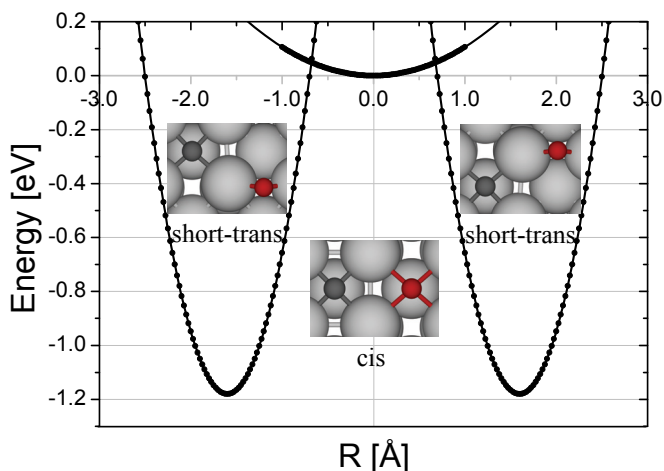


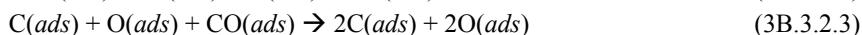
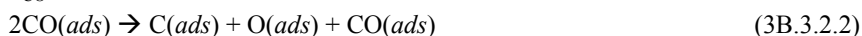
**Figure 3B.2** Potential energy plot along the direction of the diffusion of oxygen connecting the cis and short-trans configuration; the crossing point can be used as an estimate of the upper-limit of the activation energy of diffusion of oxygen from hollow in the cis configuration to bridge in short-trans configuration. The zero energy level is set to the total energy of the cis configuration.



short-trans configuration. The potential energy well for each adsorption configuration has been calculated using the harmonic vibrational frequency corresponding to the vibration of the oxygen atom along the same direction for each configuration ( $60\text{ cm}^{-1}$  and  $222\text{ cm}^{-1}$  for cis and short-trans, respectively). The zero level is set to the total energy of the cis configuration. The crossing point between the cis and short-trans curves can be thus used to obtain an estimation of the upper-limit for the activation energy of the diffusion of the oxygen atom. This upper limit is  $0.05\text{ eV}$ . The true activation energy though is probably lower than that and about  $0.01\text{--}0.03\text{ eV}$  in order to have a continuous and smooth change from one energy well to the other. This activation energy is of the same order of magnitude of our accuracy in the calculation, and, therefore, this is most likely why we have not been able to find the corresponding transition-state structure.

To assess the influence of increased surface coverage, CO dissociation has also been calculated for  $0.5\text{ ML CO}$  by using the following reactions:

$$\theta_{\text{CO}} = 0.5\text{ ML}$$



These reactions were modeled through the use of a  $\text{W}(100)\text{-}p(2 \times 2)$  slab model that contains two carbon monoxide molecules adsorbed in a tilted fourfold hollow position (Figure 3B.3), which leads to a  $\text{CO-}c(2 \times 2)$  overlayer structure. The adsorption energy thus obtained is comparable to the adsorption energy calculated using a  $c(2 \times 2)$  unit cell. The reaction energy of dissociation is  $-0.69\text{ eV}$  (reactions 3B.3.2.2 + 3B.3.2.3) (see Figure 3B.3), which is  $1\text{ eV}$  lower in energy compared to  $0.25\text{ ML CO}$  coverage.

After dissociation of around half of the CO molecules on the  $\text{W}(100)$  surface at  $0.5\text{ ML}$  coverage, carbon and oxygen atoms are coadsorbed in a cis configuration, in which the remaining CO is located trans with respect to the C atoms. The activation energy of dissociation for these initial CO molecules is  $0.25\text{ eV}$ ,  $0.06\text{ eV}$  smaller than at a surface coverage of  $0.25\text{ ML CO}$ . Dissociation of CO at  $0.25\text{ ML}$  concentration resulted in an exothermic reaction of  $-0.54\text{ eV}$  (Figure 3B.1), without diffusion, while dissociation of ca. half the CO molecules at  $0.5\text{ ML}$  (reaction 3B.3.2.2) is thermo neutral. Automatically, recombination energy is decreased to only  $0.23\text{ eV}$ , instead of  $0.85\text{ eV}$  at  $0.25\text{ ML CO}$  coverage. Dissociation of the remaining CO (reaction 3B.3.2.3), on the other hand, is exothermic and yields an energy gain of  $0.71\text{ eV}$ , leading to a surface entirely covered ( $1\text{ ML}$ ) with coadsorbed carbon and oxygen atoms. In this dissociated end-state, the carbon atoms are three- and fourfold coordinated, whereas oxygen is coordinated two- (bridge) and threefold (see Figure 3B.3). Because the preceding result shows that half of the oxygen atoms coordinate threefold in this dissociated end-state, calculations were performed of oxygen atoms solely adsorbed on  $\text{W}(100)$  in threefold positions. However, the adsorption energy of O at these threefold

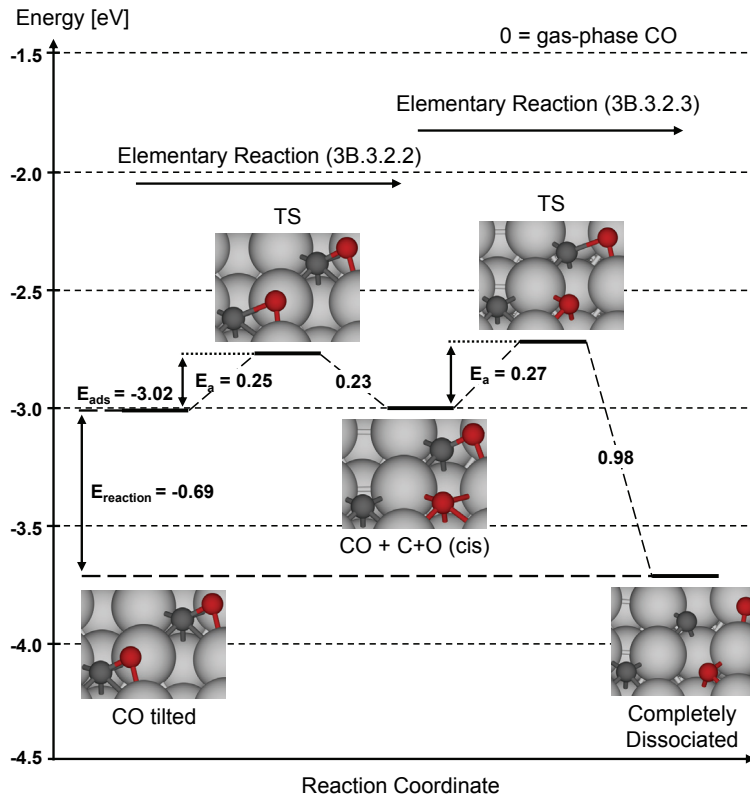


**Figure 3B.3** Energy diagram of dissociation of 0.5 ML CO on W(100) using a  $p(2 \times 2)$  unit cell. The numbers inserted represent the activation energies of the elemental steps. Energies are without ZPE correction.

positions at a surface coverage of 0.25 ML is 0.68 eV higher in energy than adsorbed oxygen at bridge sites and 0.22 eV higher than oxygen at top sites. Hence, oxygen adsorbed at threefold sites is much less stable than bridged adsorbed oxygen; thus, threefold positions were not further investigated (and not included in the tables). Adsorption of oxygen at threefold positions for the dissociated end-state, therefore, might be explained by interactions of the other adsorbates pushing the oxygen out of the most stable site, i.e., bridge, to minimize the repulsion energy. The activation energy of dissociation of the remaining CO molecules, which are coadsorbed next to carbon and oxygen atoms, is similar to that of the initial CO molecules, while the recombination energy increases drastically to 0.98 eV as compared to 0.23 eV. Thus, dissociation at 0.5 ML CO coverage is complete, because if almost half of the CO molecules have the energy to dissociate, the remaining CO would also be able to do so, as the activation energy of dissociation is similar for both CO molecules coadsorbed next to atomic and

molecular species. The resulting overall reaction energy would be exothermic by -0.69 eV. Including zero-point-energy corrections changes the energy of activation of CO dissociation and CO recombination insignificantly.

Moreover, it is worth mentioning that once a substantial fraction of CO has dissociated the adsorption energy of the remaining CO molecules decreases to -2.46 eV. This is around 0.55 eV lower for both the adsorption of CO molecules after pre-adsorption of 0.25 ML CO and the adsorption energy of CO at a surface coverage of 0.25 ML, and corresponds to a desorption temperature of around 980 K [14].

### 3B.3.2.1 Comparison of CO Dissociation Calculations with Experiments

The calculated activation energy of CO dissociation on W(100) at a surface coverage of 0.25 ML is 0.31 eV, which corresponds to a temperature of around 120 K. This agrees quite nicely with experimental CO dissociation temperatures reported to be as low as 80 K [5,7]. On the other hand, the calculated apparent recombination energy is much smaller ( $196 \text{ kJ mol}^{-1}$ ) than the values given in literature ( $347 \text{ kJ mol}^{-1}$ ) [5]. Thus,  $\beta$ -CO desorption features assigned to recombination desorption in literature do not correlate with the activation energy of recombination of atomic carbon and oxygen as we calculate them. This would indicate that the desorption peak  $\text{CO}(\beta_3)$  at 1350-1500 K is related to molecular desorption of CO, rather than recombination of atomic carbon and oxygen.

Increasing the concentration of carbon monoxide on the surface to 0.5 ML results in a slightly lower barrier for CO dissociation (0.25 eV; 100 K), although the energy gain, hence, the driving force for dissociation, is much lower. We found a similar situation in Chapter 3A for CO on Mo(100). This result is remarkable, as it goes against the Brønsted-Evans-Polanyi relation (the larger the exothermicity, the lower the activation barrier for the reaction) as well as the universality principle in heterogeneous catalysis as stated by Nørskov et al. [32].

Last, after dissociation of the initial CO molecules at a starting CO coverage of 0.5 ML, the adsorption energy of the remaining CO molecules decreases to -2.46 eV, which corresponds to a desorption temperature of around 980 K. This desorption temperature is close to either the  $\text{CO}(\beta_1)$  and  $\text{CO}(\beta_2)$  desorption peaks at 930 and 1070 K, respectively [5]. In conclusion, our calculations show that all desorption states observed experimentally with TPD experiments of CO on W(100) are molecular desorption states and are not due to a recombination reaction of carbon and oxygen atoms. Thus, the interpretation is that at those temperatures CO is in equilibrium with the dissociated state, and that the equilibrium lies strongly on the side of the atoms. Desorption, however, occurs from the molecular state.

### **3B.3.3 Comparison of the (100) Surface with the (111)**

Comparing our results for CO on the W(100) surface with those calculated by Chen et al. for CO on W(111) [11] leads to significant differences in surface reactivity between the two. The adsorption energy of CO on W(111) is -1.79 eV, whereas it is -3.01 eV on W(100). Next to this, carbon monoxide is bound in a tilted bridge-like position on W(111) with the oxygen atom pointing towards a top site with a CO stretching frequency of  $1318\text{ cm}^{-1}$ , while CO is bound in a tilted fourfold hollow configuration on W(100) with the oxygen directed toward the bridge site with a CO stretch of  $926\text{ cm}^{-1}$ . The activation energy of dissociation of CO is 0.82 and 0.31 eV, while the reaction energy of dissociation is -0.63 and -0.54 eV (without diffusion) for W(111) and W(100), respectively.

According to these results, CO adsorbs more strongly and dissociates a lot more rapidly on the (100) surface than on the (111), whereas the reaction energy is higher for the (111) surface, which might be explained by the fact that the dissociated end-state used by Chen and co-workers for the (111) surface is the optimized end-configuration for the coadsorption of C and O. In our case, the dissociated end-state for the (100) surface (without diffusion) is the so-called cis configuration (Figure 3B.1), which is not the most stable end-state. The most stable end-configuration for the coadsorption of C and O on the (100) surface is obtained after diffusion of oxygen to the bridge site (short-trans configuration in Figure 3B.1). When diffusion of oxygen is included, the reaction energy of dissociation of carbon monoxide on W(100) is -1.72 eV, which is a lot more exothermic than on the (111) surface.

To conclude, although the W(111) is a more open surface than the W(100) surface, and, hence, would be the most reactive as a general rule of thumb, calculations obviously show that not the W(111), but the W(100) surface is the most reactive of the two surfaces with respect to CO adsorption and dissociation.

### **3B.4 Concluding Remarks**

Carbon monoxide on W(100) adsorbs preferentially in a tilted geometry with the carbon atom in a fourfold hollow site and the oxygen in a bridge-bonded mode (adsorption energy -3.0 eV). At higher coverages (above 0.5 monolayer) CO starts to occupy on-top sites as well, and at a full monolayer, all CO is in this linearly bound form (adsorption energy -1.63 eV).

Tilted CO is a precursor for dissociation as soon as the temperature allows. With an activation energy of 0.25-0.30 eV, and an exothermicity of -1.72 eV –when the dissociated atoms have moved away from each other to relieve repulsion between them– is a facile process.

Lateral interactions have a profound influence. CO adsorbed in the vicinity of

the dissociation products (i.e., a C and an O atom as nearest neighbors) is destabilized from -3.0 eV to -2.46 eV. Nevertheless, the activation energy of CO dissociation is hardly changed by the presence of adjacent atoms, although the exothermicity decreases significantly due to atom–atom repulsion on neighbor sites. Hence, the behavior does not follow the Brønsted-Evans-Polanyi relationship. However, this principle was shown to hold for dissociating molecules on different surfaces, but at a fixed coverage. In the present case, we compare situations at different coverage, where the chemical environment is different. Here the BEP relation does not necessarily have to be valid. This is a point for further investigation.

Vibrations have been calculated for all geometries, to assess whether they correspond to true stable states or to transition-states. The CO stretching frequencies of the stable adsorption configurations are close to experimentally measured values. For tilted CO, the C–O stretching frequency decreases with increasing coverage, which is contrary to what is usually observed for CO in perpendicular modes and will be explained into more detail in Chapter 4.

The calculated energies of CO adsorption generally agree reasonably with the experimental values, with one important exception. High-temperature thermal desorption peaks (indicated as  $\beta$ -CO desorption peaks) have been assigned to recombinative desorption of C and O atoms. However, the calculated activation energy of recombination of carbon monoxide is much smaller than the desorption energy of tilted CO at a variety of coverages. Hence, at temperatures where recombination becomes feasible, the resulting molecular CO would still be adsorbed. Our interpretation is thus that at high temperatures molecularly and dissociatively adsorbed CO are in equilibrium, which lies strongly to the side of the atoms. Desorption, however, occurs from the molecular state. Hence,  $\beta$ -CO desorption peaks reported experimentally should be labeled as  $\alpha$ -CO desorption peaks, as  $\alpha$  stands for molecular desorption and  $\beta$  for recombination.

The (100) surface of tungsten is more reactive towards CO adsorption and dissociation than the (111) surface, which is against the general rule of thumb; the more open the surface, the more reactive.

## References

- [1] A. Adnot, J. D. Carette, *Surf. Sci.* **75** (1978) 109.
- [2] L. W. Anders, R. S. Hansen, *J. Chem. Phys.* **62** (1975) 4652.
- [3] M. A. Chesters, B. J. Hopkins, R. I. Winton, *Surf. Sci.* **59** (1976) 46.
- [4] H. Froitzheim, H. Ibach, S. Lehwald, *Surf. Sci.* **63** (1977) 56.
- [5] C. Wang, R. Gomer, *Surf. Sci.* **90** (1979) 10.
- [6] L. R. Clavenna, L. D. Schmidt, *Surf. Sci.* **33** (1972) 11.
- [7] T. V. Vorburger, D. R. Sandstrom, B. J. Wacławski, *J. Vac. Sci. Technol.* **13** (1976) 287.
- [8] J. R. Anderson, P. J. Estrup, *J. Chem. Phys.* **46** (1967) 563.

- [9] T. H. Lee, J. W. Rabalais, Surf. Sci. **75** (1978) 29.
- [10] G. H. Ryu, S. C. Park, S.-B. Lee, Surf. Sci. **427-428** (1999) 419.
- [11] L. Chen, D. S. Sholl, J. K. Johnson, J. Phys. Chem. B **110** (2006) 1344.
- [12] P. E. M. Siegbahn, U. Wahlgren, Int. J. Quantum Chem. **42** (1992) 1149.
- [13] <http://www.webelements.com>, Accessed 2009.
- [14] Z. Knor, Surf. Sci. **154** (1985) L233.
- [15] C. G. Goymour, D. A. King, J. Chem. Soc. Faraday 1 **69** (1973) 736.
- [16] D. L. S. Nieskens, A. P. van Bavel, J. W. Niemantsverdriet, Surf. Sci. **546** (2003) 159.
- [17] D. Curulla, A. Clotet, J. M. Ricart, Surf. Sci. **460** (2000) 101.
- [18] F. M. Hoffmann, Surf. Sci. Rep. **3** (1983) 107.
- [19] P. Hollins, J. Pritchard, Prog. Surf. Sci. **19** (1985) 275.
- [20] R. Linke, D. Curulla-Ferré, M. J. P. Hopstaken, J. W. Niemantsverdriet, J. Chem. Phys. **115** (2001) 8209.
- [21] D. Loffreda, D. Simon, P. Sautet, Surf. Sci. **425** (1999) 68.
- [22] F. J. E. Scheijen, J. W. Niemantsverdriet, D. Curulla-Ferré, J. Phys. Chem. C **111** (2007) 13473.
- [23] G. Blyholder, J. Phys. Chem. **68** (1964) 2772.
- [24] P. S. Bagus, K. Hermann, C. W. Bauschlicher, Jr., J. Chem. Phys. **81** (1984) 1966.
- [25] P. S. Bagus, K. Hermann, C. W. Bauschlicher, Jr., J. Chem. Phys. **80** (1984) 4378.
- [26] P. S. Bagus, W. Müller, Chem. Phys. Lett. **115** (1985) 540.
- [27] D. Curulla, A. Clotet, J. M. Ricart, F. Illas, J. Phys. Chem. B **103** (1999) 5246.
- [28] C. G. Goymour, D. A. King, Surf. Sci. **35** (1973) 246.
- [29] J. T. Yates, Jr., D. A. King, Surf. Sci. **32** (1972) 479.
- [30] H. Froitzheim, H. Ibach, S. Lehwald, Phys. Rev. B **14** (1976) 1362.
- [31] T. C. Bromfield, D. Curulla-Ferré, J. W. Niemantsverdriet, ChemPhysChem **6** (2005) 254.
- [32] J. K. Nørskov, T. Bligaard, A. Logadottir, S. Bahn, L. B. Hansen, M. Bollinger, H. Bengaard, B. Hammer, Z. Sljivancanin, M. Mavrikakis, Y. Xu, S. Dahl, C. J. H. Jacobsen, J. Catal. **209** (2002) 275.



# 4

## Adsorption and Dissociation of CO on Body Centered Cubic Transition Metals and Alloys: Effect of Coverage and Scaling Relations

### Abstract

*The adsorption and dissociation of CO have been calculated on the (100) surfaces of the bcc transition-metals Fe, Mo, Cr, and W and the alloys Fe<sub>3</sub>Mo and Fe<sub>3</sub>Cr using DFT for two CO coverages: 0.25 and 0.5 ML. A complete analysis of the vibrational frequencies was performed to check whether the calculated structures are stable geometries or transition-state structures. For coverages up to 0.25 ML, carbon monoxide adsorbs molecularly onto all four metals at fourfold hollow sites with tilting angles with respect to the surface normal of 47°, 57°, 57°, and 58° and adsorption energies of -1.53, -2.64, -3.03, and -3.01 eV for Fe, Mo, Cr, and W, respectively. The calculated CO stretching frequencies at this coverage are 1211, 1062, 1037, and 926 cm<sup>-1</sup>. At higher coverages, CO adsorption does not exhibit significant changes in both adsorption energy and tilting angle on all four metals, but leads to blue-shifts of the CO frequency for Fe and Cr and red-shifts for Mo and W. Furthermore, scaling relations apply to a bent CO species at a surface coverage of 0.25 ML of CO on all four transition metals as well as the metal alloys Fe<sub>3</sub>Mo and Fe<sub>3</sub>Cr, in the sense that the heat of adsorption of CO and the activation energy of CO dissociation scale linearly with the heat of adsorption of carbon as well as both dissociation products.*



## 4.1 Introduction

The recently growing interest in using Fischer-Tropsch synthesis for the conversion of synthesis gas (CO and H<sub>2</sub>) derived from natural gas, coal, or biomass into synthetic fuels and chemicals [1] has stimulated fundamental work on the adsorption and dissociation of CO on a range of metals. Whereas cobalt catalysts are used to produce mainly diesel fuel, iron catalysts produce a broader product spectrum, which contains olefins, paraffins, and oxygenated products. To optimize iron-based Fischer-Tropsch catalysts, the use of other body centered cubic (bcc) metals as promoters has recently attracted attention [2-5]. Metals such as chromium [6], molybdenum [7-10], and tungsten [11-14], possess a high activity for the dissociation of CO and bind carbon atoms more strongly than iron does, which may provide a way to alter the Fischer-Tropsch product spectrum.

Ab-initio quantum chemical calculations on adsorption and reactions of molecules on metal and alloy surfaces have become a generally accepted ingredient of heterogeneous catalysis [15-25]. On the basis of such calculations, Nørskov and co-workers introduced novel concepts, such as the universality principle in heterogeneous catalysis and the Pareto-optimal algorithm for finding the best catalyst for a reaction [26,27]. The universality principle rests on linear relations between the activation energy of the reaction and the adsorption energy of its respective reaction products. Such a linear relation was already observed for CO dissociation on 4d and 5d transition metals by Liu and Hu [28-30]. More recently, Nørskov and co-workers proposed a scaling model based on linear relations between the adsorption energy of species, such as CO or CH<sub>x</sub>, and the adsorption energy of the carbon atom [31,32]. All these relations enable one to make estimates for adsorption energies and activation energies on the basis of a few calculations.

In this Chapter, we compare the adsorption and dissociation of carbon monoxide on the (100) surfaces of Fe, Mo, W, and Cr metal and Fe<sub>3</sub>Mo and Fe<sub>3</sub>Cr alloys on the basis of density functional theory (DFT) calculations. Furthermore, distinct changes in CO stretching frequency in reference to coverage variations will be discussed. CO adsorption on the bcc (100) metal surfaces differs from that on face centered cubic (fcc) metals from Group VIII and Ib in that the CO binds via both ends of the molecule, with the C in the fourfold hollow and the O to the bridge position [33]. As a result of this, the molecule is no longer perpendicular to the surface. We use our results to test the validity of the scaling relations proposed by Nørskov and co-workers [31,32] for adsorption and dissociation of CO on bcc metals and alloys and find that these, indeed, apply reasonably well.

## 4.2 Computational Details

We have used the Vienna ab-initio simulation package (VASP) [34,35], which performs

an iterative solution of the Kohn-Sham equations in a plane-wave basis set. Plane-waves with a kinetic energy below or equal to 400 eV have been included in the calculation. The exchange-correlation energy has been calculated within the generalized gradient approximation (GGA) using the revised form of the Perdew, Burke, and Ernzerhof (RPBE) exchange-correlation (XC) functional [36] proposed by Hammer et al. [37]. The electron-ion interactions for C, O, Mo, W, Cr, and Fe are described by the projector-augmented wave (PAW) method developed by Blöchl [38]. This is essentially an all-electron frozen core method combining the accuracy of all-electron methods and the computational simplicity of the pseudopotential approach [39]. Fractional occupancies were calculated using a first-order Methfessel-Paxton smearing function with a width of 0.1 eV [40]. Upon convergence, energies were extrapolated to  $T = 0$  K.

Molybdenum, tungsten, chromium, and iron exhibit a bcc structure. The relative positions of the metal atoms have been fixed initially as those in the bulk, with optimized lattice parameters of 3.159, 3.175, 2.868, and 2.858 Å, for Mo, W, Cr, and Fe, respectively (the experimental values are 3.147, 3.165, 2.910, and 2.867 Å) [41]. The optimized lattice parameters of the alloys Fe<sub>3</sub>Mo and Fe<sub>3</sub>Cr were 2.920 and 2.829 Å, respectively. Optimization of the lattice parameters was achieved by calculating the bcc unit cell of the four metals and the two metal alloys, and their reciprocal space has been sampled with a  $(15 \times 15 \times 15)$   $k$ -points grid generated automatically using the Monkhorst-Pack method [42].

The CO molecule has been calculated using a  $10 \times 10 \times 10$  Å<sup>3</sup> cubic unit cell, while for atomic carbon and atomic oxygen a  $10 \times 12 \times 14$  Å<sup>3</sup> orthorhombic unit cell has been used. Non-spin-polarized calculations for the CO molecule and spin-polarized calculations for the atoms have been done at the  $\Gamma$  point.

The metal surfaces have been modeled within the slab model approximation using a five-metal layer slab model and six vacuum layers ( $>10$  Å). The alloys consist of an ABABA structure; hence, molybdenum or chromium in the third layer is situated directly under molybdenum or chromium in the first layer. Different slab models have been used throughout this Chapter: a  $p(2 \times 2)$  to study surface coverages of 0.25 ML and a  $c(2 \times 2)$  to study surface coverages of 0.5 ML. The reciprocal space of the  $p(2 \times 2)$  and  $c(2 \times 2)$  unit cells have been sampled with a  $(5 \times 5 \times 1)$  and  $(7 \times 7 \times 1)$   $k$ -points grid, respectively, automatically generated using the Monkhorst-Pack method. Unlike bulk molybdenum, tungsten, and chromium, which do not have magnetic moments, the slabs of these three metals did exhibit small magnetic moments. The calculated magnetic moments are 0.13, 0.22, and 0.84  $\mu_B$ /atom for W, Mo, and Cr(100)- $p(2 \times 2)$ , and 0.10, 0.18, and 0.82  $\mu_B$ /atom for W, Mo, and Cr(100)- $c(2 \times 2)$ , respectively. Tests on the influence of the spin character on the results showed that geometries were unaffected by such small magnetic moments and total energies were similar or slightly more stable. The estimated error that is committed in the calculation of adsorption energies and reaction energies using non-spin-polarized calculations is below 0.05 eV.

Consequently, we report non-spin-polarized results for these three metals and spin-polarized calculations for iron and iron alloys.

Partial geometry optimizations have been performed, including relaxation of the two topmost metal layers, using the RMM-DIIS algorithm [43]. In this method, the forces on the atoms and the stress tensor are used to determine the search directions for finding the equilibrium positions. Geometry optimizations were stopped when all the forces (of the degrees of freedom set in the calculation) were smaller than  $0.01 \text{ eV/\AA}$ . Vibrational frequencies have been calculated within the harmonic approximation. The second-derivative matrix (or Hessian matrix) has been calculated numerically by displacing every atom independently out of its equilibrium position twice ( $\pm 0.02 \text{ \AA}$ ). The adsorbate–surface coupling has been neglected, and only the Hessian matrix of the adsorbate has been calculated [44]. Transition-state structures have been found following a two-step strategy: (1) use of the climbing-image nudged elastic band method (CI-NEB) [45] to find a likely transition-state structure and (2) refine the structure of the transition-state by performing a geometry optimization calculation (as described above) using as a starting geometry that of the highest energy image out of the CI-NEB calculation. All transition-state structures have been characterized by calculating the vibrational frequencies.

The adsorption energy of CO and atomic carbon and oxygen is calculated with respect to its respective gas-phase species. Zero-point-energy (ZPE) corrections were not applied to the energies in the diagrams since ZPE is relevant for X–H bonds, but hardly important for X–Y bonds, such as C–O. Moreover, the energy differences fall within the calculation error ( $0.05 \text{ eV}$ ). Dissociation of CO on all four metals was studied at two coverages, at  $0.25$  and  $0.5 \text{ ML}$ , using a  $p(2 \times 2)$  model containing one and two CO molecules, respectively. On the alloys, we only did calculations for  $0.25 \text{ ML CO}$ .

## 4.3 Results

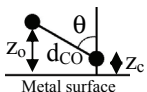
In the previous Chapters 3A and 3B, we investigated the adsorption and dissociation of carbon monoxide on molybdenum and tungsten using the revised form of the Perdew, Burke, and Ernzerhof exchange-correlation functional [46,47]. Bromfield et al. [15] performed a similar study on iron, although they used a different exchange-correlation functional, namely, the Perdew-Wang 91 (PW91) proposed by Perdew and Wang [48,49]. In this Chapter, the results are added of the adsorption and dissociation of carbon monoxide on chromium and iron employing the RPBE XC functional to be able to compare the systems.

### 4.3.1 Adsorption of CO

Following the previous strategy of Chapters 3A and 3B, calculations have been done at

0.25 and 0.5 ML CO to account for the coverage effects on the structural parameters, vibrational frequencies, activation energy of dissociation, and reaction energy. Results are displayed in Table 4.1 and Table 4.2.

**Table 4.1** Adsorption of CO at the fourfold hollow site with tilted geometry for Cr(100), Fe(100), Mo(100), and W(100) at  $\theta = 0.25$  ML and  $\theta = 0.5$  ML and for Fe<sub>3</sub>Cr(100) and Fe<sub>3</sub>Mo(100) at  $\theta = 0.25$  ML.



	$\theta$ [ML]	$\Delta E_{\text{ads}}^{[\text{a}]}$ [eV]	$d_{\text{CO}}$ [Å]	$\Delta d_{\text{CO}}^{[\text{b}]}$ [Å]	$z_{\text{c}}, (z_{\text{o}})$ [Å]	$\theta$ [°]
Cr(100)	0.25	-3.03	1.370	0.227	0.679, (1.433)	56.7
	0.50	-3.00	1.368	0.225	0.632, (1.416)	55.0
Fe(100)	0.25	-1.53	1.311	0.169	0.673, (1.561)	47.4
	0.50	-1.57	1.310	0.168	0.670, (1.548)	47.9
Mo(100)	0.25	-2.64	1.354	0.211	0.698, (1.434)	57.0
	0.50	-2.63	1.386	0.243	0.613, (1.378)	56.5
W(100)	0.25	-3.01	1.413	0.270	0.701, (1.443)	58.3
	0.50	-3.00	1.439	0.296	0.606, (1.370)	57.9
Fe <sub>3</sub> Cr(100)	0.25	-1.92	1.362	0.219	0.558, (1.453)	48.9
Fe <sub>3</sub> Mo(100)	0.25	-1.75	1.341	0.198	0.576, (1.438)	50.0

[a]  $\Delta E_{\text{ads}}$  is the adsorption energy. [b]  $\Delta d_{\text{CO}}$  is the elongation of the CO bond with respect to the gas-phase CO bond length (1.143 Å).

The calculations show that CO adsorbs molecularly on all four metals at fourfold hollow sites with the C–O axis tilted away from the surface normal. The tilting angle of the carbon monoxide is similar at both coverages. CO adsorbs strongest on chromium (-3.03 eV) and tungsten (-3.01 eV), whereas CO is slightly weaker bound on molybdenum (-2.64 eV) and significantly weaker on iron (-1.53 eV). For this bent structure, the CO stretching frequencies are 1211, 1062, 1037, and 926 cm<sup>-1</sup> on Fe, Mo, Cr, and W, respectively. Increasing the surface coverage from 0.25 to 0.5 ML does not influence the adsorption energy significantly for all four metals. A decrease in CO coverage from 0.25 to 0.11 ML, on the other hand, results in an increase of the adsorption energy of CO of 0.29 and 0.56 eV for Mo and W, respectively [46,47]. Hence, for coverages lower than 0.25 ML, the adsorption energy is influenced by CO surface coverage and CO becomes more strongly bound to the surface as coverage decreases.

We note that, in an earlier paper by our group on CO dissociation on Fe(100) [15] we reported that the CO tilting angle changed from 51° at 0.25 ML to a lower value at 0.5 ML. This appears to be a mistake, which we hereby correct. Using either PW91

or RPBE as exchange-correlation functional, we find the tilting angle to be invariant with coverage on Fe(100).

**Table 4.2** Adsorption of CO at the fourfold hollow site with tilted geometry for Cr(100), Fe(100), Mo(100), and W(100) at  $\theta = 0.25$  ML and  $\theta = 0.5$  ML and for Fe<sub>3</sub>Cr(100) and Fe<sub>3</sub>Mo(100) at  $\theta = 0.25$  ML: vibrational frequencies [cm<sup>-1</sup>] and zero-point-energy corrections to the adsorption energy.

	$\theta$ [ML]	$\nu_1$	$\nu_2$	$\nu_3$	$\nu_4$	$\nu_5^{[a]}$	$\nu_6^{[a]}$	ZPE <sup>[b]</sup> [eV]	$\Delta E_{\text{ads}}^{[c]}$ [eV]
Cr(100)	0.25	260	272	365	382	460	1037	0.17	-2.99
	0.50	276	277	365	434	459	1043	0.18	-2.96
Fe(100)	0.25	171	202	304	326	343	1211	0.16	-1.50
	0.50	178	213	286	326	381	1225	0.16	-1.54
Mo(100)	0.25	234	239	291	350	432	1062	0.16	-2.61
	0.50	241	272	316	403	433	958	0.16	-2.60
W(100)	0.25	273	276	335	388	465	926	0.17	-2.97
	0.50	260	288	352	440	452	847	0.16	-2.97
Fe <sub>3</sub> Cr(100)	0.25	167	263	319	355	394	1125	0.16	-1.89
Fe <sub>3</sub> Mo(100)	0.25	196	264	332	357	384	1118	0.16	-1.72

[a]  $\nu_5$  and  $\nu_6$  are the metal–CO stretching and CO stretching frequency, respectively. [b] ZPE is the zero-point-energy. [c]  $\Delta E_{\text{ads}}$  is the adsorption energy including the zero-point-energy of the chemisorbed and gas-phase CO.

The CO stretching frequencies we find for CO on Fe, Mo, and W(100), namely, 1211, 1062, and 926 cm<sup>-1</sup>, agree very well with the experimentally reported values of 1210 [50], 1065 [10], and 920 cm<sup>-1</sup> [51]. We could not find data for CO on Cr(100). The CO stretching frequencies are sensitive to the CO surface coverage. Iron and chromium show an increase of the CO stretching frequency for an increasing CO coverage, whereas molybdenum and tungsten behave in the opposite way.

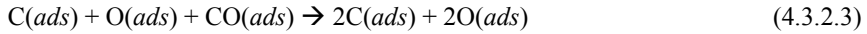
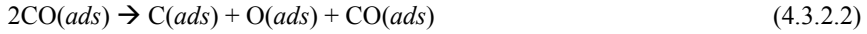
### 4.3.2 Dissociation of CO

The effect of coverage was also studied for the dissociation of carbon monoxide on the four transition-metals. First, calculations were performed to find the most stable site of both atomic oxygen and carbon at 0.25 and 0.5 ML coverage. These results are placed in the supplementary information at the end of this Chapter. The activation energy of dissociation of CO on the four metals was calculated using the following elementary reactions:

$$\theta_{\text{CO}} = 0.25 \text{ ML:}$$



$\theta_{\text{CO}} = 0.5 \text{ ML}$ :



The energy diagram of the dissociation of 0.25 ML of CO on all four transition metals is shown in Figure 4.1. Frequencies of the transition-states can be found in the

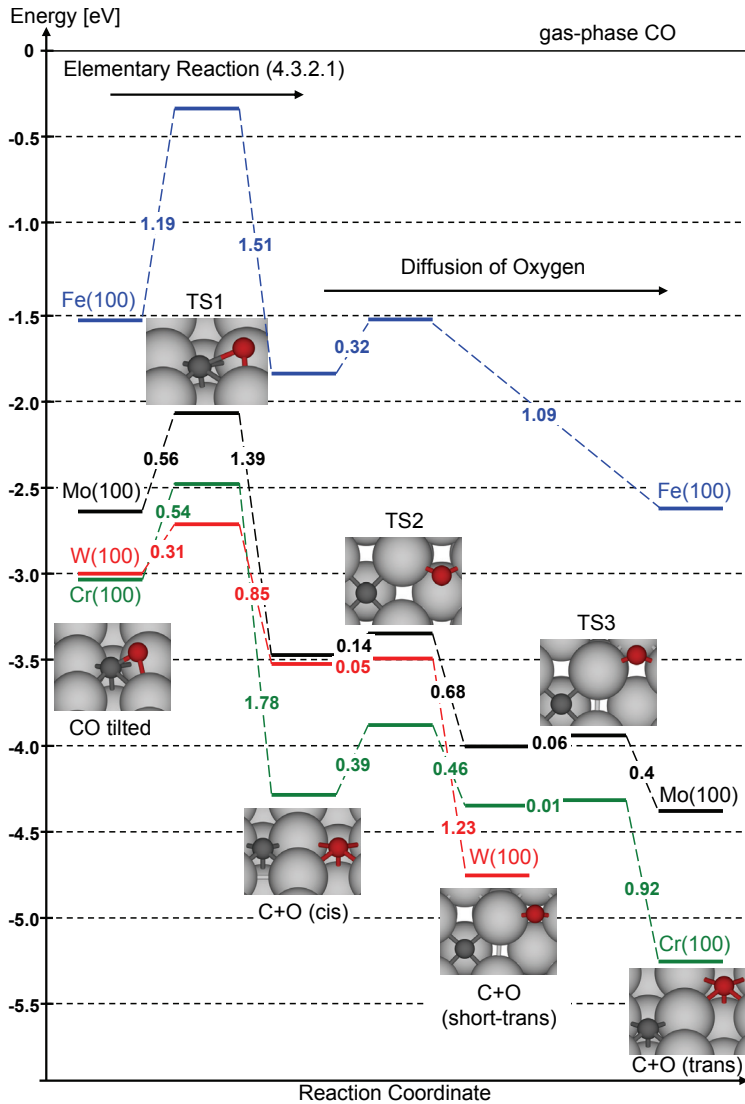


**Figure 4.1** Energy diagram of adsorption and dissociation of 0.25 ML of CO on Fe(100), Mo(100), Cr(100), and W(100) using a  $p(2 \times 2)$  unit cell. The numbers inserted represent the activation energies of the elemental steps. Energies are without ZPE correction.

supplementary information. The activation energy of dissociation of CO is the lowest for W(100) with a barrier of 0.31 eV (see Figure 4.1). Almost twice the energy is needed to dissociate CO on both chromium and molybdenum. Lastly, carbon monoxide is most difficult to dissociate on Fe(100) with an activation energy 4 times higher than for tungsten, 1.19 eV.

Dissociation of carbon monoxide is exothermic for all four surfaces with the highest reaction energy (-2.22 eV) on chromium (which includes diffusion of the oxygen atom away from the carbon to relieve repulsion). The lowest reaction energy is observed on the iron surface (-1.09 eV), whereas that on tungsten (-1.72 eV) and molybdenum (-1.71 eV) falls in between. A closer look at the dissociated end-state shows that, for iron, molybdenum, and chromium, both the carbon and oxygen atoms reside at fourfold hollow sites, whereas in the case of tungsten, the oxygen prefers the bridge position.

At a higher surface coverage of 0.5 ML (Figure 4.2), carbon monoxide still dissociates easiest on W(100). Overall, the activation energy of dissociation seems to be coverage-independent in the range between 0.25 and 0.5 ML for all four metals. Dissociating the first half CO molecules on the surface at 0.5 ML (reaction 4.3.2.2) results in a lower reaction energy compared with that at 0.25 ML (without diffusion of O) for all four metals and leads to a thermoneutral reaction on iron and tungsten. These findings seem to illustrate that the Brønsted-Evans-Polanyi (BEP) relationship [52,53] only applies to situations in which coverages are similar, showing the relevance of lateral interactions.

The effect of lateral interactions is visible through the location of the adsorbed species. At low CO coverage, where interactions are not a limiting factor, oxygen atoms prefer to reside at fourfold hollow sites, as can be seen in Figure 4.1. At 0.5 ML, space limitations and, hence, lateral interactions become important, thus forcing the oxygen atoms in threefold coordination.

Dissociation of the second half of the CO molecules (reaction 4.3.2.3) is not favorable on the Fe(100) surface. In contrast, the other three metals are still able to dissociate the remaining CO (having adsorption energies of -2.26, -2.32, and -2.46 for Mo, Cr, and W, respectively) with similar to slightly higher activation energies compared to the dissociation of the first half of the CO molecules (reaction 4.3.2.2). The dissociation of these remaining CO molecules leads to an exothermic reaction on all three metals.

Although dissociation of the first half of the CO molecules results in an endothermic reaction on W(100), the energy gain of dissociating the remaining CO molecules leads to an overall reaction that is exothermic. Because the activation energy of both elementary reactions (4.3.2.2 + 4.3.2.3) is similar on the tungsten metal, dissociation of the first half of the CO molecules automatically leads to dissociation of the remaining CO; thus, dissociation of carbon monoxide at 0.5 ML is complete on

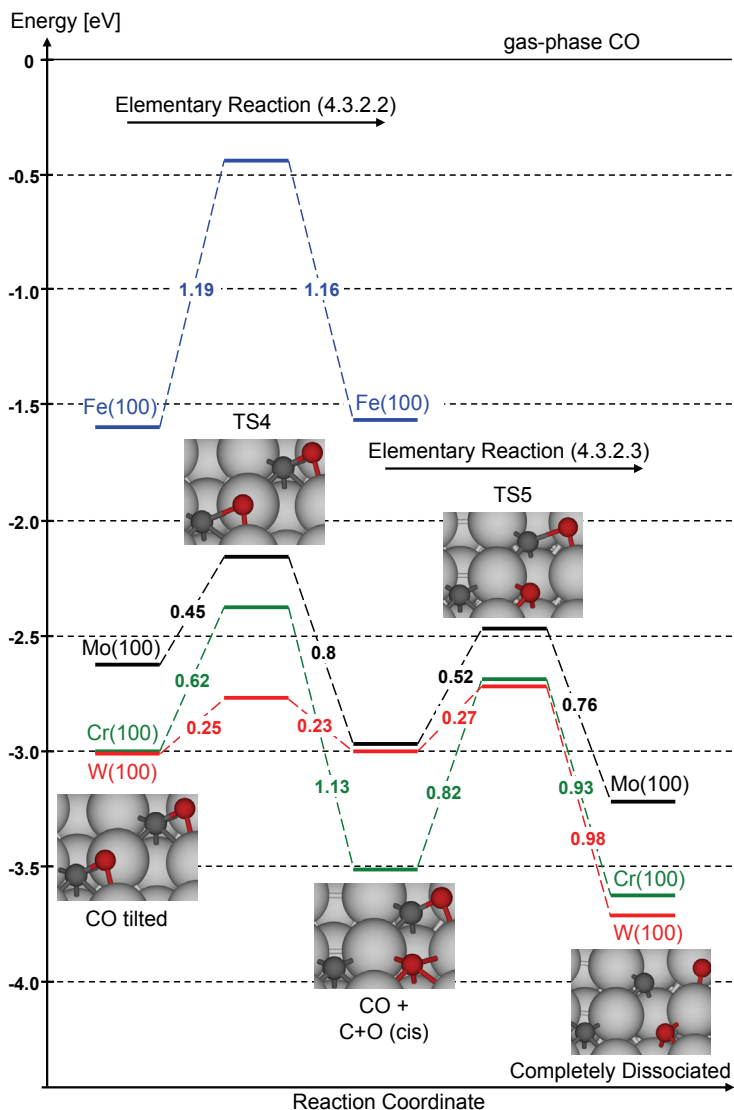


**Figure 4.2** Energy diagram of adsorption and dissociation of 0.5 ML of CO on Fe(100), Mo(100), Cr(100), and W(100) using a  $p(2 \times 2)$  unit cell. The numbers inserted represent the activation energies of the elemental steps. Energies are without ZPE correction.

W(100) as well as on Mo(100) and Cr(100).

Lateral interaction effects become clearly visible after reaction 4.3.2.3 as the energy gain drops even further for the metals molybdenum and chromium; see Figure 4.2. In the case of tungsten, however, the behavior is the opposite, as dissociation of the second half CO molecules increases the energy gain significantly.



Next to changes in exothermicity, the effect of lateral interactions at the dissociated end-state is, again, clearly visible through the locations of the adsorbed species. Because the coverage of atoms at this completely dissociated state is 1 ML, the surface is entirely covered with atomic carbon and oxygen; hence, the entire system is under stress. To reach the most stable end-situation, this stress has to be minimized by movement of the surface atoms. Therefore, not all the atoms stay coordinated at fourfold hollow sites, as is the case at 0.25 ML, but some move toward threefold or bridge sites. Thus, although oxygen prefers bridge sites for Mo and W at low coverages, oxygen adsorbs at threefold-like hollow sites when the coverage is increased.

### 4.3.3 Adsorption and Dissociation of CO on $\text{Fe}_3\text{Mo}$ and $\text{Fe}_3\text{Cr}(100)$

Since alloys are of interest as a means to affect product selectivities in the Fischer-Tropsch synthesis [4,54], we also calculated the adsorption and dissociation of CO on (100)  $\text{Fe}_3\text{Mo}$  and  $\text{Fe}_3\text{Cr}$ ; see Table 4.1 for distances and energies and Table 4.2 for frequencies. We limited ourselves to a CO coverage of 0.25 ML. Figure 4.3 shows the

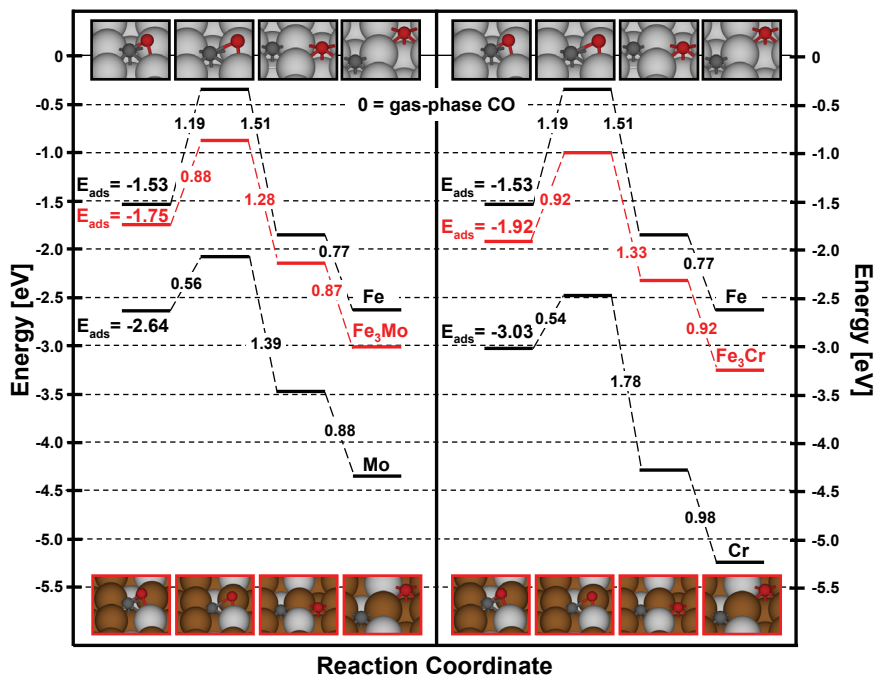


**Figure 4.3** Energy diagrams of the adsorption and dissociation of 0.25 ML CO on (left)  $\text{Fe}_3\text{Mo}(100)$ ,  $\text{Fe}(100)$ , and  $\text{Mo}(100)$  and (right)  $\text{Fe}_3\text{Cr}(100)$ ,  $\text{Fe}(100)$ , and  $\text{Cr}(100)$  using a  $p(2 \times 2)$  unit cell. The numbers inserted represent the activation energies of the elemental steps. The most stable adsorption geometry of CO on the  $\text{Fe}_3\text{Mo}$  and  $\text{Fe}_3\text{Cr}$  alloy is shown in the most left picture of the bottom row of pictures (both left and right side). Energies are without ZPE correction.

most stable CO adsorption geometry on these alloy surfaces. The carbon atom is located at a fourfold hollow site with an iron atom directly underneath in the second layer, and the oxygen is bridge-bonded toward one iron and one molybdenum or chromium atom. Hence, using this particular composition of alloy results in CO coordinated toward one molybdenum or chromium atom only. Other adsorption geometries are conceivable as well, for example, where CO can coordinate to two molybdenum or chromium atoms, but the adsorption energies for such situations differ on the order of 0.1-0.2 eV; therefore, we only consider the geometry of Figure 4.3 in this Chapter.

CO dissociation proceeds similarly as on the pure metals, with activation energies of 0.88 eV on Fe<sub>3</sub>Mo(100) and 0.92 eV on Fe<sub>3</sub>Cr(100). The exothermicities or heats of reaction are -1.27 and -1.33 eV, respectively. Figure 4.3 shows all results for the adsorption and dissociation of CO on these alloys.

## **4.4 Discussion**

The aim of this Chapter is to compare the adsorption and dissociation of CO on bcc metals such as iron and the bcc metals that may be of interest as second components in iron-based alloy catalysts for the Fischer-Tropsch synthesis. We first discuss molecular adsorption of CO, then dissociation, and finally, we consider scaling relations between the adsorption energies of CO and its dissociation products and the activation energy for dissociation.

### **4.4.1 Adsorption of CO**

In contrast to the situation on the Group VIII fcc metals, where CO at low coverages adsorbs perpendicular in top, hollow, or bridge sites, the molecule adsorbs in tilted geometry on the (100) surfaces of Fe, Cr, Mo, and W, with the carbon atom in fourfold hollow position and the oxygen bridge-bonded. Only at higher coverages does coadsorption in a perpendicular mode occur, as in the on-top mode for Fe(100) [15,50]. The calculations show that increasing the coverage from 0.25 ML to 0.5 ML does not change the CO adsorption energy significantly or its tilting angle. The CO stretching frequencies, on the other hand, do depend on coverage. We will discuss the effect to some extent next.

With increasing coverage, the CO stretching frequency shifts to higher frequencies on Fe and Cr, but to lower frequencies on Mo and W. Predominantly three effects play a role in the CO stretching frequency: (1) dipole-dipole coupling between the CO molecules, (2) Pauli repulsion, and (3) a chemical effect. The first is a purely physical effect and leads to increases in frequency when the distance between alike CO molecules decreases at higher surface coverage [55-57].

If the CO molecules come close to each other, a chemical effect can cause

further blue-shifts [56-60]. This coverage effect is straightforwardly explained by the Blyholder model [61]. According to this model, the bond of a CO molecule to a metal surface is established by electron donation from the CO  $5\sigma$  to empty levels of the metal surface and electron back-donation from the metal surface into the anti bonding CO  $2\pi^*$  orbital. A high coverage may cause the CO molecules to compete for the metal electrons, resulting in lower back-donation, and hence, the CO stretching frequency shifts toward higher frequencies. In addition, Pauli repulsion is known to blue-shift the CO frequency as well [62-65]. Hence, increased CO stretching frequencies at higher coverages tend to be the norm.

In some cases, the opposite occurs, however. This so-called ‘negative chemical effect’ has been observed for CO on the (111) surfaces of the s-metals gold and copper [66,67] and on certain gold clusters [68]. Here, the chemical effect dominates over the also present dipole–dipole coupling. Hollins and Pritchard attributed the downward shift to the character of the metal– $5\sigma$  interaction, which has a largely filled bonding and a partially filled antibonding character [67]. Back-donation is less important for Cu and Au surfaces than for other transition-metals, because of the low lying and occupied d-band. Therefore, increasing the surface coverage leads to less electron donation from the  $5\sigma$  to the carbon–metal bond. According to France and Hollins [66], this effect weakens the CO bond and, hence, leads to a red-shift of the CO frequency. Moreover, in constrained space orbital variation (CSOV), several authors [69,70] observed that, for the surface orientations (100), (110), and (111) of Pt, both  $\sigma$ -donation and  $\pi$ -back-donation contribute to the decrease in CO frequency and that the only blue-shift contribution arises from the Pauli repulsion or ‘wall effect’ identified by Bagus et al. [62-64].

Care is needed when explaining our results for CO on Fe, Cr, Mo, and W in terms of dipole–dipole coupling of the CO molecules, Pauli repulsion, and a chemical effect because, on the bcc metals, CO is bent toward the surface. This tilted geometry results in oxygen taking part in the bonding mechanism with the metal, that is, explaining the low CO frequency. As mentioned before, in the case of iron and tungsten, the shift of CO frequency is upward, whereas for molybdenum and tungsten, the opposite behavior is observed. In all four cases, an increase in coverage does not lead to a change in the adsorption energy nor to a significant alteration of the tilting angle. Dipole–dipole coupling is most likely similar on all four metals and, therefore, does not account for the difference in CO stretching behavior. On the other hand, CO ‘sinks’ slightly into the fourfold hollow site on all four metals with an increase of the coverage, which could lead to a better overlap of the CO and metal orbitals, resulting in a higher Pauli repulsion, blue-shifting the CO frequency. Although the overlap of the orbitals also leads to a higher  $\pi$ -back-donation –red-shifting the CO frequency–according to Bagus et al. [71], this mechanism is overcompensated by the effect of stretching the C–O bond against the “rigid” surface wall. We propose that this explains

why CO behaves differently on iron and chromium than on molybdenum and tungsten. Perhaps on Mo and W, the higher  $\pi$ -back-donation is not overcompensated by the Pauli repulsion, thus overall leading to a lower stretching frequency.

To further elaborate on this, increasing the surface coverage from 0.25 ML to 0.5 ML leads to a slight surface reconstruction for Mo and W, whereas such a change is hardly observed for Cr and Fe (See Figure 4.4 for the difference between Cr and Mo). Within this figure, distance  $x$  becomes slightly larger for both the Cr (0.008 nm) and Mo (0.014 nm) surface, whereas distance  $y$  decreases for the Mo surface (0.011 nm) and stays almost constant for chromium (0.003 nm). The smaller distance of  $y$  might lead to a better overlap between the orbitals of the oxygen of the CO molecule and the orbitals of the metal surface of molybdenum than that for chromium, hence, resulting overall in  $\pi$ -back-donation as the most predominant contribution in the CO frequency.

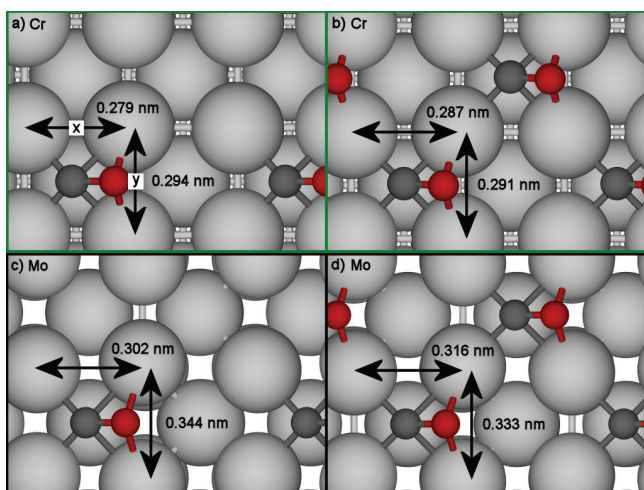


**Figure 4.4** Surface changes of Cr and Mo as a function of CO coverage. Pictures a) and c) are 0.25 ML CO on Cr and Mo, respectively. Pictures b) and d) are 0.5 ML CO on Cr and Mo, respectively.

To be sure that a slight alteration in surface geometry induces the difference in CO stretching behavior, we performed calculations using the most stable geometry of the molybdenum surface for both CO coverages and pretended the metal surface is chromium instead. These calculations were also performed the other way around, using the most stable geometry of the chromium surface for both CO coverages, while faking the metal surface to be molybdenum. The outcome of the calculations was interesting since the CO stretching frequency of carbon monoxide on the ‘imaginary’ chromium surface went down from 1176 to 888  $\text{cm}^{-1}$  and increased from 1111 to 1125  $\text{cm}^{-1}$  for molybdenum. These results, to our belief, show that the remarkable behavior of the CO stretching frequency can, indeed, be attributed to geometric effects of the surface atoms

of the metal, which could induce a switch between either Pauli repulsion or  $\pi$ -back-donation as the main contribution in the CO stretch. Further research will be needed on this particular aspect performing density of states (DOS) calculations and population analysis using Bader's theory as implemented by Henkelman [72-74].

In conclusion, due to the nature of bonding of tilted CO with the metal surface (both carbon and oxygen participate in the bonding character), interpreting CO frequency shifts as a function of coverage in terms of dipole-dipole coupling, Pauli repulsion, and chemical effect is somewhat dubious. However, geometry changes of the surface atoms of the metal, induced by variation of CO concentrations, seem to be the key in understanding the unusual behavior of the CO stretching frequency for the different metals.

#### 4.4.2 Dissociation of CO

Dissociation of CO on the bcc (100) surfaces is an exothermic process for all four metals at a surface coverage of 0.25 ML and leads to atomic carbon (in fourfold hollow sites) and oxygen (either in bridge or fourfold hollow sites); see Figure 4.1.

Although our calculations show that carbon solely adsorbs at fourfold hollow sites and oxygen on its own prefers to stay either bridge-bonded (in the case of Mo and W) or fourfold hollow-bonded (for Cr and Fe), several articles mention a third possibility for oxygen to adsorb onto, namely, near-bridge or threefold sites for W(100) [75-77] and W(110) [78] at low coverage. Even though we found that oxygen is, indeed, stable on W(100) at these threefold sites, the oxygen atoms prefer bridge sites with a higher adsorption energy of 0.68 eV. Therefore, we conclude that oxygen is bridge-bonded after dissociation of CO at a low coverage.

Dissociation at the higher CO coverage (0.5 ML) is still exothermic on Mo, W, and Cr, but thermoneutral on Fe due to a lower adsorption energy of the CO molecules in excess of 0.25 ML caused by the presence of carbon and oxygen atoms [15]. For these additional CO molecules, the adsorption energy is less than the activation energy for dissociation, and hence, they desorb.

On Mo, Cr, and W(100), dissociation of the first half of the CO molecules at 0.5 ML is less exothermic than starting from 0.25 ML because of lateral interactions of C and O with the undissociated CO. Hence, the remaining CO is destabilized, and in experiments, the lower adsorption energy is visible in shifted ' $\beta$ -CO' thermal desorption peaks [10,13,14]. These desorption features have been attributed to recombination of carbon and oxygen atoms on the surface, but our results indicate that the desorption features are due to molecular desorption of CO. The energies needed to recombine carbon and oxygen are only between 0.8 and 1 eV, and hence, temperatures needed to recombine carbon and oxygen on the surface are much lower than those observed for the ' $\beta$ -CO' features, which occur at temperatures between 900 and 1500 K

[10,13,14]. Thus, these high desorption temperatures do not reflect recombination, but rather desorption of molecular CO formed from recombination. The situation at these high temperatures is one of equilibrium between molecularly and dissociatively adsorbed CO, which lies at the side of the decomposed molecule. However, desorption is only possible from the molecular form and takes a higher activation energy than that needed for recombination.

Dissociation of the CO molecules in excess of 0.25 ML is less exothermic than that for the first 0.25 ML, whereas for tungsten, it increases. A reason for this effect may be that oxygen prefers to stay at bridge and threefold sites on W(100) than, instead, at fourfold hollow sites on the other metals. On comparison of the completely dissociated end-state with the situation 'CO and C+O(cis)' (see Figure 4.2), half the oxygen atoms move from a fourfold hollow location to a threefold position and the other half are bridge-bonded after dissociation of the remaining CO molecules. Hence, more oxygen atoms are adsorbed at their preferred adsorption sites at the completely dissociated end-state than at the 'CO and C+O(cis)' surface, thus resulting in a more stable situation for the completely dissociated surface. Although oxygen also prefers to be adsorbed at bridge sites rather than at fourfold hollow sites on Mo(100), this effect is less pronounced than that in the case of tungsten, as the energy gain of adsorbed oxygen at bridge sites on molybdenum(100) is only 0.18 eV compared with that of fourfold coordinated oxygen. On chromium, oxygen favors fourfold hollow sites; therefore, the energy gain of reaction 4.3.2.3 is even smaller.

#### **4.4.3 Scaling Relations for CO Adsorption and Dissociation**

Recently, Nørskov and co-workers reported several scaling relations for hydrogen containing adsorbates ( $\text{CH}_x$ ,  $\text{NH}_x$ ,  $\text{OH}_x$ ,  $\text{SH}_x$ ) as well as for CO and NO on many transition-metal surfaces and alloys. Adsorption energies and activation energies of dissociation were found to scale linearly with the adsorption energies of carbon, oxygen, sulfur, or nitrogen [26,31,79,80]. In Figure 4.5, we plot the CO adsorption energies and the activation energies of dissociation from this Chapter against the adsorption energy of the carbon atom (Figure 4.5, left) and against the sum of the adsorption energies for carbon and oxygen together (Figure 4.5, right), as proposed by Liu and Hu [28-30] (note the different reference energies for the left and the right plots). Both methods of plotting yield linear relations. The upper parts of Figure 4.5, that is, the plots of the activation energy of dissociation against the adsorption energy of carbon or carbon plus oxygen, are, in fact, Brønsted-Evans-Polanyi (BEP) relations [52,53].

Interestingly, the adsorption energy of CO on the  $\text{Fe}_3\text{Mo}$  and  $\text{Fe}_3\text{Cr}$  alloys equals the result one obtains by taking  $\frac{3}{4}$  of the adsorption energy of CO on Fe plus  $\frac{1}{4}$  of the adsorption energy of CO on Mo or Cr (within the error of calculation of 0.05 eV). In other words, the adsorption of CO on an  $\text{Fe}_3\text{X}$  alloy can be calculated as follows:

$$E_{ads}(CO/Fe_3X) = 3/4E_{ads}(CO/Fe) + 1/4E_{ads}(CO/X) \quad (\text{eq. 4.4.3.1})$$

Because the oxygen of CO is almost bridge-bonded, dissociating the CO molecule results in a movement of oxygen across the bridge site, which is equally influenced by both the iron and molybdenum or chromium atom. Hence, the activation energy of CO dissociation on Fe<sub>3</sub>Mo and Fe<sub>3</sub>Cr alloys is in agreement with the sum of 1/2 of the activation energy of CO dissociation on iron and 1/2 of the activation energy of dissociation of CO on Mo or Cr (within the error of calculation of 0.05 eV). For an Fe<sub>3</sub>X alloy, this means:

$$E_{act}(CO/Fe_3X) = 1/2E_{act}(CO/Fe) + 1/2E_{act}(CO/X) \quad (\text{eq. 4.4.3.2})$$

Hence, breaking the C–O bond seems to be evenly influenced by both elements in the alloy. These scaling relations for alloys are very useful in predicting the reactivity of alloy surfaces.

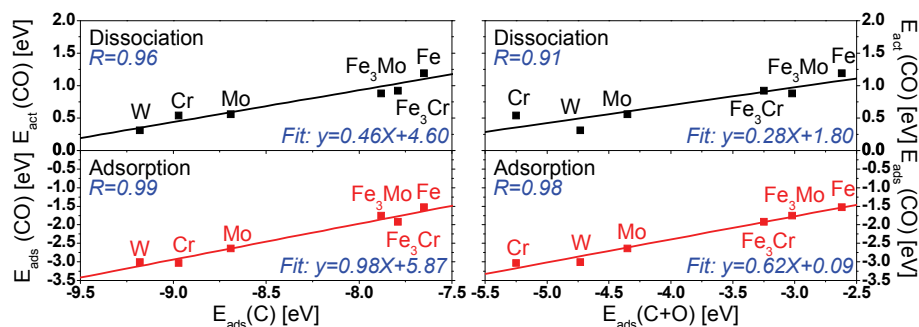


**Figure 4.5** Adsorption energies and activation energies of dissociation of CO on (100) surfaces plotted against (left) the adsorption energy of carbon with respect to carbon in the gas-phase and (right) the adsorption energy of the dissociation products carbon and oxygen with respect to CO in the gas-phase at a surface coverage of 0.25 ML CO. Energies are without ZPE correction.

## 4.5 Conclusions

Carbon monoxide adsorbs molecularly with a tilted geometry on the (100) surfaces of Fe, Mo, Cr, and W with carbon at fourfold hollow sites and the oxygen bridge-bonded. The adsorption energy and tilting angle are coverage independent between 0.25 and 0.5 ML of CO. However, the adsorption energy is influenced for CO coverages lower than 0.125 ML. The CO stretching frequency is affected by coverage changes and blue-shifts for Fe and Cr and red-shifts for Mo and W at increasing CO coverages, which is due to geometry changes of the surface atoms of the metal, changing the  $\sigma$ -donation and  $\pi$ -back-donation of electrons from the metal to the CO bond.

Dissociation of CO is an exothermic and complete process on all four metals at 0.25 ML of CO. Increasing the coverage leads to a lowering of the exothermicity of the



dissociation reaction as a result of the increase in lateral interactions, rendering the reaction thermoneutral on iron. On all other metals, full dissociation still occurs. The applicability of the BEP relation seems to be constraint to certain conditions, such as coverage.

Linear relations were found for the adsorption energy of carbon as well as both dissociation products against the adsorption energy of CO and activation energy of dissociation on the metal(-alloys) Fe, Mo, Cr, W, Fe<sub>3</sub>Mo, and Fe<sub>3</sub>Cr at a CO coverage of 0.25 ML. This result makes clear that even for CO molecules with a bent geometry –different binding mechanism than upright CO– scaling relations can be applied at a given coverage.

## References

- [1] *Studies in Surface Science and Catalysis*, A. P. Steynberg, M. Dry (Eds.), Vol. 152, Elsevier, Amsterdam, 2004.
- [2] J. G. Fan, B. N. Zong, X. X. Zhang, X. K. Meng, X. H. Mu, G. B. Yu, M. H. Qiao, K. N. Fan, *Ind. Eng. Chem. Res.* **47** (2008) 5918.
- [3] D. I. Foustoukos, W. E. Seyfried, Jr., *Science* (Washington, DC, United States) **304** (2004) 1002.
- [4] F. Hugues, M. Roy-Auberger, M.-C. Marion, European Patent 1094049 (2001), to Institut Francais Du Petrole, Eni S.p.A., and Agip Petroli S.p.A.
- [5] W. Ma, E. L. Kugler, D. B. Dadyburjor, *Stud. Surf. Sci. Catal.* **163** (2007) 125.
- [6] N. D. Shinn, T. E. Madey, *J. Chem. Phys.* **83** (1985) 5928.
- [7] M. L. Colaianni, J. G. Chen, W. H. Weinberg, J. T. Yates, Jr., *J. Am. Chem. Soc.* **114** (1992) 3735.
- [8] J. P. Fulmer, F. Zaera, W. T. Tysoe, *J. Chem. Phys.* **87** (1987) 7265.
- [9] Z. Ji, J.-Q. Li, *J. Phys. Chem. B* **110** (2006) 18363.
- [10] F. Zaera, E. Kollin, J. L. Gland, *Chem. Phys. Lett.* **121** (1985) 464.
- [11] J. E. Houston, *Surf. Sci.* **255** (1991) 303.
- [12] G. H. Ryu, S. C. Park, S.-B. Lee, *Surf. Sci.* **427-428** (1999) 419.
- [13] T. V. Vorburger, D. R. Sandstrom, B. J. Wacławski, *Surf. Sci.* **60** (1976) 211.
- [14] J. T. Yates, Jr., D. A. King, *Surf. Sci.* **32** (1972) 479.
- [15] T. C. Bromfield, D. Curulla-Ferré, J. W. Niemantsverdriet, *ChemPhysChem* **6** (2005) 254.
- [16] Y.-H. Chen, D.-B. Cao, J. Yang, Y.-W. Li, J. Wang, H. Jiao, *Chem. Phys. Lett.* **400** (2004) 35.
- [17] D. Curulla-Ferré, A. Govender, T. C. Bromfield, J. W. Niemantsverdriet, *J. Phys. Chem. B* **110** (2006) 13897.
- [18] Q. Ge, M. Neurock, *J. Phys. Chem. B* **110** (2006) 15368.
- [19] A. A. Gokhale, M. Mavrikakis, *Prepr. Pap. -Am. Chem. Soc., Div. Fuel Chem.* **50** (2005) 149.
- [20] X.-Q. Gong, R. Raval, P. Hu, *Surf. Sci.* **562** (2004) 247.
- [21] D. E. Jiang, E. A. Carter, *Surf. Sci.* **570** (2004) 167.
- [22] J. M. H. Lo, T. Ziegler, *J. Phys. Chem. C* **112** (2008) 3667.
- [23] J. M. H. Lo, T. Ziegler, *J. Phys. Chem. C* **112** (2008) 3679.
- [24] D. C. Sorescu, D. L. Thompson, M. M. Hurley, C. F. Chabalowski, *Phys. Rev. B* **66** (2002) 035416/1.
- [25] A. Travert, C. Dujardin, F. Mauge, E. Veilly, S. Cristol, J. F. Paul, E. Payen, *J. Phys. Chem. B* **110** (2006) 1261.
- [26] M. P. Andersson, T. Bligaard, A. Kustov, K. E. Larsen, J. Greeley, T. Johannessen, C. H. Christensen, J. K. Nørskov, *J. Catal.* **239** (2006) 501.
- [27] J. K. Nørskov, T. Bligaard, A. Logadottir, S. Bahn, L. B. Hansen, M. Bollinger, H. Bengaard, B. Hammer, Z. Sljivancanin, M. Mavrikakis, Y. Xu, S. Dahl, C. J. H. Jacobsen, *J. Catal.* **209** (2002) 275.
- [28] Z.-P. Liu, P. Hu, *J. Chem. Phys.* **115** (2001) 4977.



- [29] Z.-P. Liu, P. Hu, *J. Chem. Phys.* **114** (2001) 8244.
- [30] Z.-P. Liu, P. Hu, *J. Am. Chem. Soc.* **125** (2003) 1958.
- [31] F. Abild-Pedersen, J. Greeley, F. Studt, J. Rossmeisl, T. R. Munter, P. G. Moses, E. Skulason, T. Bligaard, J. K. Nørskov, *Phys. Rev. Lett.* **99** (2007) 016105.
- [32] F. Studt, F. Abild-Pedersen, T. Bligaard, R. Z. Sorensen, C. H. Christensen, J. K. Nørskov, *Science* (Washington, DC, United States) **320** (2008) 1320.
- [33] D. W. Moon, S. L. Bernasek, J. P. Lu, J. L. Gland, D. J. Dwyer, *Surf. Sci.* **184** (1987) 90.
- [34] G. Kresse, J. Furthmüller, *Phys. Rev. B* **54** (1996) 11169.
- [35] G. Kresse, J. Furthmüller, *J. Comput. Mater. Sci.* **6** (1996) 15.
- [36] J. P. Perdew, K. Burke, M. Ernzerhof, *Phys. Rev. Lett.* **77** (1996) 3865.
- [37] B. Hammer, L. B. Hansen, J. K. Nørskov, *Phys. Rev. B* **59** (1999) 7413.
- [38] P. E. Blöchl, *Phys. Rev. B* **50** (1994) 17953.
- [39] G. Kresse, D. Joubert, *Phys. Rev. B* **59** (1999) 1758.
- [40] M. Methfessel, A. T. Paxton, *Phys. Rev. B* **40** (1989) 3616.
- [41] <http://www.webelements.com>, Accessed 2009.
- [42] H. J. Monkhorst, J. D. Pack, *Phys. Rev. B* **13** (1976) 5188.
- [43] P. Pulay, *Chem. Phys. Lett.* **73** (1980) 393.
- [44] J. D. Head, *Int. J. Quantum Chem.* **65** (1997) 827.
- [45] G. Henkelman, B. P. Uberuaga, H. Jonsson, *J. Chem. Phys.* **113** (2000) 9901.
- [46] F. J. E. Scheijen, J. W. Niemantsverdriet, D. Curulla-Ferré, *J. Phys. Chem. C* **111** (2007) 13473.
- [47] F. J. E. Scheijen, J. W. Niemantsverdriet, D. Curulla-Ferré, *J. Phys. Chem. C* **112** (2008) 7436.
- [48] J. P. Perdew, J. A. Chevary, S. H. Vosko, K. A. Jackson, M. R. Pederson, D. J. Singh, C. Fiolhais, *Phys. Rev. B* **46** (1992) 6671.
- [49] Y. Wang, J. P. Perdew, *Phys. Rev. B* **44** (1991) 13298.
- [50] D. W. Moon, D. J. Dwyer, S. L. Bernasek, *Surf. Sci.* **163** (1985) 215.
- [51] A. Adnot, J. D. Carette, *Surf. Sci.* **75** (1978) 109.
- [52] J. N. Brønsted, *Chem. Rev.* **5** (1928) 231.
- [53] M. G. Evans, M. Polanyi, *Trans. Faraday Soc.* **34** (1938) 11.
- [54] F. Tihay, A. C. Roger, G. Pourroy, A. Kiennemann, *Energy & Fuels* **16** (2002) 1271.
- [55] R. M. Hammaker, S. A. Francis, R. P. Eischens, *Spectrochim. Acta* **21** (1965) 1295.
- [56] F. M. Hoffmann, *Surf. Sci. Rep.* **3** (1983) 107.
- [57] P. Hollins, J. Pritchard, *Prog. Surf. Sci.* **19** (1985) 275.
- [58] D. Curulla, A. Clotet, J. M. Ricart, *Surf. Sci.* **460** (2000) 101.
- [59] R. Linke, D. Curulla-Ferré, M. J. P. Hopstaken, J. W. Niemantsverdriet, *J. Chem. Phys.* **115** (2001) 8209.
- [60] D. Loffreda, D. Simon, P. Sautet, *Surf. Sci.* **425** (1999) 68.
- [61] G. Blyholder, *J. Phys. Chem.* **68** (1964) 2772.
- [62] P. S. Bagus, K. Hermann, C. W. Bauschlicher, Jr., *J. Chem. Phys.* **81** (1984) 1966.
- [63] P. S. Bagus, K. Hermann, C. W. Bauschlicher, Jr., *J. Chem. Phys.* **80** (1984) 4378.
- [64] P. S. Bagus, W. Müller, *Chem. Phys. Lett.* **115** (1985) 540.
- [65] D. Curulla, A. Clotet, J. M. Ricart, F. Illas, *J. Phys. Chem. B* **103** (1999) 5246.
- [66] J. France, P. Hollins, *J. Electron Spectrosc. Relat. Phenom.* **64-65** (1993) 251.
- [67] P. Hollins, J. Pritchard, *ACS Symposium Series* **137** (1980) 51.
- [68] A. Fielicke, G. Von Helden, G. Meijer, B. Simard, D. M. Rayner, *J. Phys. Chem. B* **109** (2005) 23935.
- [69] D. Curulla-Ferré, A. Clotet, J. M. Ricart, F. Illas, *J. Phys. Chem. B* **103** (1999) 5246.
- [70] F. Illas, S. Zurita, A. M. Marquez, J. Rubio, *Surf. Sci.* **376** (1997) 279.
- [71] P. S. Bagus, G. Pacchioni, *Surf. Sci.* **236** (1990) 233.
- [72] G. Henkelman, A. Arnaldsson, H. Jónsson, *Comput. Mater. Sci.* **36** (2006) 354.
- [73] E. Sanville, S. D. Kenny, R. Smith, G. Henkelman, *J. Comput. Chem.* **28** (2007) 899.
- [74] W. Tang, E. Sanville, G. Henkelman, *J. Phys.: Condens. Matter* **21** (2009) 084204/1.
- [75] H. Froitzheim, H. Ibach, S. Lehwald, *Phys. Rev. B* **14** (1976) 1362.
- [76] D. R. Mullins, S. H. Overbury, *Surf. Sci.* **210** (1989) 481.
- [77] K. Ota, M. Tanaka, S. Usami, *Surf. Sci.* **402-404** (1998) 813.
- [78] M. A. Zaluska-Kotur, S. Krukowski, Z. Romanowski, L. A. Turski, *Phys. Rev. B* **65** (2002) 045404/1.
- [79] H. Falsig, T. Bligaard, C. H. Christensen, J. K. Nørskov, *Pure Appl. Chem.* **79** (2007) 1895.

- [80] H. Falsig, T. Bligaard, J. Rass-Hansen, A. L. Kustov, C. H. Christensen, J. K. Nørskov, *Top. Catal.* **45** (2007) 117.

### **Supplementary Information**

<b>Table 4.S1</b> Adsorption of C and O at their most stable adsorption site on Cr(100), Fe(100), Mo(100), and W(100) at $\theta = 0.25$ and $\theta = 0.5$ ML.						
	$\Delta E_{\text{ads}}^{[a]}$ [eV]	$\Delta E_{\text{rel}}^{[b]}$ [eV]	$z_c^{[c]}$ [Å]	$\Delta E_{\text{ads}}$ [eV]	$\Delta E_{\text{rel}}$ [eV]	$z_c$ [Å]
	C at fourfold hollow sites at 0.25 ML			C at fourfold hollow sites at 0.5 ML		
Cr(100)	-8.97	0.21	0.547	-9.13	0.06	0.450
Fe(100)	-7.65	1.53	0.398	-7.67	1.52	0.307
Mo(100)	-8.69	0.49	0.547	-8.79	0.40	0.448
W(100)	-9.18	0.00	0.594	-9.19	0	0.488
	O at fourfold hollow sites at 0.25 ML			O at fourfold hollow sites at 0.5 ML		
Cr(100)	-7.22	0.00	0.576	-6.92	0.12	0.513
Fe(100)	-5.96	1.26	0.605	-5.92	1.12	0.524
	O at bridge sites at 0.25 ML			O at bridge sites at 0.5 ML		
Mo(100)	-6.65	0.57	1.444	-6.45	0.59	1.300
W(100)	-7.14	0.08	1.447	-7.04	0	1.321

[a]  $\Delta E_{\text{ads}}$  is the adsorption energy. [b]  $\Delta E_{\text{rel}}$  is the relative adsorption energy with respect to the strongest adsorption of the atom in question, i.e., the metal on which carbon / oxygen adsorbs strongest is set to 0 eV. [c]  $z_c$  and  $z_o$  are the height of the carbon and oxygen atom with respect to the surface level.

**Table 4.S2** Adsorption of C and O at their most stable adsorption site on Cr(100), Fe(100), Mo(100), and W(100) at  $\theta = 0.25$  and  $\theta = 0.5$  ML: vibrational frequencies [ $\text{cm}^{-1}$ ], zero-point-energy corrections to the adsorption energy and to the relative adsorption energy.

	$\nu_1$	$\nu_2$	$\nu_3^{[a]}$	ZPE <sup>[b]</sup> [eV]	$\Delta E_{\text{ads}}^{[c]}$ [eV]	$\Delta E_{\text{rel}}^{[d]}$ [eV]
C at fourfold hollow sites at 0.25 ML						
Cr(100)	485	485	560	0.09	-8.88	0.20
Fe(100)	465	465	469	0.09	-7.56	1.52
Mo(100)	442	442	558	0.09	-8.60	0.48
W(100)	492	492	572	0.10	-9.08	0
C at fourfold hollow sites at 0.5 ML						
Cr(100)	421	421	567	0.09	-9.04	0.07
Fe(100)	363	363	501	0.08	-7.59	1.52
Mo(100)	327	327	558	0.08	-8.71	0.40
W(100)	331	331	578	0.08	-9.11	0
O at fourfold hollow sites at 0.25 ML						
Cr(100)	255	255	427	0.06	-7.16	0
Fe(100)	226	226	336	0.05	-5.91	1.25
O at fourfold hollow sites at 0.5 ML						
Cr(100)	265	265	293	0.05	-6.87	0.10
Fe(100)	264	264	323	0.05	-5.87	1.10
O at bridge sites at 0.25 ML						
Mo(100)	177	336	573	0.07	-6.58	0.58
W(100)	210	332	600	0.04	-7.10	0.06
O at bridge sites at 0.5 ML						
Mo(100)	179	313	552	0.06	-6.39	0.58
W(100)	216	338	585	0.07	-6.97	0
[a] $\nu_3$ is the metal–C / metal–O stretching frequency. [b] ZPE is the zero-point energy. [c] $\Delta E_{\text{ads}}$ is the adsorption energy including ZPE. [d] $\Delta E_{\text{rel}}$ is the relative adsorption energy including ZPE.						

**Table 4.S3** Frequencies of the transition-states of the dissociation of 0.25 MLCO for Cr(100), Fe(100), Mo(100), and W(100).

	$\nu_1$	$\nu_2$	$\nu_3$	$\nu_4$	$\nu_5$	$\nu_6$	ZPE [eV] <sup>[a]</sup>
Cr(100) TS1	388i	274	384	476	485	517	0.13
Cr(100) TS2	196i	404	449	491	560	567	0.15
Cr(100) TS3	101i	349	508	513	519	545	0.15
Fe(100) TS1	315i	295	378	425	438	479	0.12
Fe(100) TS2	153i	437	453	463	490	524	0.15
Mo(100) TS1	416i	271	335	424	472	504	0.12
Mo(100) TS2	162i	386	391	423	496	558	0.14
Mo(100) TS3	127i	344	457	492	500	543	0.14
W(100) TS1 <sup>[b]</sup>	415i	284	359	462	479	523	0.13

[a] ZPE is the zero-point-energy. [b] TS2 could not be found and was assumed to be around 0.05 eV.<sup>44</sup>

**Table 4.S4** Frequencies of the transition-states of the dissociation of 0.5 MLCO for Cr(100), Fe(100), Mo(100), and W(100).

	$\nu_1$	$\nu_2$	$\nu_3$	$\nu_4$	$\nu_5$	$\nu_6$	$\nu_7$	$\nu_8$	$\nu_9$	$\nu_{10}$	$\nu_{11}$	$\nu_{12}$	ZPE <sup>[a]</sup> [eV]
Cr(100) TS4	346i	292	294	314	357	403	441	456	491	514	541	1033	0.32
Cr(100) TS5	309i	290	314	340	360	413	464	500	521	537	590	617	0.24
Fe(100) TS4 <sup>[b]</sup>	285i	244	254	294	302	364	369	397	454	472	476	1194	0.30
Mo(100) TS4	398i	263	287	293	316	379	384	427	443	485	501	954	0.29
Mo(100) TS5	434i	265	293	300	333	419	443	480	495	506	542	548	0.29
W(100) TS4	390i	280	294	306	341	397	416	451	458	503	529	873	0.30
W(100) TS5	442i	240	264	264	319	406	454	487	505	533	551	585	0.26

[a] ZPE is the zero-point-energy. [b] No TSS for Fe(100), because the remaining CO desorbs.<sup>14</sup>



# 5

## **Poly Crystalline Iron: CO Adsorption, Desorption, and Dissociation Kinetics and the Influence of Atomic Carbon and Oxygen.**

### **Abstract**

*The adsorption, desorption, and dissociation of carbon monoxide on a poly crystalline iron surface were investigated under UHV conditions TPD and SSIMS. CO adsorbs molecularly at low temperatures and dissociates roughly at room temperature with an activation energy of dissociation of CO of 72 kJ/mol and a pre-exponential factor of  $10^{10}$ . At high enough coverages of CO, both dissociation and desorption of CO take place simultaneously. However, at too high coverages space becomes a limiting factor, hence, desorption precedes dissociation until sufficient space has opened up and both processes occur concurrently again. Desorption of CO takes place at 390 and 775 K and is shown to proceed through first order desorption kinetics with activation energies of desorption of 98 and 177 kJ/mol and pre-exponential factors of  $10^{12.5}$  and  $10^{10.7}$ , respectively. A model is proposed to explain the first order desorption kinetics for the high-temperature desorption peak, which leads to the conclusion that CO desorption at 775 K is limited by the activation energy of desorption and not by the recombination energy of atomic carbon and oxygen. In addition, the influence of an overlayer of either atomic carbon or oxygen on the kinetic parameters of CO desorption is presented.*

## 5.1 Introduction

Dissociation of carbon monoxide in the Fischer-Tropsch (FT) synthesis is considered to be one of the key-steps in a couple of suggested FT mechanisms. However, other mechanisms suggest that molecular CO is the active species instead; see also Chapter 1. Hence, obtaining information on the reaction kinetics of CO dissociation may help in understanding the FT reaction mechanism on an iron surface.

Although carbon monoxide has always been one of the most investigated molecules in surface science, the number of surface science studies of carbon monoxide on poly crystalline iron is scarce [1-12]. Moreover, most of these articles are old and limited to the adsorption and desorption of CO with standard surface science techniques such as temperature programmed desorption (TPD), Ultraviolet photoelectron spectroscopy (UPS), electron energy loss spectroscopy (EELS), X-ray photoelectron spectroscopy (XPS), Auger electron spectroscopy (AES), and work function measurements. The kinetics of dissociation of CO, however, to the best of our knowledge has never been investigated in full, although a couple of groups reported that at room temperature a mixture of dissociatively and molecularly adsorbed CO is present on the poly crystalline iron surface [2,5,7,11], while at a temperature of 350 K dissociated CO remains the only species left. Hence, investigating the dissociation of CO on poly crystalline iron in more detail –especially the reaction kinetics– is a valuable addition to the known literature.

The influence of other adsorbates on the adsorption and desorption of carbon monoxide on poly crystalline iron is another subject that has briefly been investigated in literature by the group of Wedler [1,8]. They studied the interactions between coadsorbed species, such as hydrogen and oxygen, and CO and their influence on the CO desorption behavior. Since carbon monoxide almost never is the only species on the surface during reaction, but is surrounded by other adsorbates, the influence of coadsorbates on the CO adsorption, desorption, and dissociation is of great importance and needs to be investigated more closely.

In this Chapter, therefore, we will focus on the dissociation reaction of carbon monoxide using static secondary ion mass spectrometry (SSIMS) and derive the kinetic parameters for this reaction using a differential equation of Arrhenius form that has previously been used in our group for the dissociation reaction of NO on Rh(100) and Rh(111) [13,14]. Moreover, we will investigate the influence of atomic carbon and oxygen on CO using TPD and SSIMS and show that both carbon and oxygen have a repulsive character toward carbon monoxide.

## 5.2 Experimental Methods and Details

TPD and static SIMS experiments were carried out in a stainless steel ultra-high

vacuum (UHV) chamber with a base pressure of  $5 \cdot 10^{-11}$  mbar. The static SIMS spectra were taken by using a defocused 3 keV  $\text{Ar}^+$  primary ion beam with a current density of  $6.6 \text{ nA/cm}^2$  (when other current densities were used for a given spectrum, it is mentioned in the figure) at an angle of incidence of  $65^\circ$ . Secondary ions were collected under an angle of  $25^\circ$  with respect to the surface normal. These conditions were sufficient to measure in static mode for roughly 10 minutes. A typical temperature programmed experiment lasted 7 minutes at most.

A poly crystalline round iron foil with a diameter of 10 mm and a thickness of 0.27 mm was mounted on a movable sample rod by two tantalum wires of 0.3 mm diameter, spot-welded to the back of the foil. This construction allows for resistive heating to 1500 K. Because of the  $\alpha$ - $\gamma$  phase transition of iron at 1183 K, the system was protected in exceeding a maximum temperature of 1100 K. The crystal could be cooled to 90 K by flowing liquid nitrogen through the manipulator. Temperatures were measured using a chromel-alumel thermocouple spot-welded to the back of the foil.

Before the iron foil was placed in the UHV system, it was treated with 1 bar of flowing  $\text{H}_2$  (traces of water and oxygen were removed from the stream with mol sieves and copper, respectively) for ten days at a temperature of 1040 K. This was sufficient to remove sulfur, phosphor, and most of the other impurities in the foil. The remaining contaminants after this treatment, such as carbon, were removed by extended  $\text{Ar}^+$  bombardment until no more impurities were visible with SSIMS. The routine cleaning procedure of the foil consists of 30 minutes of argon<sup>+</sup> sputtering ( $0.5 \text{ keV}$ ,  $5 \mu\text{A/cm}^2$ ) at 1000 K to remove small amounts of impurities, such as carbon and oxygen. After sputtering, the crystal was kept at 1000 K for a few minutes to anneal and restore its surface ordering. This treatment resulted in SSIMS spectra of the crystal showing no contamination. After each experiment the above described procedure was repeated to ensure that any remaining carbon and oxygen on the surface is removed and that the foils' ordering is restored.

Carbon monoxide (Linde AG, 99.997% pure), ethylene (Linde AG, 99.95% pure), and technical air (Linde AG, 20%  $\text{O}_2$  : 80%  $\text{N}_2$ ) were used without further purification. Gas dosing for all experiments was done at a temperature of 150 K or lower. All temperature programmed experiments were performed at a heating rate of 2 K/s.

## **5.3 Results**

### **5.3.1 Desorption of CO from the Clean Surface**

Various amounts of carbon monoxide were dosed on the poly crystalline iron sample at a temperature and pressure of 100 K and  $10^{-8}$  mbar, respectively. Subsequently, temperature programmed desorption spectra of CO ( $m/e = 28$ ) were recorded, as



displayed in Figure 5.1. The only desorption products that were observed during the experiment were CO and a small amount of H<sub>2</sub> (background).

Before quantifying the results, we discuss the origin of the peaks in Figure 5.1. At a low amount of dosed carbon monoxide a single broad desorption feature is visible with a peak maximum at a temperature of ca. 775 K. By using SIMS, XPS, UPS, and EELS, different groups showed that at a temperature of roughly 300 K CO dissociates and that at temperatures above 350 K no more molecular CO was present on the surface [2,5,7,11]. The desorption of CO at 775 K, therefore, can be ascribed to a recombination of atomic carbon and oxygen on the surface [9]. Increasing the CO coverage leads to a

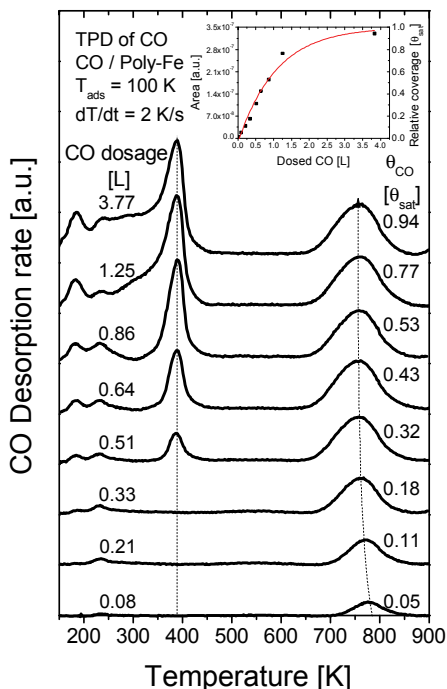


**Figure 5.1** TPD spectra of CO ( $m/e = 28$ ) obtained after exposing the clean poly crystalline iron surface to various doses of CO at a temperature of 100 K. The heating rate was 2 K/s. The inset is the uptake curve in which the area of CO underneath the TPD curve has been converted into a relative coverage.

slight decrease of the desorption temperature until a second desorption trace appears at a temperature of 390 K that results in the desorption temperature of the recombination peak to remain constant. Desorption of CO at 390 K is attributed to CO desorbing molecularly from the poly crystalline surface [9]. A further increase of CO coverage from this point on leads, apart from a constant desorption temperature of both the molecular and recombination peak, to a constant amount of CO desorbing due to

recombination of atomic carbon and oxygen, whereas the amount of CO at 390 K proportionally increases with coverage. Low-temperature features are visible at around 185 and 240 K. At dosages of above 0.86 Langmuir ( $1 \text{ L} = 1.33 \cdot 10^{-6} \text{ mbar s}$ ) a shoulder grows in at a temperature of around 300 K, while the low-temperature traces start to increase as well.

#### *5.3.1.1 Quantification of Dosed Amount CO*

Although the most predominant surface of the poly crystalline sample will be (110) oriented, because of its lowest surface free energy [15], the poly crystalline sample does not solely consist of this (110) oriented surface facet. Therefore, a poly crystalline surface does not have a well-defined surface structure, making the results acquired by TPD experiments difficult to quantify. Nonetheless semi-quantitative results based on the saturation coverage of CO can be obtained. For that reason, an uptake curve is prepared by plotting the area underneath the CO desorption traces against the dosed amount of CO, shown as the inset in Figure 5.1. Subsequently, this plot is fitted by an exponential of the form  $y(x) = y_0 + a \exp(x/b)$ . At a very high dosed amount of carbon monoxide the area underneath the CO desorption features will reach a constant value, hence, a completely covered or saturated surface with carbon monoxide. As a result, all areas can be expressed as a relative coverage with the saturation coverage denoted as 1 (completely covered), that is, the right scale in the inset of Figure 5.1.

#### *5.3.1.2 CO Desorption Kinetics*

The CO desorption kinetics for both the recombination peak at 775 K and the low-temperature desorption peak at 390 K were obtained using the Chan-Aris-Weinberg (CAW1/2) [16] method. Application of the CAW1/2 method for 2<sup>nd</sup> order desorption kinetics on the desorption feature of 775 K results in an activation energy of desorption ( $E_{des}$ ) of  $256 \pm 3 \text{ kJ/mol}$  and a pre-exponential factor ( $\nu_{des}$ ) of  $10^{16.2 \pm 0.1} \text{ s}^{-1}$  in the zero coverage limit ( $\theta_C, \theta_O = 0$ ). Using the CAW1/2 method for first order desorption kinetics on the desorption peaks of 775 K and 390 K yield  $E_{des}$  of  $177 \pm 2$  and  $98 \pm 2 \text{ kJ/mol}$  and  $\nu_{des}$  of  $10^{10.7 \pm 0.1}$  and  $10^{12.5 \pm 0.3} \text{ s}^{-1}$  in the zero coverage limit, respectively.

#### *5.3.1.3 Extent of CO Dissociation*

The relative amount of CO adsorbed onto the surface is plotted against the amounts of CO desorbed from both the low- and high-temperature desorption features in Figure 5.2. Basically, all adsorbed CO at 100 K dissociates until space becomes the limiting factor (occurring at 0.2-0.3  $\theta_{sat}$  coverage) and some of the CO starts to desorb molecularly. The maximum amount of CO dissociating is around a quarter of the saturation coverage. Hence, a surface covered with 0.5  $\theta_{sat}$  of atomic species is created. At this

point, the amount of dissociated CO remains constant, while CO desorbing molecularly increases proportionally with increasing CO coverage. Note that the coverages are relative to  $\theta_{\text{sat}}$ , and not to the total number of Fe atoms.

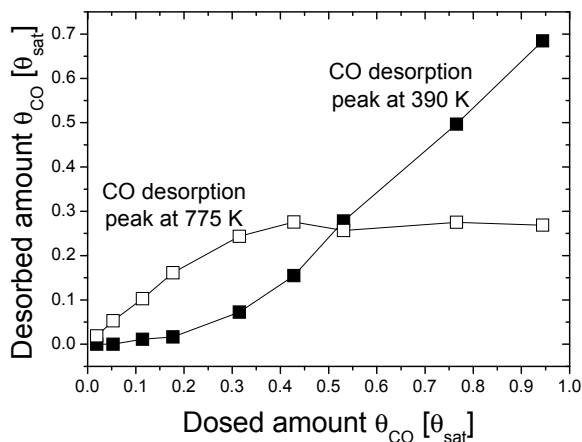


**Figure 5.2** Plot of the amount of CO desorbing from polycrystalline iron either molecularly (390 K) or by recombination of atomic carbon and oxygen (775 K) against the total dosed amount of carbon monoxide.

### 5.3.2 CO and CO related Species adsorbed on the Clean Surface

A typical static secondary ion mass spectrum of  $0.53 \theta_{\text{sat}}$  CO coverage on polycrystalline iron at 120 K is displayed in Figure 5.3. An intense peak is observed for the  $\text{Fe}^+$  signal. Peaks due to the adsorption of CO appear at  $m/e = 28$  and  $84$ , masses of the molecular ion clusters  $\text{CO}^+$  and  $\text{Fe}(\text{CO})^+$ , respectively, and are a lot less intense than the  $\text{Fe}^+$  signal. However, peaks also appear at  $m/e = 12, 18, 68,$  and  $72$  due to  $\text{C}^+, \text{O}^+, \text{FeC}^+,$  and  $\text{FeO}^+$ , respectively. Appearance of these peaks can be either due to dissociation of CO or fragmentation of molecular CO during the secondary ion emission process. According to literature [2,5,7,11], dissociation of carbon monoxide does not occur at a temperature as low as 120 K.

On the other hand, fragmentation products of molecularly adsorbed CO have been observed previously on polycrystalline iron [2] and also on a Rh(111) single crystal [17], thus, the presence of the peaks must be the result of fragmentation of molecular adsorbed CO during the secondary ion emission process. In addition to the peaks related to CO adsorption several other ion species are observed such as  $\text{Na}^+, \text{Si}^+, \text{K}^+,$  and  $\text{Ca}^+$ . These species are very easy to ionize or are already present as ions, and as a result, are standard impurities observed by SIMS. Water adsorption –particularly sensitive in SIMS [17]– originating from the residual gas during cooling and CO

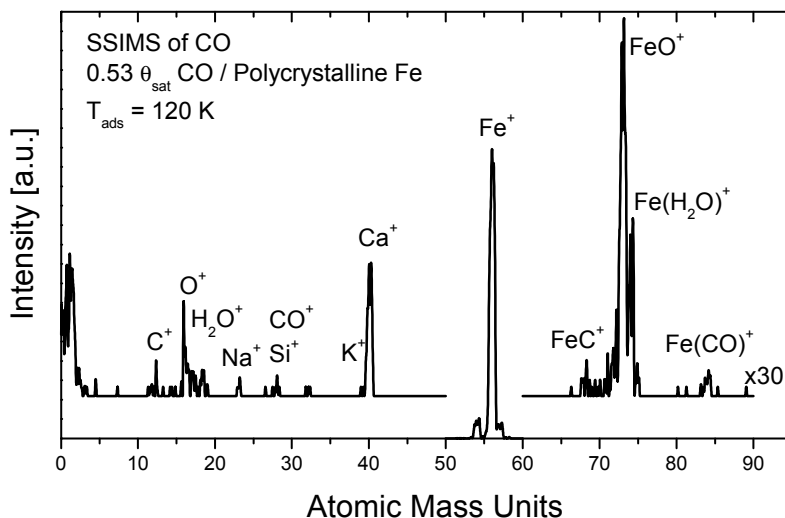


**Figure 5.3** SSIMS spectrum of the poly crystalline iron surface after an exposure of 0.53 saturation dosage of CO at 120 K. Spectrum was taken with a defocused 3 keV  $\text{Ar}^+$  primary ion beam with a current density of 12.7 nA/cm<sup>2</sup>.

adsorption at 120 K is visible through the  $\text{Fe}(\text{H}_2\text{O})^+$  ion cluster at  $m/e = 74$  and  $\text{H}_2\text{O}^+$  at  $m/e = 18$ .

It should be noted that the  $\text{Fe}(\text{CO})^+$  cluster intensity is lower than the  $\text{FeC}^+$  and  $\text{FeO}^+$  clusters, which would indicate that adsorption of CO is dissociative. However, results obtained by Barber et al. [2] show the opposite behavior, i.e., the  $\text{Fe}(\text{CO})^+$  signal is much larger than the  $\text{FeC}^+$  and  $\text{FeO}^+$  signals, hence, molecular adsorption of CO. This anomaly to our believe is caused by our quadrupole mass spectrometer, which most likely decomposes the  $\text{Fe}(\text{CO})^+$  cluster into smaller clusters resulting in an insufficient detection of the  $\text{Fe}(\text{CO})^+$  signal. Moreover, the overall sensitivity toward all CO related signals appears to be low, as a decrease in the current density of the primary ion beam to 1 nA/cm<sup>2</sup> (still twice the current density as by Barber et al. [2]) leads to zero detection of any of the CO related species.

### 5.3.2.1 Dissociation of CO – 1. Static SIMS

Unfortunately, we were not able to measure a decent  $\text{Fe}(\text{CO})^+$  ion signal at the low surface coverages of CO at which the only process occurring is dissociation. Hence, we were forced to measure at a coverage of  $0.53 \theta_{\text{sat}}$  CO instead, at which both dissociation and desorption of CO takes place. To investigate the dissociation of carbon monoxide on the poly crystalline surface static SIMS spectra ( $m/e = 0-90$ ) were taken, as shown in Figure 5.4, after heating toward the allocated temperatures. Some of the regions have

been multiplied according to the indicated number, to enhance the visibility of the picture. The SSIMS spectrum of  $0.53 \theta_{\text{sat}}$  CO coverage at 120 K has been discussed in the previous section. Raising the temperature of the iron surface toward 300 K yields no obvious change in all the secondary ion species that are related to carbon monoxide when compared to the 120 K spectrum. The water peak, on the other hand, has disappeared, thus the water has desorbed from the surface. Raising the temperature further to 350 K leads to disappearance of carbon monoxide on the surface, which can be seen by the decrease of both the  $\text{Fe}(\text{CO})^+$  intensity as well as the  $\text{Fe}^+$  signal. Carbon monoxide is known to increase the SIMS signal when adsorbed on metals [17,18], because of the increase of the work function releasing more positive secondary ions [19]. No obvious increase in the  $\text{FeC}^+$  and  $\text{FeO}^+$  secondary ion clusters is observed. Disappearance of CO at 350 K, therefore, seems to be mainly caused by desorption of CO. At a temperature of 650 K, no more CO is present on the surface, while atomic carbon and oxygen can still be seen. This indicates that part of the adsorbed CO has dissociated, but at which temperature remains unknown. Temperatures of 850 K and above also show no more atomic carbon and oxygen, in line with the recombination temperature of 775 K observed with TPD.

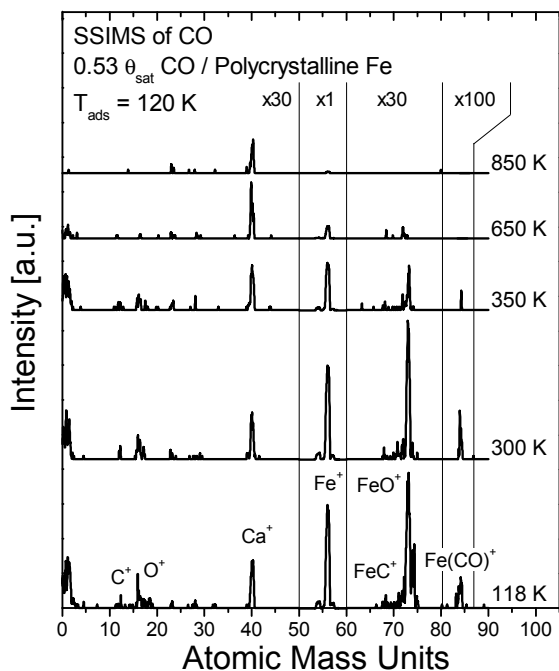


**Figure 5.4** SSIMS spectra of the polycrystalline iron surface after an exposure of 0.53 saturation dosage of CO at 120 K and subsequently heating to the indicated temperature. Spectra were taken with a defocused 3 keV  $\text{Ar}^+$  primary ion beam with a current density of  $12.7 \text{ nA/cm}^2$ .

### 5.3.2.2 Dissociation of CO – 2. TPSSIMS; Problem of Signal Noise

Following secondary ion clusters over time while raising the temperature is called temperature programmed static SIMS (TPSSIMS), which has proven itself before in the kinetics study of NO dissociation on rhodium [13,14]. To be able to determine the dissociation kinetics, SIMS is quantified in terms of adsorbate coverage on a semi-quantitative basis by normalizing the secondary ion clusters with respect to the  $\text{Fe}^+$  signal, more commonly referred to as intensity ratios [20-24]. Because of the difficulty to measure the  $\text{FeC}^+$ ,  $\text{FeO}^+$ , and  $\text{Fe}(\text{CO})^+$  ion species with the SIMS equipment, the data is extremely noisy. See the left pictures of Figure 5.5 for the secondary ion species  $\text{FeC}^+$  and  $\text{Fe}(\text{CO})^+$  at a CO coverage of  $0.11 \theta_{\text{sat}}$ .

Dividing these secondary ion clusters by the  $\text{Fe}^+$  signal (the right hand side of Figure 5.5) in particular leads to blowing up the noise level at temperatures higher than 300-350 K at which the iron signal intensity drops due to –depending on coverage– dissociation or both dissociation and desorption of CO. At a decreasing signal intensity of  $\text{Fe}^+$  the relative noise increases, which for example at a CO coverage of  $0.11 \theta_{\text{sat}}$  increases from ca. 10 percent at 150-300 K toward 20 percent at 350-600 K and to 30 percent at 800-900 K, see Figure 5.6. Thus, this increase of relative noise in the  $\text{Fe}^+$  secondary ion signal magnifies the noise of the intensity ratios at temperatures of roughly 350 K and above.

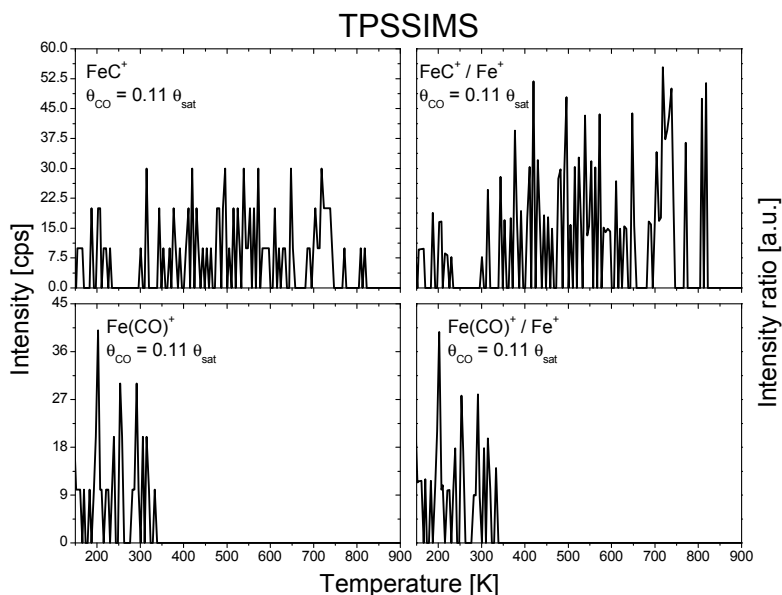


**Figure 5.5** As measured temperature programmed static secondary ion mass spectra of the species  $\text{FeC}^+$  and  $\text{Fe}(\text{CO})^+$  on the left side and both  $\text{FeC}^+$  and  $\text{Fe}(\text{CO})^+$  species divided by  $\text{Fe}^+$  on the right side at a CO coverage of  $0.11 \theta_{\text{sat}}$  on the poly crystalline Fe surface. Heating rate was 2 K/s.

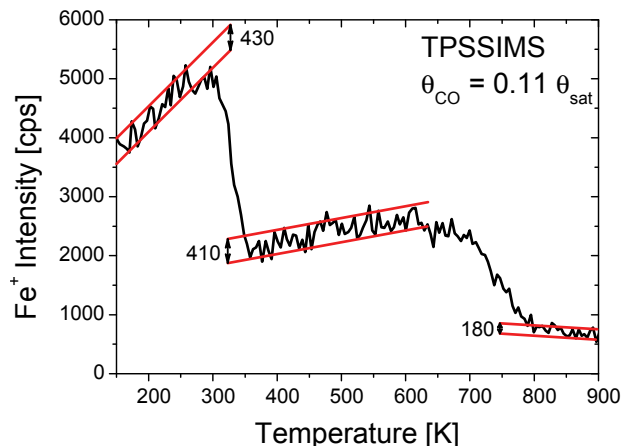


**Figure 5.6** Differences in ion intensity noise of the species  $\text{Fe}^+$  during a temperature programmed static SIMS experiment at 0.11 of the CO saturation coverage on polycrystalline iron. Heating rate was 2 K/s.

### 5.3.2.3 Dissociation of CO – 3. TPSSIMS; Smoothing of Noise

To filter out most of the noise in the signal of the secondary ions  $\text{FeC}^+$ ,  $\text{FeO}^+$ , and  $\text{Fe}(\text{CO})^+$  smoothing filters can be used. In Figure 5.7 two different smoothing methods have been applied to the raw data, i.e., the adjacent averaging (AA) technique and the fast Fourier transform (FFT) low-pass filter. One can see that the smoother curves can be obtained by applying an FFT smoothing; however, from such curves it is almost impossible to see that the raw data is very noisy. Thus, applying the adjacent averaging smoothing method is the preferred choice. Because 7 points smoothing produces a visually better curve than 5 points smoothing does, the adjacent averaging with 7 points smoothing is used throughout the rest of this Chapter, when intensity ratios are used.

### 5.3.2.4 Dissociation of CO – 4. TPSSIMS; The Results

The results of the SSIMS spectra of the  $\text{FeC}^+$ ,  $\text{FeO}^+$ , and  $\text{Fe}(\text{CO})^+$  ion species divided by the  $\text{Fe}^+$  signal are displayed in Figure 5.8. As already mentioned the obtained data is very noisy, especially for the  $\text{FeC}^+$  and  $\text{FeO}^+$  intensity ratios, making the data very difficult to interpret.

Starting at zero carbon monoxide coverage, a small amount of residual oxygen is present on the surface, whereas no carbon and carbon monoxide is observed. At a very low CO coverage (below  $0.18 \theta_{\text{sat}}$ ) no CO is desorbed at low temperatures (390 K) as observed by TPD (Figure 5.1). Hence, the disappearance of CO on the surface at these coverages can only be ascribed to dissociation of CO. At  $0.05 \theta_{\text{sat}}$  CO coverage it takes

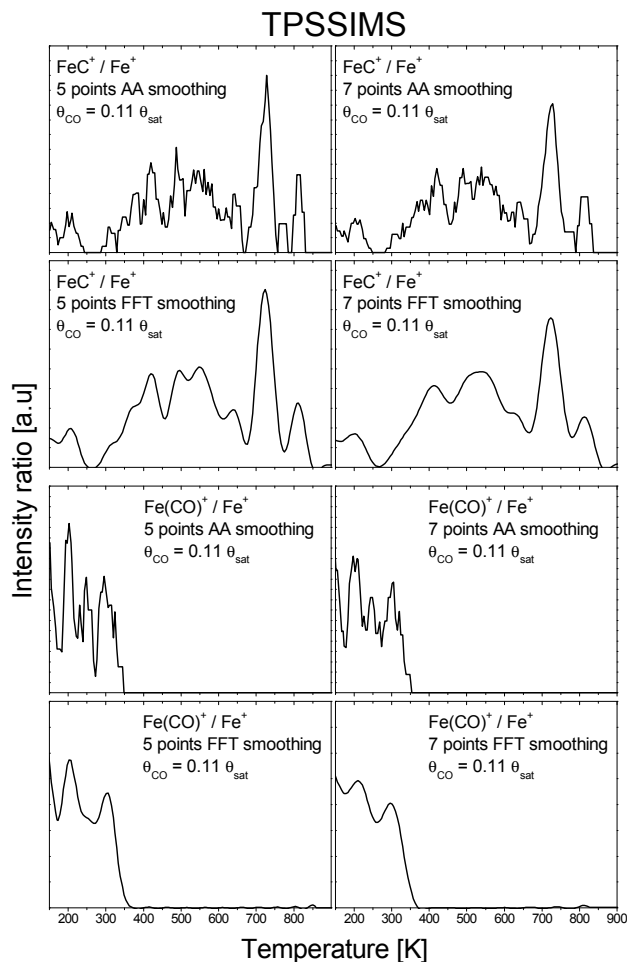


**Figure 5.7** Smoothed data of the  $\text{FeC}^+ / \text{Fe}^+$  and  $\text{Fe}(\text{CO})^+ / \text{Fe}^+$  TPSSIMS intensity ratios at a CO surface coverage of  $0.11 \theta_{\text{sat}}$  using either adjacent averaging (AA) or a fast Fourier transform (FFT) low pass filter as smoothing method. The left panes show the 5 points smoothed curves, while the right panes display the results of the 7 points smoothing.

up to ca. 310 K to completely dissociate all carbon monoxide, while roughly 375 K is needed at a CO coverage of  $0.18 \theta_{\text{sat}}$ . Determining the onset of CO dissociation is rather complicated due to the noisiness of the  $\text{Fe}(\text{CO})^+ / \text{Fe}^+$  data at these low coverages. However, the iron-carbon and iron-oxygen ion intensity ratios start to increase at around 300 K –in accordance with dissociation of CO–, which basically is the onset temperature of CO dissociation. Above temperatures of 750 K a decrease of the  $\text{FeC}^+ / \text{Fe}^+$  signal can be observed, which is consistent with desorption of carbon monoxide monitored by TPD. The iron-oxygen ion intensity ratio also seems to change



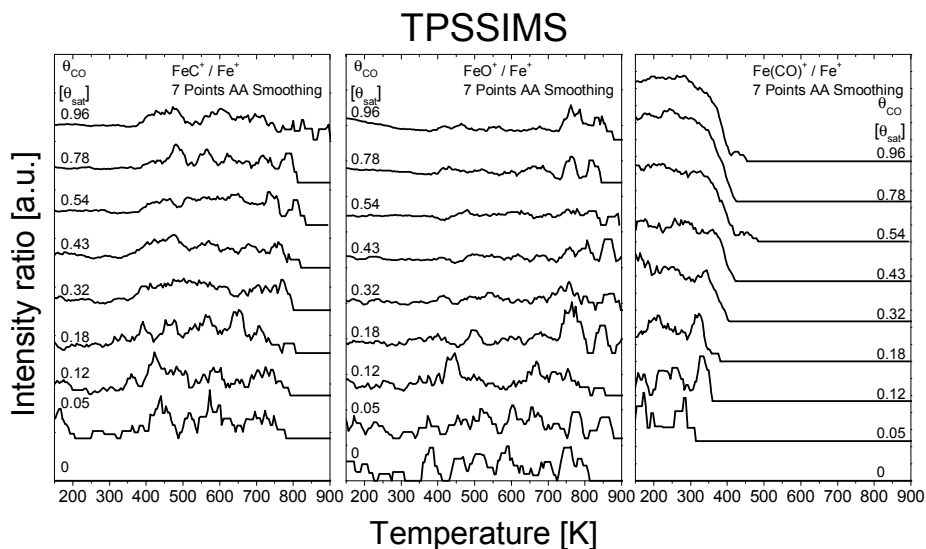


**Figure 5.8** TPSSIMS spectra of the  $\text{FeC}^+$  (left window),  $\text{FeO}^+$  (middle window), and  $\text{Fe(CO)}^+$  (right window) divided by  $\text{Fe}^+$  at different CO coverages on polycrystalline iron. A 7 points adjacent averaging smoothing is applied to the raw data. Heating rate was 2 K/s.

at temperatures above 750 K, however, a clear decrease in intensity ratio is not observed. This might be caused by the residual oxygen. Increasing the CO coverage above  $0.18 \theta_{\text{sat}}$ , one can see that there is a sudden drop in iron-CO ion intensity ratio at a temperature of roughly 375 K, which is independent of the coverage up to saturation. At around 450 K no more CO is visible on the surface. Because both the onset temperature as well as the temperature at which all CO is removed from the surface—either by dissociation or desorption—stay constant, at coverages above  $0.18 \theta_{\text{sat}}$  the process is dominated by the molecular desorption of CO at 390 K. This can be confirmed by the  $\text{FeC}^+$  and  $\text{FeO}^+$  intensity ratios (although it is almost impossible to see for the latter), which also start to increase at a temperature of 375 K at coverages higher than  $0.18 \theta_{\text{sat}}$  and are independent of the coverage up to saturation as well. Hence, at CO coverages higher than at least  $0.18 \theta_{\text{sat}}$  desorption of CO needs to occur first before dissociation can take place. In conclusion, the noisy SSIMS data allow for a qualitative view of the dissociation of carbon monoxide, but are inadequate for the determination of its kinetics.

### 5.3.3 Preparation of an Atomic Carbon Overlayer

Atomic carbon was deposited onto the poly crystalline iron surface by adding ethylene at a temperature of roughly 140 K and a pressure of  $10^{-8}$  mbar and subsequently heating

to 750 K. During heating the ethylene breaks up releasing H<sub>2</sub>, see Figure 5.9. Increasing the amount of ethylene on the surface leads to earlier dissociation of ethylene, which can be seen by the decrease in onset temperature of H<sub>2</sub> release from the iron surface. Three different amounts of ethylene were dosed onto the surface to create several carbon overlayers; 0.25, 0.5, and 1.0 Langmuir. Because quantification of carbon on the surface was not possible, as we did not determine the saturation coverage of carbon, reported carbon coverages are based on the equivalent dosage of ethylene in Langmuir; in other words, a carbon coverage of 0.25 L eq. C is a carbon layer created by exposing the foil to 0.25 L of ethylene at 140 K and subsequently heating to 750 K.

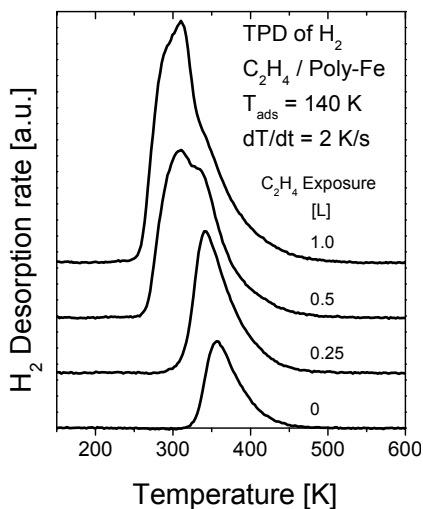


**Figure 5.9** TPD spectrum of H<sub>2</sub> after various dosages of ethylene to the clean poly crystalline iron surface at a temperature of 140 K. Heating rate was 2 K/s.

### 5.3.4 CO Desorption from a Poly Crystalline Iron Surface with a Carbon Overlayer

After preparation of the carbon overlayer on the iron surface, three different amounts of carbon monoxide were dosed onto the surface at a pressure of 10<sup>-8</sup> mbar and a temperature below 110 K. The results for these different amounts of carbon monoxide with varying carbon overlayers are presented in the top row of Figure 5.10.

At the relatively low amount of carbon monoxide on the surface (0.18  $\theta_{\text{sat}}$ ) all CO initially (without carbon on the surface) dissociates –desorption at 775 K only–. At 0.48 Langmuir of pre-adsorbed ethylene (0.48 L equivalent carbon) the appearance of molecular desorption of CO at 375 K is observed; the extra carbon leads to space restrictions, which limits the amount of CO able to dissociate, and moreover, results in a

lower desorption temperature of CO of 15 K. Space becomes more scarce at even higher loadings of pre-adsorbed carbon, thus decreasing the amount of CO dissociating further. Furthermore, a small shift in the desorption temperature maxima of both desorption traces occurs.

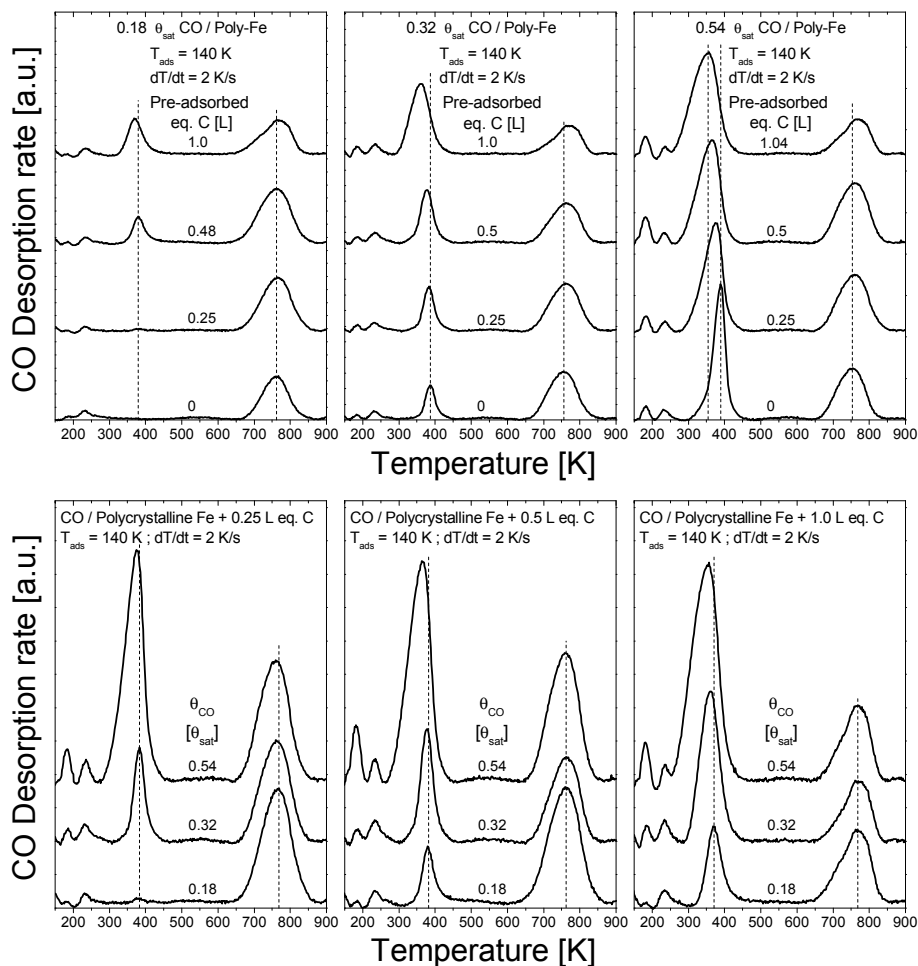


**Figure 5.10** TPD spectra of CO on polycrystalline iron that is pre-dosed with varying amounts of atomic carbon—produced by dissociation of ethylene—at a heating rate of 2 K/s. The amounts of carbon are presented as an equivalent of dosed ethylene in Langmuir. Thus, a carbon content of 0.25 L eq. C is prepared by dosage of 0.25 L ethylene at 140 K and subsequently heating to 750 K. For the top pictures; on the left a low, in the middle a medium, and on the right a high loading of CO was dosed. For the bottom pictures; the left image shows a low, the middle a medium, and the right a high loading of carbon.

At a medium CO coverage ( $0.32 \theta_{\text{sat}}$ ), CO partly dissociates and partly desorbs molecularly, with a larger amount of CO dissociating than desorbing, when no carbon overlayer is present. By adding carbon onto the surface this switches to a larger part of CO desorbing than dissociating at the point where 1.0 Langmuir of equivalent carbon is pre-dosed to the iron surface. Additional to this switch, the desorption temperature of molecular desorbed CO at 390 K decreases by roughly 30 K, while the high-temperature trace increases slightly.

At the highest amount of CO on the surface ( $0.52 \theta_{\text{sat}}$ ) most of the adsorbed CO desorbs molecularly at 390 K. Increasing the content of pre-adsorbed carbon results in growing in of a shoulder at around 310 K. Overall this leads to broadening of the molecular desorption peak of CO, ascribed to the influence of atomic carbon. Furthermore, the temperatures of the peak maxima of desorption of molecular and recombination CO are similarly influenced as the medium CO coverage.

The bottom row of Figure 5.10 displays different amounts of carbon monoxide on iron surfaces with a low, medium, and high amount of carbon in the pre-adsorbed overlayer. Regardless of the amount of carbon in the overlayer, the temperature of the recombination peak (775 K) is not influenced when the amount of carbon monoxide increases. The temperature of the molecular desorption feature, however, decreases at an increasing CO coverage for all three different overlayers.

#### *5.3.4.1 Extent of CO Dissociation*

It is interesting that the area under the high-temperature desorption trace in the bottom row of Figure 5.10 decreases at first at an increasing CO coverage, but then increases again on all surfaces with a carbon overlayer. Therefore, as a control experiment, TPD experiments were run without dosing CO after preparation of the three different carbon overlayers. From these control measurements it became apparent that residual oxygen is present on the surface –because of desorption of CO– up to 0.2 of the saturation coverage of carbon monoxide. We believe that the residual oxygen did not come from the bulk of the metal, but is a result of oxygen in the ethylene line. Hence, adding ethylene resulted in dosing oxygen as well. Because the extra oxygen will interfere with the total amount of CO supposedly desorbing as recombination of atomic carbon and oxygen, the amount of CO from the 775 K peak is adapted to deal with this effect. In other words, when the total amount of dosed CO was lower than the measured desorbed amount of CO, the extra CO was subtracted from the recombination peak to cancel out the effect of oxygen.

In Figure 5.11 the effect of pre-dosed carbon on the dissociation of CO is displayed. It is obvious that regardless of the amount of CO adsorbed on the carbon covered iron surface, the dissociated quantity of CO remains constant. However, an increase in the pre-dosed amount of carbon leads to a gradual decrease of CO that is

able to dissociate for all three CO coverages. The amount that does not dissociate any more desorbs molecularly at 375 K instead. This indicates that carbon blocks the sites needed for the dissociation of carbon monoxide. Unfortunately, we did not adsorb saturation coverage of carbon on the poly crystalline surface to find out whether complete blockage of CO dissociation is possible. Nevertheless, partial blocking of the dissociation reaction is achievable, as the highest total amount of CO dissociating on a surface with a carbon overlayer is  $0.15 \theta_{\text{sat}}$ , which is  $0.10 \theta_{\text{sat}}$  lower than on a clean surface.

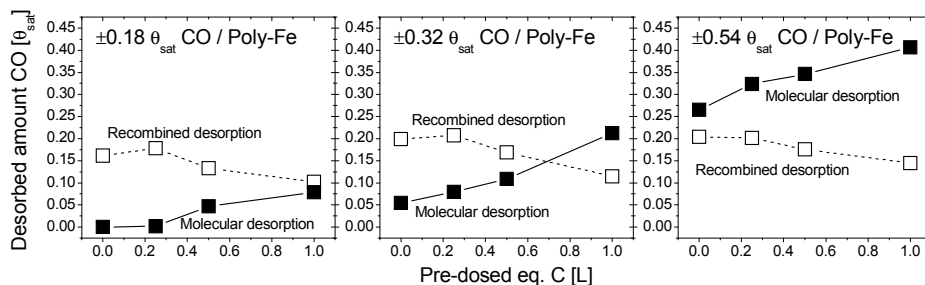


**Figure 5.11** Plots of the amount of CO desorbing from polycrystalline iron either molecularly at 375 K (filled squares) or by recombination of atomic carbon and oxygen at 775 K (open squares) as a function of the pre-dosed amount of equivalent carbon in Langmuir. The left picture displays a low, the middle a medium, and the right image a high CO coverage.

### 5.3.5 Preparation of an Atomic Oxygen Overlayer

An oxygen overlayer was created by exposing the iron surface to  $10^{-8}$  mbar of technical air at a temperature lower than 110 K. Subsequently the surface was flashed to 923 K to dissociate the oxygen. Three different amounts of technical air were dosed onto the surface to create several oxygen overlayers; 1.25, 2.5, and 5.0 Langmuir, yielding 0.25, 0.5, and 1.0 Langmuir of oxygen, respectively. Since determination of the oxygen content was not possible, reported oxygen coverages are based on  $1/5^{\text{th}}$  of the equivalent dosage of technical air in Langmuir; in other words, an oxygen coverage of 0.25 L eq. O is an oxygen layer created by exposing the foil to 1.25 L of technical air at  $<110$  K and subsequently heating to 923 K.

### 5.3.6 CO Desorption from a Poly Crystalline Iron Surface with an Oxygen Overlayer

After preparation of the oxygen overlayer on the iron surface, the iron foil was cooled down to a temperature below 110 K and consequently exposed to  $10^{-8}$  mbar of carbon

monoxide. Three CO coverages were used. Results are displayed in the top row of Figure 5.12.

At a low CO coverage and no pre-adsorbed oxygen complete dissociation occurs (desorption at 775 K). The introduction of pre-adsorbed oxygen, leads to a lower desorption temperature (740 K) of the high-temperature desorption peak. Moreover, at an exposure of 0.5 L O<sub>2</sub> some of the CO starts to desorb molecularly at 390 K, which becomes a considerable quantity at a pre-dosed amount of 1.0 L O<sub>2</sub>.

At a medium CO coverage, CO dissociates as well as molecularly desorbs. At an increasing dosage of pre-adsorbed oxygen the amount that desorbs molecularly increases with respect to the dissociated amount. At the very high amount of pre-adsorbed oxygen, the low-temperature desorption feature starts to broaden and slightly shifts to a lower temperature. A similar shift in temperature is observed for the high-temperature desorption trace.

At high CO coverage, most of the CO desorbs molecularly at 390 K, which at no pre-adsorbed oxygen is a sharp desorption peak that broadens as the amount of pre-adsorbed oxygen increases. At the highest amount of pre-exposed oxygen to the iron surface, most CO is adsorbed next to oxygen atoms, which results in the broadness of the peak as well as its shift to lower temperature. The high-temperature desorption feature behaves similarly to the lower amounts of carbon monoxide; a shift toward lower temperature at an increase of pre-adsorbed oxygen.

The bottom row of Figure 5.12 displays different amounts of carbon monoxide on iron surfaces with a low, medium, and high amount of oxygen in the pre-adsorbed overlayer. From these images it is clear that increasing the amount of CO on an oxygen overlayer (regardless of the oxygen content) leads to a new desorption feature around 40 K lower in temperature than the original low-temperature desorption trace. At a low to medium oxygen content (0.25-0.5 eq. L O) this desorption trace is visible as a shoulder growing in at the original peak, which at the high amount of oxygen becomes the main desorption peak. The temperature of the recombination desorption trace also lowers with increasing amount of CO adsorbed onto the oxygen overlayers.

#### *5.3.6.1 Extent of CO Dissociation*

To find out to what extent CO dissociates at increasing amounts of pre-adsorbed oxygen, a plot of the total amount of CO desorbed from both molecular and recombination traces as a function of the pre-dosed amount of oxygen is prepared in

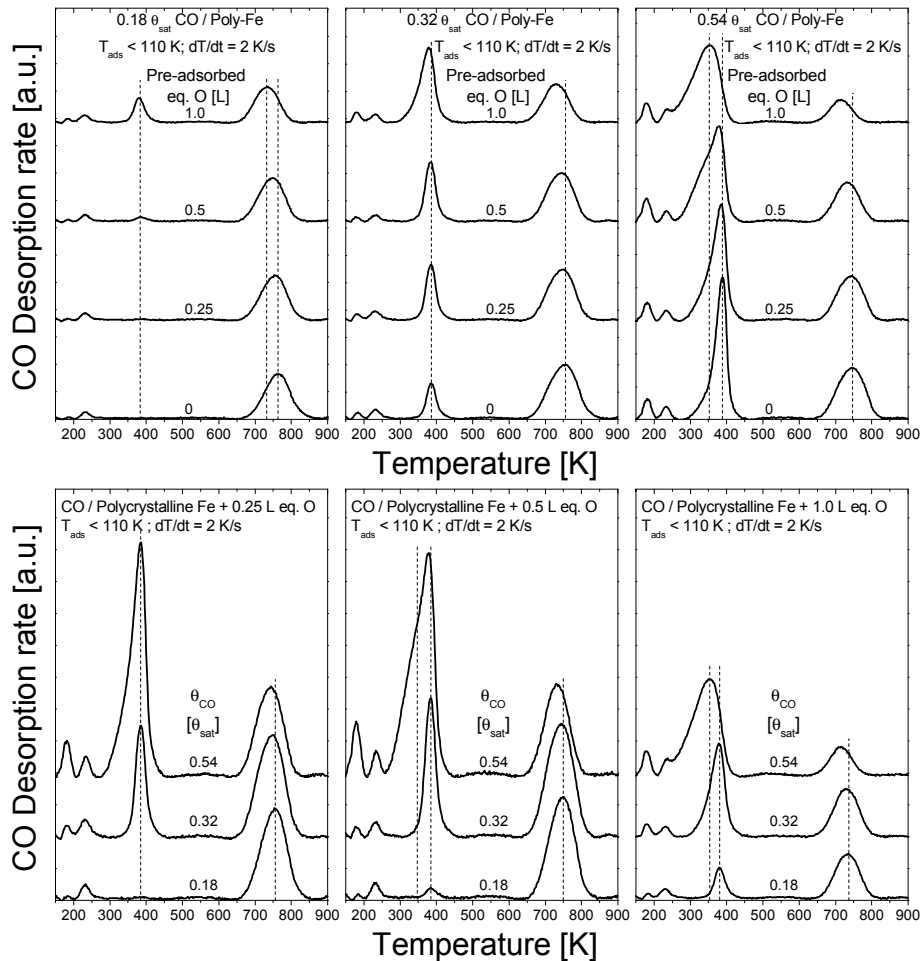


**Figure 5.12** TPD spectra of CO on poly crystalline iron that is pre-dosed with varying amounts of atomic oxygen –produced by dissociation of oxygen molecules– at a heating rate of 2 K/s. The amounts of oxygen are presented as  $1/5^{\text{th}}$  of the equivalent of exposed technical air in Langmuir. Thus an oxygen content of 0.25 L eq. O is prepared by dosage of 1.25 L technical air at  $<110$  K and subsequently heating to 923 K. The top pictures show different loadings of CO; that is, in the left picture a low, in the middle a medium, and in the right a high quantity of CO was dosed. The bottom images display different amounts of pre-adsorbed oxygen; that is, the left picture shows a low, the middle a medium, and the right a high oxygen content.

Figure 5.13. The total amount desorbing from both desorption traces adds up to the total content of CO exposed to the surface. Thus, no residual carbon is present on the surface. Irrespective of the CO content on the surface, an increase of pre-dosed atomic oxygen on the poly crystalline surface results in a decrease of dissociated CO. Since both desorption traces add up to the total amount of CO adsorbed, the amount not able to

dissociate any more desorbs molecularly at 375 K. At the highest pre-exposed oxygen surface, the maximum amount dissociating is ca. 0.15 of the saturation coverage of CO,  $0.10 \theta_{\text{sat}}$  lower than a clean surface. Therefore, atomic oxygen blocks the dissociation of carbon monoxide. As no saturation coverage of oxygen was prepared we do not know whether complete blockage of CO dissociation by oxygen is possible.

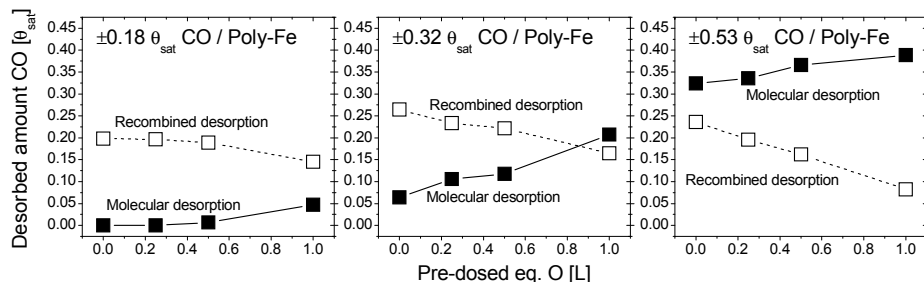


**Figure 5.13** Plots of the amount of CO desorbing from polycrystalline iron either molecularly at 375 K (filled squares) or by recombination of atomic carbon and oxygen at 775 K (open squares) as a function of the pre-dosed amount of equivalent oxygen in Langmuir. The left picture displays a low, the middle a medium, and the right a high amount of adsorbed CO.

## 5.4 Discussion

### 5.4.1 CO Desorption Kinetics

In the results section we presented the desorption kinetics of the low- (first order) and high-temperature (first and second order) desorption traces of CO on poly crystalline iron. Although the available papers in literature mention that the high-temperature desorption feature is a recombination reaction of carbon and oxygen, hence, a second order desorption process, we consider the desorption of CO at 775 K to proceed via first order kinetics rather than second order for a couple of reasons.

Before stating these reasons, we would like to mention that due to the relatively small number of papers available of CO on poly crystalline iron we additionally compared our results with literature of CO on the single crystal Fe(110). The (100) and (111) surface orientations were not compared with polycrystalline iron because of the following reasons. TPD spectra of CO on the (100) surface [25-36] do not resemble the TPD spectra of polycrystalline iron, thus, this surface is not interesting for comparison. On the basis of TPD spectra of CO, the (111) [37,38] and (110) [39,40] surfaces are almost indistinguishable from one another, and, closely resemble the TPD spectra of CO on polycrystalline iron. However, the shape of the TPD peaks resemble the (110) surface more closely than the (111) surface, and, because the (110) surface orientation is a more stable surface orientation than (111) [15], we chose to only compare the



polycrystalline results to the (110) surface. However, bare in mind that comparing our results with the Fe(110) surface still needs to be done with care (poly crystalline sample has more surface defects, rough surface, not 100% (110) structure, etc), but is a fair assumption, nonetheless.

First, the desorption energy of CO at 775 K obtained with the CAW1/2 method for first order desorption (177 kJ/mol) resembles the calculated adsorption energy of CO on Fe(110) (152-188 kJ/mol) by Jiang et al. [41] more closely than applying second order desorption kinetics (256 kJ/mol). Because DFT is known to overestimate the CO adsorption energy, Jiang et al. used a variety of exchange correlation functionals to minimize this so-called over binding effect [42]. Moreover, they included the revised form of the Perdew, Burke, and Ernzerhof exchange correlation functional [43], which is known to predict adsorption energies of CO on transition-metals fairly well.

Second, the recombination energy of CO calculated by the group of Carter [41] is substantially lower (more than 58 kJ/mol) than the desorption energy of CO. Hence, desorption of CO seems to be the limiting factor and not the recombination of atomic carbon and oxygen.

Third, the transition-state of carbon monoxide dissociation on Fe(110) was calculated in the group of Carter to be CO lying almost flat on the surface in the short-bridge site with both carbon and oxygen close to being long-bridge bonded [41]. Dissociation of this almost flat lying CO molecule on the Fe(110) surface was shown by Sorescu to proceed through a tight transition-state [44]. Therefore, a pre-exponential factor for the recombination reaction of atomic carbon and oxygen toward CO in the order of  $10^{16}$  (as calculated for 2<sup>nd</sup> order desorption) is not as likely as a pre-exponential factor of  $10^{10.7}$  calculated for 1<sup>st</sup> order desorption.

According to our results we propose that CO reacts as follows on the poly crystalline surface; CO adsorbs molecularly at low temperatures, dissociates into carbon and oxygen on the surface at ca. 300-350 K, and although able to recombine at a certain temperature CO is still adsorbed to strongly to the surface, hence, cannot desorb and immediately dissociates again. In principle this is an equilibrium situation between CO and the atomic species that is completely shifted to the dissociated state. When reaching a temperature that is sufficient to overcome the activation energy of desorption of CO, the little amount of CO that is formed immediately desorbs. This is a quasi first order reaction, where the kinetics is determined by desorption of CO and not by recombination of carbon and oxygen.

### 5.4.2 CO Dissociation Kinetics

Obtaining the kinetics of the dissociation reaction of CO on Fe(100) could not be achieved by using the secondary ion species  $\text{Fe}(\text{CO})^+$ ,  $\text{FeC}^+$ , and  $\text{FeO}^+$  because of the large noise levels. However, the signal that is most easy to detect –thus has the least

noise– is the  $Fe^+$  signal. Between the  $Fe^+$  signal and the work function of the metal a direct relation exists that can be elucidated by the following equations:

$$I_S(Fe^+) = I_p Y_{Fe} R^+ \theta_{Fe} T, \quad (\text{eq. 5.4.2.1})$$

in which  $I_S(Fe^+)$  is the intensity of the  $Fe^+$  secondary ions and  $R^+$  the ionization probability of the iron metal. The ionization probability can be expressed by:

$$R^+ \propto e^{const((\varphi-I)/v)}, \quad [\text{45}] \quad (\text{eq. 5.4.2.2})$$

from which  $\varphi$  is the work function of the iron metal. Because of this direct relation between the work function of iron and the  $Fe^+$  signal intensity, the  $Fe^+$  signal needs to change when an event takes place on the surface, such as dissociation or desorption of carbon monoxide. In other words, the  $Fe^+$  ion intensity can provide kinetic information of a particular reaction as long as the intensity of the signal is a depiction of the carbon monoxide coverage. Moreover, to obtain kinetic results of a certain reaction one needs to be sure that no other reactions occur simultaneously.

Thus, in Figure 5.14 the relative CO coverage is plotted against the averaged  $Fe^+$  signal at low temperature (100-200 K). As can be seen the  $Fe^+$  intensity increases with increasing CO surface coverage, due to an increase of the work function resulting in the higher release of positive secondary ions [19]. More interestingly, the  $Fe^+$  signal appears to vary linearly with respect to CO coverage with a certain slope until ca. 0.42-0.47 of the saturation coverage. Beyond this coverage, the  $Fe^+$  signal still varies proportionally up to saturation coverage, but with a much steeper slope. Thus, quantification of the  $Fe^+$  ion intensity is possible up to saturation coverage. This same linear behavior has also been observed by Hopstaken et al. for the ratio of  $Rh_2(NO)^+ / Rh_2^+$  on a rhodium (100) single crystal, although in their case at coverages above 0.5 ML the ratio became constant and did not reflect the actual coverage anymore [46].

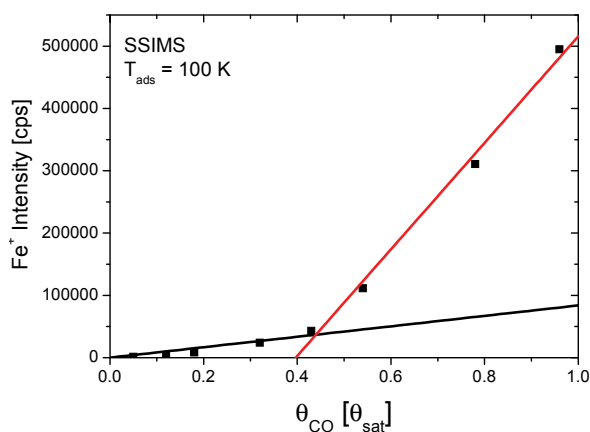


**Figure 5.14** The relative CO coverage on polycrystalline iron plotted against the  $Fe^+$  SSIMS ion intensity signal.

In Figure 5.15 (both left and right picture) the coverage of CO is shown as derived from the corresponding SSIMS  $Fe^+$  ion intensity as a function of temperature with a heating rate of 2 K/s for the three CO coverages at which the only surface reaction taking place is the dissociation of carbon monoxide. Hence, any change in  $Fe^+$  signal during this temperature regime can only be attributed to this process.

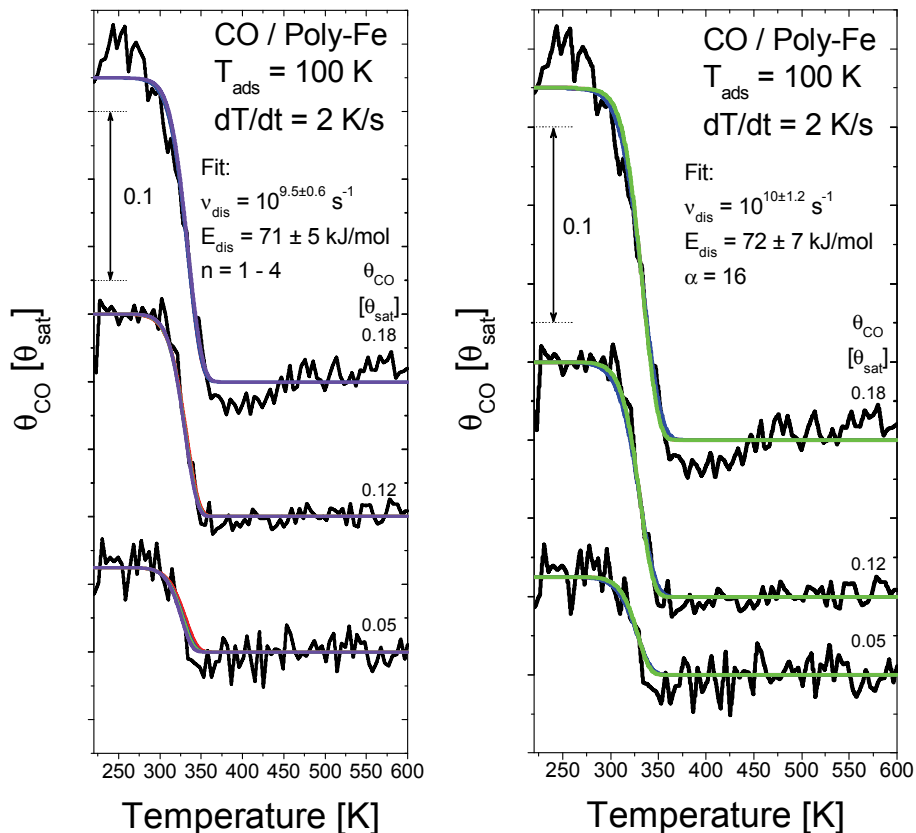


**Figure 5.15** TPSSIMS spectra of the  $Fe^+$  ion intensity converted into the CO coverage for various CO coverages (noisy data) on poly crystalline iron. Heating rate was 2 K/s. The smooth curves are the fits of the models of (left) equation 5.4.2.3 and (right) equation 5.4.2.3 and 5.4.2.4 combined.

To derive the kinetic parameters from this plot the following semi-quantitative description based on earlier studies of NO dissociation on rhodium [13,14] was used as model:

$$r_{dis} = -\frac{d(\theta_{CO} / \theta_{sat})}{dT} = \frac{v_{dis} \theta_{CO}}{\beta \theta_{sat}} \left( \frac{\theta^*}{\theta_{sat}} \right)^n \exp\left(-\frac{E_{dis}}{RT}\right), \quad (\text{eq. 5.4.2.3})$$

in which  $\theta_{CO}$  and  $\theta^*$  are both relative coverages (in  $\theta_{sat}$ ) of carbon monoxide and vacant

sites, respectively,  $\theta_{sat}$  is the saturation coverage of carbon and oxygen atoms –0.5–,  $\nu_{dis}$  and  $E_{dis}$  are the pre-exponential factor and the activation energy of dissociation, respectively, and  $\beta$  is the heating rate. This model assumes that an ensemble of empty sites ( $n$ ) is needed to dissociate the carbon monoxide and that the kinetic parameters are independent of coverage.

Equation 5.4.2.3 is numerically integrated for independent values of  $E_{dis}$ ,  $\nu_{dis}$ , and  $n$  to obtain the best fit for the measured CO coverage. The best fit is obtained with an  $n$  value of 2.79. Because  $n$  is the ensemble of empty sites needed for the dissociation, this needs to be an integer number. Thus, whole numbers were taken for  $n$ , in which  $n = 1, 2, 3$ , and 4 empty sites fall within 5% error of the optimal fit ( $n = 2.79$ ). Interestingly, this simple model (which does not include coverage effects) seems to fit the data quite satisfactory (left picture of Figure 5.15). The following kinetic parameters were derived from the fits;  $E_{dis} = 66$  kJ/mol and  $\nu_{dis} = 10^{8.9}$  s<sup>-1</sup> for  $n = 1$ ,  $E_{dis} = 69$  kJ/mol and  $\nu_{dis} = 10^{9.2}$  s<sup>-1</sup> for  $n = 2$ ,  $E_{dis} = 72$  kJ/mol and  $\nu_{dis} = 10^{9.6}$  s<sup>-1</sup> for  $n = 3$ , and  $E_{dis} = 76$  kJ/mol and  $\nu_{dis} = 10^{10.1}$  s<sup>-1</sup> for  $n = 4$ . Out of  $n = 1, 2, 3$ , and 4, an ensemble of three free sites results in the lowest absolute value for the root mean square (RMS) error, which is  $4.2 \cdot 10^{-9}$ ,  $9.5 \cdot 10^{-9}$ , and  $1.4 \cdot 10^{-8}$  for 0.05, 0.12, and 0.18  $\theta_{sat}$ , respectively. Because around 25% of the amount of CO is able to dissociate on the surface, the most plausible ensemble needed for dissociation would be three to four sites.

A second model that was used in our group by Hopstaken [46] takes the effect of lateral interactions into account and is described in an empirical way by assuming the following relation between the activation energy of dissociation and the total adsorbate coverage:

$$E_{dis}(\theta_{tot}) = E_{dis,0} + \alpha \cdot \theta_{tot}^m \cdot \bar{E}, \quad (\text{eq. 5.4.2.4})$$

in which the  $E_{dis}(\theta_{tot})$  is the activation barrier of dissociation of CO as a function of the total coverage,  $E_{dis,0}$  is the activation barrier at zero coverage,  $\alpha$  is a constant (which physical interpretation of the number is not possible),  $\theta_{tot}$  is the total adsorbate coverage  $\theta_{CO} + \theta_C + \theta_O$ , and  $\bar{E}$  is 1 kJ/mol.  $m$  is an integer, which above unity provides an artificial approach to stress that the effect of lateral interactions becomes particularly apparent at higher total coverages. Equation 5.4.2.3 and 5.4.2.4 were combined and numerically solved for independent values of  $E_{dis,0}$ ,  $\nu_{dis}$ , and  $\alpha$  to obtain the best fit over the measured temperature range for the different coverages. In order to dissociate CO one vacancy ( $n = 1$ ) was assumed to be required. In the right hand side of Figure 5.15 the fits for this model are shown from which the following kinetic parameters were obtained:  $E_{dis,0} = 72 \pm 7$  kJ/mol,  $\nu_{dis} = 10^{10 \pm 1.2}$  s<sup>-1</sup>, and  $\alpha = 16$ . The maximum absolute RMS error in the calculation for the best fit is  $4.2 \cdot 10^{-9}$ ,  $9.6 \cdot 10^{-9}$ , and  $1.4 \cdot 10^{-8}$  for 0.05, 0.12, and 0.18  $\theta_{sat}$ , respectively. It is obvious that both models result in similar fits and yield comparable kinetic parameters. This is not completely surprising as the coverages

of CO were kept very low, and, hence, lateral interactions are not extremely important. However, the model with the lateral interactions incorporated results in a slightly higher pre-exponential factor than the model without these interactions.

The only kinetic parameters determined experimentally for CO dissociation on iron to the best of our knowledge found in literature were measured by Whitman et al. [38] using the heating rate variation method for the Fe(111) surface orientation, and obtained a  $E_{dis}$  of  $84 \pm 21$  kJ/mol and  $\nu_{dis}$  of  $10^{11 \pm 2}$  s<sup>-1</sup>. In addition, activation energies of CO dissociation were calculated for Fe(110), Fe(100), Fe(111), and stepped surfaces of iron, by several groups [41,44,47,48]. The activation energies of dissociation of CO that were obtained were 147, 110, 102, and 70 and 64 kJ/mol for the Fe(110) [41], Fe(100) [47,48], Fe(111) [44], and Fe(310) and Fe(710) surfaces [44], respectively.

As one would expect that a poly crystalline sample has the most Fe(110) facets because this is the most stable surface orientation, the activation energy obtained is only half of that reported in literature. However, using an activation energy of 147 kJ/mol for fitting the data, leads to a much worse fit and results in a pre-exponential factor of  $10^{22.6}$ , which is much too high according to transition-state theory [49,50]. Of course, it is well possible that what we measure is the dissociation kinetics of CO on defects, particularly because we use SSIMS, which will create defects (the activation energy of dissociation of CO on stepped surfaces is close to our experimentally obtained value).

For the (100) orientation of iron, desorption of CO at 440 K was suggested to be stimulated by dissociation of CO by the group of Dwyer [36]. Because desorption of CO on poly crystalline iron occurs at a similar temperature (390 K) as on Fe(100), we investigated whether indeed, desorption is stimulated by CO dissociation.

When CO dissociates the  $\text{FeC}^+ / \text{Fe}^+$  and  $\text{FeO}^+ / \text{Fe}^+$  intensity ratios measured with SSIMS increase, which at low coverages occurs between temperatures of 300 to 350 K (see Figure 5.8). As soon as CO desorbs molecularly at 390 K, that is, coverages higher than  $0.18 \theta_{\text{sat}}$ , both  $\text{FeC}^+ / \text{Fe}^+$  and  $\text{FeO}^+ / \text{Fe}^+$  intensity ratios increase at temperatures of around 350-380 K; hence, dissociation is retarded by more than 50 K. The onset of CO desorption, on the other hand, is 350 K at  $0.18 \theta_{\text{sat}}$  (similar to the dissociation temperature), but decreases as the CO coverage is increased (see Figure 5.1). Because the onset of CO desorption lowers and the dissociation temperature of CO stays more or less constant, the process is not dissociation, but desorption driven, instead. Thus, dissociation can only take place when sufficient space has been made available through desorption of CO.

Although desorption of CO needs to precede dissociation at coverages higher than  $0.18 \theta_{\text{sat}}$ , the dissociation reaction is the kinetically favored process, since provided ample space all CO dissociates. Moreover, the total amount of CO dissociated already reaches a constant value at an exposure of 0.3 of the saturation coverage, indicating that at coverages where both desorption and dissociation occur the dissociation process is the much faster one. In fact by using a simple empirical expression for the rate constant

(*k*) of a reaction in the Arrhenius form of:

$$k = \nu e^{-E_a/RT}, \quad (\text{eq. 5.4.2.5})$$

in which the  $\nu$  and  $E_a$  are the pre-exponential factor and activation energy of desorption or dissociation of CO, respectively, one can show that the rate constant of dissociation is ten times higher than the desorption constant at a temperature of 390 K.

Lastly, a quarter of the CO saturation coverage is able to dissociate. On the Fe(110) surface saturation of CO produced an ordered  $c(2 \times 2)$  structure [51,52], analogous to a coverage of 0.5 ML. Gonzalez et al. [39] reported that on Fe(110) the maximum amount of CO able to dissociate corresponded to 1/8 of a monolayer. Assuming that our saturation coverage is equivalent to the saturation coverage of CO on Fe(110), i.e., '0.5 ML', our results show that on poly crystalline iron a maximum of '1/8 of a ML' dissociates as well. Hence, dissociation of CO on poly crystalline iron closely resembles the dissociation of CO on Fe(110). However, dissociation starts 80 K lower in temperature on the poly crystalline sample than on Fe(110) [39], which might be explained by more surface defects as well as defect chemistry.

### **5.4.3 Influence of Carbon and Oxygen on CO Desorption**

The atomic species carbon and oxygen have a repulsive interaction with CO, which can be seen by the decrease in temperature of the molecular desorption trace of CO. Although we cannot quantify this interaction as we do not know the exact amount of carbon and oxygen on the surface, we can calculate the activation energy of desorption when carbon or oxygen is located next to CO. Therefore, the Redhead method [53] is applied in which we use the same pre-exponential factor ( $10^{12.5}$ ) as obtained by the CAW1/2 method of the CO desorption peak at 390 K on the clean surface. The activation energy of desorption of CO thus obtained is 89 kJ/mol when either carbon or oxygen is pre-adsorbed onto the surface, and is 9 kJ/mol less than the activation energy of desorption of CO on a clean surface.

Apart from the repulsive behavior with CO, the pre-adsorption of oxygen influences the equilibrium proposed in section 5.4.1, while pre-adsorbed carbon does not. This might be explained as follows; the recombination of carbon and oxygen on the surface is attributed to the diffusion of oxygen toward carbon (shown in Chapters 3 and 4). Adding an extra amount of oxygen –as an overlayer– to the iron surface, as a result, may shift the proposed equilibrium between molecular and dissociated CO more toward the side of molecularly bound carbon monoxide (because of the higher chance of forming CO). Because carbon diffusion on the surface is not as likely as the movement of oxygen, adding extra carbon does not increase the chance of producing carbon monoxide, therefore unaffected the desorption temperature.

We believe that the marginal shift in temperature of 20-30 K when an extra

amount of oxygen is added to the surface, while no temperature shift was observed when extra carbon was introduced, is evidence that desorption of CO at a temperature of ca. 775 K is unlikely to proceed through second order desorption kinetics. When second order desorption kinetics would apply, an increase of the concentration of either atomic species on the surface would have led to a much more pronounced shift in temperature. Therefore, desorption of CO at 775 K is expected to be first order.

## 5.5 Conclusions

Dissociation of carbon monoxide on poly crystalline iron was shown in this Chapter to be the kinetically preferred reaction over desorption. However, at coverages where space becomes a limiting factor (CO adsorbs at the same adsorption sites as the dissociation products) first order desorption of CO precedes the dissociation reaction. Once enough sites have become available, dissociation of CO –being the much faster process– becomes the dominant reaction, thus, the maximum amount of dissociated species on the surface possible will always be reached.

Desorption of CO at 775 K was demonstrated to be a quasi first order process in which the kinetics are determined by desorption of CO and not by recombination of atomic carbon and oxygen. Based on this result, the following model was proposed; after dissociation of CO an equilibrium between dissociated and molecular CO is present, which is completely shifted toward the dissociated state. Although at a certain temperature (lower than the 775 K desorption trace) recombination of atomic carbon and oxygen is feasible, the activation energy of desorption is still too high. As a result, CO remains dissociated onto the surface until a sufficiently high temperature is reached to overcome the activation barrier of CO desorption.

Pre-adsorption of carbon and oxygen was shown to lead to a weaker bonding of CO onto the iron surface. Moreover, extra oxygen on the surface –being the species moving to carbon to recombine– shifts the equilibrium described above to the molecular side –due to a higher chance of recombination–, therefore, slightly lowering the temperature of the high-temperature desorption trace of CO.

## References

- [1] G. Alshorachi, G. Wedler, *Appl. Surf. Sci.* **20** (1985) 279.
- [2] M. Barber, J. C. Vickerman, J. Wolstenholme, *Surf. Sci.* **68** (1977) 130.
- [3] D. J. Dwyer, J. H. Hardenbergh, *J. Catal.* **87** (1984) 66.
- [4] G. K. Hall, C. H. B. Mee, *Phys. Stat. Sol. A* **12** (1972) 509.
- [5] K. Kishi, M. W. Roberts, *J. Chem. Soc., Faraday Trans.* **71** (1975) 1715.
- [6] H. J. Krebs, H. P. Bonzel, G. Gafner, *Surf. Sci.* **88** (1979) 269.
- [7] C. N. R. Rao, P. V. Kamath, K. Prabhakaran, M. S. Hegde, *Can. J. Chem.* **63** (1985) 1780.
- [8] G. Wedler, K. G. Colb, W. Heinrich, G. McElhiney, *Appl. Surf. Sci.* **2** (1978) 85.
- [9] G. Wedler, K. G. Colb, G. McElhiney, W. Heinrich, *Appl. Surf. Sci.* **2** (1978) 30.

- [10] D. A. Wesner, F. P. Coenen, H. P. Bonzel, *Langmuir* **1** (1985) 478.
- [11] K. Y. Yu, W. E. Spicer, I. Lindau, P. Pianetta, S. F. Lin, *Surf. Sci.* **57** (1976) 157.
- [12] D. J. Dwyer, G. A. Somorjai, *J. Catal.* **52** (1978) 291.
- [13] H. J. Borg, J. F. C. J. M. Reijerse, R. A. van Santen, J. W. Niemantsverdriet, *J. Chem. Phys.* **101** (1994) 10052.
- [14] M. J. P. Hopstaken, J. W. Niemantsverdriet, *J. Phys. Chem. B* **104** (2000) 3058.
- [15] G. Grochola, P. Russo Salvy, I. Yarovsky, K. Snook Ian, *J. Chem. Phys.* **120** (2004) 3425.
- [16] C. M. Chan, R. Aris, W. H. Weinberg, *Appl. Surf. Sci.* **1** (1978) 360.
- [17] L. A. DeLouise, N. Winograd, *Surf. Sci.* **138** (1984) 417.
- [18] T. Fleisch, G. L. Ott, W. N. Delgass, N. Winograd, *Surf. Sci.* **81** (1979) 1.
- [19] J. W. Niemantsverdriet, *Spectroscopy in Catalysis*, 3rd ed., Wiley-VCH, Weinheim, 2007.
- [20] A. Benninghoven, P. Beckmann, D. Greifendorf, K. H. Müller, M. Schemmer, *Surf. Sci.* **107** (1981) 148.
- [21] H. J. Borg, J. W. Niemantsverdriet, *Catalysis: a Specialist Periodical Report*, J. J. Spivey, A. K. Agarwal (Eds.), Vol. 11, The Royal Society of Chemistry, Cambridge, 1994.
- [22] A. Brown, J. C. Vickerman, *Surf. Sci.* **117** (1982) 154.
- [23] A. Brown, J. C. Vickerman, *Surf. Sci.* **124** (1983) 267.
- [24] A. Brown, J. C. Vickerman, *Surf. Sci.* **151** (1985) 319.
- [25] J. Benziger, R. J. Madix, *Surf. Sci.* **94** (1980) 119.
- [26] M. L. Burke, R. J. Madix, *Surf. Sci.* **237** (1990) 20.
- [27] S. D. Cameron, D. J. Dwyer, *Surf. Sci.* **198** (1988) 315.
- [28] S. D. Cameron, D. J. Dwyer, *Langmuir* **4** (1988) 282.
- [29] D. J. Dwyer, B. Rausenberger, J. P. Lu, S. L. Bernasek, D. A. Fischer, S. D. Cameron, D. H. Parker, J. L. Gland, *Surf. Sci.* **224** (1989) 375.
- [30] J. P. Lu, M. R. Albert, S. L. Bernasek, *Surf. Sci.* **217** (1989) 55.
- [31] J. P. Lu, M. R. Albert, S. L. Bernasek, *J. Phys. Chem.* **94** (1990) 6028.
- [32] D. W. Moon, S. L. Bernasek, D. J. Dwyer, J. L. Gland, *J. Am. Chem. Soc.* **107** (1985) 4363.
- [33] D. W. Moon, S. L. Bernasek, J. P. Lu, J. L. Gland, D. J. Dwyer, *Surf. Sci.* **184** (1987) 90.
- [34] D. W. Moon, D. J. Dwyer, S. L. Bernasek, *Surf. Sci.* **163** (1985) 215.
- [35] M. Nassir, D. J. Dwyer, P. Kleban, *Surf. Sci.* **356** (1996) L429.
- [36] M. H. Nassir, B. Frühberger, D. J. Dwyer, *Surf. Sci.* **312** (1994) 115.
- [37] C. E. Bartosch, L. J. Whitman, W. Ho, *J. Chem. Phys.* **85** (1986) 1052.
- [38] L. J. Whitman, L. J. Richter, B. A. Gurney, J. S. Villarrubia, W. Ho, *J. Chem. Phys.* **90** (1989) 2050.
- [39] L. Gonzalez, R. Miranda, S. Ferrer, *Surf. Sci.* **119** (1982) 61.
- [40] B. Sieben, H. P. Bonzel, *Surf. Sci.* **282** (1993) 246.
- [41] D. E. Jiang, E. A. Carter, *Surf. Sci.* **570** (2004) 167.
- [42] G. Kresse, A. Gil, P. Sautet, *Phys. Rev. B* **68** (2003) 073401.
- [43] J. P. Perdew, K. Burke, M. Ernzerhof, *Phys. Rev. Lett.* **77** (1996) 3865.
- [44] D. C. Sorescu, *J. Phys. Chem. C* **112** (2008) 10472.
- [45] J. K. Nørskov, B. I. Lundqvist, *Phys. Rev. B: Condens. Matter* **19** (1979) 5661.
- [46] M. J. P. Hopstaken, *Elementary Reaction Kinetics and Lateral Interactions in the Catalytic Reaction between NO and CO on Rhodium Surfaces*, PhD Thesis, Eindhoven University of Technology, The Netherlands, 2000.
- [47] T. C. Bromfield, D. Curulla-Ferré, J. W. Niemantsverdriet, *ChemPhysChem* **6** (2005) 254.
- [48] D. C. Sorescu, D. L. Thompson, M. M. Hurley, C. F. Chabalowski, *Phys. Rev. B* **66** (2002) 035416/1.
- [49] I. Chorkendorff, J. W. Niemantsverdriet, *Concepts of Modern Catalysis and Kinetics*, Wiley-VCH, Weinheim, 2003.
- [50] V. P. Zhdanov, *Surf. Sci. Rep.* **12** (1991) 183.
- [51] W. Erley, *J. Vac. Sci. Technol.* **18** (1981) 472.
- [52] K. Yoshida, G. A. Somorjai, *Surf. Sci.* **75** (1978) 46.
- [53] P. A. Redhead, *Vacuum* **12** (1962) 203.





# 6

## **Fe(100): CO Adsorption, Desorption, and Dissociation Kinetics and the Influence of Atomic Carbon and Oxygen.**

### **Abstract**

*The adsorption, desorption, and dissociation of CO on an Fe(100) single crystal were examined under an ultra-high vacuum environment using TPD, SSIMS, and LEED. CO adsorbs molecularly at low temperatures and dissociates at 275 K with an activation energy of 63 kJ/mol and a pre-exponential factor of  $10^{10}$ . At an increasing CO coverage, dissociation of CO becomes blocked and desorption of molecular CO needs to precede dissociation to open up space. Once enough space has been made available dissociation occurs much more rapidly than desorption of CO, therefore, maximizing the amount of dissociated CO up to saturation coverage. Desorption of molecular CO at 205, 285, and 420 K proceeds through first order desorption kinetics, with activation energies of desorption of 57, 80, and 124 kJ/mol, respectively and with pre-exponential factors of roughly  $10^{14}$  for all three desorption traces. Desorption of recombined CO can be most accurately described by a quasi first order process, in which desorption of CO is the limiting factor and not recombination of atomic carbon and oxygen. Pre-adsorption of carbon leads to blockage of  $\alpha_3$ -CO desorption and CO dissociation, whereas pre-adsorption of oxygen results in lower  $\alpha_2$ -CO desorption and CO dissociation. Blockage of CO dissociation is complete for the pre-covered oxygen surface, while part of the CO remains able to dissociate on the carbon pre-exposed surface.*

## 6.1 Introduction

The adsorption of carbon monoxide on Fe(100) [1-23] and other surface orientations such as (110) [7,11,24-35] and (111) [11,35-43] has been extensively investigated by various surface science techniques and several computational methods. Dissociation of CO, however, has been examined less comprehensively [1,2,8,14,15,17,18,23]. Besides temperatures at which dissociation takes place (or is final), no actual kinetic information was provided experimentally. Hence, apart from theoretically determined activation energies of dissociation by DFT calculations [2,23], kinetics of the reaction –to the best of our knowledge– has not yet been determined experimentally. Because the dissociation reaction of CO is regarded as an important step in the Fischer-Tropsch process, obtaining its kinetic parameters experimentally provides useful information to further elucidate the FT reaction mechanism.

Since carbon monoxide will hardly ever be the only species on the surface during reaction, numerous other species have been adsorbed next to CO, such as carbon, oxygen, hydrogen, sulfur, and potassium [1,12,14,16,18,20,44-48] to investigate their influence on the adsorption and dissociation of CO. However, most of these studies are restricted to the use of saturation coverages of these species to observe their influence. Because interactions between adsorbates on the surface have a great influence on the reaction kinetics and thermodynamics, the effect of coverage cannot be neglected. Therefore, it is worthwhile to examine the influence of coverage of some of these species on the adsorption and dissociation of CO more closely.

Apart from desorption of CO on the Fe(100) surface, which is to show that our results compare well with the known literature, we mainly discuss the dissociation reaction of CO on Fe(100) in this Chapter. We will show that the kinetic parameters of the dissociation reaction can be obtained by fitting secondary ion mass spectra by a differential equation of the Arrhenius form. Furthermore, the influence of coadsorbed carbon and oxygen on the adsorption and dissociation of CO is investigated by temperature programmed desorption (TPD).

## 6.2 Experimental Methods and Details

TPD, low energy electron diffraction (LEED), and static secondary ion mass spectrometry (SSIMS) experiments were carried out in a stainless steel ultra-high vacuum (UHV) chamber with a base pressure of  $5 \cdot 10^{-11}$  mbar. The static SIMS spectra were taken by using a defocused 3 keV  $\text{Ar}^+$  primary ion beam with a current density of  $2 \text{ nA/cm}^2$  (when other current densities were used for a given spectrum, it is mentioned in the figure) at an angle of incidence of  $65^\circ$ . Secondary ions were collected under an angle of  $25^\circ$  with respect to the surface normal. These conditions were sufficient to

measure in static mode for roughly 30 minutes. A typical temperature programmed experiment lasted 7 minutes at most.

An iron single crystal of (100) orientation with a diameter of 10 mm and a thickness of 1.2 mm was mounted on a movable sample rod by two tantalum wires of 0.3 mm diameter, pressed into small grooves on the side of the crystal. This construction allows for resistive heating to 1500 K. Because of the  $\alpha$ - $\gamma$  phase transition of iron at 1183 K, the system was protected in exceeding a maximum temperature of 1100 K. The crystal could be cooled to 90 K by flowing liquid nitrogen through the manipulator. Temperatures were measured using a chromel-alumel thermocouple spot-welded to the back of the crystal.

Before the iron single crystal was placed in the UHV system, it was treated with 1 bar of flowing  $H_2$  (traces of water and oxygen were removed from the stream with mol sieves and copper, respectively) for two weeks at a temperature of 1040 K. This was sufficient to remove all the sulfur, phosphor, and most of the other impurities in the crystal. The remaining contaminants after this treatment, such as carbon, were removed by extended  $Ar^+$  bombardment until no more impurities were visible with SSIMS. Routine cleaning of the single crystal consists of 20 minutes of argon<sup>+</sup> sputtering (0.5 keV, 5  $\mu A/cm^2$ ) at 950 K. After sputtering, the crystal was kept at 950 K for a few minutes to anneal and restore its surface ordering. This treatment resulted in SSIMS spectra of the crystal showing no contamination, and produced a LEED picture with a sharp  $p(1 \times 1)$  pattern. After each experiment the above described procedure was repeated to ensure that any remaining carbon and oxygen on the surface is removed and that the crystals' ordering is restored.

Carbon monoxide (Linde AG, 99.997% pure), ethylene (Linde AG, 99.95% pure), and technical air (Linde AG, 20%  $O_2$  : 80%  $N_2$ ) were used without further purification. For most experiments the crystal was exposed to the respective gases at temperatures of 150 K and below. All temperature programmed experiments were performed at a heating rate of 2 K/s.

## **6.3 Results**

### **6.3.1 Desorption of CO from the Clean Surface**

The Fe(100) single crystal was exposed to a pressure of  $10^{-8}$  mbar of carbon monoxide for a variety of times at temperatures lower than 150 K. Consequently, the crystal was heated at 2 K/s while traces of carbon monoxide ( $m/e = 28$ ) were detected by a quadrupole mass spectrometer, resulting in the temperature programmed desorption spectra shown in Figure 6.1. The spectra on the left side are the ones as measured, while a background subtraction has been applied to the spectra on the right. Obviously, background subtraction is not straightforward and should be done with care. Because

evolving peaks are easier to see from the baseline corrected spectra, all shown spectra throughout the rest of this Chapter are baseline subtracted.

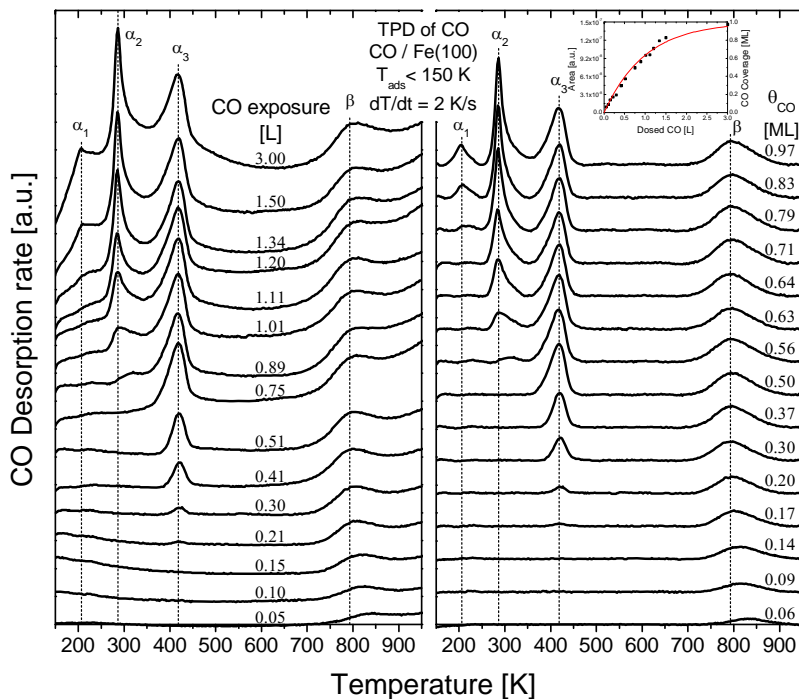


**Figure 6.1** TPD spectra of CO ( $m/e = 28$ ) obtained after exposing the clean Fe(100) surface to various doses of CO at a temperature of  $<150$  K. The heating rate was 2 K/s. The image on the left shows the as measured spectra, whereas the picture on the right displays the spectra after baseline subtraction. The inset is the uptake curve in which the area of CO underneath the TPD traces has been converted into an absolute coverage in monolayers.

Apart from CO, no other traces such as O<sub>2</sub> ( $m/e = 32$ ) and CO<sub>2</sub> ( $m/e = 44$ ) were observed. The recorded TPD spectra are in good agreement with previous reported results in literature [1,5,6,8,13,14,16-18,45-47] (small shifts of the peak temperature are due to the low heating rate). At low CO coverages only one desorption feature is visible at a temperature of ca. 835 K, which is denoted as  $\beta$ -CO desorption (recombination of carbon and oxygen atoms). Hence, complete dissociation of carbon monoxide occurs, which according to Lu et al. [8] takes place between 373 and 423 K at a coverage just before the appearance of a second desorption peak at 420 K, which is named CO( $\alpha_3$ ) desorption. This  $\alpha_3$ -CO state is the pre-cursor for CO dissociation [5,13-18,49] and has a tilted configuration with the carbon atom adsorbed at a fourfold hollow site and the oxygen bridge bonded. Consequently, tilting angles between 35° and 57° from the

surface normal were reported using X-ray photoelectron diffraction (XPD) [22] and near edge X-ray absorption fine structure (NEXAFS) [6,15]. Calculations by several groups using density functional theory (DFT) revealed tilting angles of 50-54° for CO on Fe(100) [2,19,23]. In Chapter 4 we obtained a tilting angle of 47° for CO on Fe(100) using PW-DFT calculations.

At higher coverages of CO the appearance of a third desorption state at a temperature of around 285 K is observed, which is referred to as CO( $\alpha_2$ ), and according to Moon et al. [14] can be ascribed to twofold or bridge bonded CO. At very high exposures of CO a final desorption state at 205 K is observed,  $\alpha_1$ , attributed to CO adsorbed at top sites [14]. The temperatures of all alpha peaks remain constant irrespective of the coverage of CO. The beta peak, however, shifts to a lower temperature when the CO coverage is increased, but stops shifting when the  $\alpha_3$ -CO peak appears, and henceforth remains constant.

### 6.3.1.1 Quantification of Dosed Amount CO – Ordered Structures on the Surface

The amount of adsorbed CO on the Fe(100) surface was quantified by plotting the total area underneath the desorption traces against the exposed amount of CO, depicted as the inset in Figure 6.1. When CO is added to the surface at 125 K, it orders in a  $p(1 \times 1)$  fashion at saturation coverage, shown by LEED [4,5]. Furthermore, heating the saturated surface of CO to room temperature ( $\pm 300$  K) leads to formation of an ordered  $c(2 \times 2)$  structure [4,5,21], associated with CO( $\alpha_3$ ) species. Increasing the temperature above the CO( $\alpha_3$ ) desorption temperature results in a sharpening of the  $c(2 \times 2)$  pattern and is attributed to dissociated CO [5]. The experiments described above were verified on our own Fe(100) single crystal using LEED and are shown in Figure 6.2. The same ordered structures were obtained; hence, saturation coverage of CO is chosen to be 1 ML and the areas of the TPD peaks were straightforwardly converted into the absolute coverage in monolayers (ML).

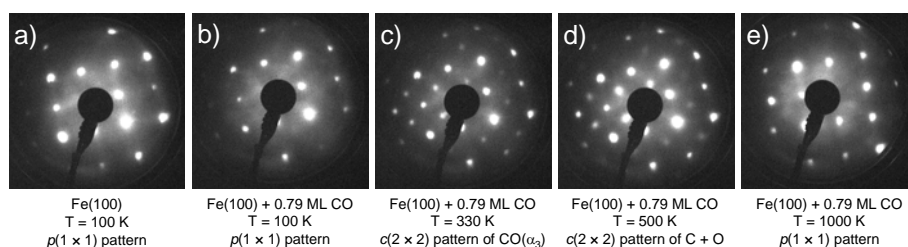


**Figure 6.2** LEED images of a) an empty Fe(100) surface at 100 K, b) Fe(100) + 0.79 ML of CO at 100 K, c) Fe(100) + 0.79 ML of CO at 330 K (pattern of CO( $\alpha_3$ )), d) Fe(100) + 0.79 ML of CO at 500 K (pattern of atomic carbon and oxygen), and e) Fe(100) + 0.79 ML of CO at 1000 K. The beam energy was 216.8 eV.

### 6.3.1.2 CO Desorption Kinetics

We employed several methods to determine the kinetic parameters of  $\beta$ -CO desorption on Fe(100). The first method that we used is the Chan-Aris-Weinberg (CAW1/2) analysis [50]. However, the obtained pre-exponential factor for the  $\beta$ -CO desorption peak was in the order of  $10^8$  and  $10^{12}$  for first and second order desorption kinetics, respectively, which is a somewhat small pre-exponential factor for carbon monoxide desorption [51]. Moreover, there is a too high uncertainty in the fitted data; differences larger than 50 percent can be obtained.

The second method that we applied is the complete analysis method proposed by King [52]. This is a method, which requires extremely good data. Because subtracting the baseline from the TPD spectra is not straightforward, it seems that our data is not good enough for this analysis. Hence, we do not obtain a linear relationship between the natural logarithm of the rate of desorption vs.  $1/\text{temperature}$ , rendering this method inapplicable.

The third and fourth method employed are the leading edge [53] and coverage corrected leading edge analysis [54]. When one plots the natural logarithm of the reaction rate constant against  $1/\text{temperature}$  there is a regime where the graph is linear. However, the exact determination of this range is not simple and, thus, leads to error margins in the results which are too large.

The fifth method is called the Redhead analysis [55], and the disadvantage of this method is that it uses first order desorption kinetics where the pre-exponential factor needs to be chosen. When one applies the Redhead formula to the  $\beta$ -CO desorption trace for pre-exponential factors between  $10^{10}$  and  $10^{16}$  the activation energy of desorption varies between 168 and 259 kJ/mol.

When we apply the CAW1/2 analysis for first order desorption kinetics on the molecular  $\alpha_3$ -CO desorption trace on Fe(100) we obtain a pre-exponential factor of  $10^{14.6 \pm 0.4}$  and an activation energy of desorption of  $124 \pm 3$  kJ/mol in the zero coverage limit. Previously reported desorption kinetics of the  $\alpha_3$ -CO trace [1,14] were guessed to be 105-110 kJ/mol, assuming a pre-exponential factor of  $10^{13}$ . However, Benziger et al. [1] mentioned that this value might be 15-20 kJ/mol too low, as the pre-exponential factor might have been assumed two to three orders too low [56]. When we use the Redhead method and take a pre-exponential factor of  $10^{13}$ , we also obtain an activation energy of desorption of 111 kJ/mol for the CO( $\alpha_3$ ) desorption feature.

For the two other molecular desorption peaks the Redhead method was applied by using pre-exponential factors of  $10^{14 \pm 1}$ , leading to activation energies of CO desorption of  $80 \pm 5$  and  $57 \pm 4$  kJ/mol for  $\alpha_2$  and  $\alpha_1$  desorption of CO, respectively, which is in good agreement with literature [1,14].

### 6.3.1.3 Extent of CO Dissociation

The amounts of desorbed carbon monoxide from the different desorption traces is plotted against the total CO coverage in Figure 6.3. All CO initially dissociates until ca. 0.15 ML of CO coverage, at which space becomes a limiting factor and CO starts to desorb molecularly at 420 K ( $\alpha_3$  peak). At an exposure of 0.5 ML of CO the  $\beta$ -CO and  $\alpha_3$ -CO desorption traces both reach a maximum amount of ca. 0.25 ML and CO starts to desorb from the  $\alpha_2$  peak. At around  $\frac{3}{4}$  of the saturation coverage, the final desorption feature CO( $\alpha_1$ ) becomes visible, which along with the CO( $\alpha_2$ ) trace increases proportionally till saturation coverage. Similar individual coverages were obtained by Nassir et al. [18]. However, filling of the states seems to occur differently, as our results show that CO desorption from the  $\alpha_2$  trace starts after maximum desorption of CO from the  $\alpha_3$  state, whereas the group of Dwyer found a concurrent increase of the  $\alpha_2$ -CO and  $\alpha_3$ -CO state [18].

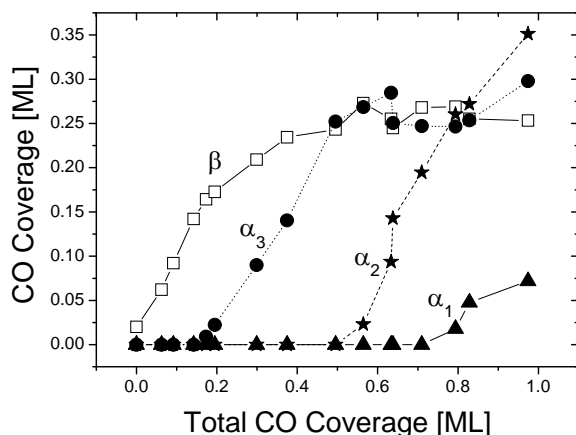


**Figure 6.3** The individual coverages of each desorption trace plotted against the total amount of adsorbed CO on Fe(100).

### 6.3.2 CO and CO Related Species Adsorbed on the Clean Surface

A typical static secondary ion mass spectrum of a saturated Fe(100) surface with CO at a temperature of 145 K is displayed in Figure 6.4. The  $\text{Fe}^+$  signal is the most intense peak of the spectrum. Other parts of the spectrum need to be blown up more than 50 times to observe the peaks related to the adsorption of carbon monoxide on the surface, i.e.,  $m/e$  of 28 and 84. Besides these peaks, masses of 12, 16, 68, and 72 atomic mass units (amu) are detected, ascribed to carbon<sup>+</sup>, oxygen<sup>+</sup>,  $\text{FeC}^+$ , and  $\text{FeO}^+$  secondary ion species, respectively. Because dissociation of CO at 145 K does not occur according to



literature [1,5,16,21,48,49], fragmentation of CO during the secondary ion emission process is responsible for these four observed species. Apart from species related to adsorbed CO, other secondary ion species such as  $\text{Li}^+$ ,  $\text{Na}^+$ ,  $\text{Al}^+$ ,  $\text{K}^+$ , and  $\text{Ca}^+$  are observed, due to their relative ease to ionize or existence as ions on the surface. In addition, a small peak attributed to copper is detected, which comes from the sample holder. Water, originating from the residual gas during cooling and CO adsorption at 145 K is observed at  $m/e = 74$  as the  $\text{Fe}(\text{H}_2\text{O})^+$  ion cluster.

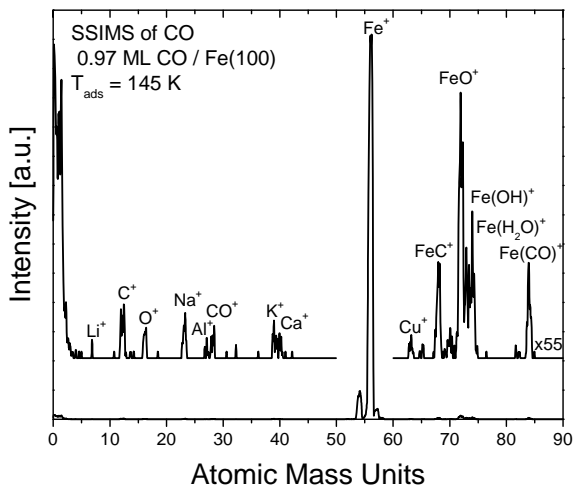


**Figure 6.4** SSIMS spectrum of the Fe(100) surface after saturation dosage of CO at 145 K. A defocused 3 keV  $\text{Ar}^+$  primary ion beam with a current density of  $6.6 \text{ nA/cm}^2$  was used for the measurement.

### 6.3.2.1 Dissociation of CO – 1. Isothermic Static SIMS

At low CO coverage, where all adsorbed CO dissociates, the  $\text{Fe}(\text{CO})^+$  ion intensity was too low to be detected by our system. Therefore, we performed isothermic measurements on a saturated surface with CO, shown in Figure 6.5. The spectrum has been multiplied by 70, apart from the region between 50 and 60 amu, to show that the  $\text{Fe}^+$  signal is much more intense than all the other signals, and moreover, to be able to make a better comparison.

Since the 145 K spectrum was discussed in the previous section, we will start by explaining the spectrum at 240 K. Because at this temperature  $\alpha_1$ -CO has desorbed from the surface, slightly lower intensities of all secondary ions are observed. Once CO( $\alpha_2$ ) desorption occurs (above 285 K), an enormous drop in signal intensity is observed, due to halving of the CO coverage, which results in a much lower release of positive secondary ions. Nonetheless, all secondary ions observed at lower temperatures remain visible up to 330 K. However, raising the temperature to 460 K leads to the loss of the

$\text{Fe}(\text{CO})^+$  secondary ion signal, while very small  $\text{FeC}^+$  and  $\text{FeO}^+$  ion intensities remain visible. Thus, part of the CO on the surface at 330 K has dissociated somewhere in between 330 and 460 K. As CO is known to increase the work function of the metal, the iron signal is very hard to detect once all molecular CO is either desorbed or dissociated. At 860 K (after  $\beta$ -CO desorption) all atomic carbon and oxygen has recombined into CO and is removed from the surface, hence, no signals related to atomic carbon and oxygen as well as molecular CO were detected.

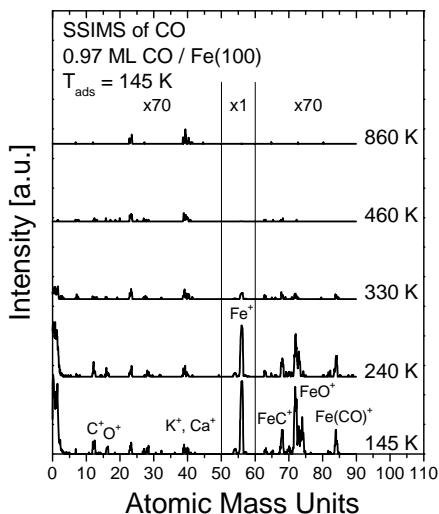


**Figure 6.5** SSIMS spectra of the *Fe(100)* surface after saturation dosage of CO at 145 K and subsequent heating to the displayed temperature. Spectra were taken with a defocused 3 keV  $\text{Ar}^+$  primary ion beam with a current density of 6.6 nA/cm<sup>2</sup>.

Because all the secondary ions and ion clusters that are related to the dissociation of carbon monoxide are already present at 145 K –where no dissociation occurs–, and no straightforward increase of these secondary ions at any of the measured temperatures could be observed, the isothermic results cannot be used to determine the temperature at which dissociation takes place. For this purpose, temperature programmed static SIMS (TPSSIMS) experiments were performed.

### 6.3.2.2 Dissociation of CO – 2. TPSSIMS

In Chapter 5 we showed that detection of the secondary ion species  $\text{FeC}^+$ ,  $\text{FeO}^+$ , and  $\text{Fe}(\text{CO})^+$  on poly crystalline iron was complicated and led to large noise levels in the data. Because an *Fe(100)* single crystal contains a lot less surface defects and the surface area is much lower (poly crystalline samples are rough, single crystals smooth) than poly crystalline iron, observation of a clear signal from these secondary ion

clusters proved to be practically impossible. Therefore, we did not look at the  $\text{FeC}^+$ ,  $\text{FeO}^+$ , and  $\text{Fe}(\text{CO})^+$  species for the temperature programmed SSIMS measurements, but focused exclusively on the  $\text{Fe}^+$  signal (in principle the work function of the metal). Since the  $\text{Fe}^+$  intensity was shown to depend linearly on the CO coverage in Chapter 5, kinetic data of the dissociation reaction of CO can be obtained.

To link the changes in  $\text{Fe}^+$  signal (or work function) to either dissociation or desorption of CO, TPD and TPSSIMS experiments were performed simultaneously, as depicted in Figure 6.6. Up to coverages of 0.14 ML, desorption of CO is only observed at 835 K. However, the  $\text{Fe}^+$  signal decreases already at a temperature of 275-300 K (difficult to see for the lowest coverage). The signal is then more or less constant between 400 and 700 K, decreases between 700 and 900 K, and finally remains constant at higher temperatures. The decrease of  $\text{Fe}^+$  signal between 700 and 900 K can be attributed to the recombination of atomic carbon and oxygen, desorbing as CO. Because no other desorption peaks were observed, the decrease in  $\text{Fe}^+$  signal between 275 and 400 K can only be ascribed to dissociation of CO. To the best of our knowledge only the group of Bernasek [8] investigated the dissociation of CO at a sufficiently low CO coverage where dissociation is the only process on the surface at low temperatures. For a CO coverage of 0.1 L (comparable to our 0.17 ML) they obtained dissociation between 373 and 423 K. Our results show dissociation between roughly 290 and 400 K.

At coverages higher than 0.17 ML CO, one cannot distinguish desorption from dissociation of CO from the decrease in the  $\text{Fe}^+$  signal, because both processes clearly take place concurrently. However, once desorption of CO at 420 K is sufficiently present (above a CO coverage of 0.20 to 0.3 ML) the decrease of the  $\text{Fe}^+$  signal is postponed by roughly 50 K. We assume that most likely space is the limiting factor for CO to dissociate at these coverages, hence, part of the CO needs to desorb first to make sufficient room for the remaining CO to dissociate.

Once the  $\text{CO}(\alpha_2)$  desorption feature is present at 285 K, the  $\text{Fe}^+$  signal starts to decrease at this temperature with a certain slope, which changes steepness when  $\text{CO}(\alpha_3)$  desorption starts to take place. For coverages higher than 0.37 ML an inset of the temperature regime 450-950 K is used to show the decrease of the  $\text{Fe}^+$  intensity when  $\beta$ -CO desorption occurs.

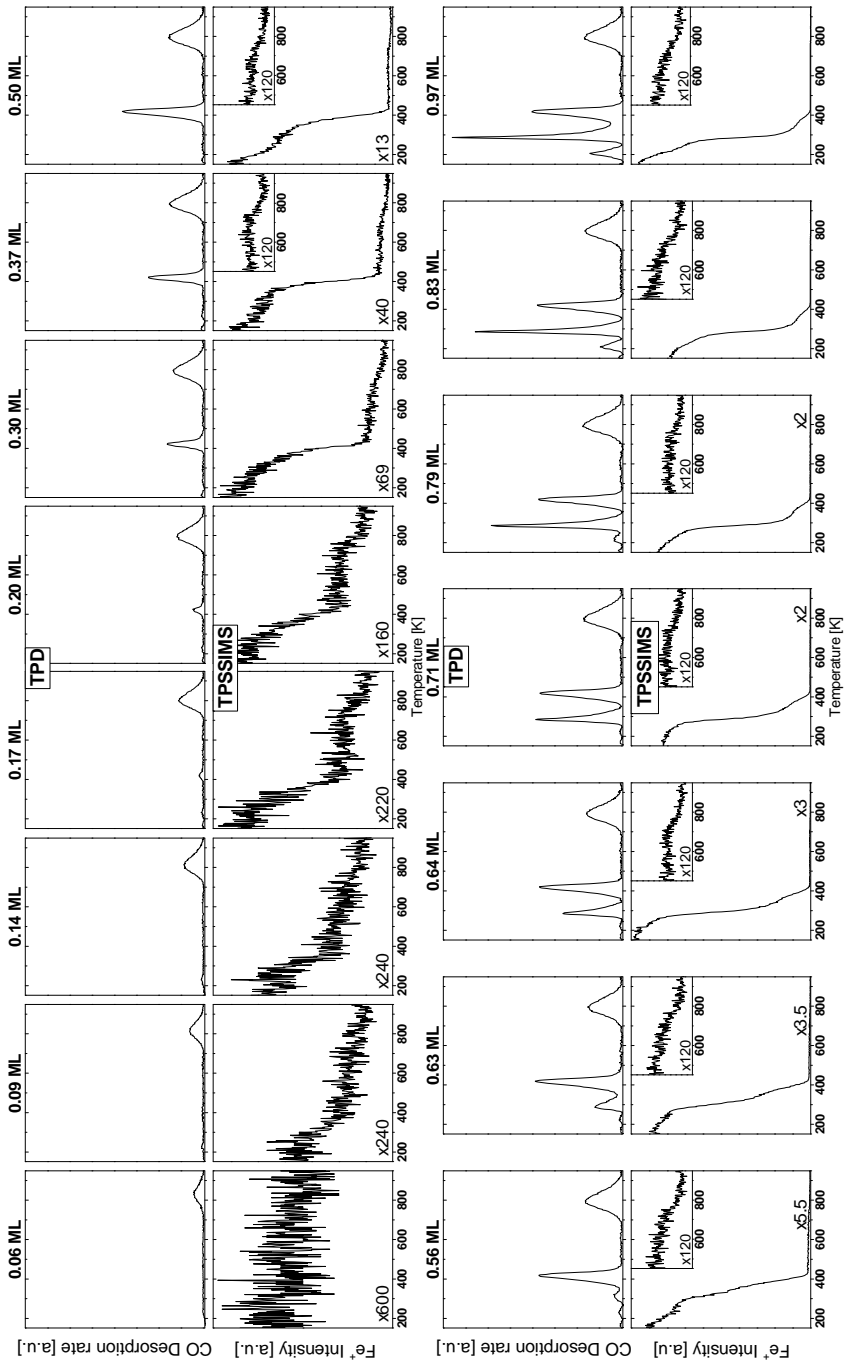


**Figure 6.6** TPD and TPSSIMS spectra of the Fe(100) surface after various dosages of CO at 145 K. Heating rate was 2 K/s.

### 6.3.3 Preparation of an Atomic Carbon Overlayer

To create a carbon overlayer on the Fe(100) surface, ethylene was exposed to the surface at a temperature of 145 K and a pressure of  $10^{-8}$  mbar and subsequently heated to 530 K. During the heating process ethylene decomposes into  $H_2$  and atomic carbon, a reaction that has been investigated in detail by Hung and Bernasek [57]. In Figure 6.7 various amounts of ethylene were exposed to the Fe(100) surface after which a TPD of  $H_2$  was recorded. The recorded desorption spectra closely resemble the measured spectra from literature [57]. At saturation coverage of ethylene and subsequent heating to 530 K, a  $c(2 \times 2)$  structure of atomic carbon was obtained with LEED (right image in Figure 6.7). This  $c(2 \times 2)$  pattern of carbon has been observed by several other groups [21,48,57-59], who concluded with additional techniques such as X-ray photoelectron spectroscopy (XPS) that the maximum amount of carbon on the surface is 0.5 ML with carbon adsorbed in the fourfold hollow sites. Accordingly, the area underneath the TPD traces was converted into the carbon coverage in monolayers. Three different carbon loadings were used as overlayers; 0.06, 0.25, and 0.5 ML carbon.

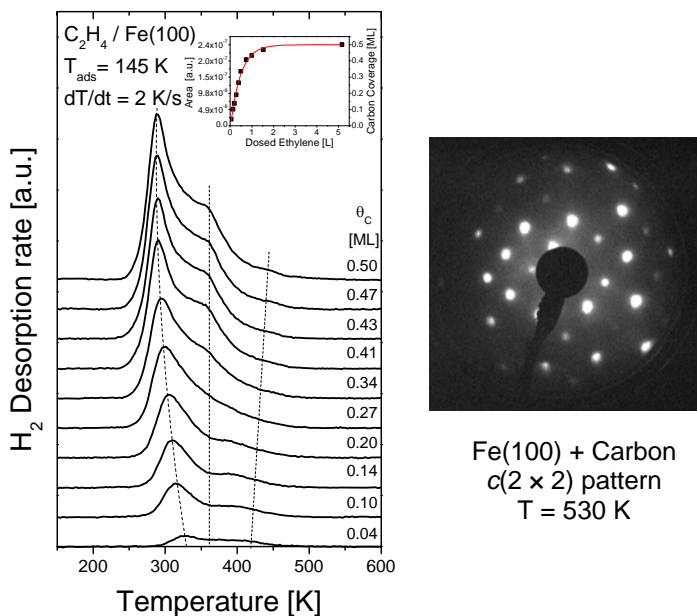


**Figure 6.7** The image on the left shows TPD spectra of  $H_2$  desorption after dosage of various amounts of ethylene on Fe(100) at 145 K. The inset shows the uptake curve in which the areas of the  $H_2$  desorption traces have been converted into the absolute carbon coverage. The right picture is a LEED image of a saturated surface of ethylene dosed at 145 K and heated subsequently to 530 K, resulting in a  $c(2 \times 2)$  ordered structure of atomic carbon.

### 6.3.4 CO Desorption from an Fe(100) Surface with a Carbon Overlayer

The effect of carbon on the desorption and dissociation of carbon monoxide was investigated by dosing various amounts of carbon monoxide at a pressure of  $10^{-8}$  mbar and a temperature of 145 K to the carbon covered Fe(100) single crystal and consequently recording a TPD spectrum at a heating rate of 2 K/s, as shown in Figure 6.8. Unfortunately, we were unable to determine the absolute coverage of CO on the surface, because of the change in sensitivity of the mass spectrometer towards CO each day. Hence, the desorbed amount of CO is normalized to different saturation coverage for each panel, and thus, not relative to saturation of CO on the clean surface.

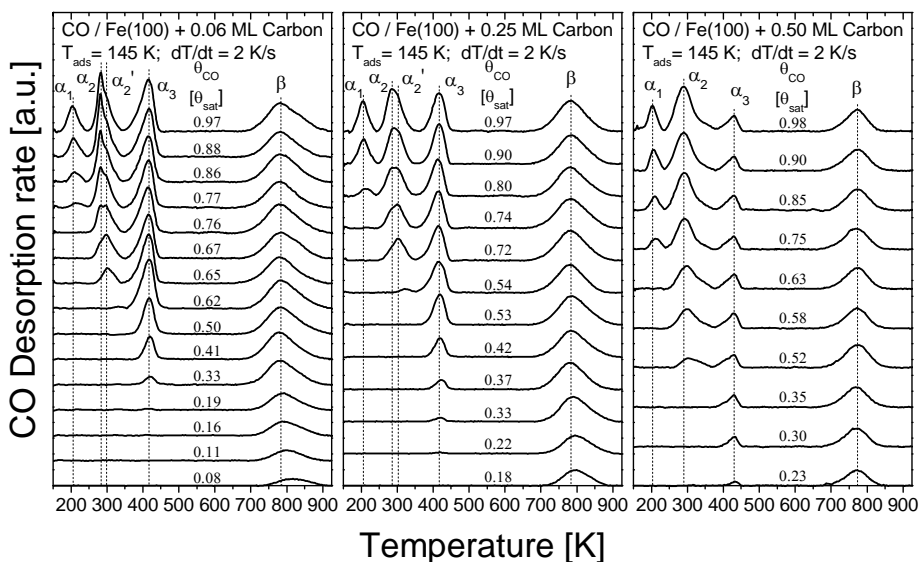


**Figure 6.8** TPD spectra of CO on Fe(100) that is pre-dosed with varying amounts of atomic carbon –produced by dissociation of ethylene– at a heating rate of 2 K/s. The left image shows a low amount, the middle a medium quantity, and the right the maximum loading of carbon.

For the overlayer with low carbon content carbon monoxide completely dissociates at low CO coverages –desorption of CO at 810 K only–. At 0.33  $\theta_{\text{sat}}$  CO coverage the CO( $\alpha_3$ ) desorption trace appears, which fills up as the coverage is further increased. At coverages of 0.62  $\theta_{\text{sat}}$  and above, a peak is observed at around 300 K. A similar peak was observed by Lu et al. [47] at 340 K, although they did not pre-dose carbon. They assigned this peak ( $\alpha_2'$ ) to CO in the bridge site with another CO molecule as next nearest neighbor in the fourfold hollow site. The  $\alpha_2$ -CO desorption peak, which they observed at 305 K, was assigned to CO in the bridge site with CO in the fourfold hollow site as nearest neighbor. Since we do not observe this peak with

only CO on the surface, it is more likely that the ( $\alpha_2'$ )-CO peak (which we observe at 300 K) can be attributed to CO in the bridge site with carbon as nearest neighbor in the fourfold hollow site. Apparently, this CO is stabilized by the carbon atoms, because the CO( $\alpha_2$ ) peak –associated with CO in bridge sites with no carbon as nearest neighbor, but more likely CO– grows in as a shoulder at 280 K, thus, the less strongly adsorbed molecule on the surface. Nevertheless, at high enough CO coverages, the CO( $\alpha_2$ ) desorption trace becomes the larger peak of the two –which is in accordance that CO desorbing as  $\alpha_2$  has CO as nearest neighbor–.

Increasing the carbon amount on the surface toward 0.25 ML still favors CO to dissociate at very low CO coverages. The difference between the lowest amount of carbon and this medium carbon content is the lower  $\alpha_2$ -CO peak, which seems to reach an equal amount as the  $\alpha_2'$ -CO desorption trace. Because 0.5 ML is the highest coverage possible for CO( $\alpha_3$ ) desorption (CO in the fourfold hollow site), half of these sites are now occupied by carbon atoms. Hence, this would explain why both CO( $\alpha_2$ ) and CO( $\alpha_2'$ ) desorption features desorb by an equal amount.

At the highest possible carbon level on Fe(100), i.e., 0.5 ML most of the fourfold hollow sites are blocked, which results in much lower sites available for  $\alpha_3$ -CO to desorb from. However, complete blockage of CO( $\alpha_3$ ) desorption and dissociation of CO by atomic carbon does not happen. Both desorption features still remain visible, although, very small. Although one would expect that a perfect 0.5 ML carbon coverage completely blocks CO dissociation, a  $c(2 \times 2)$  structure determined by LEED indicates that the coverage is 0.5 ML locally, but that the overall coverage might be lower; thus, dissociation remains possible. Moreover, both CO( $\alpha_2$ ) and CO( $\alpha_2'$ ) seem to have merged into one desorption peak at 290 K, which will mostly be bridge CO adsorbed next to fourfold hollow adsorbed carbon.

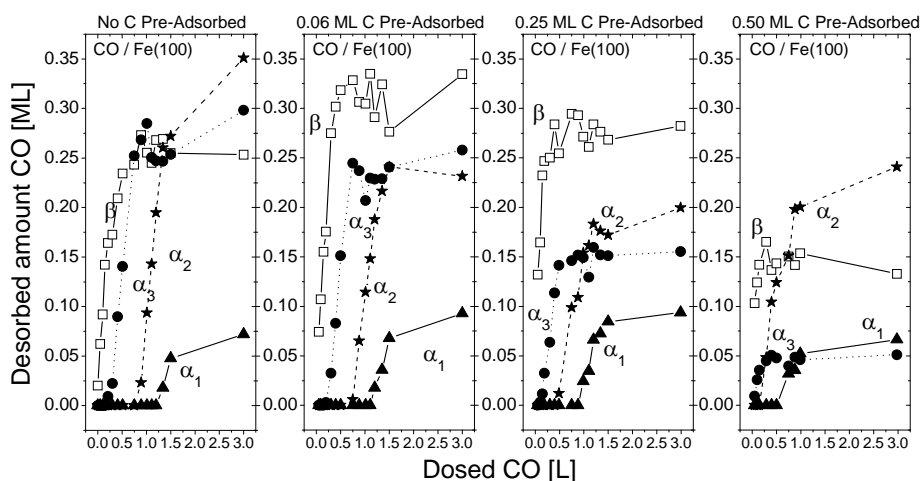
#### 6.3.4.1 Extent of CO Dissociation

Figure 6.9 shows the amounts of CO desorbing from the various desorption traces plotted against the exposed amount of CO for the carbon free and carbon pre-covered surfaces. For this figure, the assumption is made that carbon effectively blocks the adsorption of carbon monoxide, thus, the maximum amount of CO goes down by the amount of carbon adsorbed.

A small amount of pre-adsorbed carbon results in a higher fraction of dissociated CO than the carbon-free surface. Moreover, less CO exposure is needed to dissociate the same amount of CO. A similar observation is seen for the molecular desorption peaks; higher carbon contents on the iron surface decrease the CO exposure needed for the molecular desorption features to appear. As the carbon level increases, so does the amount of CO desorbing from fourfold hollow sites ( $\alpha_3$ ) decrease. At the

highest loading of carbon, that is 0.5 ML, desorption of CO from the  $\alpha_3$  state ends up as the least amount of CO desorbing from the surface, whereas CO desorbing from the  $\alpha_2$  state becomes the largest fraction.

Hence, these four images clearly demonstrate that pre-adsorption of carbon blocks the adsorption of CO in fourfold hollow sites –CO( $\alpha_3$ ) desorption–, because atomic carbon binds stronger to iron at fourfold hollow sites than CO does. The amount of CO desorbing from the  $\alpha_2$ - and  $\alpha_1$ -states more or less remains constant at increasing carbon pre-exposure, thus carbon does not block these CO states. Interesting to note is that although the amount of CO that dissociates decreases at increasing carbon coverage, CO dissociation –despite the extra amount of carbon on the surface– still remains 2-3 times more favorable than desorption does.



**Figure 6.9** Plots of the amount of CO desorbing molecularly (filled circles – $\alpha_3$ –, stars – $\alpha_2$ –, and triangles – $\alpha_1$ –) and by recombination of atomic carbon and oxygen (open squares – $\beta$ –) as a function of the dosed amount of CO. The pictures from left to right show the Fe(100) surface with increasing amounts of pre-adsorbed carbon content, starting from a carbon-free surface.

### 6.3.5 Preparation of an Atomic Oxygen Overlayer

An oxygen covered surface was created by exposing the Fe(100) single crystal to technical air (20% O<sub>2</sub> : 80% N<sub>2</sub>) at a pressure of 10<sup>-8</sup> mbar and a temperature of 145 K. At this temperature oxygen adsorbs dissociatively [60]. Subsequently the sample was heated toward 500 K to obtain a better ordering of the oxygen on the surface. The absolute coverage of oxygen on the Fe(100) could not be determined with the set-up. Therefore, results are displayed in equivalent O<sub>2</sub> in Langmuir. Three overlayers



containing different loadings of oxygen were prepared; 0.09, 0.36, and 1.0 Langmuir of equivalent  $O_2$ .

### 6.3.6 CO Desorption from an Fe(100) Surface with an Oxygen Overlayer

After oxygen exposure to the Fe(100) surface at 145 K and subsequently heating to 500 K, the oxygen covered surface was cooled down back to 145 K where CO was added at  $10^{-8}$  mbar for different amounts of time to produce a variety of CO coverages on the surface. The results for all three pre-covered oxygen surfaces are depicted in Figure 6.10. We were unable to determine the absolute coverage of CO on the surface, because of the change in sensitivity of the mass spectrometer towards CO each day. Hence, the desorbed amount of CO is normalized to different saturation coverage for each panel, and thus, not relative to saturation of CO on the clean surface.

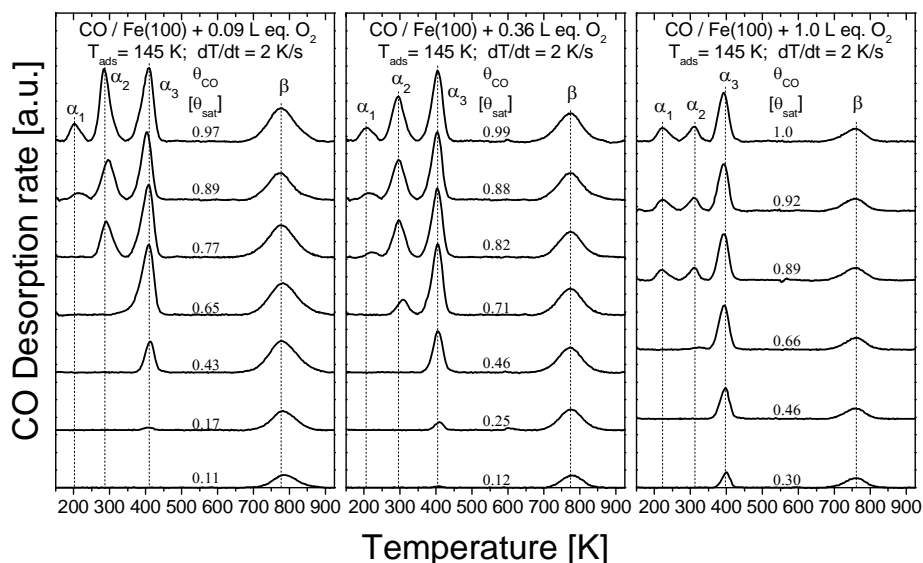


**Figure 6.10** TPD spectra of CO on Fe(100) that is pre-dosed with varying amounts of atomic oxygen –produced by dissociation of  $O_2$ – at a heating rate of 2 K/s. The left image shows low, the middle medium, and the right high loadings of oxygen in the overlayer.

From these graphs it is clear that an increase of the oxygen content on the surface leads to the decrease of CO desorbing from the  $\alpha_2$  desorption trace and a much lower extent of CO dissociation. Although the  $CO(\alpha_3)$  peak decreases as well, its decrease is much less pronounced. Hence, oxygen seems to push CO out of the bridge sites, which is an interesting observation as oxygen adsorbs preferably at fourfold

hollow sites according to numerous papers in literature [60-63]. However, as oxygen is quite mobile on the surface [64], and in addition is stable at bridge sites –though weaker than at fourfold hollow sites [2,23]–, it might be possible that CO displaces the fourfold hollow adsorbed oxygen toward bridge sites. Moreover, an increase of the atomic oxygen content on the surface leads to slightly higher desorption temperatures of the CO( $\alpha_1$ ) and CO( $\alpha_2$ ) peak, whereas to a somewhat lower temperature of the CO( $\alpha_3$ ) peak. The beta desorption feature does not seem to be affected by a change in oxygen loading. Thus, although oxygen displaces a lot of CO from the bridge sites, the CO that is still adsorbed becomes more strongly bound to the surface.

### 6.3.6.1 Extent of CO Dissociation

To find out to what extent CO dissociates while pre-adsorbed oxygen is present on the Fe(100) surface, the desorbed amount from each CO desorption trace was plotted against the exposed CO to the surface. This is shown in Figure 6.11. It should be noted here that the desorbed amount of CO is normalized to different saturation coverage for each panel, and thus, not relative to saturation of CO on the clean surface. The reason for this is that we did not measure saturation coverage of CO on the clean surface the same day the experiments were performed with the oxygen pre-covered surfaces, hence, the sensitivity of the mass spectrometer changed, making it impossible to present the results relative to the saturation coverage of CO on the clean surface. Thus, the results are presented each with a different normalization. Obviously pre-adsorption of oxygen

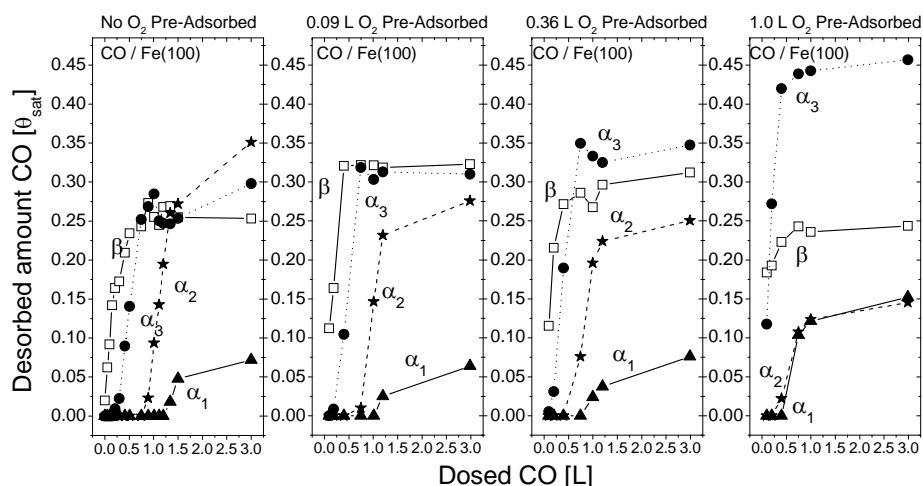


**Figure 6.11** Plots of the amount of CO desorbing molecularly (filled circles – $\alpha_3$ –, stars – $\alpha_2$ –, and triangles – $\alpha_1$ –) and by recombination of atomic carbon and oxygen (open squares – $\beta$ –) as a function of the dosed amount of CO. The pictures from left to right show the Fe(100) surface with increasing amounts of pre-adsorbed oxygen content, starting from an oxygen-free surface.

changes the fractions of the different desorption traces. In particular the  $\alpha_2$ -CO desorption peak decreases a lot when the oxygen content on the surface is increased, while the  $\alpha_3$ -CO fraction increases. Hence, oxygen influences CO in the bridge site, rather than CO fourfold hollow adsorbed. This can also be seen by the fraction of CO that dissociates, which as well becomes a little smaller. The ratio  $\text{CO}(\alpha_3)$  to  $\text{CO}(\beta)$  for the highest loading of oxygen is 2:1, which is opposite to carbon pre-adsorption. Unfortunately we did not expose the Fe(100) surface to the saturation coverage of oxygen to find out whether complete blockage of certain desorption states or dissociation was possible, since according to literature it should be possible to completely block the dissociation of CO [1].

## 6.4 Discussion

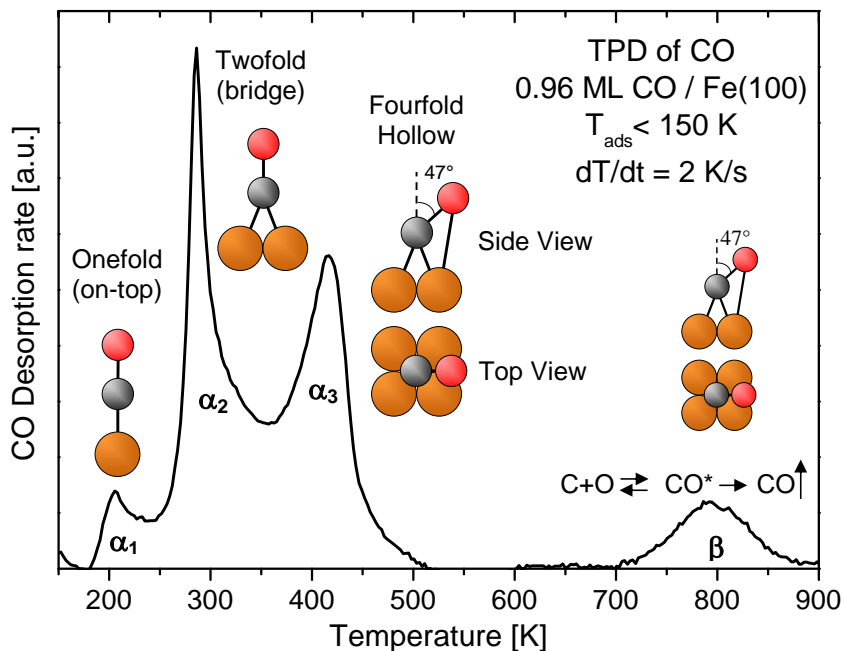
### 6.4.1 CO Desorption Kinetics

The structures of bonded CO to Fe(100) with the respective kinetic parameters that lead to the observed desorption states with TPD are shown in Figure 6.12. Obtaining the kinetic parameters for CO desorbing from the  $\beta$ -CO state proved to be extremely difficult. Although five different methods were used to extract kinetic data from this desorption peak, none of them did provide accurate results and each had their own drawbacks as described in the results section. The group of Madix [1] already mentioned in 1980 that desorption of  $\text{CO}(\beta)$  could not be described by a simple first or second order process. Instead, they found reaction orders between 1.8 and 1.3 from low to high CO coverages, respectively. For this reason, when one tries to determine the kinetic parameters with either one of these five analyses, one assumes either first or second order desorption kinetics. Because the process appears to be more complicated than a simple first or second order desorption process, these methods seem to run into problems. Hence, a more sophisticated model should be used or dynamic Monte Carlo simulations need to be performed to gather more accurate kinetic parameters. Nevertheless, we have put the most likely kinetic parameters of the  $\beta$ -CO desorption state in Figure 6.12.

Since the molecular desorption traces are first order processes, we did not encounter any of the described problems when extracting the kinetic parameters.

### 6.4.2 CO Dissociation Kinetics

To determine the kinetics of the dissociation reaction of CO no other process must take place at the same time. Therefore, CO coverages lower than 0.17 ML were used. Next, the  $\text{Fe}^+$  ion intensity acquired with SSIMS was converted into the CO coverage in monolayer and plotted against the temperature, as shown in Figure 6.13. Here we



	$\alpha_1$	$\alpha_2$	$\alpha_3$	$\beta$
$E_{\text{des}}$ [kJ/mol]	$57 \pm 4$	$80 \pm 5$	$124 \pm 3$	$214 \pm 46$
$v_{\text{des}}$ [ $\text{s}^{-1}$ ]	$10^{14 \pm 1}$	$10^{14 \pm 1}$	$10^{14.6 \pm 1}$	$10^{13 \pm 3}$

**Figure 6.12** TPD plot of a CO saturated Fe(100) surface with the several bonding structures of CO that represent the corresponding desorption states. The most likely kinetic parameters of the desorption states are given in the table.

implicitly assume that the  $\text{Fe}^+$  ion intensity depends linearly on the CO coverage. Consequently we use a semi-quantitative description based on earlier studies of NO dissociation on rhodium by Hopstaken [65] to model the data:

$$r_{\text{dis}} = -\frac{d(\theta_{\text{CO}} / \theta_{\text{sat}})}{dT} = \frac{v_{\text{dis}} \theta_{\text{CO}}}{\beta \theta_{\text{sat}}} \left( \frac{\theta_*}{\theta_{\text{sat}}} \right)^n \exp\left(-\frac{E_{\text{dis}}(\theta_{\text{tot}})}{RT}\right), \quad (\text{eq. 6.4.2.1})$$

in which  $\theta_{\text{CO}}$  and  $\theta_*$  are the absolute coverages (in ML) of carbon monoxide and vacant sites, respectively,  $\theta_{\text{sat}}$  is the total saturation coverage of carbon and oxygen atoms  $\sim 0.5 \text{ ML}$ .  $v_{\text{dis}}$  and  $E_{\text{dis}}$  are the pre-exponential factor and the activation energy of dissociation, respectively,  $\beta$  is the heating rate, and  $n$  is the number of vacancies needed for dissociation (assumed to be 1).

When the semi-quantitative description (eq. 6.4.2.1) –which does not take the lateral interactions into account– is used, the data cannot be modeled properly and

extremely low pre-exponential factors and activation energies of CO dissociation ( $2.14 \pm 0.47 \text{ s}^{-1}$  and  $16 \pm 1.8 \text{ kJ/mol}$ , respectively) are acquired. Hence, lateral interactions are introduced into the model in an empirical way by the following equation:

$$E_{dis}(\theta_{tot}) = E_{dis,0} + \alpha \cdot \theta_{tot}^m \cdot \bar{E}, \quad (\text{eq. 6.4.2.2})$$

in which  $E_{dis}(\theta_{tot})$  is the activation barrier of dissociation of CO as a function of the total coverage,  $E_{dis,0}$  is the activation barrier at zero coverage,  $\alpha$  is a constant (which physical interpretation of the number is not possible),  $\theta_{tot}$  is the total adsorbate coverage  $\theta_{\text{CO}} + \theta_{\text{C}} + \theta_{\text{O}}$ , and  $\bar{E}$  is 1 kJ/mol.  $m$  is an integer, which above unity provides an artificial approach to stress that the effect of lateral interactions becomes particularly apparent at higher total coverages. Both equations 6.4.2.1 and 6.4.2.2 were combined and numerically solved for independent values of  $E_{dis,0}$ ,  $\nu_{dis}$ , and  $\alpha$  to obtain the best fit over the measured temperature range for the different coverages.

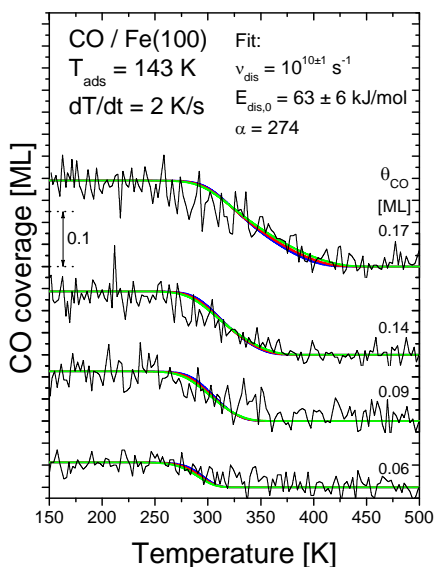


**Figure 6.13** TPSSIMS spectra of the  $\text{Fe}^+$  ion intensity converted into the CO coverage for various CO coverages (noisy data) on Fe(100). Heating rate was 2 K/s. The smooth curves are the fits of the model based on equation 6.4.2.1 in combination with 6.4.2.2.

However, because the data is still very noisy the best fits were obtained for a pre-exponential factor of 12 with an activation energy of 18 kJ, which is very similar to the model without the lateral interactions and is much too low. Hence, a fixed value for the pre-exponential factor needed to be used. From literature we know that pre-exponential factors between  $10^9$  and  $10^{12} \text{ s}^{-1}$  were acquired for the dissociation reaction of simple diatomic molecules on various metal surfaces [66]. Moreover, the pre-

exponential factor collected from the dissociation reaction of CO on poly crystalline iron in Chapter 5 was  $10^{10\pm 1}$ . Therefore, we applied the same pre-exponential factor ( $10^{10\pm 1}$ ) for the dissociation reaction of CO on the Fe(100) single crystal. This leads to an activation energy of dissociation of  $63 \pm 6$  kJ/mol with an  $\alpha$  of 274 (see Figure 6.13). The maximum absolute RMS error in the calculation for this fit is  $1.5 \cdot 10^{-6}$ ,  $2.0 \cdot 10^{-6}$ ,  $2.0 \cdot 10^{-6}$ , and  $1.8 \cdot 10^{-6}$  for 0.06, 0.09, 0.14, and 0.17 ML, respectively.

Dissociation of CO is the preferred reaction on Fe(100), as observed by a combination of TPSSIMS and TPD experiments. However, at coverages of CO higher than 0.17 ML, both dissociation and desorption occur. Nassir et al. [17] proposed that desorption of CO on Fe(100) is dissociation-stimulated and that desorption and dissociation are coupled sequential reactions rather than parallel ones. In this coupled mechanism a CO molecule is first dissociated to generate atomic fragments. Because these dissociated species as well as molecular CO compete for the same adsorption sites on the surface, the atomic fragments would effectively displace and desorb neighboring CO molecules, due to their higher heat of adsorption. Although from calculations (see Chapters 3 and 4 in this thesis) we saw that atomic species indeed have a much larger influence on the adsorption energy of CO than molecular CO and that the dissociation products definitely compete for the same adsorption sites, we believe that desorption of CO at 420 K takes place due to lack of space for CO to dissociate.

This is illustrated by the  $\text{Fe}^+$  signal in the SSIMS experiment of Figure 6.6, which drop in intensity (caused by dissociation at low CO coverages) is retarded by 50 K once CO starts to sufficiently desorb from the surface. Hence, the assumption is that this retardation of temperature at coverages higher than 0.20-0.30 ML is caused because dissociation of CO cannot occur before enough CO has desorbed. Then, when dissociation takes place (around 1000 times faster than desorption of CO at 420 K, calculated from a simple Arrhenius form of the rate constant) its dissociation products may stimulate desorption of CO as a logical consequence of atom-molecule repulsions and speed up the entire process.

The activation energy of dissociation that we collected is half the energy compared to calculated values [2,23]. Because SSIMS induces defects on the surface, we are aware that the low dissociation energy obtained might be ascribed to defect chemistry. This finding is supported by results obtained by Sorescu for CO dissociation on stepped surfaces of iron [67], who reported activation energies of dissociation in the order of 60-90 kJ/mol for the Fe(710) and Fe(310) stepped surfaces. Of course, by using a Kelvin-Probe, which does not create defects on the surface, these results need to be verified in the future. Nonetheless, with respect to the FTS mechanism, it is relevant to note that our results demonstrate that iron surfaces may contain sites that enable CO dissociation at relatively low activation energy of 65 kJ/mol. Since CO dissociation cannot be rate determining, otherwise no carbon build up occurs, these sites might be

necessary to form the iron carbides, which are believed to be the active species in the FTS (see ref. [68] and refs. therein).

### 6.4.3 Influence of Carbon and Oxygen on CO Desorption

Carbon when added to the Fe(100) surface preferentially adsorbs at fourfold hollow sites [2,23,64]. Therefore, desorption of CO at 420 K (CO adsorbed in fourfold hollow sites) decreases as the carbon content increases on the surface. Because less CO is adsorbed as  $\alpha_3$  –pre-cursor of CO dissociation– the amount of CO that dissociates goes down as well. However, twice the amount of CO desorbs as recombined carbon and oxygen than as molecular CO at 420 K. This can be explained by the fact that oxygen at higher coverages adsorbs besides fourfold hollow sites at bridge sites as well. Thus, to dissociate CO one does not need an extra free fourfold hollow site for this. Since the maximum amount of carbon on the surface is 0.5 ML (determined by LEED, which means that locally 0.5 ML is observed, but overall a lower coverage is possible), at some of these locally lower coverages of carbon, CO still has sufficient space to dissociate. As dissociation is favored over desorption, even on the pre-covered surface with the highest carbon content more CO is able to dissociate than desorb from the  $\alpha_3$ -state.

Pre-adsorption of oxygen, on the other hand, leads to a clear decrease of CO( $\alpha_2$ ) desorption. Hence, oxygen tends to move toward bridge sites when CO is post-dosed. Did we observe that dissociation is preferred over desorption of CO at fourfold hollow sites when carbon is pre-adsorbed, oxygen as an overlayer leads to the preference of CO desorption instead of dissociation. Although we did not achieve complete blockage of CO dissociation, as we did not adsorb saturation coverage of oxygen on the surface, we know from literature that complete blockage of CO dissociation is achievable [1]. This is possible, as in contrast to carbon twice the amount of oxygen can be adsorbed on the surface [1,21,48,59,60,62]. Because of the tendency of oxygen to move to bridge sites at higher coverages, CO can still adsorb at fourfold hollow sites. However, because of the high oxygen loading, CO does not have the ensemble of sites needed to dissociate.

Although temperatures of all desorption traces are barely affected by the coadsorption of carbon on the surface, a new desorption state was observed for CO adsorbed in the bridge site with most likely atomic carbon as nearest neighbor.

Pre-adsorption of oxygen influences the desorption temperatures of the peaks slightly, in which the CO( $\alpha_1$ ) and CO( $\alpha_2$ ) peaks move to slightly higher temperatures (stronger bonding to the surface), whereas the CO( $\alpha_3$ ) peak is somewhat destabilized and decreases in temperature. The recombination peak at 775 K is not much affected.

As the temperature of the  $\beta$ -CO peak is not affected by an increase of both atomic surface species oxygen and carbon, this desorption process is not expected to proceed through second order desorption kinetics. Desorption of CO at 780 K, on the

other hand, is most likely a quasi first order process that is limited by the desorption energy of CO and not by the recombination energy of atomic carbon and oxygen, which was also shown by calculations [2,64]. Moreover, calculated adsorption energies of CO of -1.55 to -1.84 eV [23,64] when converted to the desorption temperature [69] are close to the experimentally observed desorption temperature of CO at 775 K.

## **6.5 Conclusions**

Carbon monoxide adsorbs molecularly on Fe(100) at low temperatures <150 K at fourfold hollow sites. When the surface is heated, dissociation of CO exclusively takes place provided ample space is available. Once space becomes scarcer, because the dissociation products adsorb at fourfold hollow sites too, dissociation does not occur unless some of the CO desorbs. Since dissociation is much faster than desorption of CO (roughly 1000 times at 420 K), the amount of desorbed recombined CO does not go down at the point where molecular desorption of CO at 420 K is observed, but keeps increasing to a coverage of ca. 0.25 ML, and thereafter stays constant. The activation energy of CO dissociation that we obtain is half the energy reported by calculations from literature; hence, it is possible that what we measure is defect chemistry instead, as SSIMS undoubtedly creates defects on the surface.

First order desorption kinetics were assumed for the molecular desorption features, which correlated nicely with literature. Desorption of recombined CO, on the other hand could not be determined as a typical first or second order process. However, quasi first order desorption kinetics were established for desorption of recombined CO, in which CO desorption is the limiting factor and not the recombination energy of atomic carbon and oxygen.

When carbon is added to the surface, it occupies fourfold hollow sites, and thus, the availability of these adsorption sites drops, resulting in less adsorption of carbon monoxide in the  $\alpha_3$ -state. Because this state is the pre-cursor for CO dissociation, less CO is able to dissociate as well. However, complete blockage of CO dissociation is not possible by pre-adsorption of carbon. Pre-exposure of oxygen, on the other hand, can result in complete blockage of CO dissociation, which is due to a higher saturation content of oxygen on the surface compared to carbon. Moreover, oxygen seems to move to the bridge sites, as the CO( $\alpha_2$ ) state is affected the most.

The applicability of SSIMS to determine the kinetic parameters of CO dissociation was shown to be on the edge of what is possible; instead of directly looking at carbon, oxygen, and CO species on the surface, we needed to switch to the iron signal, because of the insufficient detection of the species themselves. However, when dissociation of CO was examined with either pre-adsorbed atomic carbon or oxygen, even the iron signal was not of high enough quality to use. Moreover, SSIMS induces defects on the surface, which can dictate the complete surface chemistry. To determine



the kinetic parameters of CO dissociation more accurately because of the described SSIMS limitations, we would suggest using a Kelvin-Probe, which is expected to have a much better signal to noise ratio, and moreover, does not create defects on the surface. Thus, defect chemistry can be excluded to a certain extent. To be able to observe carbon, oxygen, and CO species directly on the surface we would advise performing synchrotron XPS experiments.

## References

- [1] J. Benziger, R. J. Madix, *Surf. Sci.* **94** (1980) 119.
- [2] T. C. Bromfield, D. Curulla-Ferré, J. W. Niemantsverdriet, *ChemPhysChem* **6** (2005) 254.
- [3] N. B. Brookes, A. Clarke, P. D. Johnson, *Phys. Rev. Lett.* **63** (1989) 2764.
- [4] C. R. Brundle, *IBM J. Res. Dev.* **22** (1978) 235.
- [5] S. D. Cameron, D. J. Dwyer, *Langmuir* **4** (1988) 282.
- [6] D. J. Dwyer, B. Rausenberger, J. P. Lu, S. L. Bernasek, D. A. Fischer, S. D. Cameron, D. H. Parker, J. L. Gland, *Surf. Sci.* **224** (1989) 375.
- [7] O. L. J. Gijzeman, T. J. Vink, O. P. Van Pruissen, J. W. Geus, *J. Vac. Sci. Technol. A* **5** (1987) 718.
- [8] J. P. Lu, M. R. Albert, S. L. Bernasek, *Surf. Sci.* **217** (1989) 55.
- [9] J. P. Lu, M. R. Albert, S. L. Bernasek, D. J. Dwyer, *Surf. Sci.* **199** (1988) L406.
- [10] T. E. Meehan, J. D. Head, *Surf. Sci.* **243** (1991) L55.
- [11] S. P. Mehandru, A. B. Anderson, *Surf. Sci.* **201** (1988) 345.
- [12] P. B. Merrill, R. J. Madix, *Surf. Sci.* **271** (1992) 81.
- [13] D. W. Moon, S. L. Bernasek, D. J. Dwyer, J. L. Gland, *J. Am. Chem. Soc.* **107** (1985) 4363.
- [14] D. W. Moon, S. L. Bernasek, J. P. Lu, J. L. Gland, D. J. Dwyer, *Surf. Sci.* **184** (1987) 90.
- [15] D. W. Moon, S. Cameron, F. Zaera, W. Eberhardt, R. Carr, S. L. Bernasek, J. L. Gland, D. J. Dwyer, *Surf. Sci. Lett.* **180** (1987) L123.
- [16] D. W. Moon, D. J. Dwyer, S. L. Bernasek, *Surf. Sci.* **163** (1985) 215.
- [17] M. Nassir, D. J. Dwyer, P. Kleban, *Surf. Sci.* **356** (1996) L429.
- [18] M. H. Nassir, B. Frühberger, D. J. Dwyer, *Surf. Sci.* **312** (1994) 115.
- [19] S. K. Nayak, M. Nooijen, S. L. Bernasek, P. Blaha, *J. Phys. Chem. B* **105** (2001) 164.
- [20] J. Paul, *Surf. Sci.* **224** (1989) 348.
- [21] T. N. Rhodin, C. F. Brucker, *Solid State Commun.* **23** (1977) 275.
- [22] R. S. Saiki, G. S. Herman, M. Yamada, J. Osterwalder, C. S. Fadley, *Phys. Rev. Lett.* **63** (1989) 283.
- [23] D. C. Sorescu, D. L. Thompson, M. M. Hurley, C. F. Chabalowski, *Phys. Rev. B* **66** (2002) 035416/1.
- [24] G. Broden, G. Gafner, H. P. Bonzel, *Appl. Phys.* **13** (1977) 333.
- [25] W. Erley, *J. Vac. Sci. Technol.* **18** (1981) 472.
- [26] G. Ertl, J. Küppers, F. Nitschke, M. Weiss, *Chem. Phys. Lett.* **52** (1977) 309.
- [27] R. Feder, G. Gafner, *Surf. Sci.* **57** (1976) 45.
- [28] G. Gafner, R. Feder, *Surf. Sci.* **57** (1976) 37.
- [29] L. Gonzalez, R. Miranda, S. Ferrer, *Surf. Sci.* **119** (1982) 61.
- [30] E. S. Jensen, C. W. Seabury, T. N. Rhodin, *Solid State Commun.* **35** (1980) 581.
- [31] D. E. Jiang, E. A. Carter, *Surf. Sci.* **570** (2004) 167.
- [32] T. Maruyama, Y. Sakisaka, H. Kato, Y. Aiura, H. Yanashima, *Surf. Sci.* **304** (1994) 281.
- [33] T. N. Rhodin, M. H. Tsai, R. V. Kasowski, *Appl. Surf. Sci.* **22-23** (1985) 426.
- [34] A. Stibor, G. Kresse, A. Eichler, J. Hafner, *Surf. Sci.* **507-510** (2002) 99.
- [35] K. Yoshida, G. A. Somorjai, *Surf. Sci.* **75** (1978) 46.
- [36] C. E. Bartosch, L. J. Whitman, W. Ho, *J. Chem. Phys.* **85** (1986) 1052.
- [37] S. L. Bernasek, M. Zappone, P. Jiang, *Surf. Sci.* **272** (1992) 53.
- [38] R. Chen, C. Satoko, *Surf. Sci.* **223** (1989) 101.

- [39] Y.-H. Chen, D.-B. Cao, J. Yang, Y.-W. Li, J. Wang, H. Jiao, *Chem. Phys. Lett.* **400** (2004) 35.
- [40] P. Jiang, M. Zappone, S. L. Bernasek, *J. Chem. Phys.* **99** (1993) 8120.
- [41] U. Seip, M. C. Tsai, K. Christmann, J. Küppers, G. Ertl, *Surf. Sci.* **139** (1984) 29.
- [42] K. Ueda, M. Enatsu, *Surf. Sci.* **159** (1985) L421.
- [43] L. J. Whitman, L. J. Richter, B. A. Gurney, J. S. Villarrubia, W. Ho, *J. Chem. Phys.* **90** (1989) 2050.
- [44] J. B. Benziger, R. J. Madix, *Surf. Sci.* **115** (1982) 279.
- [45] M. L. Burke, R. J. Madix, *Surf. Sci.* **237** (1990) 20.
- [46] S. D. Cameron, D. J. Dwyer, *Surf. Sci.* **198** (1988) 315.
- [47] J. P. Lu, M. R. Albert, S. L. Bernasek, *J. Phys. Chem.* **94** (1990) 6028.
- [48] T. J. Vink, O. L. J. Gijzeman, J. W. Geus, *Surf. Sci.* **150** (1985) 14.
- [49] C. Benndorf, B. Krüger, F. Thieme, *Surf. Sci.* **163** (1985) L675.
- [50] C. M. Chan, R. Aris, W. H. Weinberg, *Appl. Surf. Sci.* **1** (1978) 360.
- [51] J. W. Niemantsverdriet, *Spectroscopy in Catalysis*, 3rd ed., Wiley-VCH, Weinheim, 2007.
- [52] D. A. King, *Surf. Sci.* **47** (1975) 384.
- [53] E. Habenschaden, J. Küppers, *Surf. Sci.* **138** (1984) L147.
- [54] M. J. P. Hopstaken, J. W. Niemantsverdriet, *J. Chem. Phys.* **113** (2000) 5457.
- [55] P. A. Redhead, *Vacuum* **12** (1962) 203.
- [56] R. J. Madix, J. Benziger, *Ann. Rev. Phys. Chem.* **29** (1978) 285.
- [57] W. H. Hung, S. L. Bernasek, *Surf. Sci.* **339** (1995) 272.
- [58] J. B. Benziger, R. J. Madix, *J. Electron Spectrosc. Relat. Phenom.* **20** (1980) 281.
- [59] J. P. Lu, M. R. Albert, C. C. Chang, S. L. Bernasek, *Surf. Sci.* **227** (1990) 317.
- [60] J. P. Lu, M. R. Albert, S. L. Bernasek, D. J. Dwyer, *Surf. Sci.* **215** (1989) 348.
- [61] P. Blonski, A. Kiejna, J. Hafner, *Surf. Sci.* **590** (2005) 88.
- [62] K. O. Legg, F. P. Jona, D. W. Jepsen, P. M. Marcus, *J. Phys. C: Solid State Phys.* **8** (1975) L492.
- [63] J. M. Van Zoest, J. M. Fluit, T. J. Vink, B. A. Van Hassel, *Surf. Sci.* **182** (1987) 179.
- [64] F. J. E. Scheijen, D. Curulla Ferré, J. W. Niemantsverdriet, *J. Phys. Chem. C* **113** (2009) 11041.
- [65] M. J. P. Hopstaken, J. W. Niemantsverdriet, *J. Phys. Chem. B* **104** (2000) 3058.
- [66] C. T. Campbell, Y. K. Sun, W. H. Weinberg, *Chem. Phys. Lett.* **179** (1991) 53.
- [67] D. C. Sorescu, *J. Phys. Chem. C* **112** (2008) 10472.
- [68] J. M. Gracia, F. F. Prinsloo, J. W. Niemantsverdriet, *Catal. Lett.* **133** (2009) 257.
- [69] Z. Knor, *Surf. Sci.* **154** (1985) L233.



# Iron Oxide Nano Particles as Model Catalysts for the Fischer-Tropsch Synthesis: Morphology and Composition Study

## Abstract

*Monodisperse 18 nm spherical magnetite ( $Fe_3O_4$ ) nano particles were synthesized from goethite ( $FeO(OH)$ ) through a one-pot synthesis. Via the flat model approach, i.e., spin-coating of the nano particles on a flat  $SiO_2$  substrate, TEM was used to image the particles. From these images a particle size distribution of  $17.5 \pm 1.5$  nm was determined. To minimize the mobility of the particles on the  $SiO_2$  support under reaction conditions, the calcination temperature of the particles after spin-coating –to remove the surfactant– proved to be essential. Three different methods to activate (reduce) the magnetite particles were studied, that is,  $H_2$ , CO, and a mixture of  $H_2$  and CO (synthesis gas). Using  $H_2$  leads to faceting of part of the particles and to the appearance of core-shell particles with metallic iron as the core and iron oxide as shell. When CO is applied as reduction gas most of the particles become faceted. However, no core-shell particles, and moreover, carbide phases were detected. Flowing a mixture of  $H_2$  and CO for 7 days over the magnetite nano particles resulted in substantial changes in the morphology of the particles, but did not lead to any detection of carbide phases either. Instead, magnetite was the only crystalline phase present after syngas treatment. Moreover, regardless of the reduction gas, the behavior of the magnetite particles is different from one particle to another. This means that some of the particles –even after a week in syngas– did not change at all and remained spherical magnetite, whereas others ended up as deformed shaped particles. Hence, although the synthesized particles appear very homogeneous in shape and size, their chemistry apparently does not.*

## 7.1 Introduction

Different synthesis routes to obtain monodisperse iron oxide nano particles have been studied extensively [1-9], because nano-sized particles in general possess interesting electrical, magnetic, optical, and chemical properties. Due to these unique properties, many nano-sized particles have found their implementation in diverse fields such as environmental remediation, electronics, sensors in biotechnology, and magnetic resonance imaging [9]. Iron oxide nano particles, however, can also be used as catalysts in the Fischer-Tropsch synthesis (FTS) to produce almost sulfur free transportation fuels. Before they can be employed as an active FTS catalyst, though, these iron oxides need to be activated, which can be done by either H<sub>2</sub>, CO, or a mixture of H<sub>2</sub> and CO [10-16]. What happens to their morphology and composition during the activation process, i.e., do they sinter, get different shapes, etc., is important for their application. In addition, to know the composition of the catalyst under reaction conditions is imperative to provide mechanistic insight of the reaction (iron oxides are generally inactive in FTS, but are known to possess water-gas-shift (WGS) activity), but also to identify the practical constraints with respect to attrition, dusting, mechanical strength, sintering, etc. (iron carbides for example tend to be brittle and break up).

In this Chapter we examine the morphology behavior of monodisperse iron oxide particles when treated by H<sub>2</sub>, CO, or a mixture of H<sub>2</sub> and CO, with the main purpose to show the potency of the applied model system, in which a flat substrate of SiO<sub>2</sub> is used as support to study the iron oxide particles (see Chapters 1 and 2 for more details). The nano-sized iron particles were imaged with transmission electron microscopy (TEM) and their composition was determined by electron diffraction in the TEM, and by measuring X-ray absorption near edge structure (XANES) and extended X-ray absorption fine structure (EXAFS) at the beamline of Argonne National Laboratory in Chicago.

## 7.2 Experimental Methods and Details

### 7.2.1 Preparation and Purification of the Iron Oxide Nano Particles

The iron oxide nano particles were prepared according to the method of Yu et al. [9], which has the advantage of being a single pot reaction. A mixture of 0.177 g goethite (FeO(OH)) (2 mmol) 50-80 mesh, 3.39 g of oleic acid (12 mmol), and 7.5 g 1-octadecene was added to a glass tubular reactor equipped with a condenser and mechanic overhead stirrer (see Figure 7.1). The tubular reactor was fitted into an aluminum heating block, which contained a hole with the same dimensions as the reactor for optimum heat transfer. Subsequently, the solution was stirred at 200 RPM and heated at a heating rate of 3-5 °C/min toward 320 °C, while undesired side-

reactions –such as oxidation of oleic acid– were avoided by continuously flowing  $N_2$  through the set-up. The reaction mixture was then kept at  $320\text{ }^\circ\text{C}$  for 80 minutes, which resulted in the solution turning from clear brown/red to turbid black. Consequently, the mixture was allowed to cool down to room temperature under additional stirring.

Ethanol was added to the cooled-down reaction mixture to act as an anti-solvent, thus, precipitating the iron oxide particles. The slimy black/brown precipitate was obtained by centrifuging the iron oxide containing mixture for 30 minutes at 7000 RPM. Subsequently, the precipitate was washed three times with ethanol, and thereafter, dissolved in toluene. The colloidal solution was centrifuged for another 30 minutes at 7000 RPM to remove agglomerated particles and stored after decantation.

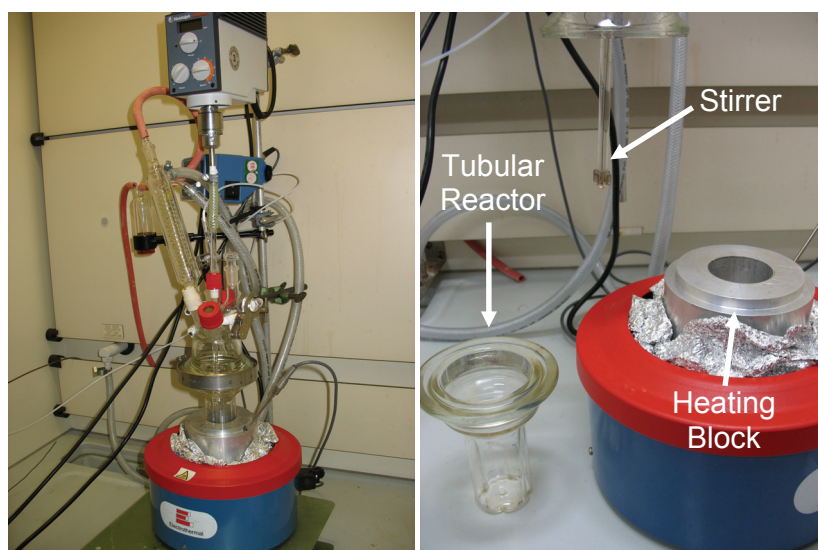


**Figure 7.1** Left picture shows the reactor that was used for preparation of the iron oxide nano particles. The right image displays the stirrer, heating block, and glass tubular reactor.

### **7.2.2 Spin-Coating of the Iron Oxide Nano Particles on the TEM Grids**

A wafer containing 36 silica TEM grids (prepared as described in Chapter 2) is placed inside the spin-coating device and cleaned by adding  $600\text{ }\mu\text{l}$  of toluene and subsequent evaporation by rotating the chuck at 2800 RPM. Thereafter,  $600\text{ }\mu\text{l}$  of the iron oxide toluene solution is drop casted onto the wafer followed by rotation of the chuck at 2800 RPM for ca. 15-20 s, sufficient to evaporate all the toluene on the surface. The wafer is then either placed into an oven at  $450\text{ }^\circ\text{C}$  or positioned under an ultraviolet (UV) lamp that produces ozone at  $60\text{ }^\circ\text{C}$  to burn off the surfactant surrounding the iron oxide particles.

### 7.2.3 Iron Oxide Nano Particles Treatment with Reactive Gas

Before the TEM grids with the spin-coated iron oxide nano particles (without surfactant) were placed inside the tubular quartz reactor and exposed to a certain reactive gas, carbon impurities were removed by cleaning the grids in a UV ozone generator. Next, the TEM grids were positioned in the tubular reactor and heated under inert atmosphere of argon to the desired temperature with a heating rate of 10 °C/min. At the desired temperature the inert gas was switched for the reactive gas, i.e., H<sub>2</sub>, CO, or a mixture of H<sub>2</sub> and CO. The reaction was then carried out for a given time, after which the reactor was allowed to cool down to room temperature, where the reactive gas was switched back to argon to purge the reactor (enough to remove the reactive gas). Lastly, the reactor was opened to air at the inlet point of the gases to passivate the particles.

## 7.3 Results

### 7.3.1 Removal of Surfactant from the Iron Oxide Particles

As already mentioned, two different methods were used to burn off the surfactant from the iron oxide nano particles; removal via ozone at 60 °C or through calcination at 450 °C. The difference between these two methods is depicted in Figure 7.2. Both samples

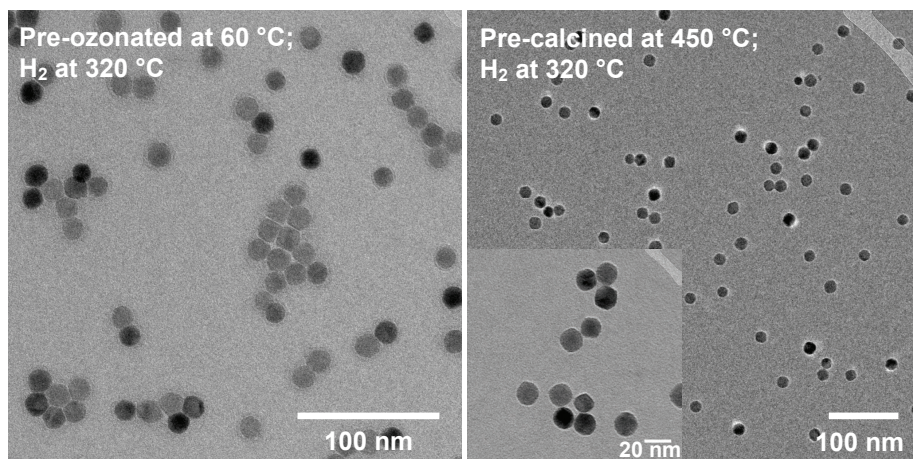


**Figure 7.2** TEM images of the 18 nm iron oxide nano particles showing the difference between ozonated and calcined samples. The ozone pre-treated nano particles display a larger tendency to cluster together than the calcined ones, thus the distance between the particles is smaller.

were reduced with hydrogen at 320 °C for one hour after the surfactant had been burned off. Ozonation results in a larger mobility of the particles than calcination, i.e., the

particles have a greater tendency to cluster together, and therefore, are much closer to one another. Because a high mobility of the particles is undesired, as sintering of the particles may occur much faster due to either particle migration (coalescence) or Ostwald ripening, all samples discussed in the rest of this Chapter were pre-treated by calcination at 450 °C.

### 7.3.2 Particle Size Distribution

The spin-coated particles after calcination at 450 °C were investigated with a transmission electron microscope to determine the particle size distribution. Two different surface area coverages of iron oxide nano particles were prepared; ca. 4.5% and 18%. Figure 7.3 shows two images of the corresponding samples, each with a

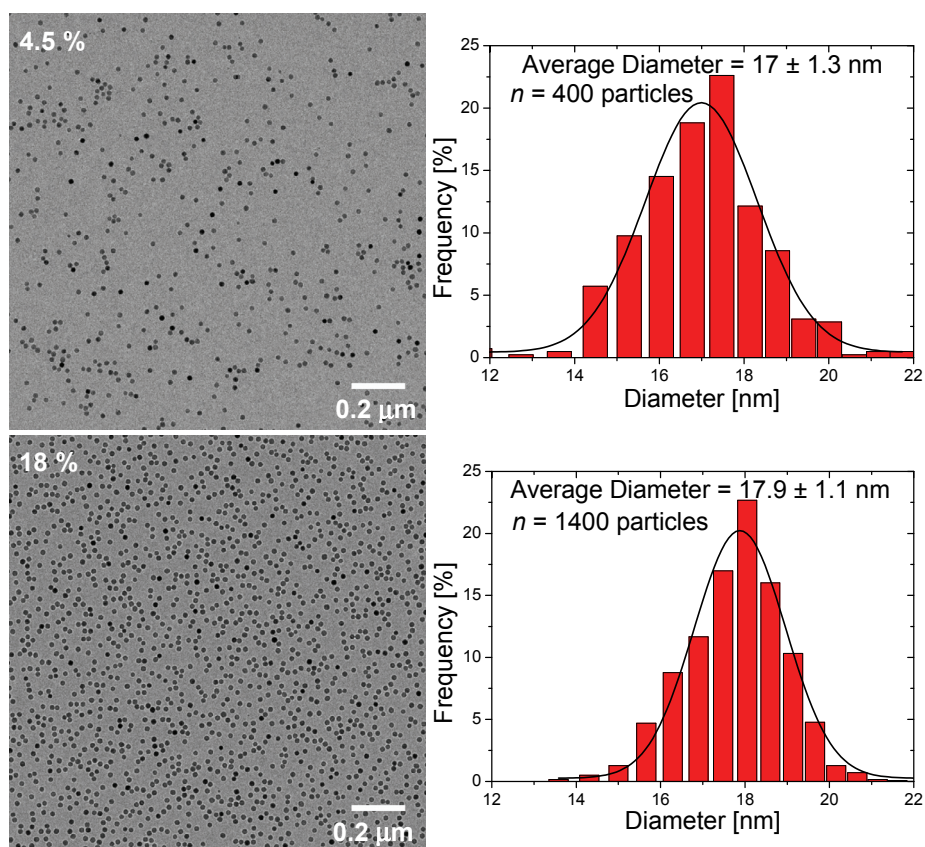


**Figure 7.3** TEM images –left side– of the two different loadings of iron oxide particles with on the right side the corresponding particle size distribution (obtained with the program ImageJ). The data is fitted by a Gaussian curve (LogNormal curve fits similarly), which shows that the synthesized particles are ca.  $17.5 \pm 1.5$  nm in size.



particle size distribution. These overview images reveal to what extent the particles cover the SiO<sub>2</sub> model support, and are well suited for determining a statistically reliable particle size distribution, because of the large numbers of particles used in the distribution. However, between the two loadings a small difference of 1 nm in the average diameter is observed, which can be ascribed to the dissimilarity in focus between the two images. To circumvent such errors, particle size distributions were also made from zoomed-in images of the particles, where the error caused by difference in focus is much smaller. Based on both the overview and close-view images, we conclude that the average size of the iron oxide nano particles is  $17.5 \pm 1.5$  nm.

### 7.3.3 Composition of the Iron Oxide Particles

To determine the composition of the particles after spin-coating and subsequent calcination, a diffraction pattern was recorded (Figure 7.4). The image is black and white inverted to enhance the visibility of the diffraction rings. Because the recorded area is roughly 25-30  $\mu\text{m}^2$  a lot of particles were measured, which leads to a ring structure rather than individual spots. In the figure a magnetite (Fe<sub>3</sub>O<sub>4</sub>) reference has been incorporated for comparison with the recorded diffraction pattern.

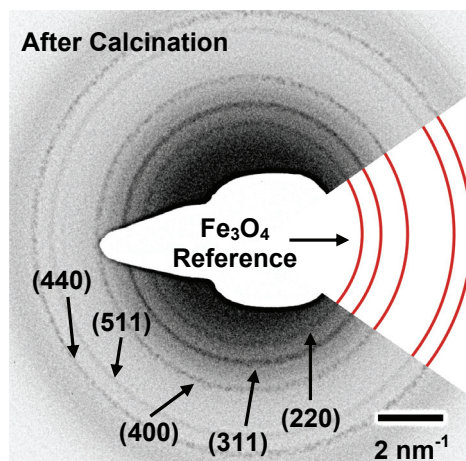


**Figure 7.4** The diffraction pattern of the 18 nm iron oxide nano particles after calcination at 450 °C, which shows that the composition of the particles is magnetite (Fe<sub>3</sub>O<sub>4</sub>).

It should be noted, however, that maghemite ( $\gamma$ -Fe<sub>2</sub>O<sub>3</sub>) cannot be distinguished from magnetite by electron diffraction. Even with X-ray diffraction (XRD), differences in the *d*-spacings between the magnetite and maghemite phase are only 0.5-1%. Hence, using maghemite as reference in the image leads to a similar result. However, Park et al.

showed on the basis of X-ray absorption spectroscopy (XAS) and X-ray magnetic circular dichroism spectroscopy (XMCD) that small particles in the order of 5 nm are pre-dominantly  $\gamma$ -Fe<sub>2</sub>O<sub>3</sub>, particles between 5 and 22 nm in size consist of mixed phases of  $\gamma$ -Fe<sub>2</sub>O<sub>3</sub> and Fe<sub>3</sub>O<sub>4</sub>, and nano particles larger than 22 nm are mostly magnetite [4]. Hence, we assume that the composition of our 18 nm prepared particles will mainly be magnetite.

Apart from electron diffraction we performed XANES and EXAFS on the prepared particles (Figure 7.5). These experiments were proof of principle measurements of an exploratory nature to test the applicability of our planar samples in synchrotron measurements. As such, we only compared our iron oxide nano particles with hematite and magnetite references (the two most common oxide phases of iron) and not with maghemite. Thus, we do not have a maghemite reference to compare our particles with. Nonetheless, EXAFS data, which is relatively similar for different oxides in the Fe-O bond distances, on the other hand, is distinctive for especially the imaginary part in the higher shells. Because the higher shells of the prepared nano particles fit nicely (especially the imaginary part) with the magnetite reference, it is not very likely that a similar fit would have been achieved with a maghemite reference, as the imaginary part is characteristic for a certain oxide phase. In addition, because the authors who developed the method we used to prepare the particles also mention that their produced particles are magnetite [9], it is fair to assume that our 18 nm prepared nano particles consist of magnetite, and not out of maghemite.

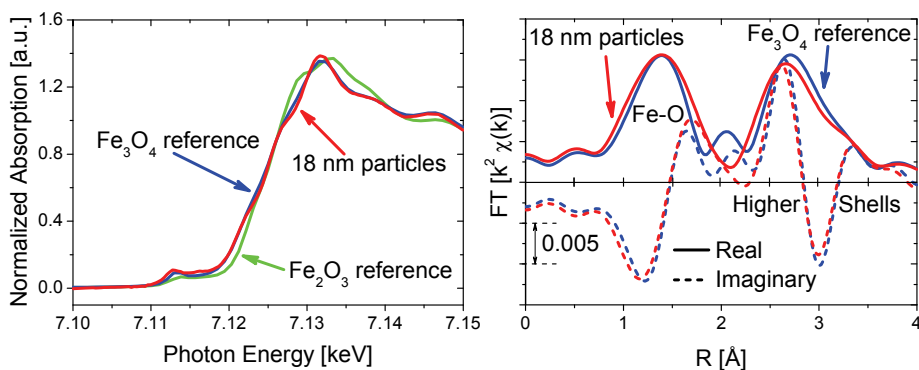


**Figure 7.5** XANES spectra of the as-prepared 18 nm particles along with magnetite and hematite references are shown in the left image and the Fourier-transformed EXAFS data of the as-prepared particles with the magnetite reference is displayed in the right picture.

Figure 7.6 shows TEM images of individual nano particles after calcination displaying several surface orientations of the magnetite phase. Each of these surface orientations has a distinct *d*-spacing that can be determined directly in the TEM picture

Fe <sub>3</sub> O <sub>4</sub>	
(hkl)	<i>d</i> -spacing (Å) [1,2]
(111)	4.852
(220)	2.967
(311)	2.532
(400)	2.099
(511)	1.616
(440)	1.485

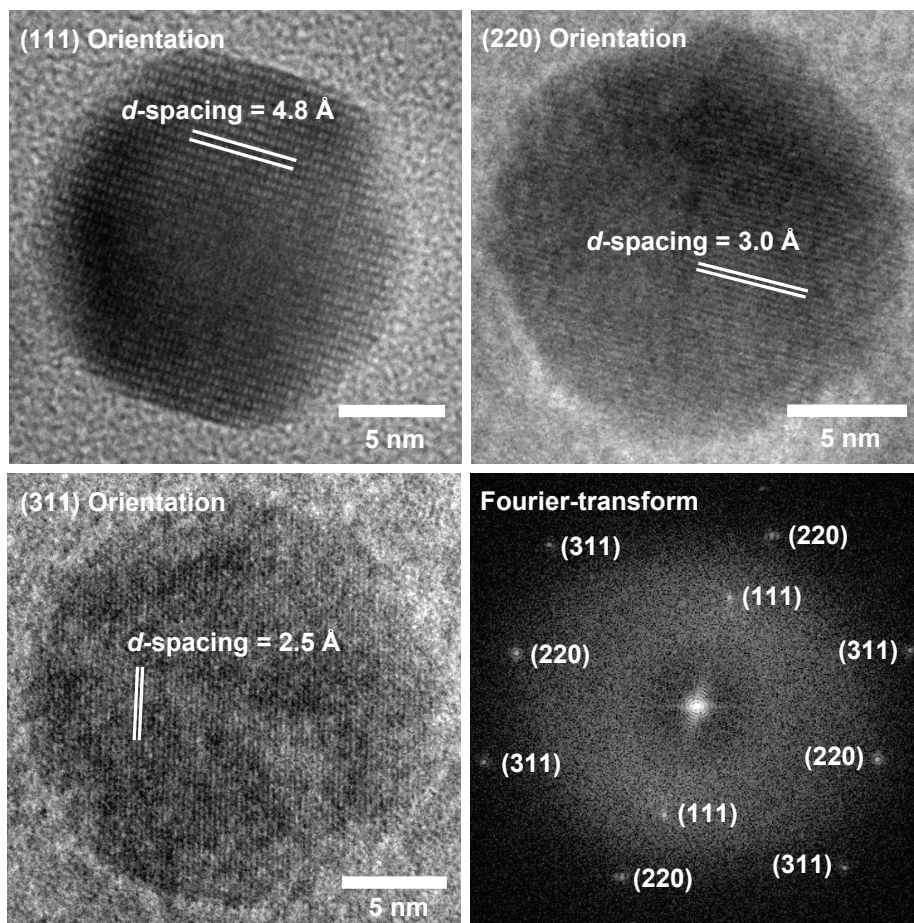


**Figure 7.6** TEM images of the 18 nm iron oxide nano particles showing different surface orientations of the magnetite phase. In the lower-right image the Fourier-transform of the top-left particle is provided displaying the diffraction spots of three different lattice planes. The table shows the *d*-spacings of the different lattice planes of magnetite.

by measuring the distance between two lattice fringes. Another method to determine the *d*-spacing is to apply a Fourier-transform of the recorded TEM image, as done in the

lower-right image of Figure 7.6. In this Fourier-transformed picture, the visible diffraction spots are produced by the various surface orientations present in the particle, which each have a distinct  $d$ -spacing. These spots can be assigned to the respective lattice planes on the basis of measured lattice spacings by XRD. In conclusion, TEM diffraction, XANES, EXAFS, and even TEM images themselves, all lead to the same result that the particles after calcination are magnetite.

### **7.3.4 Morphology Behavior of the Magnetite Nano Particles under Different Reactive Environments**

The aim is to observe the change in morphology behavior of magnetite nano particles when different reactive gases are used for their reduction. In particular the influence of temperature is investigated. The particles are treated as explained in section 7.2.3.

#### *7.3.4.1 Passivation Effects*

Iron is very reactive towards oxygen, hence, oxidation of the metal occurs rapidly [17]. Therefore, it is important that passivation of the reduced iron nano particles proceeds with extreme caution. To achieve this, an inert atmosphere was created inside the reactor by purging argon. Once the reactor was under inert atmosphere, the inlet gas valve was opened to the air, so that oxygen could slowly diffuse inside. However, it appears that when this is not done carefully, passivation effects can occur, as displayed in Figure 7.7. The TEM image shows hollow particles, which arise because iron atoms diffuse outward to the interface when oxidation takes place (the Kirkendall effect [18]). In this particular case it seems that oxygen diffused inside the reactor too quickly after the magnetite particles were reduced by  $H_2$  at  $500\text{ }^\circ\text{C}$ , which resulted in a fast re-oxidation of the reduced iron particles opening them up by the Kirkendall effect.

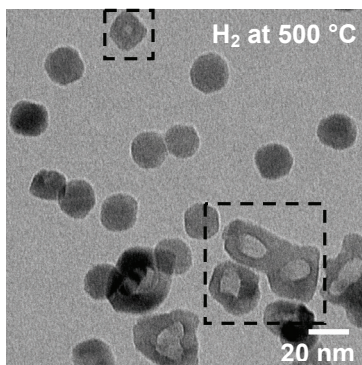


**Figure 7.7** Passivation effect on the 18 nm iron oxide nano particles, due to exposure of previously reduced particles to air, opening up the particles.

#### 7.3.4.2 Reduction of the Particles with H<sub>2</sub>

Reduction of the magnetite nano particles was performed with H<sub>2</sub> at several temperatures, i.e., 320, 500, 700, and 800 °C for one hour. TEM images and the diffraction patterns of the particles after these treatments are shown in Figure 7.8.

After reduction at 320 °C, the particles appear unaltered compared to the calcined ones. Moreover, the diffraction pattern did not change and resembles the magnetite (Fe<sub>3</sub>O<sub>4</sub>) phase. A temperature of 320 °C, therefore, is insufficient to reduce the iron oxide nano particles.

At 500 °C the particles have a tendency to become faceted, as square particles are observed. However, besides these square particles, others seem unaffected. Although part of the particles becomes faceted, the diffraction pattern does not alter and Fe<sub>3</sub>O<sub>4</sub> remains the only phase present. Hence, 500 °C is still not enough to reduce the magnetite particles.

When the reduction temperature is raised to 700 °C, however, major differences can be seen. Although particles do not seem to have become faceted at this temperature, some core-shell particles are detected, while others appear completely unaltered. It seems that these particles have a metallic core with an iron oxide shell surrounding them. The diffraction pattern shows rings that can be attributed to both bcc and fcc metallic iron. Moreover, the most intense ring (*d*-spacing of 2.5 Å) according to XRD references (taken from the XRD database) of Fe<sub>3</sub>O<sub>4</sub> is the one pinpointed by the arrow in the 500 °C diffraction image, whereas the most intense ring of metallic iron (*d*-spacing of 2.0 Å) is the one shown by the arrow in the 700 °C diffraction picture. It is obvious that the intensity of the Fe<sub>3</sub>O<sub>4</sub> ring decreases as the reduction temperature is raised from 500 to 700 °C and that the intensity of the metallic iron ring increases. Thus, partial reduction has taken place at a temperature of 700 °C.

To obtain further evidence for reduction, we performed XANES and EXAFS experiments on the 700 °C reduced iron nano particles, which are shown in Figure 7.9. These results show that the intensity of the absorption edge has decreased after reduction at 700 °C. Moreover, the absorption edge shifts to lower energies. Both these observations illustrate that reduction has taken place. The XANES spectrum is consistent with Fe<sup>2+</sup>, but does not resemble metallic iron or FeO. The EXAFS looks very much like Fe<sub>3</sub>O<sub>4</sub> in the Fe-O and higher shell region. The higher shell region is smaller, but the imaginary part is very similar. According to these results, it is plausible that the particles have reduced partially to FeO or completely to Fe at the outer surface, but that the shell did not reduce and still remained Fe<sub>3</sub>O<sub>4</sub>. Such a structure is hard to determine by EXAFS. Of course more research would be needed to verify this.

Reduction is complete when a temperature of around 800 °C is reached. At this temperature no more diffraction patterns are visible, which indicates that the reduced iron particles have been completely re-oxidized toward amorphous iron oxides on the SiO<sub>2</sub> surface. This is a bit puzzling, because in the case of H<sub>2</sub> reduction at 700 °C



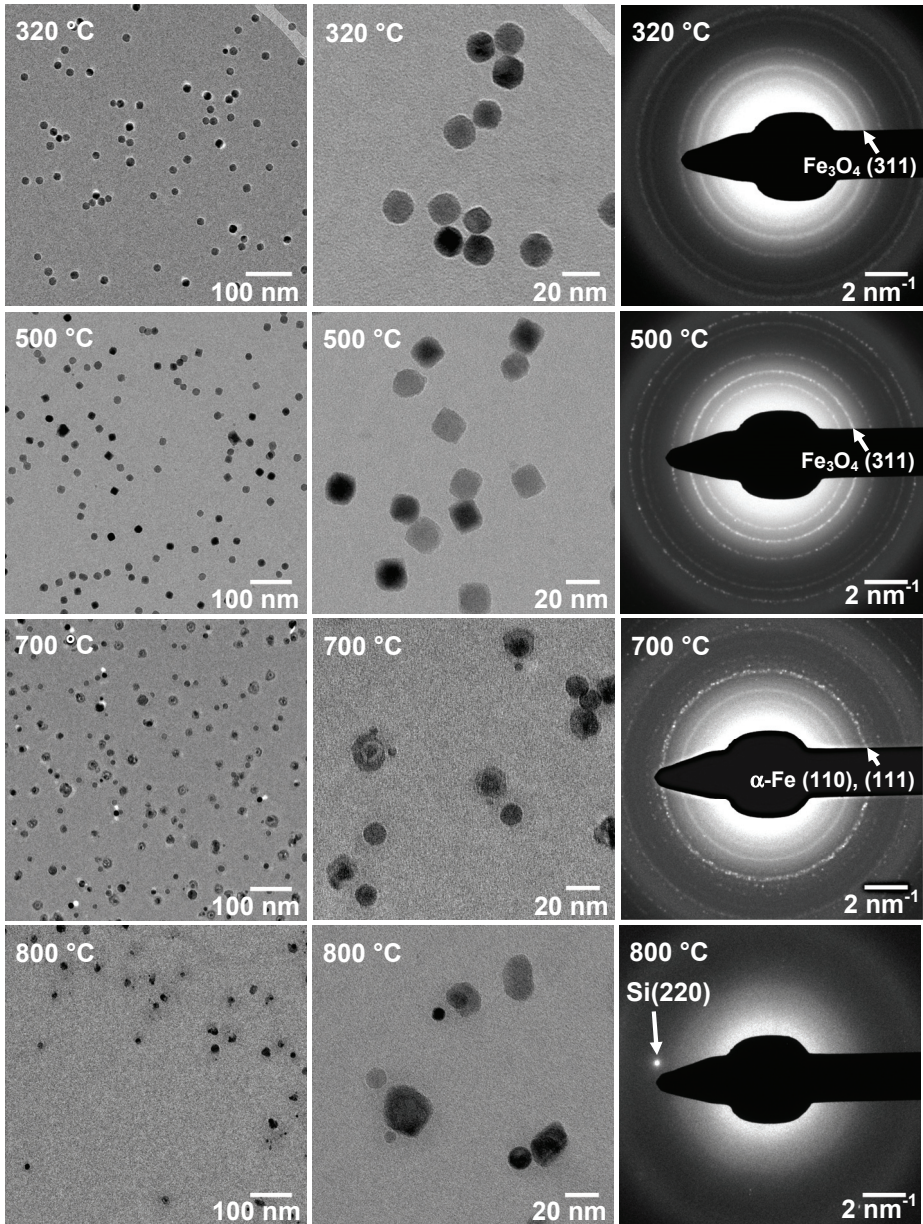


**Figure 7.8** TEM images of the 18 nm nano particles (4.5% loading) after one hour of flowing  $H_2$  at the indicated temperature. The pictures on the left are overview images, the pictures in the middle a zoom in of the particles, and the right images the diffraction patterns corresponding to the particles. The arrow in the right image depicts the brightest line in the diffraction pattern.

metallic iron was observed with electron diffraction, even after 5 months of storage in air. In that case the small oxide layer surrounding the metal phase acted as a barrier for oxidation of the remaining iron metal. However, clear core-shell particles were not observed at 800 °C. Instead, a large number of particles agglomerated on the silica surface, which led to an overall smaller number of particles present. This agglomeration appeared to be worse for some areas than for others (not shown in pictures). Presumably in the case of 800 °C, re-oxidation of the reduced iron particles occurred too quickly, which led to complete re-oxidation. Hence, to obtain nice core-shell particles, which remain stable in air for a couple of months, we suspect that the formation of a thin oxide layer around the metallic iron core needs to proceed very slowly, preferably under glove-box conditions. When not done carefully, the formation of such a protective layer is not readily formed and iron completely re-oxidizes.

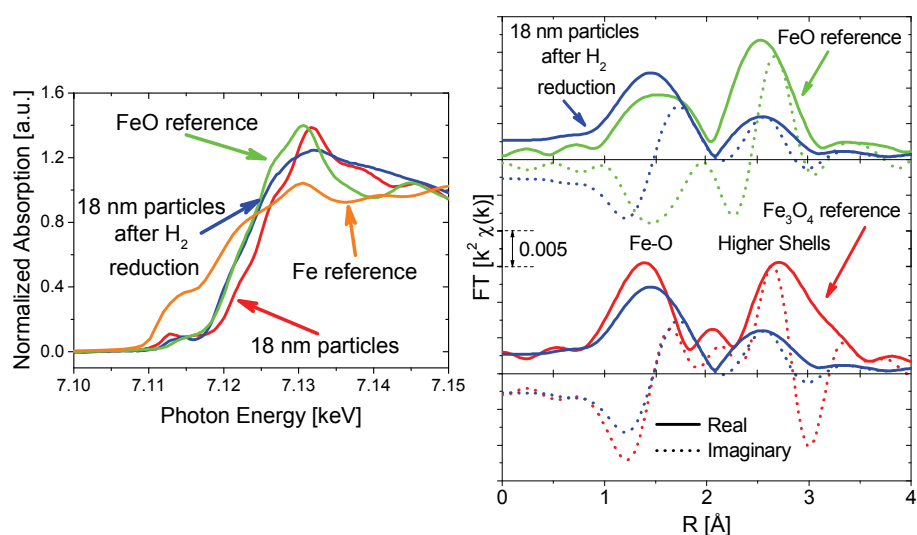


**Figure 7.9** XANES spectra of the 18 nm particles as synthesized and after reduction at 700 °C with Fe and FeO references are shown in the left image and the Fourier-transformed EXAFS data of the reduced particles with the FeO and Fe<sub>3</sub>O<sub>4</sub> references are displayed in the right picture.

### 7.3.4.3 Reduction of the Particles with CO

To find out what happens to the morphology of the magnetite nano particles when exposed to a CO environment for one hour at various temperatures, TEM images were recorded, which are depicted in Figure 7.10. In addition, diffraction patterns of the nano particles were measured to find out whether reduction took place.

At a relatively low reduction temperature of 320 °C, nothing happens that is visible in TEM to the magnetite particles. The shape stays more or less the same as the

spin-coated particles and the diffraction pattern also shows no difference. Therefore, these results seem to suggest that no reduction has taken place at this temperature.

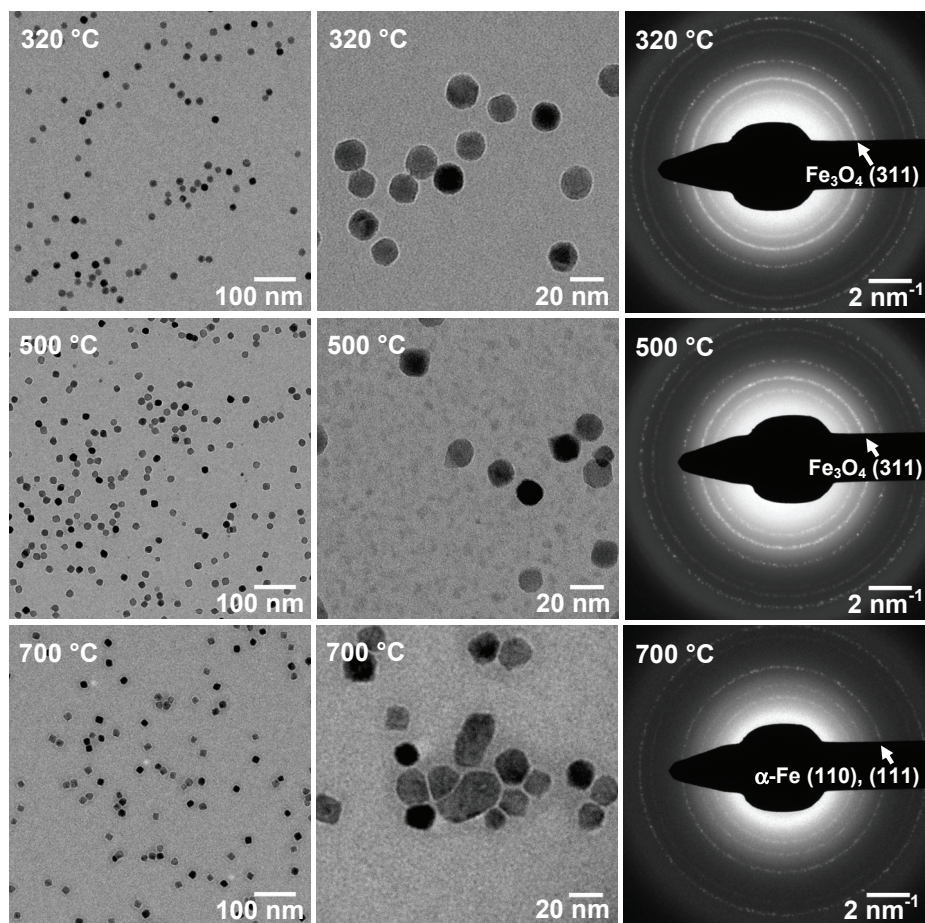


**Figure 7.10** TEM images of the 18 nm nano particles (4.5% loading) after one hour of flowing CO at the indicated temperature. The pictures on the left are overview images, the pictures in the middle a zoom in of the particles, and the right images the diffraction patterns corresponding to the particles. The arrow in the right image depicts the brightest line in the diffraction pattern.

When the reduction temperature is increased to 500 °C, part of the particles becomes faceted, which shows up as cubic structures in the TEM pictures. However, the diffraction pattern is still that of magnetite and, thus, although some particles are faceted any sign of reduction is not visible by the TEM images.

At 700 degrees centigrade almost all the particles become faceted and have a cubic shape. Although some of the particles have agglomerated, most of them appear to



be close to one another, yet not really touching, as a small gap is visible between them. However, the particles that are in a close vicinity of one another affect each other. This can be seen through the shape of the particles, which when another particle is close by does not stay cubic, but changes into faceted particles of various shapes. From the diffraction pattern it is clear that not all particles are fully reduced. Though the most bright diffraction ring has decreased a lot in intensity and the ring that can be appointed to the metal phase becomes brighter, this temperature is still not sufficient to completely reduce the magnetite particles. Again, we suspect that the reason why no core-shell particles are observed can be attributed to the passivation process, which seems to prevent the formation of a thin protective oxide layer because re-oxidation proceeds too rapidly.

#### 7.3.4.4 Reaction with $H_2:CO$ (2:1)

Reaction of the 18 nm magnetite nano particles with  $H_2$  and CO at a ratio of 2:1 at 380 °C was performed for about a week. The results for both particle loadings, i.e., 4.5 and 18% are shown in Figure 7.11. Regardless of the loading, the particles appear to behave similarly, although a slightly higher percentage has agglomerated at the higher coverage. However, most of the particles did not agglomerate, while their morphology changed significantly and some of the particles have opened up. There is no apparent favored morphology that the particles possess and most of them are oddly shaped. The diffraction pattern still resembles magnetite and although iron catalysts are known to form carbide phases once synthesis gas is used as reactive gas [19-25], no evidence of any kind of carbide phase can be found in the diffraction pattern.

The most interesting result that was obtained with this experiment is that some of the particles after reaction of synthesis gas for a week at 380 °C did not change morphology at all –as shown by the  $d$ -spacings in the bottom pictures of Figure 7.12–, while the morphology of others changed completely (top image in Figure 7.12).

So, although the monodisperse calcined nano particles appear similar in shape and size in TEM images, their behavior is far from the same. This observation implies that one needs to be careful when interpreting results from certain spectroscopy techniques. For example take X-ray photoelectron spectroscopy (XPS); from these results you will get an overall composition of the particles, which hypothetically say exists for 70% out of magnetite and 30% out of metallic iron. Because the prepared particles are so homogeneous in size and shape, researchers tend to assume that the composition of these particles then is 30% metallic iron and 70% magnetite (most probably a core-shell particle). However, our results show that some of the particles are completely magnetite (did not change at all), whereas others are mixed phases and have completely different shapes. Thus, although the overall composition might look like 3:7 (metallic iron:magnetite) in XPS, one needs to be careful to suggest that this is the

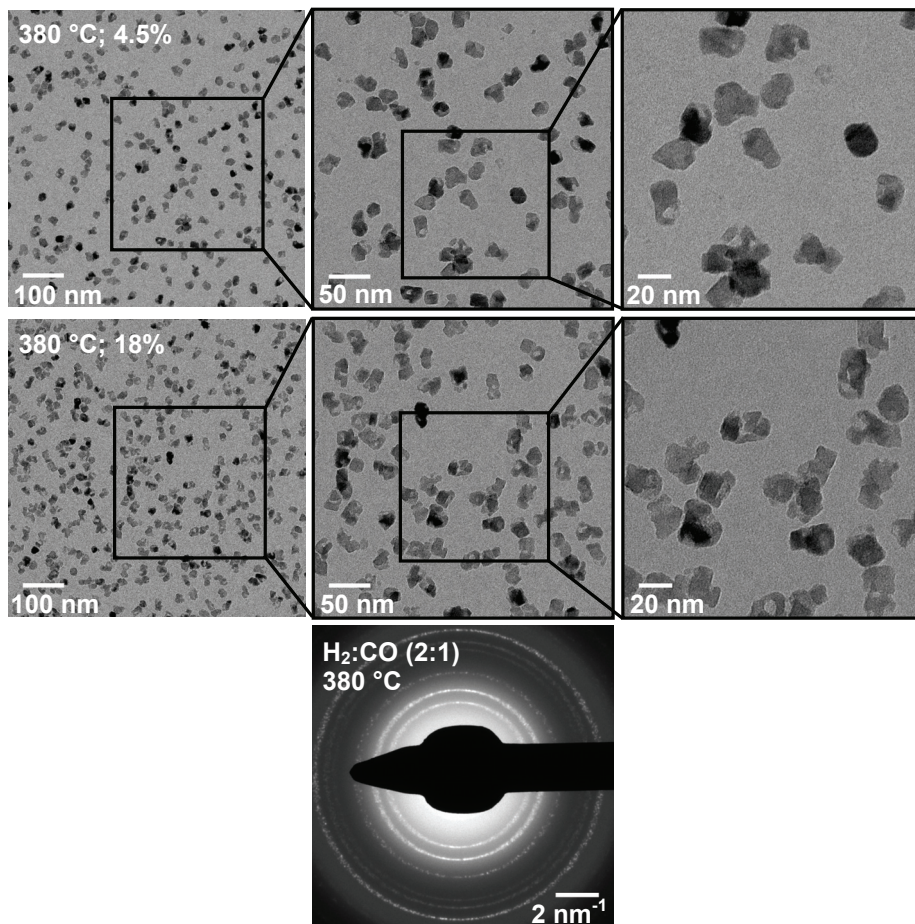


**Figure 7.11** TEM images of the 18 nm iron oxide nano particles after seven days of  $H_2:CO$  (2:1) at 380 °C. The top row pictures show the lower coverage of nano particles, while the middle row the higher loading. For both rows the left image depicts an overview, which is zoomed in for the given area when proceeding to the right. The bottom image shows the diffraction pattern of the particles, which resembles the  $Fe_3O_4$  phase.

overall particle composition, as our results show otherwise.

Besides the reaction of the 18 nm magnetite nano particles with synthesis gas for 7 days at 380 °C, another reaction was performed in which the magnetite particles (18% loading) were pre-reduced with  $H_2$  at 700 °C for one hour and subsequently reacted with synthesis gas at 380 °C for 2 days. The TEM images are depicted in Figure 7.13.

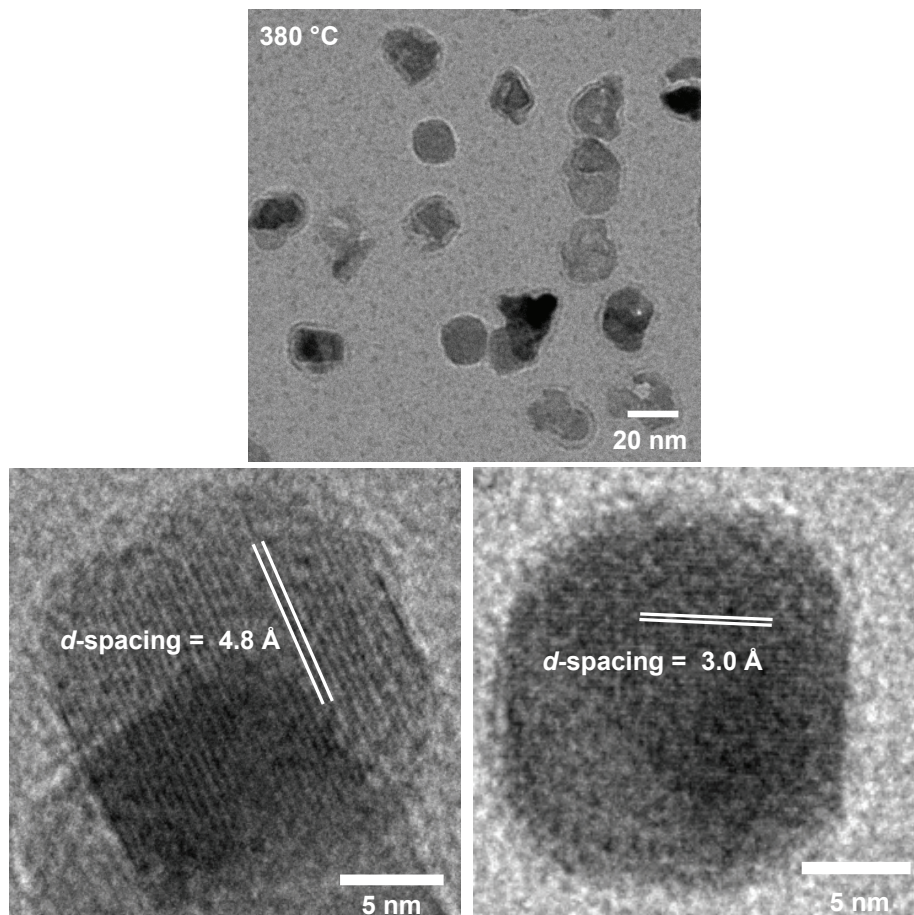


**Figure 7.12** TEM images of the 18 nm iron oxide nano particles after seven days of  $H_2:CO$  (2:1) at 380 °C. In the top image different particles are visible; particles that have agglomerated, particles that are oddly shaped, particles that did not change at all, and particles that have some kind of layer surrounding them. In the lower images, particles are shown which did not change at all and still show typical d-spacings of  $Fe_3O_4$ .

Pre-reducing the magnetite particles leads to an almost uniform particle behavior in which many of the particles have opened up, although some of the particles did not change. The diffraction pattern, however, is still magnetite. Because no carbide phases were observed, the open particles have most likely magnetite shells, which were created by re-oxidation of the reduced iron particles under reaction conditions ( $H_2:CO$  (2:1) at 380°C).



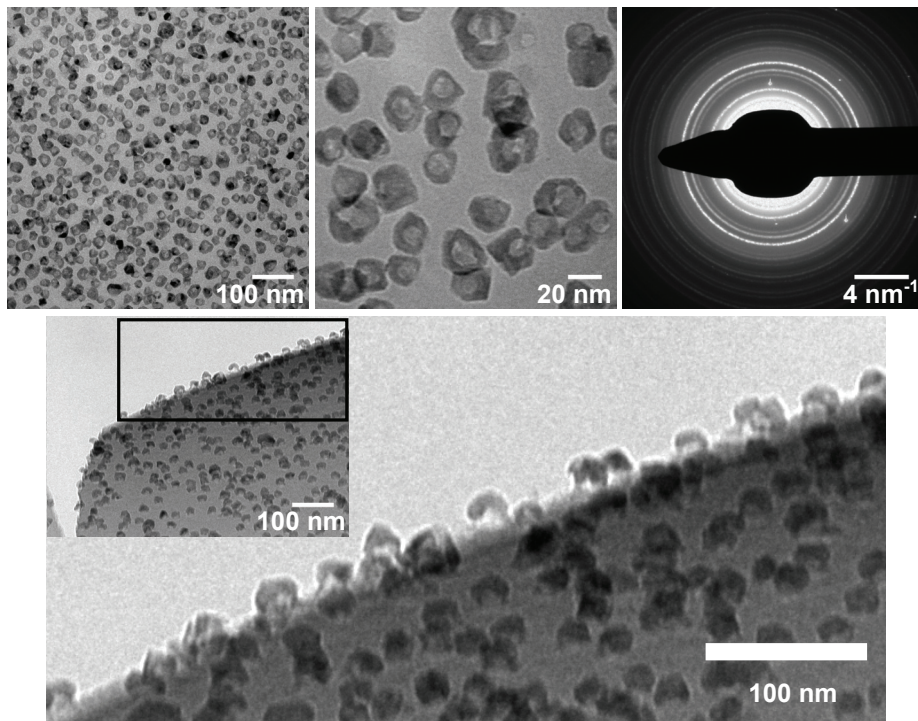


**Figure 7.13** TEM images of the 18 nm magnetite particles pre-reduced with  $H_2$  at 700 °C for one hour and subsequently treated in flowing  $H_2$  and :CO (2:1) for 2 days at 380 °C. The top images from left to right show the particles in an overview picture, then a zoom in, and lastly the diffraction pattern, which resembles magnetite. The bottom picture displays the particles from the side, with the zoom in as the large image, in which hollow particles are clearly observed.

## 7.4 Discussion

The possibility to apply a flat  $SiO_2$  model support for studying the composition and morphology of monodisperse iron oxide nano particles was investigated in this Chapter. The particles were spin-coated onto the flat silica support and ‘anchored’ via calcination. The particle (size) distribution, morphology, and composition were checked by TEM imaging and diffraction. The study revealed that although the particles appear homogeneous in size and shape, their chemistry is not. Using CO results in a larger fraction of faceted particles than  $H_2$ , while using both gases in a 2:1 ( $H_2$ :CO) ratio leads to particles of various shapes. In addition, the model was shown to be suited for synchrotron measurements, which enables us to in-situ determine the composition of the iron oxide nano particles during reactions. However, while investigation of noble metals with the model system is rather straightforward, studying iron is much more complicated due to its high reactivity and ease to re-oxidize. Hence, although the

investigation of iron oxide nano particles is feasible with the model system, we encountered several issues, which will be highlighted in the following session.

First one is the particle–support interaction. This interaction determines the degree in mobility of the nano particles on the silica support. Hence, a decrease in particle mobility on the surface is the result of a stronger particle–support interaction. Calcination at 450 °C leads to better ‘anchoring’ of the particles to the SiO<sub>2</sub> support than ozonation at 60 °C does. Whether this anchoring proceeds via Fe–O–Si bonds or that some of the Fe atoms in the particle are substituted for Si atoms [26], thus ‘incorporating’ the particle into the support we do not know. What we do know is that the particle–support interaction is not negligible and can be varied –most likely by changing the calcination temperature– noticeably.

Secondly, differences in preparation method lead to different interaction with the support. Iron oxide particles were found to flatten out on the silica model support after calcination by Moodley et al. [27], thus appearing larger in the TEM images. However, we did not observe such a behavior for our particles, which simply maintained the same size. There might be a few reasons why we observe a different behavior. First, it should be noted that Moodley et al. etched the silicon wafers before spin-coating, whereas we did not do this. Second, Moodley et al. used an O<sub>2</sub> / Ar mixture for calcination, whereas we used air (containing water). Third, the particles of Moodley et al. were prepared by a different method [4], where the iron-oleate complex was synthesized first and subsequently used in the reaction to prepare the particles. Perhaps this method leads to a different iron oxide formation than our method, which appears to be more reactive. However, whatever the reason is, the particles of Moodley et al. have a larger tendency to form Fe–O–Si bonds than our nano particles.

The third issue to take into account is that the support also plays a role in the reduction of the magnetite particles. Quite high reduction temperatures of 800 °C are required to completely reduce the particles with H<sub>2</sub>, which is similar to previous reported reduction temperatures of iron oxides on Si supports [20,28]. Moreover, the degree of reduction has been shown to be affected by the support [29,30] at which the reduction temperature can change significantly as well [31]. Although reduction of magnetite toward metallic iron should proceed via wüstite (FeO) [20,28], we could not observe this phase by TEM, probably due to the instability of wüstite in air [20]. On the other hand, the XANES and EXAFS results show neither a true FeO nor Fe signal. We believe, therefore, that at a reduction temperature of 700 °C, which is still insufficient to completely reduce magnetite, the particle consists of a mixture of both FeO as well as metallic iron in the outer layer and magnetite as core. As these XANES and EXAFS measurements were performed as proof of principle experiments, we did not use another reducing agent nor reduce the particles at 800 °C to see whether complete reduction is indeed possible. Further research would be needed to verify this.

Finally, we note the apparently absence of carbides when CO or synthesis gas is

used as reactive gas. Applying CO as reduction gas, the phases that we detect with TEM are magnetite and some metallic iron. Although several groups have reported the formation of carbides when iron catalysts are activated with CO [20-23,25], it should be noted that their catalysts possess promoters such as potassium and copper and have been prepared by precipitation methods, thus having large size differences. Moreover, another important difference is that the iron oxide catalysts from these groups are mixtures between  $\text{Fe}_2\text{O}_3$  and  $\text{Fe}_3\text{O}_4$ , whereas our prepared particles consist of  $\text{Fe}_3\text{O}_4$  only. The group of Li [20,25] observed that the initial oxide phase present in the catalyst plays a significant role in the final phase of the catalyst after CO activation. When the amount of  $\text{Fe}_3\text{O}_4$  in the initial catalyst was raised, the carbide phases after CO activation decreased. These results seem to suggest that carbide phases are more readily formed from hematite than magnetite. Additionally, Rao et al. [23] discovered that the amount of  $\text{SiO}_2$  in the catalyst influences the formation of carbides as well when treated by CO, in the sense that a higher  $\text{SiO}_2$  content leads to lower carbide formation. Taking both results into account, i.e., the more difficult formation of carbides from magnetite than hematite and the use of a  $\text{SiO}_2$  support with a relatively large support-particle interaction, formation of carbide phases by using CO might be extremely difficult on our uniform magnetite nano particles.

When the 18 nm magnetite nano particles are placed into a  $\text{H}_2$ :CO (2:1) environment (either pre-reduced with  $\text{H}_2$  at 700 °C or not) diffraction patterns show magnetite and maybe a small amount of iron in its metallic form, but yet again no carbide phases. Nonetheless, the particles underwent structure changes, as most of them did not retain their shape. Furthermore, some of the particles from the non pre-reduced nano particles have a small layer surrounding them (Figure 7.12). What this layer is, we are not sure, though we have observed such as layer after  $\text{H}_2$  treatment as well, while not for CO. Thus, it is not as likely that the layer is carbon, as was observed by Shroff et al. [24]. Because (partial) encapsulation of iron particles on a  $\text{SiO}_2$  support after  $\text{H}_2$  reduction by an iron silicate layer has been reported previously by Wielers et al. [32], it is more probable that the observed layer consists of iron silicate instead. Moreover, formation of iron silicates is known to occur when  $\text{H}_2$  is used to reduce iron oxides ( $\text{Fe}_2\text{O}_3$ ) on  $\text{SiO}_2$  supports [33,34].

There appears to be a large difference in morphology between the non- and pre-reduced particles when placed under a  $\text{H}_2$ :CO (2:1) atmosphere. When the particles are pre-reduced with  $\text{H}_2$  at 700 °C most of them become hollow, while this is not the case for the calcined only particles. Apparently most of these final hollow particles were reduced toward the metallic phase, and once under synthesis gas environment have been re-oxidized toward  $\text{Fe}_3\text{O}_4$  as seen by the diffraction pattern. Since the diffraction pattern of magnetite is still so bright, this seems to suggest that the shell of these hollow particles consists of crystalline magnetite formed at 380 °C.

Although as concluded on the structure no carbide formation was observed with

TEM imaging and diffraction, an electron energy loss (EEL) detector on the TEM would be needed to really verify this result by mapping the elemental composition of the particles, as it may be that amorphous carbide phases are present. Moreover, the EEL detector will be helpful to figure out what the composition of the layer around the particles after H<sub>2</sub> reduction is and whether the shell of the open particles after syngas treatment is crystalline magnetite or something else. In addition, passivation needs to be done with much more care (in the glove-box) than we did in this study to be sure to rule out passivation effects.

### **7.5 Concluding Remarks / Preliminary Outlook**

Although few experiments are conclusive, the potency of a flat model approach for the investigation of iron oxide nano particles is shown in this Chapter. The main advantage of using a thin flat substrate (SiO<sub>2</sub> in our case) as a model support is the possibility to image the particles with TEM. Hence, these TEM images were used to provide valuable information on the particle (size) distribution and the morphology change as a function of the different chemical treatments (H<sub>2</sub>, CO, and H<sub>2</sub>:CO (2:1)). Moreover, TEM diffraction was employed to identify the composition of the particles (oxide, carbide, or metal) before and after chemical treatment. In addition, the use of XANES and EXAFS was shown to be feasible for the flat model system. This enables the possibility to also determine the composition of the particles during reaction. Knowing both the composition as well as the morphology of the particles during chemical reaction is a powerful tool to get a better understanding of the respective reaction on the nano-size level, which would not have been possible without the flat model approach.

One of the most remarkable results that we obtained in this study is that the iron oxide nano particles appearing homogeneous in size and shape, do not behave similarly. However, most spectroscopy studies only provide a general picture of the composition of the catalyst after reaction, which according to our results is not necessarily correct as the composition and morphology varies from particle to particle. To understand the origin in differences in particle morphology and composition after reaction for the homogeneously prepared particles, studies should, thus, be focused on a more local level instead.

As this study was of an exploratory nature to show the applicability of iron oxide nano particles on planar SiO<sub>2</sub> samples in TEM and synchrotron measurements, a lot of questions were raised during the study that still need to be answered. Some of these are:

- The role of the support; does it stabilize the magnetite particles? Does SiO<sub>2</sub> prevent the formation of carbides?
- The role of the oxide phase; is Fe<sub>3</sub>O<sub>4</sub> less reactive than Fe<sub>2</sub>O<sub>3</sub>? Does Fe<sub>3</sub>O<sub>4</sub> hinder the formation of carbides?

➤ The role of passivation; does water block the formation of core-shell particles?

The method that we showed in this Chapter is suited to answer these questions. However, further research is needed. Therefore, in the final Chapter an outlook will be provided to help solve these questions.

## References

- [1] Y.-H. Deng, C.-C. Wang, J.-H. Hu, W.-L. Yang, S.-K. Fu, *Colloids Surf., A* **262** (2005) 87.
- [2] T. Hyeon, S. S. Lee, J. Park, Y. Chung, H. B. Na, *J. Am. Chem. Soc.* **123** (2001) 12798.
- [3] F. Jiao, J.-C. Jumas, M. Womes, V. Chadwick Alan, A. Harrison, G. Bruce Peter, *J. Am. Chem. Soc.* **128** (2006) 12905.
- [4] J. Park, K. An, Y. Hwang, J.-G. Park, H.-J. Noh, J.-Y. Kim, J.-H. Park, N.-M. Hwang, T. Hyeon, *Nat. Mater.* **3** (2004) 891.
- [5] S. Peng, S. Sun, *Angew. Chem. Int. Ed.* **46** (2007) 4155.
- [6] S. Peng, C. Wang, J. Xie, S. Sun, *J. Am. Chem. Soc.* **128** (2006) 10676.
- [7] F. X. Redl, C. T. Black, G. C. Papaefthymiou, R. L. Sandstrom, M. Yin, H. Zeng, C. B. Murray, S. P. O'Brien, *J. Am. Chem. Soc.* **126** (2004) 14583.
- [8] M. Yin, Z. Chen, B. Deegan, S. O'Brien, *J. Mater. Res.* **22** (2007) 1987.
- [9] W. W. Yu, J. C. Falkner, C. T. Yavuz, V. L. Colvin, *Chem. Commun.* (2004) 2306.
- [10] D. B. Bukur, X. Lang, J. A. Rossin, W. H. Zimmerman, M. P. Rosynek, E. B. Yeh, C. Li, *Ind. Eng. Chem. Res.* **28** (1989) 1130.
- [11] D. B. Bukur, Z. Nowicki, R. K. Manne, X. Lang, *J. Catal.* **155** (1995) 366.
- [12] A. K. Datye, M. D. Shroff, M. S. Harrington, A. G. Sault, N. B. Jackson, *Stud. Surf. Sci. Catal.* **107** (1997) 169.
- [13] T. Herranz, S. Rojas, F. J. Perez-Alonso, M. Ojeda, P. Terreros, J. L. G. Fierro, *J. Catal.* **243** (2006) 199.
- [14] A. J. H. M. Kock, H. M. Fortuin, J. W. Geus, *J. Catal.* **96** (1985) 261.
- [15] A. G. Sault, *J. Catal.* **140** (1993) 121.
- [16] H. H. Storch, N. Golumbic, R. B. Anderson, *The Fischer-Tropsch and Related Syntheses*, John Wiley & Sons, Inc., New York, 1951.
- [17] C. M. Wang, D. R. Baer, J. E. Amonette, M. H. Engelhard, Y. Qiang, J. Antony, *Nanotechnology* **18** (2007) 255603/1.
- [18] A. D. Smigelkas, E. O. Kirkendall, *Trans. Am. Inst. Min. Eng.* **171** (1947) 130.
- [19] E. de Smit, A. M. Beale, S. Nikitenko, B. M. Weckhuysen, *J. Catal.* **262** (2009) 244.
- [20] T. Li, Y. Yang, Z. Tao, C. Zhang, H. Xiang, Y. Li, *Fuel Process. Technol.* **90** (2009) 1247.
- [21] R. J. O'Brien, L. Xu, D. R. Milburn, Y.-X. Li, K. J. Klabunde, B. H. Davis, *Top. Catal.* **2** (1995) 1.
- [22] R. J. O'Brien, L. Xu, R. L. Spicer, B. H. Davis, *Energy Fuels* **10** (1996) 921.
- [23] K. R. P. M. Rao, F. E. Huggins, V. Mahajan, G. P. Huffman, V. U. S. Rao, B. L. Bhatt, D. B. Bukur, B. H. Davis, R. J. O'Brien, *Top. Catal.* **2** (1995) 71.
- [24] M. D. Shroff, D. S. Kalakkad, K. E. Coulter, S. D. Koehler, M. S. Harrington, N. B. Jackson, A. G. Sault, A. K. Datye, *J. Catal.* **156** (1995) 185.
- [25] B. Wu, L. Tian, H. Xiang, Z. Zhang, Y.-W. Li, *Catal. Lett.* **102** (2005) 211.
- [26] C. R. F. Lund, J. A. Dumesic, *J. Phys. Chem.* **85** (1981) 3175.
- [27] P. Moodley, F. J. E. Scheijen, J. W. Niemantsverdriet, P. C. Thüne, submitted to *Top. Catal.* (2009)
- [28] H. H. P. Yiu, M. A. Keane, Z. A. D. Lethbridge, M. R. Lees, A. J. el Haj, J. Dobson, *Nanotechnology* **19** (2008) 255606/1.
- [29] H. Jung, W. J. Thomson, *J. Catal.* **128** (1991) 218.
- [30] J. Liu, J. Shen, X. Gao, L. Lin, *J. Therm. Anal.* **40** (1993) 1245.
- [31] A. Venugopal, M. S. Scurrell, *Appl. Catal., A* **258** (2004) 241.
- [32] A. F. H. Wielers, A. J. H. M. Kock, C. E. C. A. Hop, J. W. Geus, A. M. Van der Kraan, *J. Catal.* **117** (1989) 1.



- [33] E. de Smit, I. Swart, J. F. Creemer, G. H. Hoveling, M. K. Gilles, T. Tyliczszak, P. J. Kooyman, H. W. Zandbergen, C. Morin, B. M. Weckhuysen, F. M. F. de Groot, *Nature* **456** (2008) 222.
- [34] C.-H. Zhang, H.-J. Wan, Y. Yang, H.-W. Xiang, Y.-W. Li, *Catal. Commun.* **7** (2006) 733.

# 8

## Summary and Outlook

### The Surface Chemistry of CO on Iron and other bcc Metals

#### *8.1 Summary*

Synthesis gas is an important intermediate in the preparation of a wide variety of chemicals. The way this synthesis gas is used is largely determined by the chemistry of carbon monoxide. For the formation of synthetic hydrocarbon fuels, CO needs to be dissociated. Therefore, the main inspiration behind the research in this dissertation is to elucidate the dissociation reaction of carbon monoxide on body centered cubic (bcc) transition metals –in particular iron– with respect to reaction kinetics and the influence of adsorbate interactions. This was done at different levels of control and definition using computations and a variety of surface science techniques, i.e., plane-wave density functional theory (PW-DFT), temperature programmed desorption (TPD), static secondary ion mass spectrometry (SSIMS), and low energy electron diffraction (LEED). The system closest to real catalysts –iron oxide nano particles on a flat silica support– was investigated using transmission electron microscopy (TEM), electron diffraction, X-ray absorption near edge spectroscopy (XANES), and extended X-ray absorption fine structure (EXAFS). In contrast to the other research in this thesis, this study explored the possibility of using a flat model approach for the investigation of the morphology and composition behavior of iron oxide nano particles under different reactive environments.

CO adsorption and dissociation on the (100) surfaces of molybdenum (Mo) and tungsten (W) was extensively studied by PW-DFT calculations for different CO coverages (*Chapter 3A and B*). On both surfaces, CO preferentially adsorbs in fourfold hollow sites with a tilted geometry, which is the precursor for dissociation provided temperature allows. At coverages higher than 0.5 monolayer (ML) CO starts to occupy on-top sites, which eventually completely excludes the fourfold hollow bound CO at full monolayer coverage. As the high-temperature desorption peaks were shown to be

kinetically limited by the activation of the CO bond with the surface and not by recombination of atomic carbon and oxygen, desorption of CO proceeds through first order kinetics for all desorption states.

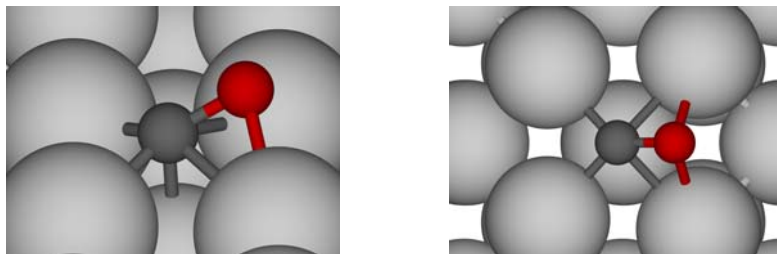


**Figure 8.1** Side- (left) and top-view (right) images of the most stable adsorption geometry of CO, that is, tilted CO, on the (100) surface of Mo, W, Fe, and Cr.

In addition to Mo and W, the (100) surfaces of iron (Fe) and chromium (Cr) were studied by PW-DFT calculations for CO adsorption and dissociation (*Chapter 4*). This allowed us to make a comparison between CO on all the (100) surfaces of these bcc metals. For all four metals, the adsorption energy and tilting angle are coverage-independent between 0.25 and 0.5 ML of CO, whereas the CO stretching frequency is affected by coverage changes and blue-shifts for Fe and Cr and red-shifts for Mo and W at increasing CO coverage. This was explained by geometry changes of the surface atoms of the metal, which change the  $\sigma$ -donation and  $\pi$ -back-donation of electrons from the metal to the CO bond. Dissociation of CO is an exothermic and facile process at low coverages –below 0.25 ML–, which due to the profound influence of lateral interactions at higher coverages –above 0.25 ML– becomes much less exothermic for Mo, W, and Cr, and even thermoneutral for Fe. On the other hand, the activation energy of dissociation does not change significantly, which is a behavior that does not follow the Brønsted-Evans-Polanyi (BEP) relationship. The applicability of the BEP relationship, therefore, appears to be constrained to certain conditions, such as coverage.

For the lower CO coverage, that is, 0.25 ML, two alloy systems, namely  $\text{Fe}_3\text{Mo}(100)$  and  $\text{Fe}_3\text{Cr}(100)$  were included as well. Interestingly, the adsorption energy of CO on the alloys could be obtained by a linear combination of the adsorption energies of CO on the respective metals according to the following equation:

$$E_{\text{ads}}(\text{CO}/\text{Fe}_3\text{X}) = 3/4E_{\text{ads}}(\text{CO}/\text{Fe}) + 1/4E_{\text{ads}}(\text{CO}/\text{X}) \quad (\text{eq. 8.1.1})$$

Similarly, a relation was acquired for the activation energy of CO dissociation:

$$E_{\text{act}}(\text{CO}/\text{Fe}_3\text{X}) = 1/2E_{\text{act}}(\text{CO}/\text{Fe}) + 1/2E_{\text{act}}(\text{CO}/\text{X}) \quad (\text{eq. 8.1.2})$$

Furthermore, scaling relations were found for the adsorption energy of carbon as well as both dissociation products against the adsorption energy of tilted CO and activation energy of dissociation on the metal(-alloys) Fe, Mo, W, Cr,  $\text{Fe}_3\text{Mo}$ , and  $\text{Fe}_3\text{Cr}$  at a CO

coverage of 0.25 ML (*Chapter 4*). The importance of such energy scaling relations is that they enable predictions for the behavior of CO on similar surfaces on the basis of inter and extrapolation. The groups of Nørskov [1] and of Hu [2,3] have proposed such relations for adsorption on face centered cubic (fcc) metals. Our –modest– contribution to the subject of energy scaling is that we have explored such relations for adsorption on the bcc metals and alloys.

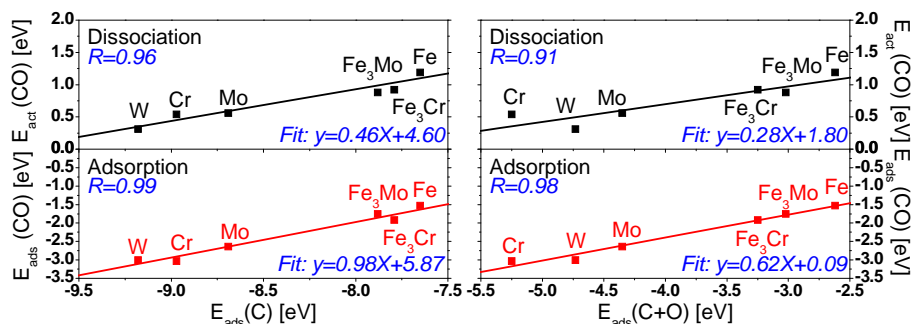


**Figure 8.2** Adsorption energies and activation energies of dissociation of CO on (100) surfaces plotted against (left) the adsorption energy of carbon with respect to carbon in the gas-phase and (right) the adsorption energy of the dissociation products carbon and oxygen with respect to CO in the gas-phase at a surface coverage of 0.25 ML CO.

With the aim to validate the computational results for CO adsorption and dissociation on Fe(100) we attempted to measure the kinetics of the CO dissociation reaction, in an approach similar as was done previously for NO on the surface of rhodium [4,5], using SSIMS. Whereas molecular NO and its dissociation products on rhodium showed up clearly in secondary ions of the type  $\text{Rh}_2(\text{NO})^+$ ,  $\text{Rh}_2\text{N}^+$ , and  $\text{Rh}_2\text{O}^+$ , such molecular clusters could not or hardly be observed for CO on iron. Hence, determination of kinetic parameters of the dissociation reaction of CO on polycrystalline iron and Fe(100) proved to be on the edge of what is possible with SSIMS (*Chapters 5 and 6*). We had to rely on the effect of the work function on the SSIMS intensity of the secondary iron ions. The principle behind this is that a higher work function diminishes the chance that a positive ion is neutralized upon ejection. As CO increases the work function of iron, its disappearance by dissociation or desorption decreases the work function, and hence, the signal intensity of the  $\text{Fe}^+$  ion changes as well. It appeared possible to relate the ion intensity to the state of CO on the surface in this way. However, collected activation energies of dissociation using a kinetic model of an Arrhenius type were much lower than reported ones, 57-79 against 103-118 kJ/mol. We assign this to the possibility of defect chemistry, as SSIMS is known to induce defects on the surface, and, moreover activation energies of CO dissociation on stepped surfaces of iron have been reported to be in the order of 60-90 kJ/mol [6].

Dissociation of CO is shown to be kinetically favored over desorption. But, because CO adsorbs at the same sites as the dissociation products, dissociation becomes hampered at certain CO coverage and desorption of part of the CO molecules is required to open up sufficient space for the remaining part to dissociate. Desorption of CO at low temperatures proceeds through first order desorption kinetics, while the high-temperature desorption of CO is quasi first order (limited by the activation energy of desorption and not recombination). In experiments on poly crystalline iron where carbon or oxygen were pre-adsorbed, CO binds weaker to the surface and dissociation of CO is partially blocked (*Chapter 5*). The same experiments were repeated on the better defined Fe(100) surface. Here pre-adsorption of carbon or oxygen was seen to block desorption of CO from fourfold hollow and bridged positions, and in addition it obstructed the CO dissociation (*Chapter 6*).

Investigation of the behavior of iron oxide nano particles as to morphology, structure, and composition on a flat SiO<sub>2</sub> model support was shown to be very well possible as a function of different chemical treatments (H<sub>2</sub>, CO, and H<sub>2</sub>/CO) (*Chapter 7*). The synthesis method employing a one-pot mixture of goethite and oleic acid, produced Fe<sub>3</sub>O<sub>4</sub> particles of uniform size, which could straightforwardly be deposited on flat supports by spin-coating. Owing to the use of special wafers with windows etched in the back side of the wafers, TEM could be used to image the particles and to obtain electron diffraction patterns. Moreover, the system was established as a suited method for synchrotron experiments such as XANES and EXAFS. However, due to the reactivity and ease of re-oxidation of the iron nano particles a more delicate approach, such as passivation in a glove-box or in-situ work, would be required than the one used in this exploratory study. Nonetheless, the study proved the feasibility of the flat model approach and revealed that particles of homogeneous size and shape behave differently under the same reaction conditions. Apparently the prepared particles appear homogenous in TEM images, yet we seem unable to control certain parameters that lead to the difference in behavior. Perhaps the –as so often in catalysis research– elusive interaction of the particles with the support is different from one particle to another, which might be caused by an inhomogeneous support. Additionally, the difference in intrinsic reactivity / inertness of Fe<sub>3</sub>O<sub>4</sub> is a likely cause of the dissimilar behavior, possibly determined by the crystallinity of the particle, but maybe also the differences in reactivity between surface facets.

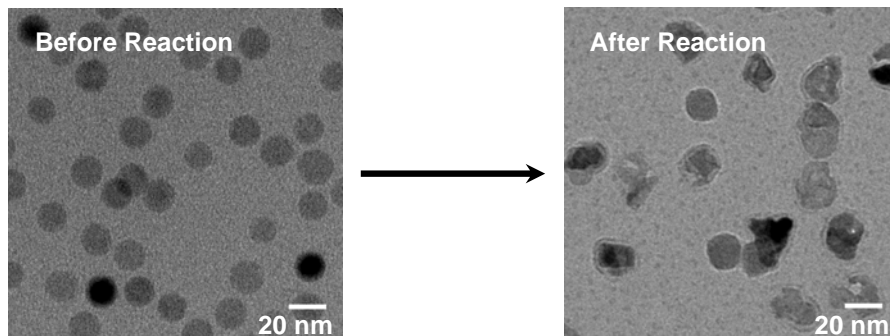


**Figure 8.3** Example of a TEM image of nano particles on a special 'window' support showing iron oxide before and after reaction in synthesis gas. The images illustrate the difference in behavior of apparently homogeneously sized and shaped particles. While some particles have clearly reacted, others remain virtually unchanged, implying that certain parameters such as for example the interaction between the particles and the silica substrate are not under control. Note that the images are purely meant for illustrating purposes; they do not show the exact same particles before and after reaction.

## 8.2 Outlook

### 8.2.1 Computational Studies on the bcc Metals and Alloys

The surface chemistry of CO on iron and other bcc metals, and the influence of adsorbate interactions stood central in this dissertation. Calculations were performed for (100) surfaces of iron and various other metals (*Chapters 3 and 4*) with the idea to possibly alloy iron with one of the examined bcc metals to eventually affect the selectivity of the surface, by changing the chain-growth parameter and product spectrum of the Fischer-Tropsch synthesis (FTS). We note, however, that the bcc metals are not stable under synthesis gas. Iron for example forms carbides in the Fischer-Tropsch synthesis, and these carbides are held responsible for the actual reactivity [7]. Since the time that we investigated the alloy systems, we have learnt that Fe-Cr or Fe-Mo combinations are bound to segregate into iron carbide and chromium or molybdenum oxide under synthesis gas. Hence, our results are largely of interest for the early stages of such catalytic surfaces in synthesis gas reactions, but not for the working catalyst.

Nevertheless, as the iron carbides appear more active in FTS, calculations should be more focused on carbides in relation to FTS. In particular the FT mechanism, although a discussion point for almost 85 years, has only been proposed for metallic iron. Obviously, the FT mechanism will be different on iron carbides, and thus, needs to be elucidated. Recently our group has proposed such a mechanism for the methanation reaction on the  $\text{Fe}_5\text{C}_2$  surface [8]. In addition to clarifying the FT mechanism, it would be valuable to explore what is the most active carbide phase for FTS by means of computational techniques. This would open up the possibility to tune this most active

carbide phase in such a manner that with an optimum activity the desired products can be obtained. Lastly, besides iron carbides, iron oxides are formed as well in the FT reaction, which are known to possess water-gas-shift activity. Research should focus on the reaction mechanism of this process as well, as it might help to produce a much more efficient catalyst in low H<sub>2</sub> to CO ratio syngas feeds.

### 8.2.2 UHV Techniques

Iron, Fischer-Tropsch chemistry and UHV surface science form a somewhat problematic combination. Metallic iron is reactive, and therefore, difficult to control under UHV, while Fischer-Tropsch needs higher pressures to retain at least some hydrogen on the surface at reaction temperature. Nevertheless, some relevant surface reaction steps such as CO dissociation could be studied in this dissertation.

Hence, apart from DFT calculations, kinetic parameters were obtained for the dissociation reaction of CO on poly crystalline iron and Fe(100) (*Chapters 5 and 6*). Because SSIMS was operated on the edge of what is possible to determine kinetic parameters, including the influence of lateral interactions of either carbon or oxygen was not possible. Additionally, since SSIMS induces defects on the surface, the measured activation energy of CO dissociation (half of that reported in literature) might possibly be the activation energy of dissociation of CO on defects. In fact, the measurement relied on the work function changes as reflected in the SSIMS intensities.

Supplementary techniques are needed to confirm the obtained kinetic data. One of these techniques that would be suited is the Kelvin-Probe (KP), which determines the work function of the surface in a non-destructive way [9]. Hence, compared to SSIMS the KP does not induce defects on the surface, and therefore, kinetic data obtained can only be ascribed to the dissociation reaction of CO. Unfortunately, the downside of the KP is that the technique cannot distinguish species from one another on the surface. Synchrotron X-ray photoelectron spectroscopy (XPS), on the other hand, allows real-time quantification of all the species on the surface, i.e., carbon, oxygen, and CO. Moreover, the influence of pre-adsorbed carbon or oxygen on the dissociation kinetics of CO can be made visible with this technique.

### 8.2.3 'In-Situ' Techniques

The idea behind the use of a flat model approach for the investigation of the morphology and composition behavior of iron oxide nano particles under different chemical environments was the possibility to employ TEM, XANES, and EXAFS, which all can be applied 'in-situ' (*Chapter 7*). Because of the exploratory nature of the study, the main goal consisted of showing the applicability of investigating iron oxide nano particles on a flat substrate by these three techniques. Although this main goal was

achieved, the study raised many other questions, from which the most important ones are summarized inside a separate text box below. These questions are of such nature that at least a new project for a PhD candidate is required to answer them. In the next few paragraphs a list of ideas is presented for the next PhD candidate to use in the pursuit of the answers to the raised questions.

Open questions from the studies with  $\text{Fe}_3\text{O}_4$  nano particles  
on a flat silica support in Chapter 7

- Silica support:
  - Does it prevent reduction of the magnetite particles?
  - Does it produce iron-silicates?
  - Does it prevent the formation of iron carbides?
- Particles consisting of  $\text{Fe}_3\text{O}_4$ :
  - Are they less susceptible for reduction than  $\text{Fe}_2\text{O}_3$  particles?
  - Do they hinder the formation of iron carbides?
  - Is the crystallinity more important for the reducibility?
- Is the shell of the pre-reduced particles formed under syngas treatment crystalline  $\text{Fe}_3\text{O}_4$ ?
- What is the reason that particles of the same composition and morphology on the same  $\text{SiO}_2$  support behave, nevertheless, differently from one another?
- Would such differences remain when studies could be done under truly in-situ conditions?

One of the most important factors that need to be elucidated is the effect of passivation. To understand passivation effects, the reduced iron particles would need to be passivated under different conditions; (1) use of dry  $\text{O}_2$  in argon and vary the percentage of  $\text{O}_2$ , (2) use of wet  $\text{O}_2$  in argon and vary the percentage of both oxygen and water, (3) use of a glove-box, and (4) compare these results with a sample that was directly placed in a TEM transfer-cell after reduction. Of course, the ideal situation would be to do all studies under in-situ conditions. However, possibilities for this are limited.

Once the major passivation effects have been clarified, the influence of the oxide phase and crystallinity of the particles with respect to reducibility needs further investigation. Contrary to common experience that iron oxides can readily be reduced to the metallic phase, we found strong resistance to reduction in the  $\text{Fe}_3\text{O}_4$  nano particles. Hence, instead of magnetite particles, hematite, or goethite particles should be prepared with similar size. Moreover, these particles would require to be either crystalline, amorphous, or a mixture. Then, reduction experiments need to be performed with various reduction gases ( $\text{H}_2$ ,  $\text{CO}$ , and syngas) to understand the difference.

Apart from the crystallinity and difference in oxide phase, the support plays a large role as well. Silica may prevent the reduction of particles and the formation of



carbides. Thus, studies on other supports such as carbon, TiO<sub>2</sub>, and Al<sub>2</sub>O<sub>3</sub> would be desirable.

For understanding the fact that particles do not behave similarly, although appearing homogenous in size and shape, the same particles need to be observed before and after treatment by TEM measurements. Moreover, an electron energy loss (EEL) detector on the TEM would be required to map the composition of the particles. The EEL detector would also show the formation of iron-silicates and display whether the shell of the open particles produced by syngas is magnetite or not. Additionally, it would be interesting to explore the behavior of different sized particles; in other words to find out whether a particle size effect can be observed.

For all the above experiments (besides the ‘effect of passivation’ study) a TEM transfer-cell is required for the best possible ‘in-situ’ imaging of the particles [10,11]. In addition, all experiments would need to be performed under truly in-situ conditions at a synchrotron. XANES and EXAFS were shown to be feasible and maybe other techniques such as grazing-incidence small-angle X-ray scattering (GISAXS) to determine the shape of the particles can be applied as well [12,13]. The advantage of these techniques is that higher pressures can be investigated, which is an additional interesting variable to examine.

### 8.3 Final Words

Gaining more insight into the iron oxide nano particle behavior can help in developing a more active catalyst for not only the FT process, but also for the synthesis of ammonia, which is one of the most abundant produced inorganic chemical all over the world. Nevertheless, the focus of the research should eventually be shifted to the real catalyst system under operating conditions. High surface area mesoporous SBA may be considered as a suitable support, as it is applicable in TEM to visualize the catalyst [14]. Moreover, the support is perfect for in-situ measurements with XANES, EXAFS, and other synchrotron techniques [15].

Finally one should always consider to what extent studies on simplified model systems are suited to understand the behavior of a complex catalyst. As Albert Einstein said: ‘everything should be made as simple as possible, but not simpler’.

### References

- [1] J. K. Nørskov, T. Bligaard, A. Logadottir, S. Bahn, L. B. Hansen, M. Bollinger, H. Bengaard, B. Hammer, Z. Sljivancanin, M. Mavrikakis, Y. Xu, S. Dahl, C. J. H. Jacobsen, *J. Catal.* **209** (2002) 275.
- [2] Z.-P. Liu, P. Hu, *J. Chem. Phys.* **114** (2001) 8244.
- [3] Z.-P. Liu, P. Hu, *J. Am. Chem. Soc.* **125** (2003) 1958.

- [4] H. J. Borg, J. F. C. J. M. Reijerse, R. A. van Santen, J. W. Niemantsverdriet, *J. Chem. Phys.* **101** (1994) 10052.
- [5] M. J. P. Hopstaken, J. W. Niemantsverdriet, *J. Phys. Chem. B* **104** (2000) 3058.
- [6] D. C. Sorescu, *J. Phys. Chem. C* **112** (2008) 10472.
- [7] J. W. Niemantsverdriet, A. M. Van der Kraan, W. L. Van Dijk, H. S. Van der Baan, *J. Phys. Chem.* **84** (1980) 3363.
- [8] J. M. Gracia, F. F. Prinsloo, J. W. Niemantsverdriet, *Catal. Lett.* **133** (2009) 257.
- [9] D. P. Woodruff, T. A. Delchar, *Modern Techniques of Surface Science*, 2nd edition, Cambridge University Press, Cambridge, 1994.
- [10] S. Janbroers, J. N. Louwen, H. W. Zandbergen, P. J. Kooyman, *J. Catal.* **268** (2009) 235.
- [11] F. M. Ross, *Sci. Microsc.* **1** (2007) 445.
- [12] R. E. Winans, B. Lee, S. Seifert, S. Lee, J. W. Elam, M. J. Pellin, I. Barke, A. Kleiber, K. Sell, V. von Oeynhause, K. H. Meiwes-Broer, S. Vajda, *Prepr. Symp. - Am. Chem. Soc., Div. Fuel Chem.* **54** (2009) 114.
- [13] B. R. Fingland, F. H. Ribeiro, J. T. Miller, *Catal. Lett.* **131** (2009) 1.
- [14] Y. Li, Y. Guan, R. A. van Santen, P. J. Kooyman, I. Dugulan, C. Li, E. J. M. Hensen, *J. Phys. Chem. C* **113** (2009) 21831.
- [15] G. Du, S. Lim, M. Pinault, C. Wang, F. Fang, L. Pfefferle, G. L. Haller, *J. Catal.* **253** (2008) 74.



## Acknowledgments

Het klinkt als een cliché, maar de periode als promovendus is een tijd geweest die voorbij is gevlogen. Toch is deze periode niet zonder slag of stoot voorbij gegaan en had ik deze niet tot een goed einde kunnen brengen zonder de hulp van de volgende personen.

Te beginnen met mijn eerste promotor Hans. Zonder jou was dit alles natuurlijk niet mogelijk geweest. Ik wil je bedanken dat je mij deze kans hebt gegeven, nadat ik in eerste instantie gekozen had om mijn promotie bij Marc Koper te willen volbrengen, maar dit door zijn verhuizing naar Leiden niet is doorgegaan. Ik heb het altijd heel erg gewaardeerd dat je een enorm vertrouwen in mij hebt gehad dat ik deze promotie tot een goed einde zou brengen. In het bijzonder tijdens de momenten waarbij ik de wanhoop nabij was zorgde je er altijd weer voor dat de storm in mijn hoofd ging liggen. Wat ik buitengewoon op prijs heb gesteld was de vrijheid in mijn werk, waarbij ik zelf aan kon geven in welke richting ik graag mijn onderzoek zag gaan, waarbij je altijd oplette dat we het einddoel niet uit het oog verloren. Hans, bedankt voor al je steun tijdens de moeilijke periodes, je hulp bij het schrijven van artikelen en het continu ‘enHansen’ van presentaties.

Ten tweede wil ik mijn copromotor Dani bedanken voor de aangename discussies die we hadden tijdens je periode in onze groep. Jij hebt me kennis laten maken met de wereld die DFT heet, wat geleid heeft tot drie mooie artikelen in JPC. Dani, door je enorme kennis betreffende DFT berekeningen wist je altijd kritische vragen te stellen die me hoofdbrekkende uurtjes hebben bezorgd, maar uiteindelijk wel hebben bijgedragen tot een veel beter eindresultaat. Voor dit alles mijn dank.

Peter, de geweldige chaoot van de groep. Het is voor mij een plezier geweest om met je te werken en ik wil je bedanken dat je altijd tijd vrijmaakte om ideeën uit te wisselen. Zonder jouw hulp was het laatste hoofdstuk niet geworden zoals het nu is. Bovendien hebben onze goede discussies er mede voor gezorgd dat je mij coauteur gemaakt hebt van één van je laatste artikelen, iets waar ik me nog steeds zeer vereert door voel. Hopelijk zullen er nog mooie successen gaan volgen op het gebied van modelkats, waarmee je hopelijk Angewandte Chemie kunt scoren; ik gun het je van harte.

I would like to thank Jeffrey Miller for the opportunity to come to Chicago and perform measurements at the ANL beam line. It was a very nice learning-experience and I enjoyed working with you and with all the very nice people in your group. You were all very kind to me when I was there. Also thanks to all the staff working at ANL who helped in one way or another, I really appreciated it. My special thanks goes out to Neng, who picked me up from the airport in his new beamer and showed me Chicago in one of the most terrible rain storms I have ever experienced. Thanks for the wonderful day. Let me know if some day I can return the favor.

Maarten, 3 maanden na mij begonnen aan je promotie moesten wij de nieuwe UHV experts worden van onze groep, waarbij jij gewerkt hebt aan de 'green mean machine' en ik op de zilveren/oranje SIMS machine. Mede hierdoor, ben je mijn meest gewaardeerde collega geworden op het werk. Ik wil je bedanken voor alle hulp in het lab, de gezellige tijd die we samen hebben doorgebracht met het voeren van discussies (zowel nuttig als nutteloos), het doden van tijd door middel van stress balletjes spellen, pc spelletjes, race spelletjes in het lab, Tiny over de kook helpen, en andere 'nuttige' tijddodende zaken. Bedankt voor de gezelligheid tijdens de jaarlijkse N3C conferentie (waar je trouw waakte over mijn dekbed...), de Schiermonnikoogcursus, de ECOSS conferentie in Parijs, en dan nog die schitterende zomerschool in Århus, Denemarken, waarbij je dacht dat groene gobelin mannetjes je paspoort mee hadden genomen. Maar nu even zonder gekkigheid; tegen de tijd dat je dit leest zul je schitterende proefschrift al af hebben en wens ik je succes met je verdediging en met het vinden van een nieuwe baan. Het ga je goed.

Het werk in het lab was nooit zo vlekkeloos verlopen als we niet de hulp hadden gehad van onze Tinus. Ik heb veel bewondering voor je enorme kennis van alle apparaten die we in het lab hebben staan. Bedankt voor alle keren dat je geholpen hebt om het UHV apparaat weer helemaal in orde te maken wanneer dat nodig was. Verder wil ik je bedanken voor de gezelligheid die je in de groep brengt. Het kijken van cabaretstukjes, de nodige sport bloopers, K1 gevechten en formule 1 beelden heb ik zeer gewaardeerd.

Naast Tinus wil ik Wout bedanken voor al zijn tijd die hij gestoken heeft in het draaiend houden van het UHV apparaat. Ook de mensen van de GTD wil ik bij dezen bedanken voor alle goede zorg van het apparaat. Het is indrukwekkend dat jullie elke keer weer binnen een kort tijdsbestek mij uit de brand hebben weten te helpen.

I would especially like to thank my room mates of STW 3.49 Adelaida, Emiel, Noor, Gilbère, and Ajin for the nice working atmosphere. Adelaida, bedankt voor de prettige sfeer die je bezorgde in ons kantoor. Er waren slechts weinig dagen waarop jij niet kon zorgen voor een lach op mijn gezicht. Emiel, de bescheidenheid zelf, bedankt voor alle goede gesprekken (is er ook iets waar je niets van weet...?). Noor, thank you for the productive time here, and maybe one day I will come to Malaysia to see your beautiful country. Your green mug is still standing here in the office to remember you by. Gilbère, succes met je promotie (nog maar 2 jaar te gaan en die zijn om voor je het weet...) en hopelijk komen er nog mooie resultaten uit je onderzoek rollen. Ik wil je verder bedanken voor alle weekend warm-ups, het introduceren van de IJslandse muziekgenerator op ons kantoor en de SKA tripjes die je organiseerde. Lastly, good luck to you Ajin with your PhD project. You still have more than 3 years to go and I trust you make the most of it. For the both of you (Gilbère and Ajin): take care of our plant in the office.

Dan wil ik natuurlijk ook Thérèse-Anne en Marianne bedanken voor alle goede zorgen de afgelopen paar jaren. Bedankt voor de gezellige kletsuurtjes.

Furthermore, I would like to thank the following people; Vijay, Denzil, Prabashini, Henno, Kees-Jan, José, Akhtar, Ashriti, Başar, Murat, Elizabeth, Ernie, Wei Han, Bruce, Davy, Oguz, Cansin, Jonathan, Suriya, Jos W, Michèle, Arjan, Dennis, Bart, Patrick, Andreas, Jarno, Leandra, Laura, Jos O, Paul, Merijn, Christian, Ton, Emiel, and all other SKA members whose name I did not specifically mention here for all the nice group meetings and time together during the annual group trips, SKA seminars, Christmas drinks, and coffee breaks.

Buiten mijn collega's op het werk zijn mijn vrienden van onmisbaar belang geweest de afgelopen jaren. Bij dezen wil ik graag mijn goede vriend Thomas samen met zijn vriendin Amparo bedanken voor de fijne gesprekken elke dag tijdens de lunch en buiten het werk. Ik ga jullie beide ontzettend missen de komende 2 jaar dat jullie in Amerika zijn voor jullie postdoc. Ik wens jullie veel succes toe. Verder wil ik Bart en Ellen, Koen en Anje, Martin en Tom en Verena bedanken voor hun vriendschap de afgelopen jaren. Jullie zijn mij allemaal erg dierbaar.

Afgezien van mijn vrienden heb ik veel liefde en steun gekregen van mijn familie. Mam en pap, Els en Frits, ook al laat ik misschien niet altijd blijken dat ik het zeer waardeer wat jullie voor mij gedaan hebben en nog steeds doen, weet dat ik ontzettend trots ben op ouders zoals jullie. Bedankt voor alles. Ook mijn beide zussen Karen en Ellen wil ik hierbij natuurlijk niet vergeten. Ik ben buitengewoon trots op wat jullie de afgelopen jaren bereikt hebben in jullie leven. Het doet me bijzonder goed om jullie zo gelukkig te zien, wat mede komt door jullie partners Nico en Bart.

Buiten mijn eigen familie, heb ik er de laatste jaren ook een nieuwe familie bij gekregen, namelijk die van mijn vriendin. Ik had me geen betere 'schoonfamilie' kunnen wensen. De manier waarop jullie mij opgenomen hebben in de familie is hartverwarmend. Jan, José, Selma, Andor, Savannah, Tim en Jacqueline bedankt hiervoor. Verder wil ik ook graag oma Vermeulen en opa van Dorst mijn dank betuigen. Ik ben jullie de afgelopen jaren als mijn eigen oma en opa gaan zien. Jullie betekenen heel veel voor me. Ook al heeft oma van Dorst deze wereld een paar maanden geleden verlaten, toch wil ik ook nog een paar woorden tot haar richten en vertellen dat ook zij veel voor me betekend heeft en dat haar liefde die ze gaf nog steeds aanwezig is.

Als laatste wil ik mijn allergrootste liefde vanuit de grond van mijn hart bedanken dat ze me altijd is blijven steunen gedurende mijn promotietijd. Ik weet dat dit niet altijd even gemakkelijk voor je geweest is en daarom waardeer ik ook al je liefde die je me elke dag gegeven hebt en nog steeds geeft. Zonder jou was dit boekje er nooit gekomen. Jij hebt me echt door deze periode heen weten te loodsen en daarvoor kan ik je nooit genoeg bedanken. Lieve Ester dit boekje is voor jou.



## List of Publications

F.J.E. Scheijen, J.W. (Hans) Niemantsverdriet, D. Curulla Ferré, *Density Functional Theory Study of CO Adsorption and Dissociation on Molybdenum(100)*, J. Phys. Chem. C, **2007**, *111*, 3473.

F.J.E. Scheijen, J.W. (Hans) Niemantsverdriet, D. Curulla Ferré, *Adsorption, Desorption, and Dissociation of CO on Tungsten(100), a DFT Study*, J. Phys. Chem. C, **2008**, *112*, 7436.

F.J.E. Scheijen, D. Curulla Ferré, J.W. (Hans) Niemantsverdriet, *Adsorption and Dissociation of CO on Body-Centered Cubic Transition Metals and Alloys: Effect of Coverage and Scaling Relations*, J. Phys. Chem. C, **2009**, *113*, 11041.

M.M.M. Jansen, F.J.E. Scheijen, J. Ashley, B.E. Nieuwenhuys, J.W. (Hans) Niemantsverdriet, *Adsorption/Desorption studies of CO on a rhodium(100) surface under UHV conditions: A comparative study using XPS, RAIRS, and SSIMS*, Catal. Today, in press **2009**, DOI: 10.1016/j.cattod.2009.11.014.

P. Moodley, F.J.E. Scheijen, J.W. Niemantsverdriet, P.C. Thüne, *Iron oxide nanoparticles on flat oxidic surfaces – introducing a new model catalyst for Fischer-Tropsch Catalysis*, Top. Catal., submitted **2009**.

### Other Publications:

J. Peeters, A.R.A. Palmans, M. Veld, F. Scheijen, A. Heise, E.W. Meijer, *Cascade Synthesis of Chiral Block Copolymers Combining Lipase Catalyzed Ring Opening Polymerization and Atom Transfer Radical Polymerization*, Biomacromolecules, **2004**, *5*, 1862.

F.J.E. Scheijen, G.L. Beltramo, S. Hoepfener, T.H.M. Housmans, M.T.M. Koper, *The electrooxidation of small organic molecules on platinum nanoparticles supported on gold: influence of platinum deposition procedure*, J. Solid State Electrochem., **2008**, *12*, 483.





## Curriculum Vitae

Freek Scheijen was born on the 7<sup>th</sup> of March 1982 in Sittard, situated in Limburg, the most southern province of the Netherlands. After graduating from his secondary school "Bisschoppelijk College Echt" in 2000, he started the study Chemical Engineering at the Eindhoven University of Technology (The Netherlands). After obtaining his Bachelor of Science, Freek specialized in topics such as heterogeneous and homogeneous catalysis, surface chemistry, electrochemistry, and biochemistry. He did an internship at Johnson Matthey Technology Centre, situated in Reading (United Kingdom), working on the NENA project developing a method to test the activity of oxygen reducing catalysts for the production of hydrogen peroxide. In 2005 he obtained his Master of Science degree with honours on the subject of "Electrooxidation of small organic molecules on platinum nano particles supported on gold" under the supervision of prof. dr. M.T.M. Koper. In the same year he started as a PhD student in the group of Physical Chemistry of Surfaces under the supervision of prof. dr. J.W. Niemantsverdriet, where he worked on "The surface chemistry of CO on iron and other bcc metals". The most important results of this study are presented in this thesis.

Freek Scheijen werd geboren op 7 maart 1982 te Sittard. Na het atheneum aan het "Bisschoppelijk College Echt" afgerond te hebben in 2000, begon hij aan de studie Scheikundige Technologie aan de Technische Universiteit Eindhoven. Na het verkrijgen van zijn bachelorgraad, heeft Freek zich gespecialiseerd in onderwerpen zoals heterogene en homogene katalyse, oppervlakte chemie, electrochemie en biochemie. Hij heeft stage gelopen bij Johnson Matthey Technology Centre in Reading (Engeland), waar hij gewerkt heeft op het NENA project om een methode te ontwikkelen om zuurstof reducerende katalysatoren te testen op hun activiteit bij het produceren van waterstofperoxide. In 2005 verkreeg hij zijn graad als Master of Science (ir.) met lof afgesloten met een afstudeerproject genaamd: "Electro oxidatie van klein organische moleculen op platina nano deeltjes op een goud drager" onder supervisie van prof. dr. M.T.M. Koper. In hetzelfde jaar begon hij als promovendus in de Physical Chemistry of Surfaces groep van prof. dr. J.W. Niemantsverdriet, waar hij gewerkt heeft aan het onderwerp "De oppervlakte chemie van CO op ijzer en andere bcc metalen". De belangrijkste resultaten van deze studie zijn beschreven in dit proefschrift.

